博　士　論　文

Tsunami Vulnerability Assessment Using Integrative Remote Sensing and GIS Approaches

(統合的リモートセンシングと GIS を用いた津波脆弱性の評価)

Abu Bakar Sambah

Department of Environmental Science and Engineering
Graduate School of Science and Engineering
Yamaguchi University Japan
September 2014

A dissertation submitted in partial fulfillment of the requirements
for the degree of Doctor of Engineering

Commitee members:

Prof. Fusanori Miura (supervisor)
Prof. Norikazu Shimizu
Prof. Toshihiko Aso
Prof. Hideaki Nakamura
Assoc. Prof. Koji Asai

SUMMARY

The development of remote sensing technology and its applications including Geographical Information System (GIS) application enable the use of satellite imagery for mapping the distribution of an area damaged by a disaster and to assess vulnerable areas. Disaster mitigation and reconstruction plan due to tsunami can be implemented with various actions. An integration of spatial analysis through GIS application and multi-criteria analysis through Analytical Hierarchy Process (AHP) is one of the methods for tsunami inundation and impact assessment. The research aimed to apply a method that is easy, user-friendly, and flexible enough to be replicable. The main objective of this research is to develop an integrative remote sensing and GIS approach in tsunami vulnerability assessment.

This research is the first attempt to assess tsunami vulnerability using three different resolutions of DEM data, introduce the application of hydrological analysis and the use of soil-adjusted vegetation index in the input parameter, and develop the threshold of vegetation index, water index, soil index, and soil-adjusted vegetation index in the tsunami-inundated area observation. This research also introduces the possibility use of AHP in spatial multi-criteria analysis and the use of weighted-raster overlay in tsunami vulnerability mapping.

Chapter 4 describes about tsunami vulnerability mapping using different DEM data. The purpose of this chapter is to investigate the elevation data of SRTM V.4 and ASTER GDEM V.2 over the coastal area of Miyagi and Iwate Prefecture in comparison with GSI DEM for the application of tsunami vulnerability mapping. The parameter of elevation, slope, coastal proximity, and land use was used as the input parameters, and weighed raster overlay was applied to generate tsunami vulnerability map. Although the results using SRTM V.4 show close enough to the tsunami-reference data, but statistically, all DEM show non-significant different for the result of tsunami-inundation mapping.

Chapter 5 describes about remote sensing and multi-criteria analysis for tsunami vulnerability assessment in Kesennuma city, Miyagi Prefecture. The purpose is to develop a method for vulnerability assessment through integration of spatial data and remote sensing data using SRTM DEM and ALOS AVNIR-2 images. The hydrological analysis was introduced as one of the input parameters. NDVI was applied to create land use map, in which decision tree classification methods using vegetation index was applied. The results show that the elevation is the most influential parameter. Most of the high vulnerability area was spread along coastal area. The result shows similar to the historical data of tsunami event in the research area, where 17.68 km^2 of the area identified as inundated area.

Hydrological analysis shows the potential affected area by tsunami wave may spread far to the hinterland by the role of the river of water canal

Chapter 6 describes about the integration of spatial analysis for tsunami inundation and impact assessment in Ofunato city, Iwate Prefecture. The purpose is to assess the tsunami inundated and impact area by introducing the use of ASTER GDEM and soil-adjusted vegetation index (SAVI) as one of the input parameters. Spatial data modelling and raster calculator were used in the analysis. The results show that 8.13 km^2 of the building area in the research area were in the tsunami-inundated area, while the highest elevation in the inundated area was 20.5 m.

Chapter 7 describes about the application of remote sensing, GIS, and AHP for assessing tsunami vulnerability in Rikuzentakata city, Iwate Prefecture. The purpose is to develop a method for vulnerability assessment using integration of spatial data and AHP in a concept of spatial data modeling. High resolution of GSI DEM was introduced and used as input parameter, Moreover, modified soil-adjusted vegetation index (MSAVI) was introduced to generate vegetation density map. The results show that inundated area was 14.35 km^2, in which concentrated in the range elevation of 4.43 m.

Chapter 8 describes the use of remote sensing in observing tsunami-affected area. A different time acquisitions of ALOS AVNIR-2 images, before and after tsunami event, were used. This study aims to recognize potentially affected area by tsunami, and to develop a new method for extracting the required information from satellite images for the purpose of tsunami-affected area observation in the coastal area of Miyagi and Iwate Prefecture.

A suitable set of parameters can be applied to obtain a result that is close enough to that of a real event. The parameters of elevation, slope, coastal proximity, hydrological feature, vegetation, and land use that applied in this research are good enough in the tsunami vulnerability, tsunami inundation, and tsunami impact assessment. Due to the limitation of high resolution of DEM data in some area, the use of SRTM V.4 is powerful. High resolution of DEM data using particular methods of point interpolation, and the application of this study in other areas including tsunami run-up modelling and GIS approach to model evacuation time and evacuation route will be the future work.

CONTENTS

LIST OF FIGURE

LIST OF TABLE

PART I
INTRODUCTION, LITERATURE REVIEW, AND METHODOLOGY

CHAPTER 1
Introduction

1.1 Overview of Tsunami

1.1.1 General Description

As a series of waves created by an impulsive disturbance in the water body, tsunami cause severe damage to coastal areas. A tsunami wave could be less than 1 meter high in the open ocean and traveling at up to 800 km/hour in which the wave energy will be extended from the surface to the ocean floor. The wave energy of tsunami will be compressed into a much shorter distance when approaches the coastline and creating potentially large destructive to the coastal areas (National Geophysical Data Center/World Data Service (NGDC/WDS), 2014).

When the sea floor abruptly deforms and a bottom layer of water body displaces the overlying water vertically, tsunamis can be generated. One kind of earthquake that is related to the crustal deformation of the earth is tectonic earthquakes. When these earthquakes happen in the bottom of the sea, the water layer above the deformed area is displaced from its equilibrium position. Waves are formed as the displaced water mass, which occurs due to the impact of gravity. A tsunami can be generated when large areas of the sea floor subside.

In the deep water of the open ocean, the speed of tsunami waves can be up to 800 km/hour. Tsunami wave will slows dramatically when it approaches the coast, but its height can be 10 times or more and have catastrophic consequences to the coastal areas. As a result, the low-lying areas of the coast and the areas near bay mouths or tidal flats will be highly vulnerable to the tsunamis hazard.

Figure 1.1 describes a tsunami diagrams in which can be divided into four special events. Moreover, **Figure 1.2** concludes the distribution of tsunami in the world based on the effect and magnitude, which describes that mostly this event occurred in the “ring of fire”, a zone of active earthquakes and volcanoes, surrounds much of the Pacific Ocean.

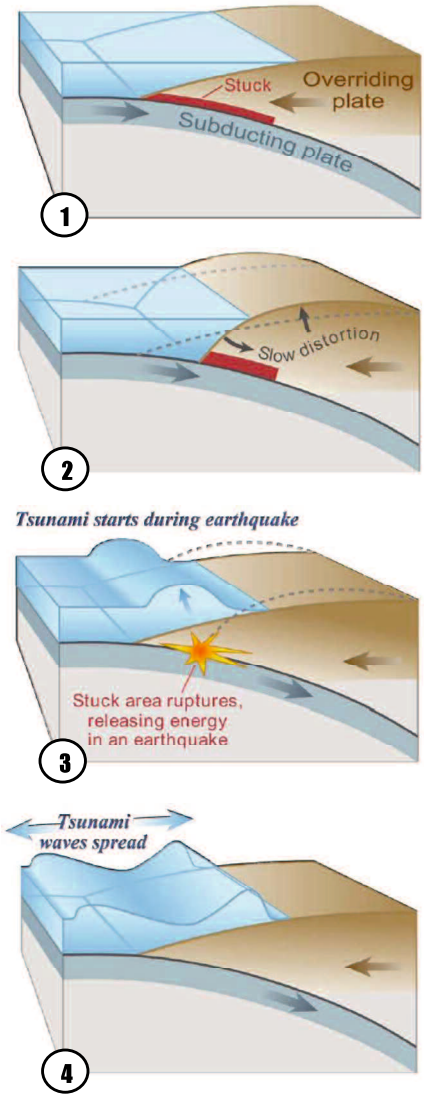

1. Subduction Zone

One of the many plates that make up earth's outer shell descent under an adjacent plate. This kind of boundary is called a subduction zone. When the plates move suddenly in an area where they usually stick, an earthquake will happens.

2. Between Earthquakes

Stuck to the subducting plate, the overriding plate gets squeezed. Its leading edge is dragged down, while an area behind bulges upward. This movement goes on for decades or centuries, slowly building up stress.

3. During Earthquakes

An earthquake along a subduction zone happens when the leading edge of the overiding plate breaks free and springs seaward, raising the sea floor and water above it. This uplift starts a tsunami. Meanwhile, the bulge behind the leading lead collapses, flexing the plate downward and lowering the costal area.

4. After Earthquakes

Part of the tsunami races toward nearby land, growing taller as it comes in to shore. Another part heads across the ocean toward distant shores.

Figure 1.1 Tsunami generation
(http://pubs.usgs.gov/circ/c1187/)

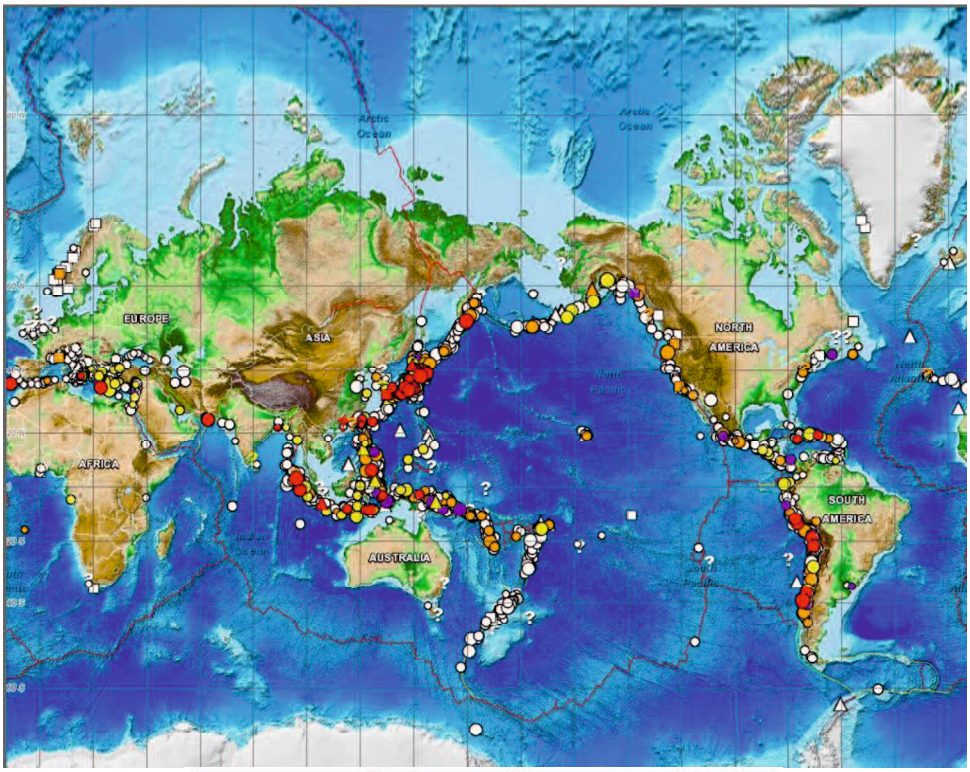

Effects of the tsunami	Volcanic eruption	Landslide	Unknown cause	Earthquake Magnitude ≥9	≥8	≥7	≥6	<6
Very many deaths (~1001 or more deaths)	▲	■	?	●	●	●	●	●
Many deaths (~101 to 1001 deaths)	▲	■	?	●	●	●	●	●
Some deaths (~51 to 100 deaths)	▲	■	?	●	●	●	●	●
Few deaths (~1 to 50 deaths)	▲	■	?	●	●	●	●	●
No deaths/Unknown	△	□	?	○	○	○	○	○

Figure 1.2 Tsunami distribution in the world based on the effect and magnitude (Modified from http://ngdc.noaa.gov)

1.1.2 Japan Tsunami

Located in one of the most active seismic and volcanic zones in the world, Japan is frequently affected by earthquakes and volcanic disasters. Japan Meteorological Agency (JMA) operationally monitors seismic and volcanic activities throughout the country and issues relevant warnings and information to mitigate damage caused by disasters related to earthquakes, tsunamis and volcanic eruptions.

In addition, during the periods of April 2006 until April 2013, JMA reported at least 51 events of earthquake around Japan with the magnitude of above 4.5, in which list of the historic tsunami on the Tohoku coast is shown in **Table 1.1**. Earthquake distribution of the major earthquakes that occurred around Japan is shown in **Figure 1.3**, while **Figure 1.4** describes the different magnitude of recent

earthquake that shows the comparison between Japan tsunami and other tsunami events in some countries.

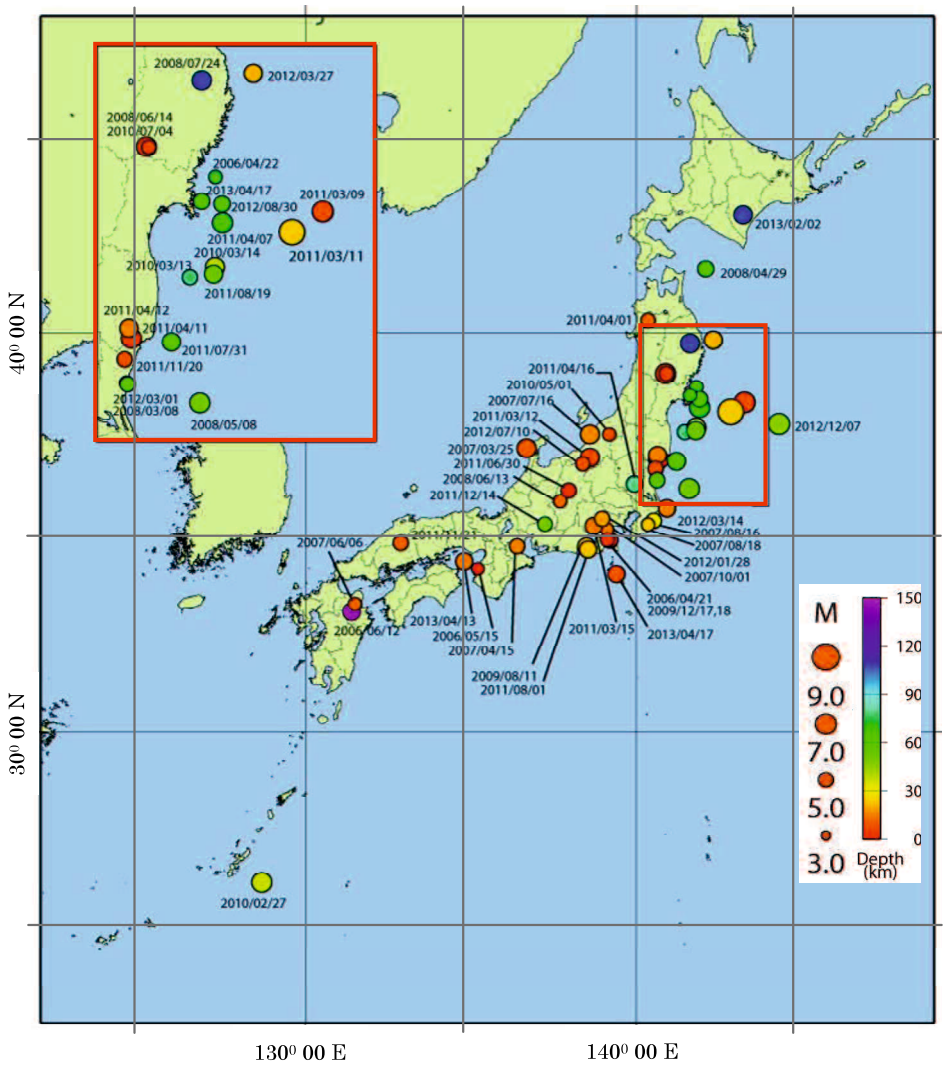

Figure 1.3 Epicenter distribution of the major earthquakes that occurred near Japan (http://www.jma.go.jp/jma/en/Activities/earthquake.html**)**

Table 1.1 Historic tsunami on the Tohoku coast
(Yeh and Stein, 2011; Kawasaki et al., 2011; EERI Special Earthquake Report, 2011)

Year	Earthquake	M	Max. run up height (meters)
869	Jogan-Sanriku	M 8.3 – 8.6	Paleo-tsunami sand deposit found 4 km inland on Sendai plain
1611	Keiho-Sanriku	M 8.1	20 m
1896	Meiji-Sanriku	M 8.2 – 8.5	38 m
1933	Showa-Sanriku	M 8.1	28.7 m
1960	Chile	M_w 9.5	5.3+ m
2011	Great East Japan	M_w 9.0	38 – 40 m

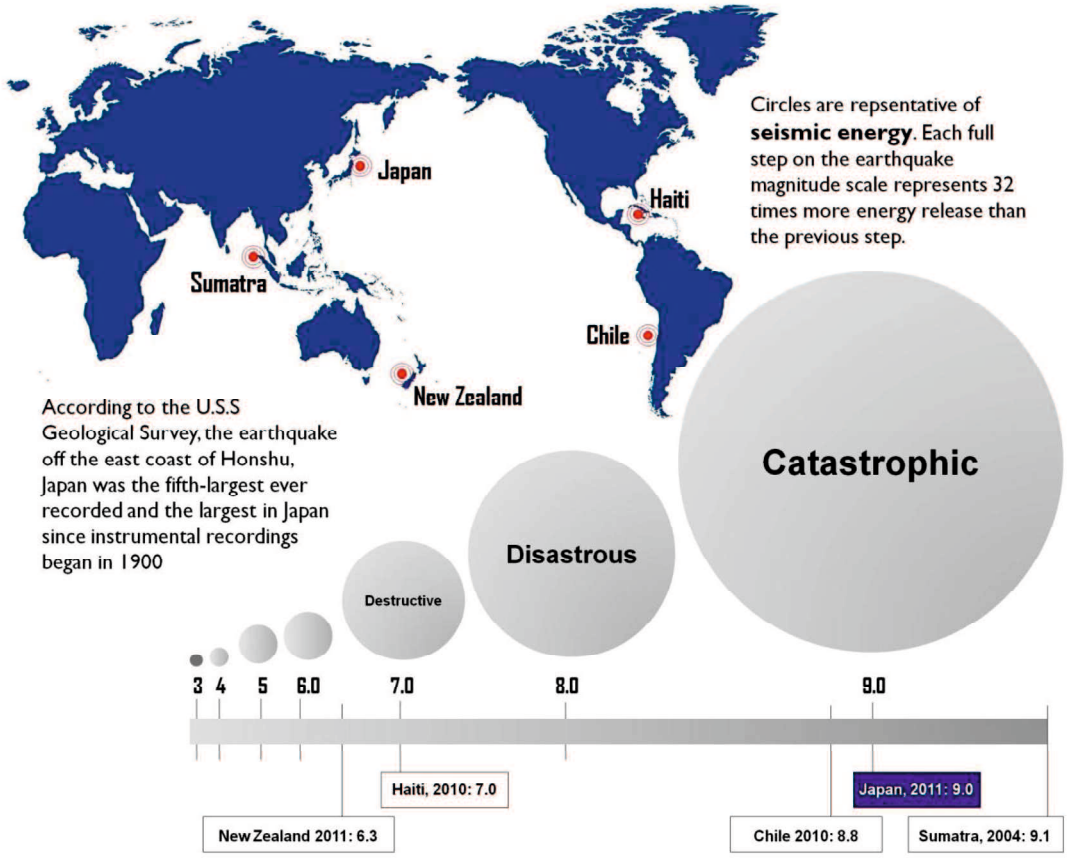

Figure 1.4 The different Magnitude of recent earthquake
(modified from http://www.ouramazingplanet.com and McConnell, 2012**)**

A massive earthquake of magnitude of 9.0 occurred Friday 11 March, 2011 off the Pacific coast of the northeastern part of the Japanese main land (Tohoku Region), causing devastating damages. The JMA named this earthquake "The 2011 off the Pacific coast of Tohoku Earthquake." The earthquake triggered a devastating tsunami that inundated the northeast coast of Japan within minutes (http://www.jma.go.jp/jma/en/2011_earthquake/Information_on_2011_earthquake.html)

The scale and severity of losses - human, economic, debris generated - were extraordinary, creating unprecedented challenges for emergency management, sheltering, housing, and recovery planning. Current loss estimates indicate 22,626 persons killed or missing nationwide (of which 15,534 are confirmed deaths), 107,000 buildings collapsed, and another 111,000 partially collapsed (National Police Agency, 2011; EERI Special Earthquake Report, 2011).

U.S Geological Survey reported a shake map of the 2011 Tohoku earthquake that related to the earthquake intensity and potential damage. Moreover, after the earthquake occurred, the 2011 Tohoku Earthquake Tsunami Joint Survey Group reported the potential tsunami inundation and run up in Tohoku coast. This report describes that mostly tsunami inundation and run up concentrated in the coastal area of Miyagi Prefecture and Iwate Prefecture, in the latitude of 40^0. Tsunami run up was identified reach the height of 40 meters (See **Figure 1.5 (b)** and **(c)**).

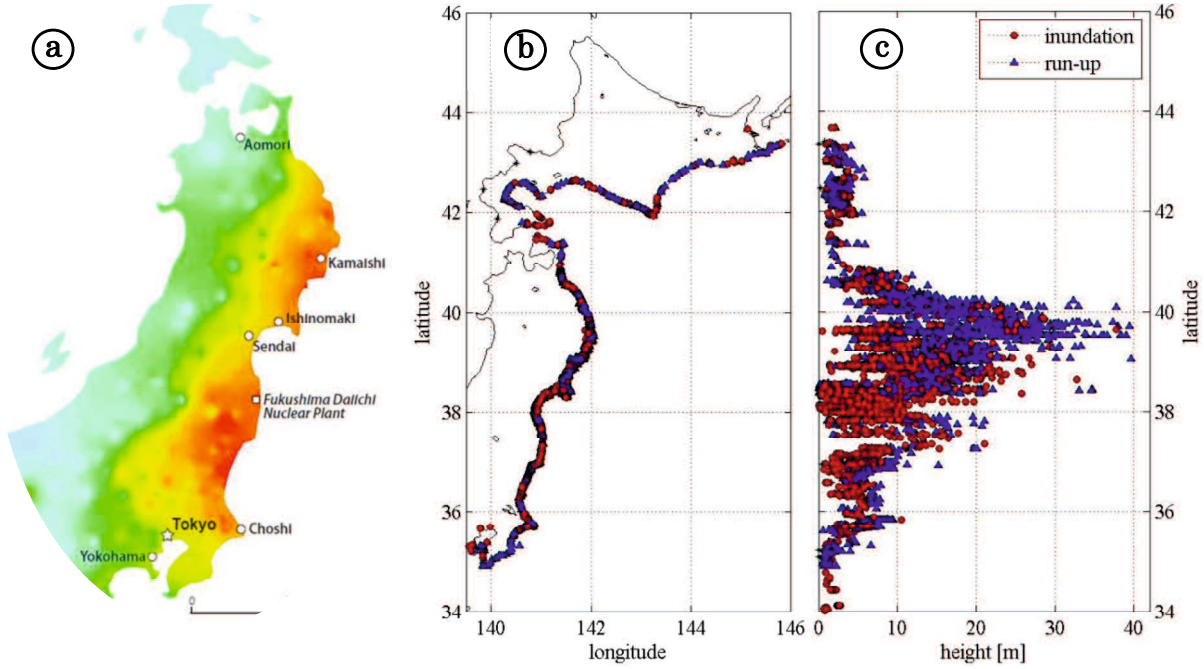

Figure 1.5 (a) Shake map of the 2011 Tohoku earthquake (http://earthquake.usgs.gov/earthquakes/shakemap); (b) Tsunami inundation and run-up from the 2011 Tohoku Earthquake Tsunami Joint Survey Group based on latitude and longitude information; (c) Tsunami inundation and run-up from the 2011 Tohoku Earthquake Tsunami Joint Survey Group on 29 December 2012 based on height (meter) (Mori et al., 2011)

The map in **Figure 5(a)** is designed as rapid response tools to portray the extent and variation of ground shaking throughout the affected region immediately following significant earthquakes. The color ramp in this map is described by the intensity classes as shown in **Table 1.2**.

Table 1.2. The intensity classes of ground shaking
(http://quake.abag.ca.gov/shaking/mmi/)

Perceived Shaking	Not felt	Weak	Light	Moderate	Strong	Very strong	Severe	Violent	Extreme
Potential Damage	None	None	None	Very light	Light	Moderate	Moderate/heavy	Heavy	Very heavy
Intensity	I	II-III	IV	V	VI	VII	VIII	IX	X+
Description	Not felt	II. Felt by people sitting or on upper floors of buildings III. Felt by almost all indoors. Hanging object swing. Vibration like passing of light trucks. May not be recognized as an earthquake.	Vibration felt like passing of heavy trucks. Stopped cars rock. Hanging objects swing. Windows, dishes, doors rattle. Glasses dink. In the upper range of IV, wooden walls and frames creak	Felt outdoors. Sleepers wakened. Liquids disturbed, some spille. Small unstable objects displaced or upset. Doors swing. Picture move. Pendulum docks stop.	Felt by all. People walk unsteady. Windows crack. Dishes, glassware, knickknacks, and books fall off shelves. Pictures off walls. Furniture moved or overturned. Weak plaster, adobe buildings, and some poorly built masonry buildings cracked. Trees and bushes shake visibly	Difficult to stand or walk. Noticed by drivers of cars. Furniture broken. Damage to poorly built masonry buildings. Weak chimneys broken at roof line. Fall of plaster, loose bricks, s tiles, cornices, stones, unbraced parapets and porches. Some cracks in better masonry buildings. Waves on ponds	Steering of cars affected. Extensive damage to unreinforced masonry buildings, including partial collapse. Fall of some masonry walls. Twisting falling of chimneys and monuments. Wood-frame houses moved on foundations if not bolted; loose partition walls thrown out. Tree branches broken.	General panic. Damage to masonry buildings ranges from collapse to serious damage unless modern desig wood-frame structures rack, and, if not bolted, shifted off foundations. Underground pipes broken.	Poorly built structures destroyed with their foundations. Even some well-built wooden structures and bridges heavily damaged and needing replacement. Water thrown on banks of canals, rivers, lakes, etc. Pipelines may be completely out of service

1.2 Research Motivation

It is impossible to reduce the occurrence of natural phenomena such as tsunamis that cause disasters, but the impact of these events can be minimized by performing an initial assessment by mapping vulnerable areas. Together with hazard probability, exposure, and capacity measures, vulnerability is one of the parameters used to determine disaster risk (Pelling, 2003; Bollin *et al*., 2003).

The development of remote sensing technology and its applications enable the use of satellite imagery for mapping the distribution of an area damaged by a disaster and to assess vulnerable areas. Satellite images have the advantage of being able to deliver simultaneous images of wide areas (Karen *et al*., 2009; Yamazaki *et al*., 2006; Yamazaki and Matsuoka, 2007). In addition, with the aid of the Geographical Information System (GIS), spatial multi criteria analysis helps prioritize the decision-making process using geo-reference data. Spatial multi criteria analysis is vastly different from conventional Multi Criteria Decision Making (MCDM) techniques, due to the inclusion of an explicit geographic element. In contrast to conventional MCDM analysis, spatial multi criteria analysis uses information on both the criterion values and the geographical positions of alternatives, in addition to the decision maker's preferences with respect to a set of evaluation parameters

(Carver, 1991; Jankowski, 1995).

Some of the previous studies on tsunami vulnerability have analyzed remote sensing data, primarily to assess the physical vulnerability and risk of coastal areas. In addition to such studies, the application of remote sensing in hazard and vulnerability assessment related to ecological and socio-economic vulnerability has been analyzed. Previous studies have also applied moderate-resolution optical satellite images and integrated analysis using GIS to identify inundation areas due to tsunamis (Eckert *et al*., 2012; Romer *et al*., 2012; Mahendra *et al*., 2011; Strunz *et al*., 2011). GIS mapping of tsunami vulnerability has also applied using the Shuttle Radar Topography Mission (SRTM) to obtain the topographic data of the study area (Sinaga *et al*., 2011). Another spatial analysis method has applied soil type, urban form and social type system for the potential natural hazard mapping (Hsien and Sheng, 2011) and has determined the tsunami-vulnerable area by comparing building damage map with the topography data, which is discussed with regard to land elevation, land use, and the distance from the coast (Gokon and Koshimura, 2012). Mapping of the 2011 Tohoku earthquake tsunami inundation and run-up by survey also has been published (Mori *et al*., 2011).

A novel approach from the Coastal Risk Analysis for Tsunamis and Environmental Remediation (CRATER) project was applied for assessing tsunami vulnerability on a regional scale using ASTER imagery and SRTM-version 3. This work analyzed the vulnerability of coastal zones and inland areas using the parameters of infrastructural, geo-morphological and ecological features for coastal zones, and parameters of land use, altimetry and distance from the shoreline for inland areas (Dall'Osso *et al*., 2010). The Papathoma Tsunami Vulnerability Assessment (PTVA) model is a useful tool for providing initial assessments of the vulnerability of buildings (Papathoma *et al*., 2003; Papathoma and Dominey-Howes, 2003). In addition, a critique of previous studies was undertaken to revise the original PTVA model by taking account of newly published data related to attributes affecting building vulnerability to tsunamis, and to introduce the use of multi-criteria analysis and Analytical Hierarchy Process (AHP) (Dall'Osso *et al*., 2009).

This research tried to propose the use of some data, input parameters, and methodologies for tsunami vulnerability and impact assessment that can be apply

easily in any part of the world. Many study is dealing with vulnerability mapping using social point of view, many of them propose a numerical model to assess tsunami risk, this study take a part in proposing an integrative analysis of remote sensing data and GIS in the assessment of tsunami vulnerability and impact. For this propose, in general, the dissertation will introduce several methodology and data processing, starts from the comparison of Digital Elevation Model data from different product for tsunami vulnerability mapping, and followed by the analysis of remote sensing data and multi-criteria analysis through the use of AHP for tsunami vulnerability mapping that applied in three areas in Japan where got the impact of the 2011 Tohoku earthquake. The potential use of satellite remote sensing image analysis for tsunami impact assessment will be described in the last chapter.

The diagram on **Figure 1.6** describes research motivation.

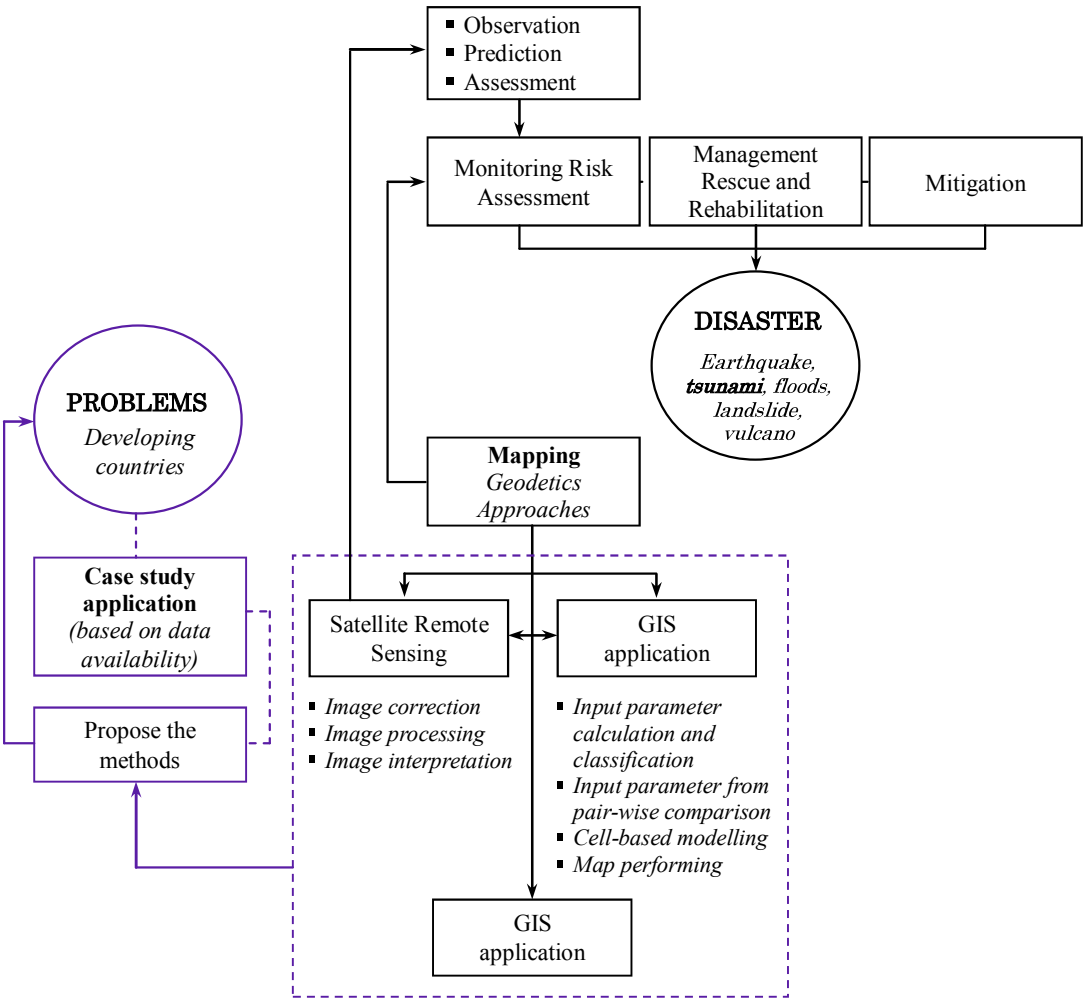

Figure 1.6 Flow diagram describes research motivation

1.3 Research Problem

The research is devoted to provide decisive parameters for an efficient tsunami vulnerability assessment in order to reduce the impact of tsunami. For this purpose, different research aspects and approaches are examined. The research questions that will be answered are stated below.

Problems were found :

- Due to the intensity of tsunami occurrences in Japan and other Asian countries, tsunami can cause human, physical and economic losses. The study of tsunami vulnerability mapping is important to reduce the impact of disaster.
- To reduce the impact of tsunami, a better mapping of vulnerability area and rapid observation is necessary due to the limit of the time when disaster occurred.
- The method that is applied to tsunami vulnerability mapping is various, using complex algorithm and numerical modeling. Using integrative remote sensing and GIS is a chance to contribute one of the methods in tsunami vulnerability assessment.

1.4 Research Scope and Objectives

The objectives of this research are :

1. To develop an integrative remote sensing and GIS approach in vulnerability assessment to tsunami hazard.
2. To develop methods for tsunami vulnerability assessment using integration of spatial data and AHP in a concept of spatial data modeling.
3. To identify the areas that vulnerable and potentially affected by tsunami hazard.
4. To develop a concept and method for extracting the required information from satellite images for early-disaster observation in the scope of tsunami impact assessment.

1.5 Research Structure and Outline

This research is dealing with vulnerability mapping due to tsunami hazards in which remote sensing approach was applied in order to prepare the entire data. The analysis was carried out using spatial multi-criteria analysis through AHP and GIS work. The main target of this study is vulnerability mapping, and analysis of satellite images to assess the impact of tsunami hazards. All study cases are in Japan, both Miyagi and Iwate Prefecture. The study tried to propose a method that can be apply to other places.

The dissertation is divided into two parts. The first part contains an introduction and overview of general issues in chapter 1. The second part of this dissertation contains a research work at three different study areas and the analysis of remote sensing data. **Figure 1.7** describes outline of the dissertation.

The dissertation is organized into eight chapters, as follows:

Chapter 1

Introduction of the research is described in this chapter. The chapter discusses the general introduction and basic motivation of this research. The research problem and research scope are listed and the research objectives are given.

Chapter 2

This chapter describes literature review. This chapter explains the concept of remote sensing and Geographical Information System in disaster observation and vulnerability study. This chapter focuses on the theoretical, conceptual and practical backgrounds of the research topic. Closely related topics discussed in this chapter include vulnerability concepts and methods.

Chapter 3

This chapter discusses data that used in this research and research methodology. The technical procedures and steps also explained in this chapter. Technical procedures and steps include parameter definition, processing of raw data, and application of remote sensing and GIS in vulnerability assessment.

Chapter 4

Chapter 4 describes the results of this research. The results presented in this chapter show the comparison of Digital Elevation Model (DEM) from different data source in tsunami vulnerability mapping.

Chapter 5

Chapter 5 describes the results of this research. The results are presented sequentially based on the steps of the methodology. The results presented in this chapter show the vulnerability mapping in research area-1. Pre-processing of data, satellite image analysis, and vulnerability classification were explained.

Chapter 6

Chapter 6 describes the results of this research. The results are presented sequentially based on the steps of the methodology. The results presented in this chapter show the vulnerability mapping in research area-2 using different input parameter.

Chapter 7

Chapter 7 describes the results of this research. The results are presented sequentially based on the steps of the methodology. The results presented in this chapter show the vulnerability mapping in research area-3 using different input parameter.

Chapter 8

Chapter 8 describes the results of this research. The potential use of remote sensing in tsunami impact assessment is presented in this chapter.

Chapter 9

Chapter 9 presents the conclusions of the research.

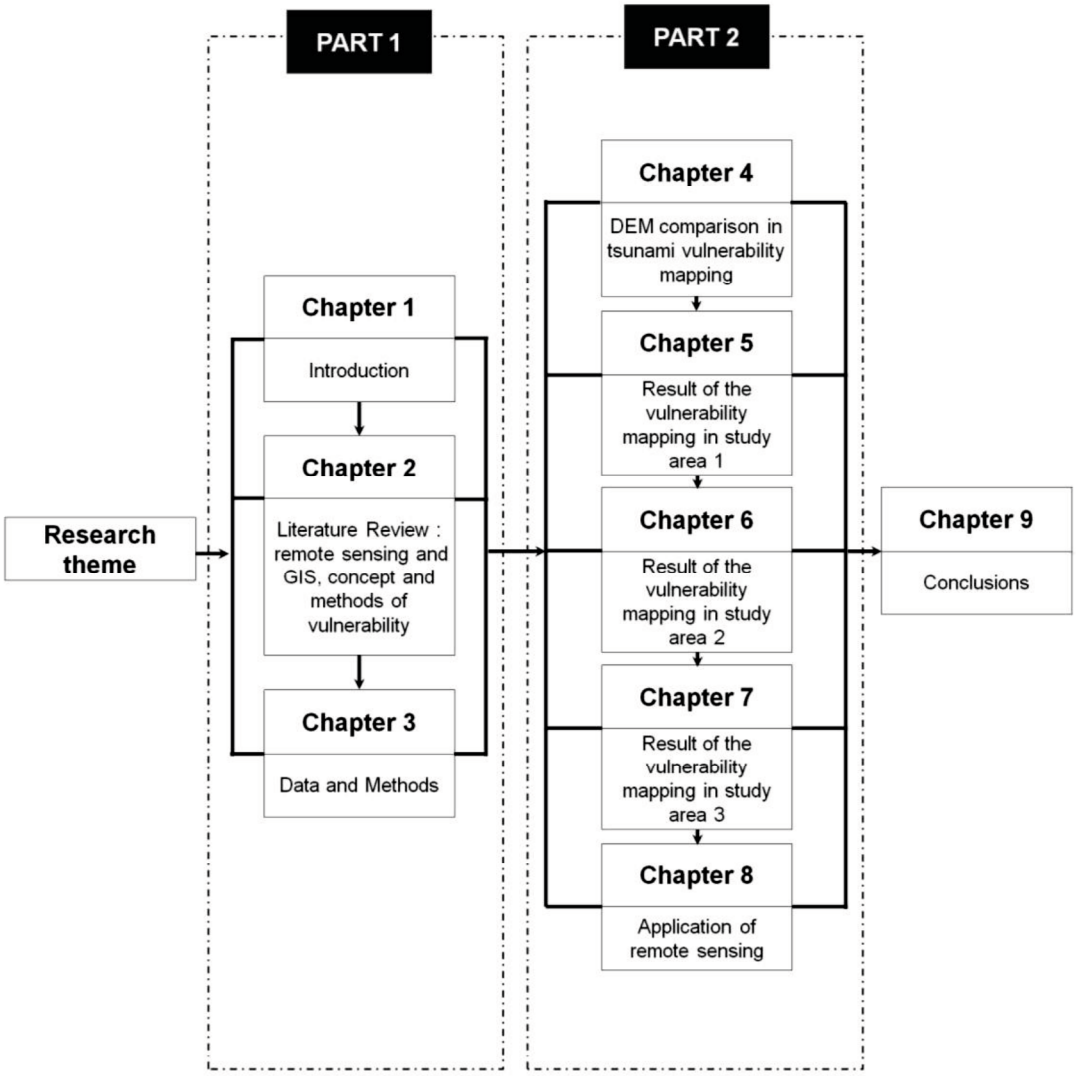

Figure 1.7 Outline of the dissertation

1.6 Overview of Study Area

The research was conducted in three study areas; Kesennuma city in Miyagi Prefecture Japan, Rikuzentakata city and Ofunato city in Iwate Prefecture Japan (see **Figure 1.8**). Those areas were affected by tsunami attack during the 2011 Tohoku earthquake in which 4,062 peoples were dead and missing (see **Table 1.3**).

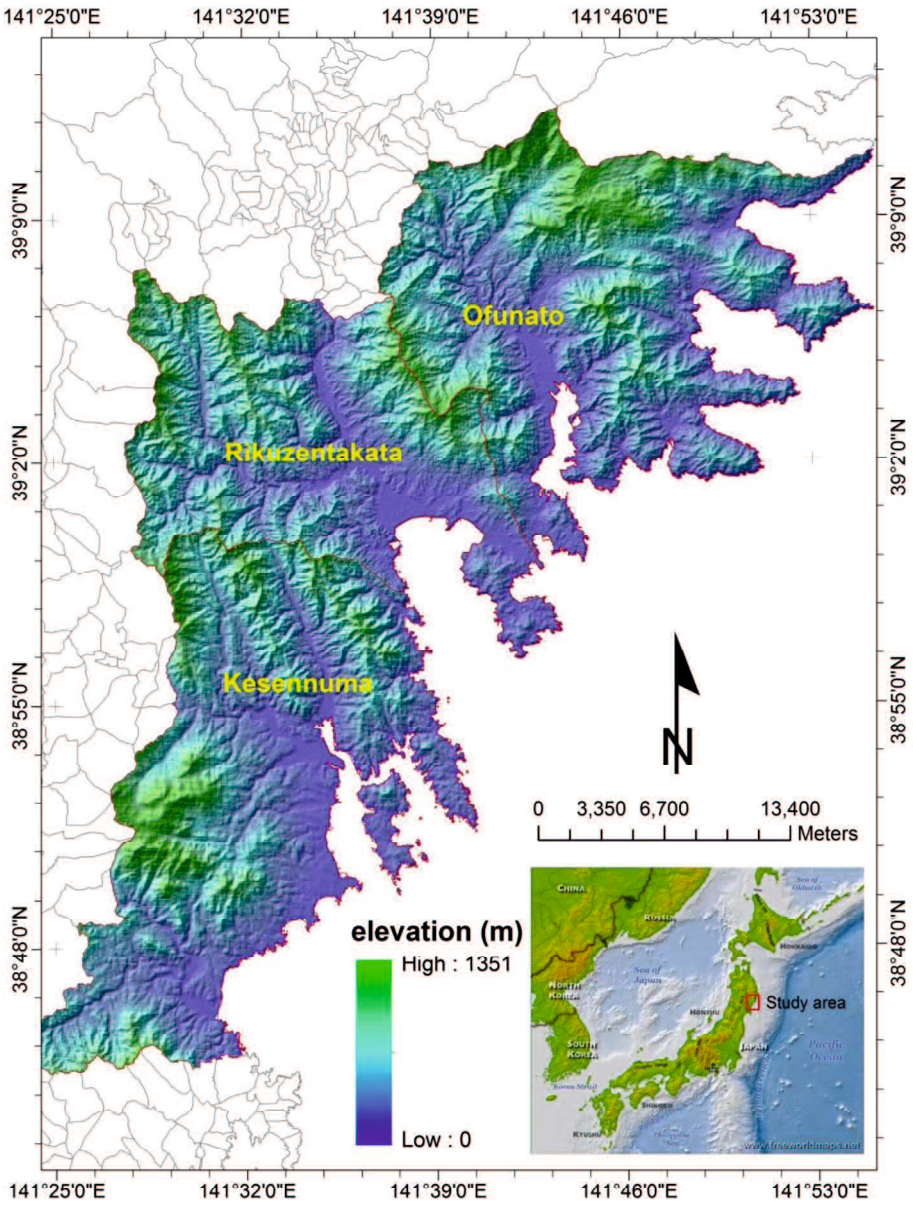

Figure 1.8 Map of study area

Tabel 1.3 Population and casualties in Town and cities that affected by tsunami of the 2011 Tohoku earthquake
(EERI Special Earthquake Report, 2011)

Town/City [1]	Population in 2010[2] [A]	Dead and Missing Persons[4]	
		Number[2,3] [B]	As Percent of Population [A/B]
Kuji	36,900	4	0.01%
Miyako	59,400	772	1.3%
Otsuchi	15,300	1,606	10.5%
Kamaishi	39,600	1,253	3.2%
Ofunato	40,700	462	1.1%
Rikuzentakata	23,300	2,133	9.2%
Kesennuma	73,500	1,467	2.0%
Minamisanriku	17,400	1,205	6.9%
Ishinomaki	160,700	5,867	3.7%
Sendai	1,046,000	755	0.07%
Natori	73,100	1,026	1.4%

Notes:
[1] Many of these towns/cities consist of an amalgamation of several smaller, geographically separate communities
[2] Source from Statistical Bureau, Government of Japan
[3] Reported as of 06/16/2011. Sum of numbers of dead and missing persons.
[4] As of 07/05/2011, the National Police Agency reported 15,534 dead and 7,092 missing in the entire event, for a total of 22, 626. Of these 6,744 were in Iwate Prefecture, 13,910 in Miyagi Prefecture, 1,902 in Fukushima, and 70 in 9 other prefectures.

1.6.1 Kesennuma city, Miyagi Prefecture

Kesennuma city is located in the northeast of the Miyagi Prefecture in Japan (see **Figure 1.9**). It wraps around the western part of Kesennuma Bay and includes the island of Oshima. Its coastline forms the southern boundary of the Rias Coastline National Park, which stretches north all the way to the Aomori Prefecture. Kesennuma city borders Hirota Bay, Kesennuma Bay, and the Pacific Ocean to the east, and Minamisanriku town, Miyagi Prefecture, to the south. Iwate Prefecture makes up the remainder of its borders, with Murone village to the west and Rikuzentakata city to the north.

The highest point in Kesennuma city is 711.9 m above sea level, on the border with Motoyoshi, while the lowest point is at sea level. The total area of Kesennuma city is 333.38 km^2 and the population of this area is 73,489, with a density of 220.4/km^2. The Kesennuma city was chosen as our study area based on the fact that the

2011 Tohoku earthquake had a big impact there, and it was reported as one of the areas with the largest number of casualties in the Miyagi Prefecture. Large sections of the city were destroyed by the 2011 Tohoku earthquake and tsunami and major fires on March 11, 2011.

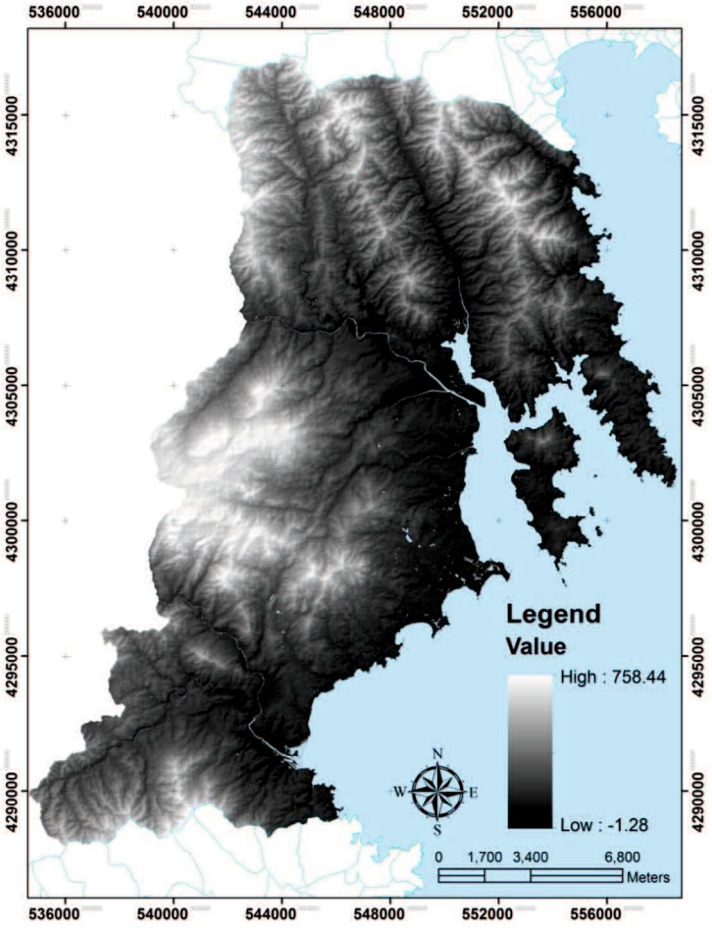

Figure 1.9 Map of Kesennuma city.
(Legend on the map describes value of elevation)

Kesennuma city is a port community located at the end of a long, narrow ria in northern Miyagi Prefecture. The city is the largest population center between Kuji and the Oshika Penninsula, the region closest to the earthquake's epicenter. The first tsunami wave crashed ashore at the head of Kessenuma Bay 20 minutes after the seismic event. The sea rose to heights in excess of 18 m at the bay mouth, funneling a tremendous volume of water into the 8 km long leading to the city (Kakinuma, Tsujimoto, Yasufa et al. 2012). As the tsunami passed through the Kesennuma narrows, flow-velocities exceeded 0.025 km/hour (Fritz et al., 2012). A survey team

found that the run-up heights at the end of Kesennuma Bay were slightly lower than those found in adjacent communities, but the damage was equally as catastrophic. An inundation height of 7.9 m was found in Kesennuma Port, whereas a height of 11.8 m was found a short distance away at the head of the Okawa River (Mikami et al., 2012).

1.6.2 Rikuzentakata city, Iwate Prefecture

Rikuzentakata is a city located in Iwate Prefecture, Japan (see **Figure 1.10**). The city was founded on January 1, 1955. In the quinquennial census of 2010, the city has a population of 23,302 and a population density of 100 persons per km² (Ministry of Internal Affairs and Communications, 2011). Rikuzentakata city in southern Iwate Prefecture was one of the cities hardest hit by the 2011 Tsunami. Caught unprepared for an event of such magnitude, the city center was damaged as the result of the 13 meter high waves that swept away the majority of the buildings and homes.

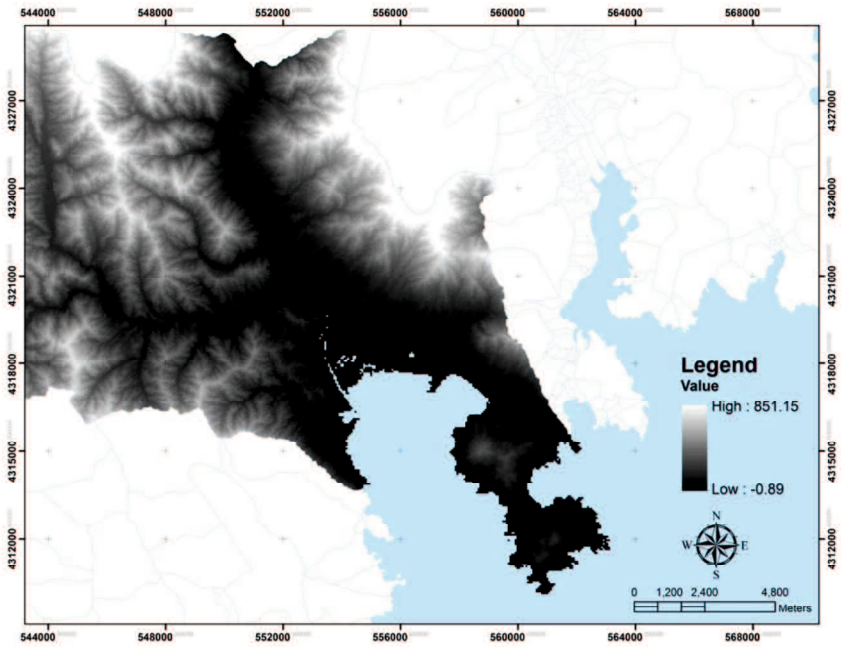

Figure 1.10 Map of Rikuzentakata city.
(Legend on the map describes value of elevation)

Rikuzentakata city is located in a large, hammerhead-shaped bay near the southern border of Iwate Prefecture. The city, like most along the jagged Tohoku coastline, is notoriously vulnerable to tsunamis. Several damaging events have impacted the area in the past 100 years, the most severe being the 1960 Pacific Ocean

tsunami, which originated 16,093 km away in Chile. In order to combat the threat of tsunamis, the city built an elaborate harbor barrier and planted a forest of 70,000 pine trees as a shoreline buffer. Rikuzentakata city experienced the most catastrophic damage of any city affected by the tsunami. Inundation heights over 16.8 m were surveyed throughout the city, and a run-up height of 21.3 m was found inland and just east of the bay center (Liu et al., 2013). Flow-depths between 13.1 m and 15.2 m were surveyed in the primary residential area of Rikuzentakata city (Yeh, et al., 2013).

1.6.3 Ofunato city, Iwate Prefecture

Ōfunato is a city located in Iwate Prefecture, Japan (see **Figure 1.11**). As of February 2014, the city had an estimated population of 38,616 and a population density of 119 persons per km². The city of Ofunato suffered severe damage in the 2011 tsunami. Like many port communities in the area, the city is located at the end of a long with a narrow entrance to the Pacific Ocean. Amateur footage from the city indicates that the tsunami commenced as a deceptively subtle sea level rise along the bay-front. As the tsunami funneled through the narrow waterway towards the city, Ofunato Bay turned into a raging river of mud and debris. The water reversed the Sakari River and sent torrents of water upstream, spilling over floodwalls and enveloping city streets. Residents in the bottom floors of buildings near the port were overcome as the freezing waters rose above second floor ceilings.

The inundation height of the tsunami averaged approximately 8.5 m in Ofunato city, half the value surveyed in many adjacent areas. The shorefront property in the city was destroyed, with many wood-framed structures swept completely away. Apartment complexes nearly 3 km up the Sakari River were severely damaged by the surge, and tracts of commercial buildings on the western shore of Ofunato Bay were left as bare concrete slabs. The city's large industrial area likely buffered residential areas farther inland, reducing the death toll to under 500. Tsunami height: 7.9 – 9.4 m (http://extremeplanet.me/2014/02/04/detailed-imagery-of-the-2011-japan-tsunami/comment-page-1/)

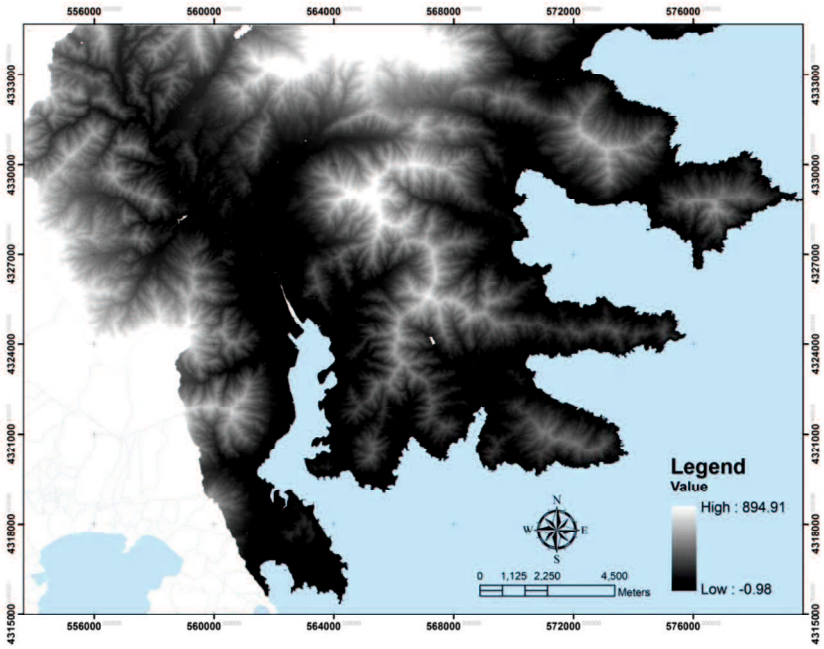

Figure 1.11 Map of Ofunato city.
(Legend on the map describes value of elevation)

CHAPTER 2
Literature Review

2.1 Vulnerability: a definision

A disaster occurs when a significant number of vulnerable people experience a hazard and suffer severe damage and disruption of their livelihood system in such a way that recovery is unlikely without external aid (Blaikie, 1994). Turner and Kasperson (2003) developed one of the most comprehensive multidimensional vulnerability frameworks which focuses particularly on the linkages and feedbacks between social and ecological systems and thus does not restrict analyses to humans but rather looks at the integrated vulnerability of human-environment systems.

The developers of the framework see vulnerability in a wider context of global environmental change and sustainability science, which aims to understand the functioning and inter-linkages of human-environment systems as a reaction to these ongoing global changes.

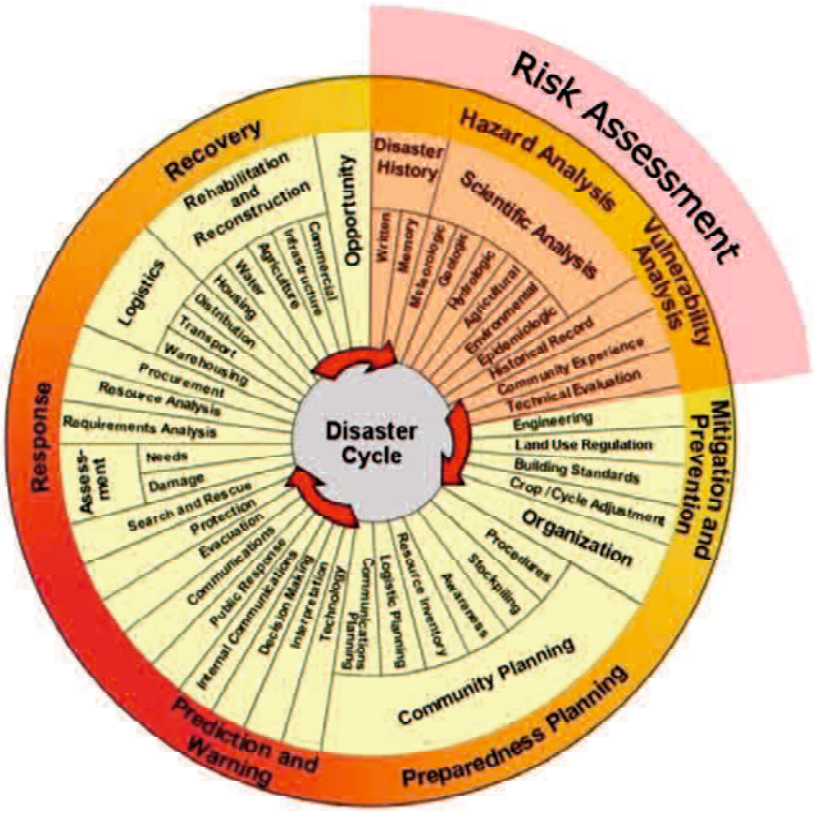

Figure 2.1 The "traditional" disaster cycle and the role of risk assessment
(UN-ISDR, 2005)

A general strategy for disaster risk reduction must firstly establish the risk management context and criteria, and characterize the potential threats to a community and its environment (hazard); secondly it should analyze the social and physical vulnerability and determine the potential risks from several hazardous scenarios in order to, finally, implement measures to reduce them (see **Figure 2.1**). The final goal, reduction of disaster risk in the present and control of future disaster risk, should be achieved by combining structural and non-structural measures that foster risk management as an integrating concept and practice which are relevant and implemented during all stages of a community's development process and not just as a post-disaster response. Disaster risk management requires deep understanding of the root causes and underlying factors that lead to disasters in order to arrive at solutions that are practical, appropriate and sustainable for the community at risk (UN/ISDR, 2004).

Multiple definitions and different conceptual frameworks of vulnerability exist, because several distinct groups have different views on vulnerability. Academic staff from different disciplines, Disaster management agencies, development corporations, climatic change organization etc. An overview is given on the website of the ProVention Consortium (http://www.proventionconsorti um.org/) and in the book on Vulnerability edited by Birkmann (2005).

The first definition is still related only to physical vulnerability while in the other definitions we find that vulnerability is influenced by several factors, mostly mentioned are physical, economic, social and environmental factors. The definitions of vulnerability of Provention and Blaikie clearly show that besides vulnerability the elements at risk also have capacities. According to the UN, in their report Living with Risk (UN/ISDR, 2004), risk is rooted in conditions of physical, social, economic and environmental vulnerability that need to be assessed and managed on a continuing basis (**Figure 2.2**).

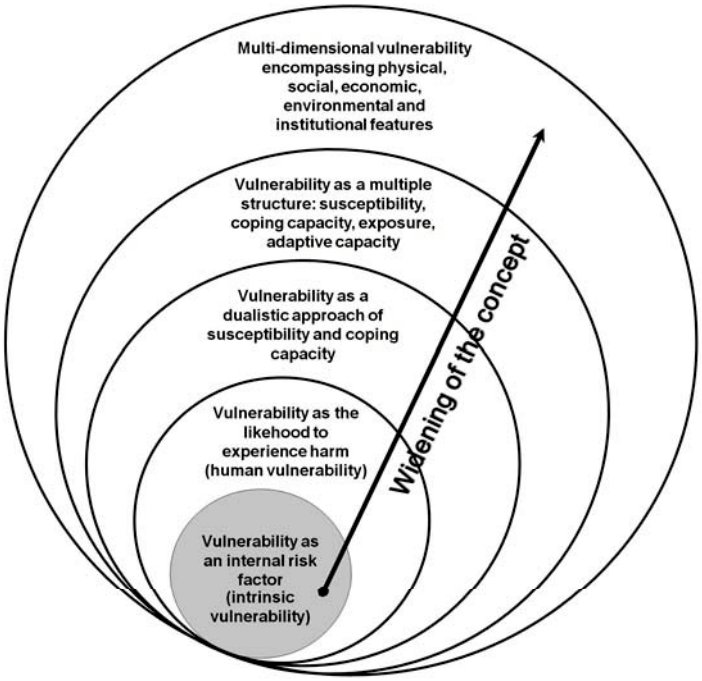

Figure 2.2 Key spheres of the concept of vulnerability
(Birkmann, 2005)

General definitions of vulnerability:

Vulnerability is:

- "The degree of loss to a given element at risk or set of elements at risk resulting from the occurrence of a natural phenomenon of a given magnitude and expressed on a scale from 0 (no damage) to 1 (total damage)" (UNDRO, 1991).
- "Exposure to risk and an inability to avoid or absorb potential harm (Pelling, 2003). In this context, he defines physical vulnerability as the vulnerability of the physical environment; social vulnerability as experienced by people and their social, economic, and political systems; and human vulnerability as the combination of physical and social vulnerability" (Vilagrán de León, 2006).
- "The characteristics of a person or group in terms of their capacity to anticipate, cope with, resist and recover from impacts of a hazard" (Blaikie, 1994).
- "A human condition or process resulting from physical, social, economic and environmental factors, which determine the likelihood and scale of damage from the impact of a given hazard" (UNDP, 2004).
- "The conditions determined by physical, social, economic and environmental factors or processes, which increase the susceptibility of a community to the impact of hazards " (UN/ISDR, 1994).
- "The intrinsic and dynamic feature of an element at risk that determines the expected damage/harm resulting from a given hazardous event and is often even affected by the harmful event itself. Vulnerability changes continuously over time and is driven by physical, social, economic and environmental factors" (UNU-EHS, 2006).

- "The potential to suffer harm or loss, related to the capacity to anticipate a hazard, cope with it, resist it and recover from its impact. Both vulnerability and its antithesis, resilience, are determined by physical, environmental, social, economic, political, cultural and institutional factors" (Prevention Consortium, 2007).

2.2 Vulnerability: Conceptual Framework

In the last decades different frameworks on vulnerability were developed. In this dissertation some of the conceptual framework will describe briefly. In the conceptual framework of Davidson, adopted by Bollin et al. (2003), risk is seen as the sum of hazard, exposure, vulnerabilities and capacity measures. Hazard is characterized by probability and severity; exposure elements are structures, population and economy; capacity and measures is concerned with physical planning, management, social and economic capacity.

The Risk-Hazard (RH) model introduced by Turner and Kasperson (2003) describes the impact of a hazard is seen as a function of exposure of a system to the hazard event and the response of the system as shown in **Figure 2.3**, where the concept of vulnerability is commonly implicit.

Figure 2.3 The Risk-Hazard model
(Turner and Kasperson, 2003)

Moreover, a more elaborate model of Turner and Kasperson (2003) was developed at multiple spatial (the world, region and local place), functional and temporal scales, in which the interactions take place (see **Figure 2.4**). According to Turner and Kasperson (2003), vulnerability is registered not by exposure to hazards alone but also resides in the sensitivity and resilience of the system experiencing such hazards. The sensitivity to exposure is defined by the human-environmental conditions. The human-environmental conditions, e.g., social and biophysical capital, influence the coping mechanisms, when the impact is experienced, also influencing

the coping mechanisms adjusted or created because of the experience. In some cases coping responses lead to adaptation and changes in the human-environmental conditions.

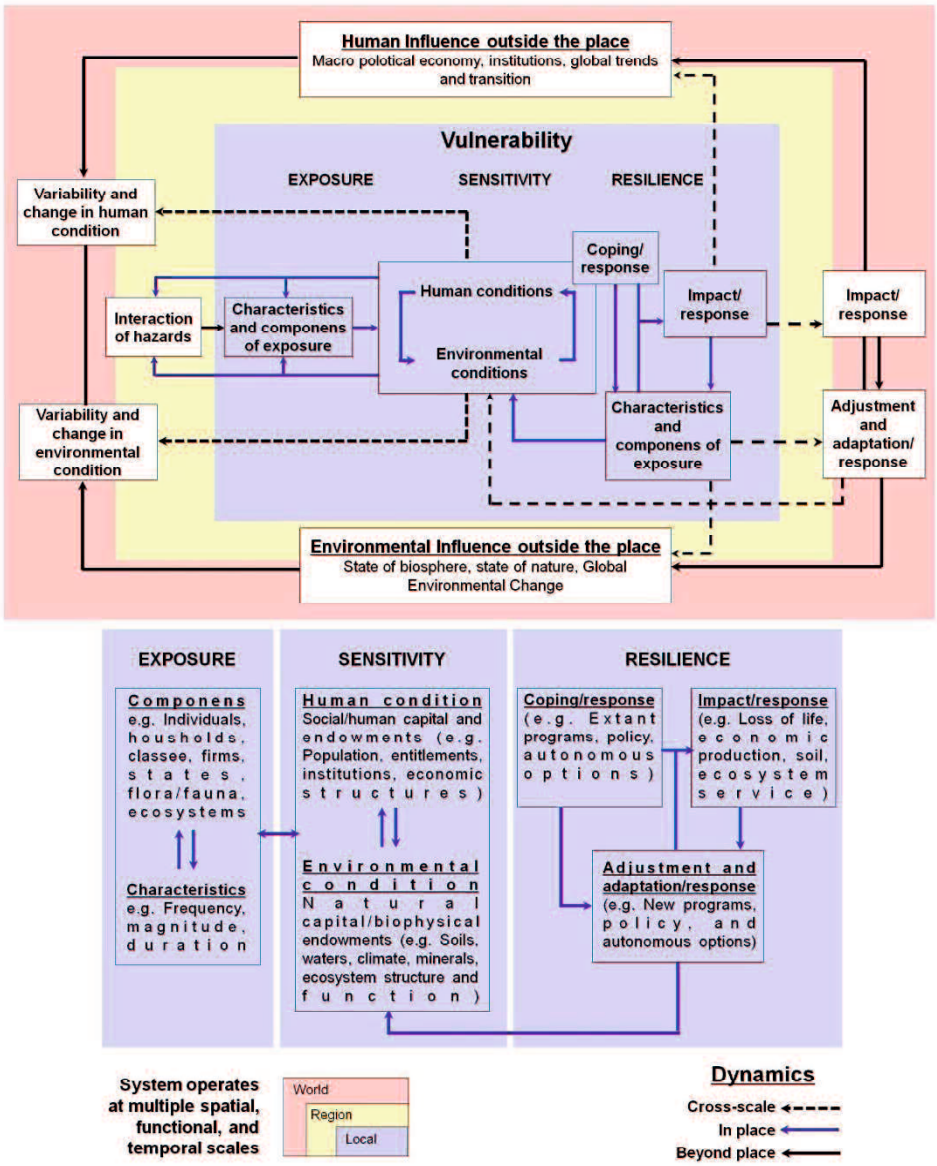

Figure 2.4 Vulnerability framework; multi-scale
(Turner and Kasperson, 2003)

The United Nations University - Institute for Environment and Human Security (UNU-EHS) developed two frameworks for vulnerability. The onion framework (Bogardi and Birkmann 2004), has a natural event sphere, an economic (monetary)

sphere and a social (disutility sphere) crossed by an "opportunity" (or probability) axis and a "reality" axis (certainty).

The BBC framework (see **Figure 2.5**) is a combination of existing models, and is mainly based on the conceptual work of Bogardi and Birkmann (2004) and Cardona (1999). According to the authors it tries to link vulnerability, human security and sustainable development. It underlines the need to view vulnerability as dynamic, focusing on vulnerabilities, coping capacities and potential intervention tools to reduce it (feedback-loop system) (Birkmann, 2005). Environmental, social and economic spheres are considered in defining vulnerability, coping capacities, risk and their vulnerability/risk reduction measures.

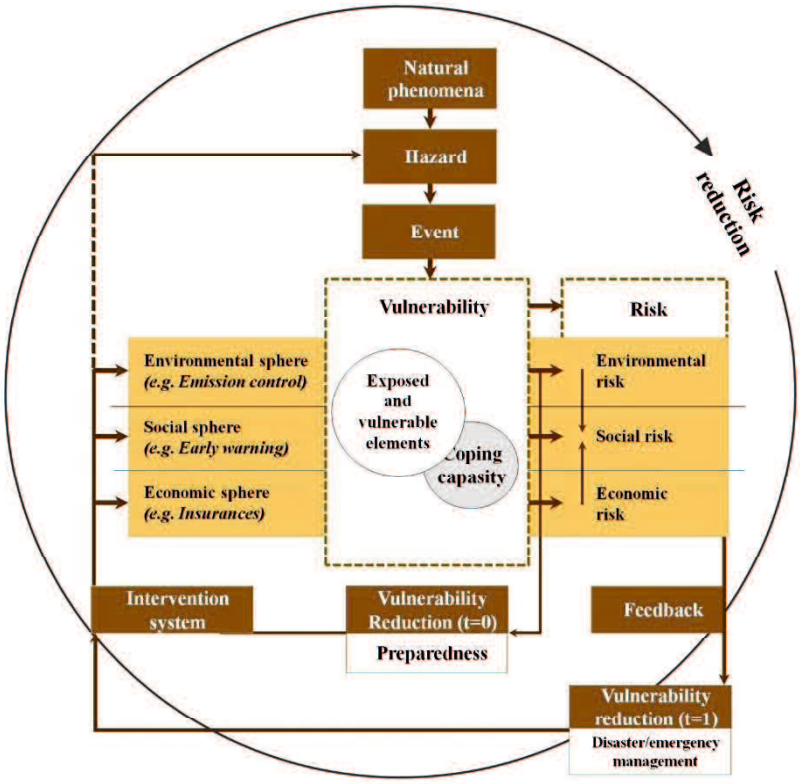

Figure 2.5 The BBC conceptual framework.
(Bogardi and Birkmann, 2004)

2.3 Vulnerability Mapping

A vulnerability map gives the precise location of sites where people, the natural environment or property are at risk due to a potentially catastrophic event that could result in death, injury, pollution or other destruction. Such maps are made in

conjunction with information about different types of risks. A vulnerability map can show the housing areas that are vulnerable to a chemical spill at a nearly factory. But it just as likely, could delineate the commercial, tourist, and residential zones that would be damaged in case of a 100-year flood or, more devastation, a tsunami.

Vulnerability maps are most often created with the assistance of computer technology called geographic information systems (GIS) and digital land survey equipment designed for use in the field. However, vulnerability maps can also be created manually using background maps such as satellite imagery, property boundaries, road maps, or topographic maps. In such cases the municipality's planning office should be involved in order to take advantage of the base maps that have already been made for other purposes.

Vulnerability maps can be of use in all phases of disaster management: prevention, mitigation, preparedness, operations, relief, recovery and lessons-learned. In the prevention stage planners can use vulnerability maps to avoid high risk zones when developing areas for housing, commercial or industrial use. Technical experts can be alerted about places where the infrastructure can be affected in case of a disaster. Fire departments can plan for rescues before a potentially dangerous event is at hand. During an exercise where a predetermined scenario takes place, the rescue crews may use the map to determine where to respond first to save human lives, the environment or property. They can also be used to evacuation routes to test the effectiveness of these routes for saving large numbers of residents and tourists and moving special groups such as senior citizens, children and those with handicaps. The operations officer can be updated about the disaster situation and the need for and the location of sensitive areas. The vulnerability map can also include evacuation routes to test their effectiveness for saving lives.

2.4 Spatial Multi Criteria Analysis for Vulnerability Assessment

The theoretical background for the multi-criteria evaluation is based on the Analytical Hierarchical Process (AHP) developed by Saaty (1980). The AHP has been extensively applied on decision-making problems (Saaty and Vargas 2001), and extensive research has been carried out to apply AHP to risk assessment. The input of spatial multi-criteria analysis is a set of maps that are the spatial representation of

the criteria, which are grouped, standardized and weighted in a 'criteria tree.' The output is one or more 'composite index maps,' which indicates the realization of the model implemented.

AHP was developed by Saaty (1980), in which the hierarchy of components of the decisions was used in decision-making process. The AHP is essentially an interactive one where a decision-maker or group of decision-makers relay their preferences to the analyst and can debate or discuss opinions and outcomes (Proctor, 2000). The AHP is based upon the construction of a series of Pair-Wise Comparison Matrices (PCMs), which compare all the criteria to one another.

Although a variety of techniques exist for the development of weight, one of the most promising would appear to be that of pairwise comparison developed by Saaty (1977) in the context of a decision making process known as AHP. The first introduction of this technique to a GIS application was that Rao et al. (1991). In the procedure for multi-criteria analysis using weighted linear combination, it is necessary that the weight sum to be 1. In Saaty's technique, weight of the nature can be derived by taking the principal eigenvector of a square reciprocal matrix of pairwise comparisons between the criteria. The comparison concern the relative importance of the two criteria involved in determining suitability for the state objective. Ratings are provided on a nine-point continuous scale (see **Figure 2.6**). For instance, if one felt that elevation was very strongly more important than coastal proximity in determining a vulnerability area due to tsunami, one would enter a 5 or 7 on the scale. If the inverse were the case (coastal proximity was very strongly more important than elevation), one would enter 1/5 or 1/7.

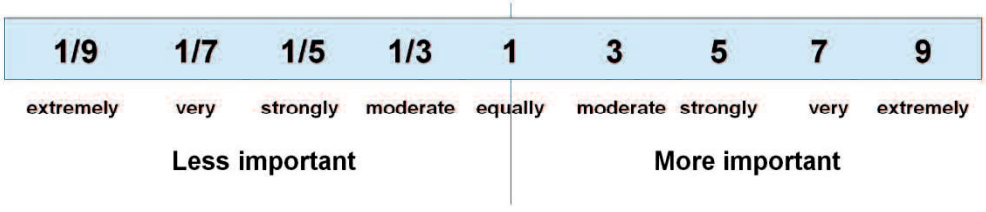

Figure 2.6 The continuous rating scale used for the pairwise comparison of factors in multi-criteria analysis

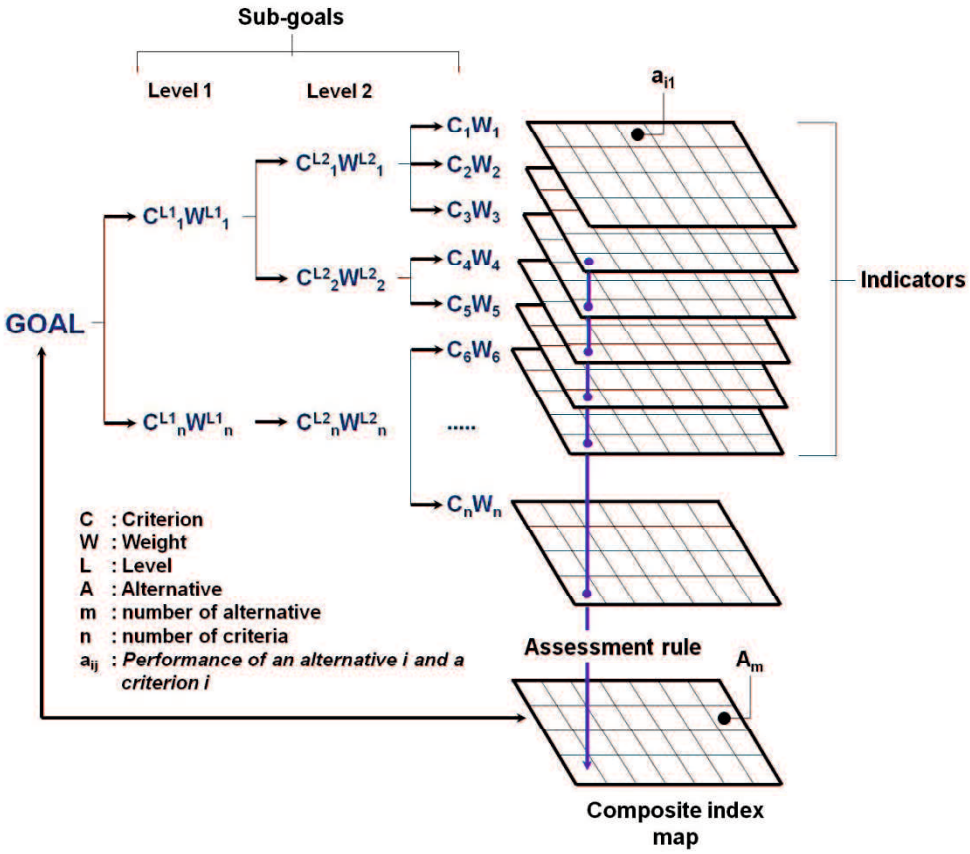

Figure 2.7 Schematic procedures for spatial multi-criteria analysis on the Analytical Hierarchical Process

From a decision-making perspective, multi-criteria evaluation can be expressed in a matrix as shown in **Table 2.1**. The matrix A contains the criteria in one axis (C_1 to C_n), and a list of possible alternatives, from which a decision has to be taken on the other axis (A_1 to A_m). Each cell in the matrix (a_{ij}) indicates the performance of a particular alternative in terms of a particular criterion. The value of each cell in the matrix is composed of the multiplication of the standardized value (between 0 and 1) of the criterion for the particular alternative, multiplied by the weight (W_1 to W_n) related to the criterion. Once the matrix has been filled, the final value can be obtained by adding up all cell values of the different criteria for the particular alternative.

Table 2.1 Multi-criteria decision matrix

	C_1 (W_1	C_2 W_2	C_3 W_3	C_4 W_4	C_5 W_5	... ...	C_n W_n)
A_1	a_{11}	a_{12}	a_{13}	a_{14}	a_{15}	...	a_{1n}
A_2	a_{21}	a_{22}	a_{23}	a_{24}	a_{25}	...	a_{2n}
.	.	.	.	.	.	.	.
.	.	.	.	.	.	.	.
.	.	.	.	.	.	.	.
A_m	a_{m1}	a_{m2}	a_{m3}	a_{m4}	a_{m5}	...	a_{mn}

For implementing this matrix according to the AHP, three principle steps need to be considered. The first one decomposes the problem (and the weights) into a hierarchical structure. The second one considers the weighting process, employing the pairwise comparisons of the criteria, and the synthesis is related to the multiplications among the hierarchical levels. Additionally, in the spatial implementation of this procedure, every criterion (C_j) becomes a raster layer, and every pixel (or set of pixels) of the final composite index map eventually becomes an alternative A_j. The goal (risk index) has been decomposed into criteria levels C_{L1} and C_{L2}. The intermediate levels are often indicated as sub-goals or objectives (e.g. in level 1, the sub-goals are a 'hazard index' and a 'vulnerability index'). Each criterion of each level will also have an assigned weight.

Therefore, the values for the layers of the intermediate levels are obtained through the summation of the performance for the alternative at lower levels. As the criteria consist of raster maps, their spatial performance (a_{ij}) and the alternative (A_i) will be identified for particular raster cells. The composite risk index map (e.g. tsunami risk) is obtained by an assessment rule, which is calculated by adding up the performance of all cell values of the different criteria (a_{ij}) for the particular alternative. The performance of every element in the matrix (a_{ij}) is applying by **Eq. 2.1.**

$$a_{ij} v_{ij} \prod_{L=o}^{h} w_j^L \qquad \text{(Eq. 2.1)}$$

In this equation, v_{ij} refers to the standardized value of criterion (C_j) for alternative (A_i), and weight wL_j refers to the weight of criterion (C_j) for level L (0–h levels). During the analysis, it could be desirable to produce the intermediate criteria maps. In this case, Eq. 2.1 should not be applied because weights need to be multiplied with the standardized values only up to the specific level of the intermediate maps. The intermediate maps might also be combined using different methods. When designing vulnerability indicators, it is necessary to take into account the socio-economic conditions, which may vary from country to country (Westen & Kingma, 2009, Abella, 2008, Thirumalaivasan et al, 2003).

2.5 Remote Sensing for Tsunami Disaster

In the field of disaster management, in particular, remote sensing can help to analyze areas that are prone to natural and man-made hazards and potential damages. Risk and vulnerability assessments are an important part of disaster management and can be supported by remote sensing for pre-disaster analyses. Regarding tsunami risk and vulnerability assessment and modeling, remote sensing techniques have been used in damage assessment and rapid mapping to support the emergency response phase immediately after a disaster has occurred. Remote sensing also give a contributions to vulnerability and risk assessment in the pre-disaster phase by deriving relevant information such as land use, settlement areas and buildings, elevation, etc. and monitoring of reconstruction and rebuilding in the post-disaster phase.

2.5.1 Damage Assessment

In general, there are two main goals using remote sensing data for analyzing damage: rapid mapping assessment (Belward et al., 2007) and mapping the affected hazard impact zone (McAdoo et al., 2007; Iverson and Prasad, 2007). The latter is very important in risk and vulnerability assessment in order to know the important parameters for tsunami hazard mapping. For example, the tsunami run-up is influenced by the topography of a region (McAdoo et al., 2007), the geomorphologic conditions, mangroves, and coral reefs influenced the characteristics of the tsunami inundation in Aceh (Chatenoux and Peduzzi, 2007), and the landscape analysis is

used to model the tsunami damage in Aceh Province (Iverson and Prasad, 2007, Suppasri, et al., 2012).

Figure 2.8 shows damage detection from satellite remote sensing thought the comparison images of before and after The 2011 Japan tsunami attack in Kesennuma, Miyagi Prefecture and Rikuzentakata, Iwate Prefecture.

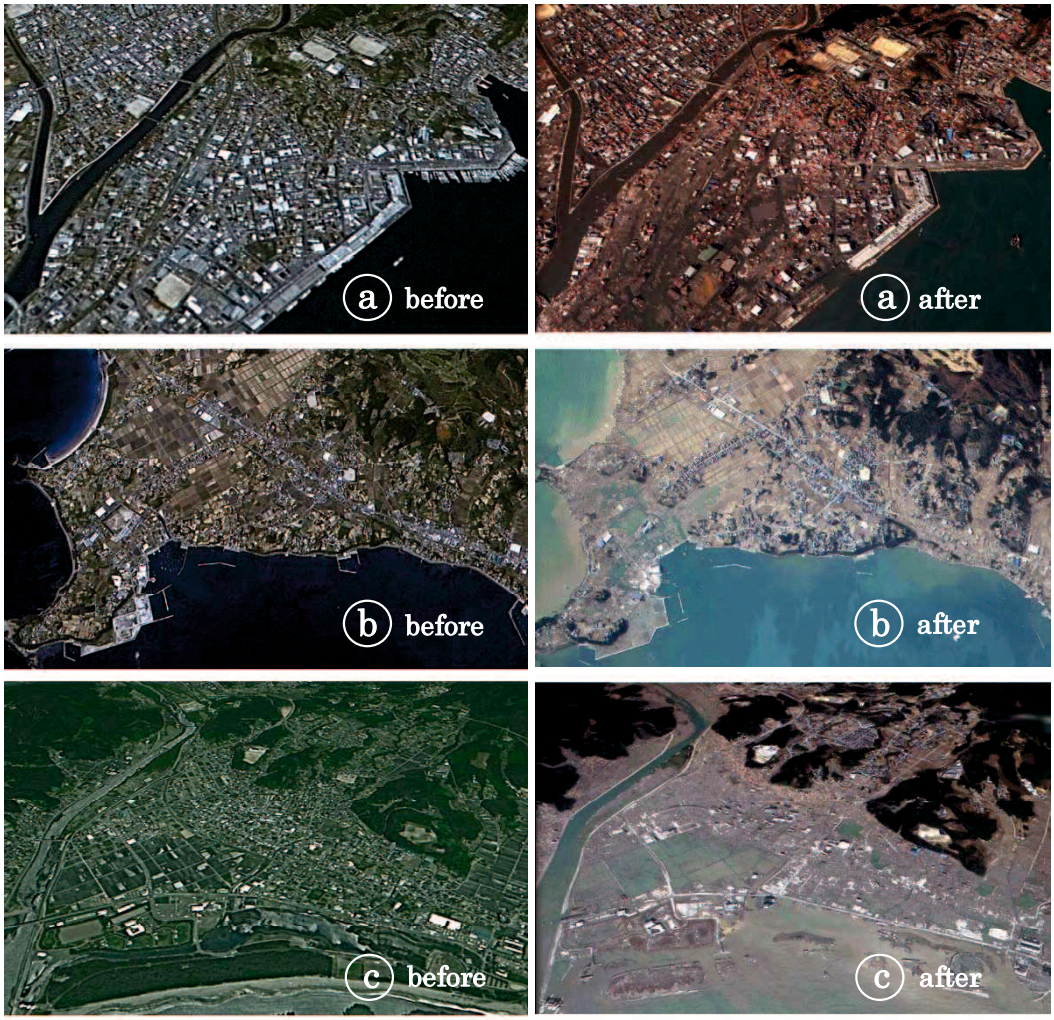

Figure 2.8 Satellite remote sensing images of before and after The 2011 Japan tsunami attack in (a) Fishing port area of Kesennuma, Miyagi Prefecture; (b) South coast of Kesennuma, Miyagi Prefecture; and (c) Rikuzentakata, Iwate Prefecture.

Satellite images which captured the affected areas before and after the event were fully employed in field investigations and in tsunami damage mapping. Since the affected areas are vast, moderate resolution satellite images were quite effective in change detection due to the tsunami. Using high-resolution optical satellite images

acquired before and after the earthquake, the areas of building damage were extracted based on pixel-based and object-based land cover classifications and their accuracy was compared with visual inspection results (Yamazaki and Matsuoka, 2007).

2.5.2 General Satellite Image Analysis for Tsunami-Affected Areas

Recent advances in remote sensing technologies have expanded the capabilities of detecting the spatial extent of tsunami-affected areas and damage to structures. The highest spatial resolution of optical imageries from commercial satellites is up to 60–70 centimeters (QuickBird owned by DigitalGlobe, Inc.) or 1 meter (IKONOS operated by GeoEye). Since the 2004 Sumatra-Andaman earthquake tsunami, these satellites have captured images of tsunami-affected areas, and the images have been used for disaster management activities, including emergency response and recovery. To detect the extent of a tsunami inundation zone, NDVI (Normalized Difference Vegetation Index) is the most common index obtained from the post-event imagery, focusing on the vegetation change due to the tsunami penetration on land. In addition to apply the NDVI algorithm to detect the impact of tsunami, the use of soil (NDSI) and water (NDWI) also can be apply in tsunami impact prediction (Yamazaki and Matsuoka, 2007).

Figure 2.9 shows the change of land coverage thought the vegetation analysis of satellite remote sensing before and after The 2011 Japan tsunami attack in Kesennuma, Miyagi Prefecture, Rikuzentakata, and Ofunato, Iwate Prefecture. Areas covered by vegetation are shown in red, while cities and un-vegetated areas are shown in shades of blue-gray.

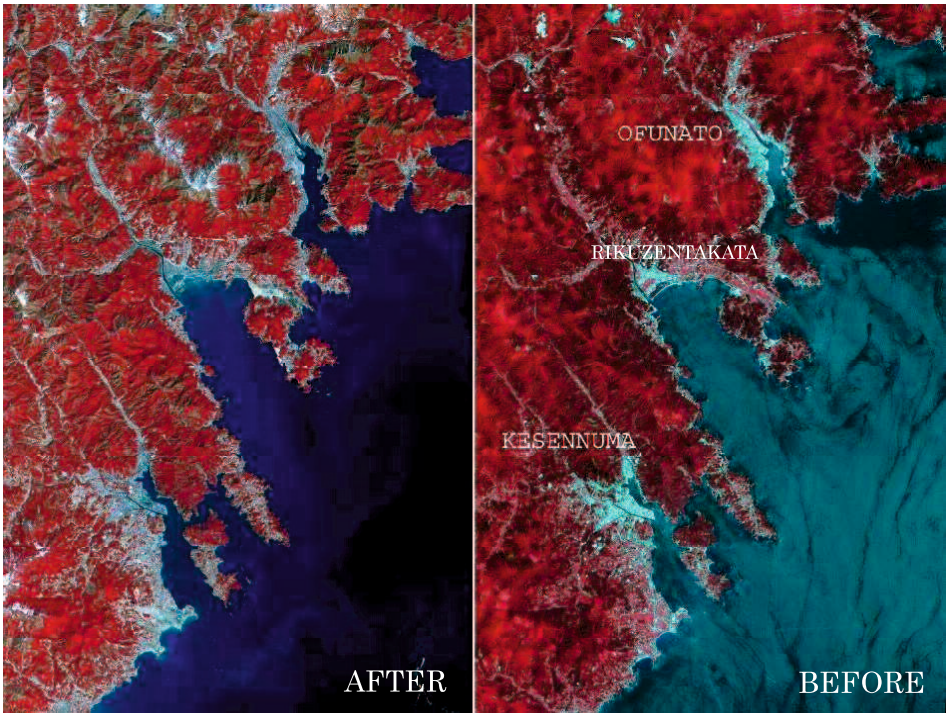

Figure 2.9 These ASTER images compare a March 14, 2011 image of the northeastern Japan coastal cities of Kesennuma, Rikuzentakata, and Ofunato, with a similar image taken in August, 2008.
(ASTER images courtesy of NASA, Goddard Space Flight Center (GSFC), Japan's Ministry of Economy Trade and Industry (METI), Earth Remote Sensing Data Analysis Center (ERSDAC), Japan Resource Observation System (JAROS), U.S./Japan ASTER Science Team, and the Land Processes Distributed Active Archive Center (LP DAAC))

2.5.3 SAR Image Analysis for Tsunami Disaster

Among the various sensors, SAR (Synthetic Aperture Radar) is remarkable for its ability to record the physical value of the Earth's surface (Henderson and Lewis, 1998). Unlike passive optical sensors, SAR enables the observation of surface conditions day or night, even through clouds. SAR interferometric analyses using phase information have successfully provided quantification of relative ground displacement levels due to natural disasters (Massonnet et al., 1993).

Intensity information obtained from SAR represents a physical value (backscattering coefficient) that is strongly dependent on the roughness of the ground surface and the dielectric constant. Based on this idea, models for satellite C- and L-band SAR data were developed to detect building damage areas due to earthquakes by clarifying the relationship between the change in the backscattering coefficient from pre- and post-event SAR images and then applying the models to

tsunami-induced damage areas (Matsuoka & Yamazaki, 2004; Matsuoka & Nojima, 2009; Koshimura & Matsuoka, 2010; Suppasri et. al., 2012).

Inundated areas also show a lower backscattering coefficient because of the smooth surface and the dielectric constant of water bodies (**Figure 2.10(a)**). Inundated areas can be observed by examining the backscattering characteristics in the tsunami damage areas for the different type of land cover. Several factors need to be considered for better analysis of after-tsunami TerraSAR-X images. Surface earth change could be one of the factors. Scattered debris from collapsed buildings, visible in the agriculture areas and bare land in the after-tsunami image show brighter reflections than in the before-tsunami image (Suppasri et. al., 2012).

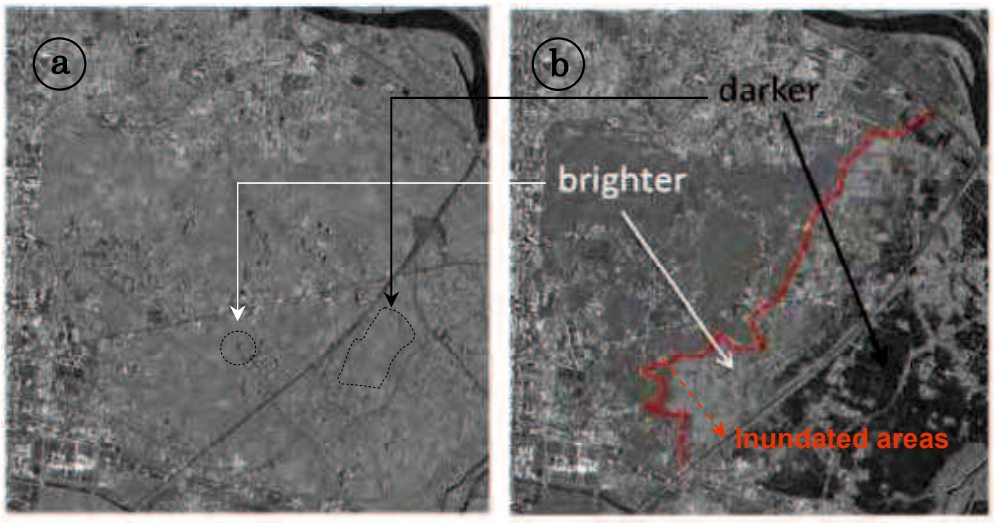

Figure 2.10 (a) TerraSAR-X before (2010/10/20); and
(b) TerraSAR-X after tsunami 2011/03/12
(modified from Suppasri et al., 2012)

In addition, a meteorological satellite also can be used in order to observe the post disaster event quickly due to the high temporal resolution of the satellite. **Figure 2.11** describes a Defense Meteorological Satellite Program (DMSP) observes Japan area before and after the 2011 Japan tsunami.

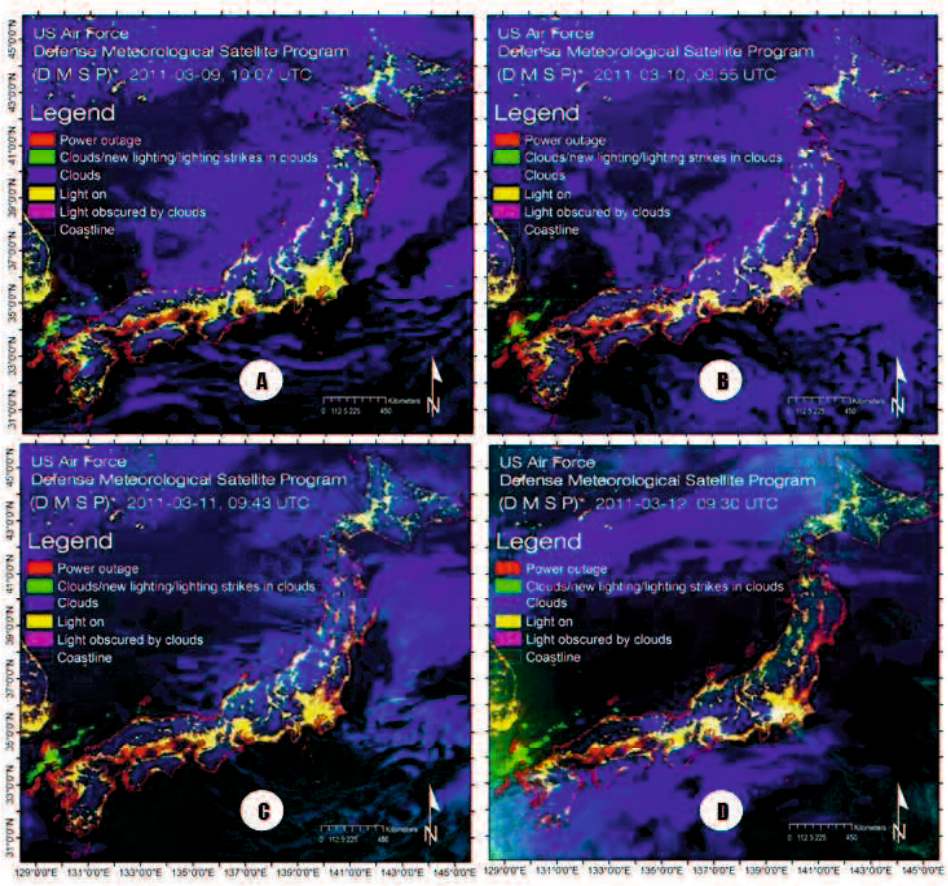

Figure 2.11 describes a Defense Meteorological Satellite Program (DMSP) observes Japan area; (a)(b) before the 2011 Japan tsunami; (c) during the 2011 Japan tsunami; and (d) after the 2011 Japan tsunami

Color image designed to show power outages detected using U.S. Air Force Defense Meteorological Satellite Program (DMSP) satellite F-18 image data in the earthquake region of Japan on March 12, 2011. The data were acquired by the Operational Line-scan System (OLS), the primary imager flown on all the DMSP satellites. The OLS collects visible and thermal band image data with a 3000 km swath.

The power outage image is a color composite made using the 2010 stable lights as red, that night's visible band data as green and that night's thermal band data as blue. The blue is then inverted to make cold clouds look bright blue. The yellow areas are locations where the lights were on. The red areas had lighting present in the 2010 stable lights, but no light detections when the satellite passed over on March 12. With moonlight increasing, clouds are showing up as mixtures of blue and green.

Where stable lights are present in the cloud areas with no light detection on March 12, the result is a magenta color. Power outages are indicated by the red color surrounding Mito (north of Tokyo), Sendai, and a belt extending north from Sendai.

CHAPTER 3
Data and Methods

3.1 Data

Several datasets are required for the tsunami vulnerability mapping using multi-criteria through AHP technique and analysis of image satellite for tsunami impact observation. The data contains images raster data of satellite (see **Table 3.1**) and vector data of study area map. In addition to support the analysis, secondary data such as the observation data is used.

3.1.1 Raster Data (Satellite images)

The ALOS has three remote sensing instruments: the Panchromatic Remote-sensing Instrument for Stereo Mapping (PRISM) for digital elevation mapping, the Advanced Visible and Near Infrared Radiometer type 2 (AVNIR-2) for precise land coverage observation, and the Phased Array type L-band Synthetic Aperture Radar (PALSAR) for day-and-night and all-weather land observation. In order to utilize fully the data obtained by these sensors, the ALOS was designed with two advanced technologies: the former is the high speed and large capacity mission data handling technology and the latter is the precision spacecraft position and attitude determination capability. They will be essential to high-resolution remote sensing satellites in the next decade. AVNIR-2 is used for providing the input parameter in multi-criteria analysis; land cover mapping, and the calculation of normalized difference vegetation, soil, and water index, while PRISM is used in the pan-sharpening process.

AVNIR-2 is a visible and near infrared radiometer for observing land and coastal zones and provides better spatial land coverage maps and land-use classification maps for monitoring regional environment. The AVNIR-2 provides 10-meter spatial resolution mages compared with the 16 m resolution of the AVNIR in the multi spectral region. The higher resolution was realized by improving the CCD detectors.

Moreover, PRISM is a panchromatic radiometer with 2.5m spatial resolution at nadir which has three independent optical systems for viewing nadir, forward and

backward producing a stereoscopic image along the satellite's track. Each telescope consists of three mirrors and several CCD detectors for push-broom scanning. The nadir-viewing telescope covers a width of 70km; forward and backward telescopes cover 35km each (see **Table 3.2** for the ALOS sensor characteristics).

.

Table 3.1 List of ALOS satellite images

Sensor	*SceneID*	*ObservationDate*	*UTM_ZoneNo*	
AVNIR-2	ALAV2A167602820	2009/03/18	54	
AVNIR-2	ALAV2A273502830	2011/03/14	54	
PRISM	ALPSMB274962875	2011/03/24	54	Nadir (70km) + Backward (35km)
PRISM	ALPSMB241412875	2010/08/06	54	
PRISM	ALPSMF277442760	2011/04/10	54	Triplet observation mode using Forward, Nadir, and Backward views (Swath width is 35km)
PRISM	ALPSMB154182875	2008/12/16	54	

Table 3.2 ALOS Sensor Characteristics

Resolution	2.5m panchromatic 10m multispectral
Launch Vehicle	H-IIA Rocket
Launch Site	Tanegashima Space Center
Satellite Weight	Approximately 4,000kg (at Lift-off)
Power	Approximately 7,000W (End of Life)
Designed Life	3 to 5 years
Orbit	Sun Synchronous Sub-Recurrent Orbit Recurrent Period: 46 days Sub cycle: 2 days Altitude: Approximately 692km (above the equator) Inclination: Approximately 98.2 degrees

AVNIR-2

Band	Wavelength Region (μm)	Resolution (m)	TM/ETM
1	0.42-0.50 (blue)	10	0.45-0.52
2	0.52-0.60 (green)	10	0.52-0.60
3	0.61-0.69 (red)	10	0.63-0.69
4	0.76-0.89 (near-IR)	10	0.76-0.90

Spatial Resolution	10m (at Nadir)
Swath Width	70km (at Nadir)
S/N	>200
MTF	Band 1 through 3 : >0.25 Band 4 : >0.20
Number of Detectors	7000/band
Pointing Angle	- 44 to + 44 degree
Bit Length	8 bits

PRISM	
Number of Bands	1 (Panchromatic)
Wavelength	0.52 to 0.77 micrometers
Number of Optics	3 (Nadir; Forward; Backward)
Base-to-Height ratio	1.0 (between Forward and Backward view)
Spatial Resolution	2.5m (at Nadir)
Swath Width	70km (Nadir only) / 35km (Triplet mode)
S/N	>70
MTF	>0.2
Number of Detectors	28000 / band (Swath Width 70km) 14000 / band (Swath Width 35km)
Pointing Angle	-1.5 to +1.5 degrees (Triplet Mode, Cross-track direction)
Bit Length	8bit

Source:
- http://www.jaxa.jp/projects/sat/alos/index_e.html,
- http://www.satimagingcorp.com/satellite-sensors/alos.html
- https://earth.esa.int/c/document_library/get_file?folderId=19584&name=DLFE-262.pdf

3.1.2 Vector Map

A hardcopy and softcopy of vector map was obtained from Geospatial Information Authority of Japan (GSI Japan). A list of vector map is displayed in **Table 3.3**.

Table 3.3 List of vector map

Location	*Type*	*Scale levels*	*Coordinate system*
Kesennuma, Miyagi Prefecture (31 January 2013)	Reference point of the survey	1:2500	JGD2000_Japan_Zone_13
	Point Type boundaries of administrative areas road edge, elevation, shoreline, water, buildings	1:2500	
	Line Type Shoreline, water, building center line, boundaries of administrative areas, road edge, elevation	1:2500	
	Point Type boundary of the city/ district	1:2500	
	Point elevation (DEM)	1:2500	
	Point elevation (DEM)	1: 25,000	
Rikuzentakata, Iwate Prefecture (31 January 2013 and 4 April 2010)	Reference point of the survey	1:2500	JGD2000_Japan_Zone_13
	Point Type boundaries of administrative areas road edge, elevation, shoreline, water, buildings	1:2500	
	Line Type Shoreline, water, building center line, boundaries of administrative areas, road edge, elevation	1:2500	
	Point Type boundary of the city/ district	1:2500	

	Point elevation (DEM)	1:2500	
	Point elevation (DEM)	1: 25,000	
Ofunato, Iwate Prefecture (31 January 2013 and 4 April 2010)	Reference point of the survey	1:2500	JGD2000_Japan_Zone_13
	Point Type boundaries of administrative areas road edge, elevation, shoreline, water, buildings	1:2500	
	Line Type Shoreline, water, building center line, boundaries of administrative areas, road edge, elevation	1:2500	
	Point Type boundary of the city/ district	1:2500	
	Point elevation (DEM)	1:2500	
	Point elevation (DEM)	1: 25,000	

3.1.3 Digital Elevation Model (DEM)

A different product of Digital Elevation Model is used in the surface analysis to provide input parameter of the study. **Table 3.4** shows list of DEM data.

Table 3.4 List of DEM data

	Location	***Product name***	***Resolution***		***Source***
Digital Elevation Model	Miyagi and Iwate prefecture, Japan	SRTM V.3	3 arc-second	90m	USGS
		SRTM V.4	3 arc-second	90m	CGIAR-CSI
		SRTM WRS.2	3 arc-second	90m	GLCF
		Aster GDEM V.2	1 arc-second	30m	USGS
		Aster GDEM V.2	1 arc-second	30m	jspacesystems
		GSI DEM	0.2 arc-second	5m	GSI Japan

(1) SRTM V.4

The current dataset (Version 4) has been produced based on the finished-grade 3 arc-second SRTM data released by NASA and distributed by the USGS through ftp access (ftp://edcsgs9.cr.usgs.gov/pub/data/srtm/version1/). The original data came with data voids, where insufficient contrast was available in the radar data to extract the elevation. These data voids tend to occur over water bodies (lakes and rivers), areas with snow cover and in mountainous regions. The CGIAR-CSI SRTM dataset has undergone post-processing of the NASA data to “fill in” the no data voids through interpolation techniques. The result is seamless, complete coverage of elevation for the globe. Version 4 uses a number of interpolations techniques, described by Reuter et al. (2007), uses extra auxiliary DEMs to fill the voids and SRTM30 for large voids, and this Version 4 differs from Version 3

with a ½ grid pixel shift which definitively solves this confusion (Jarvis et al., 2008). The CGIAR-CSI GeoPortal is able to provide SRTM 90m Digital Elevation Data for the entire world.

SRTM is composed of the main and outboard antennas of SIR-C/X-SAR (see **Table 3.5**) which uses two frequency bands, Attitude & Orbit Determination Avionics (AODA; electronic equipment used to determine attitude and orbit) a mast that extends 60m from the shuttle, and a canister to store the mast, and a structure to support all the equipment.

Table 3.5 Major specification of SIR-C/X-SAR

item		***SIR-C Spaceborne Imaging Radar-C***	***X-SAR X-band Synthetic Aperture Radar***
Size	Main antenna	12.0m X 3.5m	12.0m X 0.5m
	Outboard antenna	8.1m X 0.9m	6m X 0.4m
Frequency		5.3GHz	9.6GHz
Wavelength		5.8cm	3.1cm
Resolution	Horizontal	30m	30m
	Vertical	16m	16m
Altitude		233km	233km
Swath width		225km *2	50km
Polarization *1		HH,HV,VH,VV	VV
Off nadir		23 - 63 degree *2	52 degree

*1 FHH (Horizontal transmit,Horizontal receive)
HV (Horizontal transmit,Vertical receive)
VH (Vertical transmit,Horizontal receive)
VV (Vertical transmit,Vertical receive)

*2 FSIR-C is designed with Scan SAR.The beam can be electronically steered.

(2) ASTER GDEM V.2

The ASTER Global Digital Elevation Model (ASTER GDEM) is a joint product developed and made available to the public by the Ministry of Economy, Trade, and Industry (METI) of Japan and the United States National Aeronautics and Space Administration (NASA). It is generated from data collected from the Advanced Spaceborne Thermal Emission and Reflection Radiometer (ASTER), a spaceborne earth observing optical instrument. The ASTER GDEM is the only DEM that covers the entire land surface of the Earth at high resolution.

Version 2 of the ASTER GDEM is developed, employing an advanced algorithm to improve GDEM resolution and elevation accuracy and reprocessing a total of

1.5 million scene data including additional 250,000 scenes acquired after the previous release. Accuracy of this latest version is validated by the collaborate effort between Japan and the United States, which shows significant improvements over Version 1.

The methodology used by Japan's Sensor Information Laboratory Corporation (SILC) to produce the ASTER GDEM involves automated processing of the entire ASTER Level-1A archive. Stereo-correlation is used to produce over one million individual scene-based ASTER DEMs, to which cloud masking is applied to remove cloudy pixels. All cloud-screened DEMS are stacked and residual bad values and outliers are removed. Selected data are averaged to create final pixel values, and residual anomalies are corrected before partitioning the data into 1 degree (°) x 1° tiles. The ASTER GDEM covers land surfaces between 83°N and 83°S and is comprised of 22,702 tiles. Tiles that contain at least 0.01% land area are included (http://www.jspacesystems.or.jp/ersdac/GDEM/E/1.html).

(3) GSI DEM

The Geospatial Information Authority of Japan (GSI) provides a high spatial resolution of DEM. Based on the surveying methods, a 5m mesh of elevation data is divided into two types. First was created based on the airborne laser, which is the center point grid of mesh on the basis of data equivalent to those published (digital elevation map of 5m mesh) and longitude difference at the surface and separated by interval 0.2 seconds latitude difference. This method has been applied for the target of metropolitan areas.

The second one is based on the photogrammetric. In this methods, the mesh 0.2 seconds difference in latitude (about 5m) interval, the data of the ground surface is created by removing bridge and houses, trees, etc. the target of this methods is urban areas and used for the application of city planning.

The comparison of some DEMs is shown in **Table 3.6**, while the interface menu view for downloading the DEM data is shown in **Figure 3.1**.

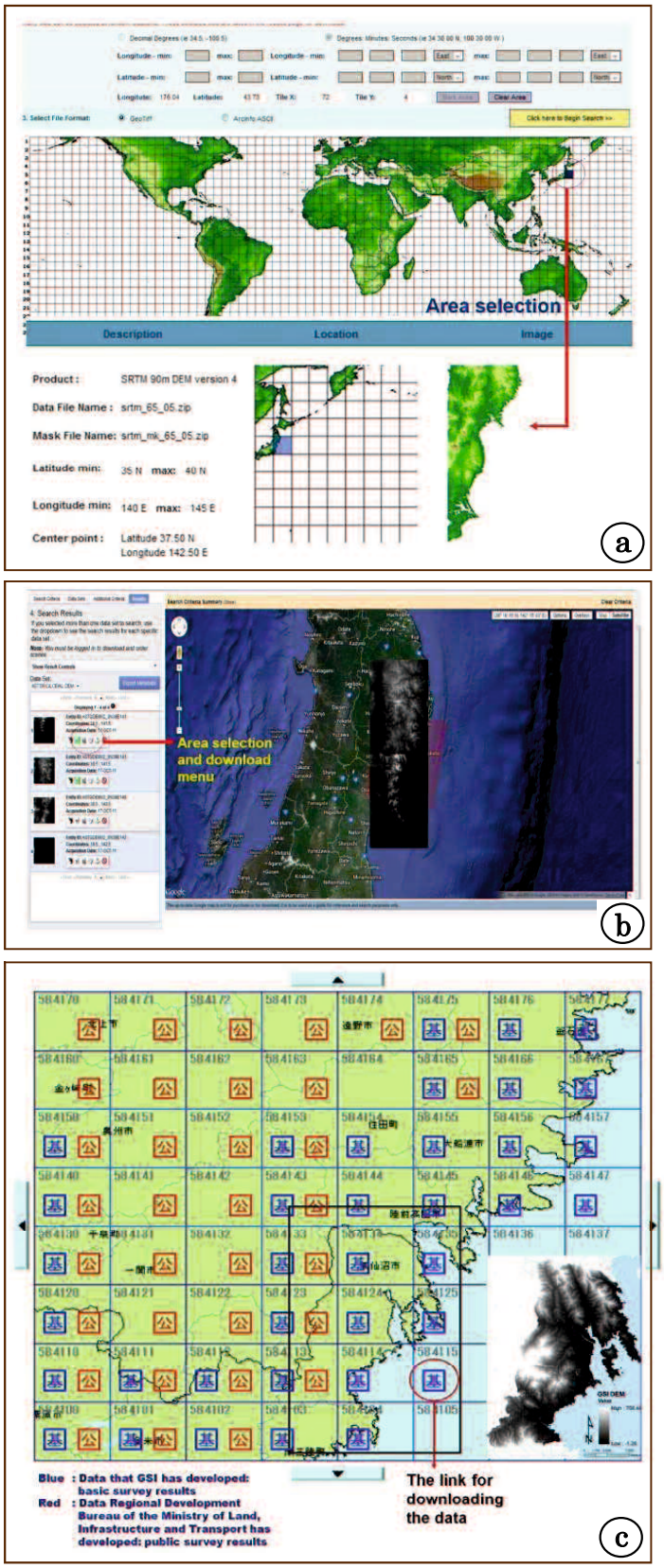

Figure 3.1 Menu view for data downloading;
(a) SRTM DEM; (b) ASTER GDEM; and (c) GSI DEM

Table 3.6 Comparison of some DEMs

	ASTER GDEM	*SRTM3**	*GTOPO30***	*10 m mesh digital elevation data*
Data source	ASTER	Space shuttle radar	From organizations around the world that have DEM data	1:25,000 topographic map
Generation and distribution	METI/NASA	NASA/USGS	USGS	GSI Japan
Release year	2009 ~	2003 ~	1996 ~	2008~
Data acquisition period	2000 ~ ongoing	11 days (in 2000)		
Posting interval	30m	90m	1000m	about 10m
DEM accuracy (stdev.)	7~14m	10m	30m	5m
DEM coverage	83 degrees north ~ 83 degrees south	60 degrees north ~ 56 degrees south	Global	Japan only
Area of missing data	Areas with no ASTER data due to constant cloud cover (supplied by other DEM)	Topographically steep area (due to radar characteristics)	None	None

Other examples of available DEMs
- NED: with a resolution of 30 m, covering the entire U.S.A., provided by USGS
*SRTM3: Shuttle Radar Topography Mission Data at 3 Arc-Seconds
**GTOPO30: Global 30 Arc-Second Elevation Data Set

3.2 Spatial Data Analysis in GIS

In general, a GIS can be considered to have several components such as spatial, graphical, numerical, and textual components (Worboys, 1995; Abdul-rahman and Pilouk, 2007). These system components have several important building blocks such as data modeling, data structures, and types of applications.

Principally, there are three spatial data component that need to be stored in GIS format; geometric data, thematic data, and a link identification/ID. Geometric component deals with the location of the data by means, for instance, of a reference coordinate system and the thematic component provides the attribute value of the data (Abdul-rahman and Pilouk, 2007).

Figure 3.2 describe design and construction phases for a geo-spatial model in integration with AHP.

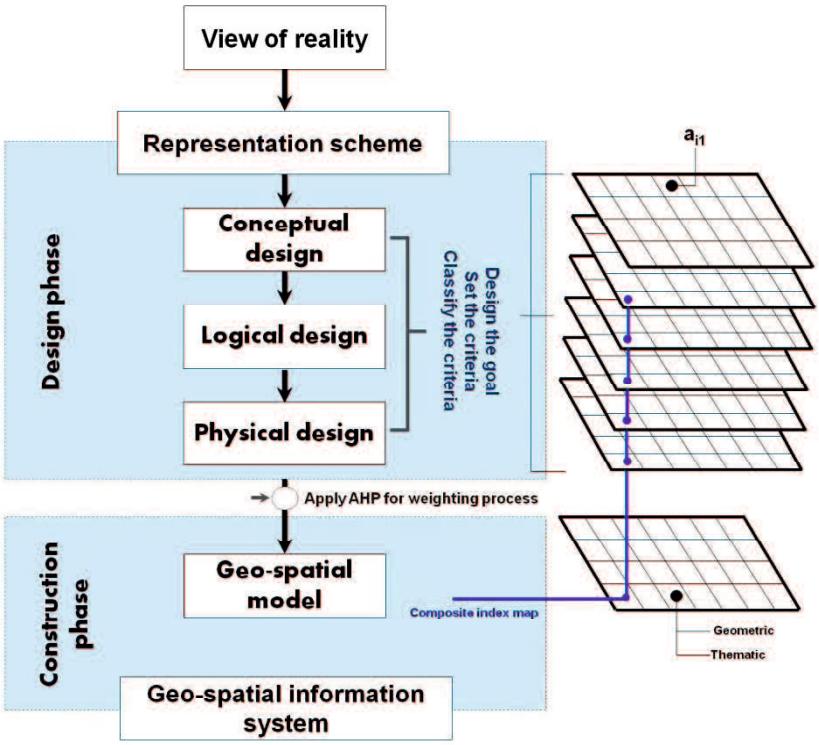

Figure 3.2 Design and construction phases for a geo-spatial model

In order to run a model in multi-criteria analysis, the creating of spatial data are necessary. The creation of spatial data should follow the design phase (see **Figure 3.2**). A spatial data that used as the input parameter for multi-criteria analysis describes as below;

(1) Elevation

Elevation is created using DEM data derived both from satellite image in raster data type and point data of elevation in vector file.

(2) Slope

For an analytical surface, $F(x,y)$, slope is defined as the magnitude of the first derivative of the surface function:

$$S = \sqrt{\left(\frac{\delta F}{\delta x}\right)^2 + \left(\frac{\delta F}{\delta y}\right)^2} \qquad \text{(Eq. 3.1)}$$

This formula is not based on a rise-over-run calculation over a fixed interval, but rather assumes that a plane surface can be placed at any point on the surface $F(x,y)$ in such a way that it only just touches the surface — it is a tangential plane and relies on the notion of infinitesimally small distances. It is closely related to the formula for Euclidean distance, and simply shows how much the surface F rises with a small fixed increment in x and y. However, surfaces within GIS are rarely if ever represented by analytic functions — typically they will be modeled as TINs or grids, with a finite resolution. Hence slope calculations will use approximations to the formula above depending on the surface model used, which is itself an approximate representation of the true surface. In almost all instances software packages apply grid-based computation, with TINs being first converted to grid format. Strictly speaking such conversion is not necessary, since TINs can provide interpolated surface values at every point, and use of a suitable (generally non-linear) function could then provide slope (and aspect) values directly (Smith et al., 2006)

The output slope raster can be calculated in two types of units, degrees or percent (percent rise). The percent rise can be better understood if we consider it as the rise divided by the run, multiplied by 100. **Figure 3.3** describes the comparison value for slope in degree and percent. Consider triangle *B* below. When the angle is 45 degrees, the rise is equal to the run, and the percent rise is 100 percent. As the slope angle approaches vertical (90 degrees), as in triangle *C*, the percent rise begins to approach infinity. The rates of change (delta) of the surface in the horizontal (dz/dx) and vertical (dz/dy) directions from the center cell determine the slope.

The basic algorithm used to calculate the slope is:

$$Slope\ radian = ATAN\left(\sqrt{\left(\left[dz/dx\right]^2 + \left[dz/dy\right]^2\right)}\right) \quad \text{(Eq. 3.2)}$$

Slope is commonly measured in units of degrees, which uses the algorithm:

$$Slope\ degrees = ATAN\left(\sqrt{\left(\left[dz/dx\right]^2 + \left[dz/dy\right]^2\right)}\right) \times 57.29578 \quad \text{(Eq. 3.3)}$$

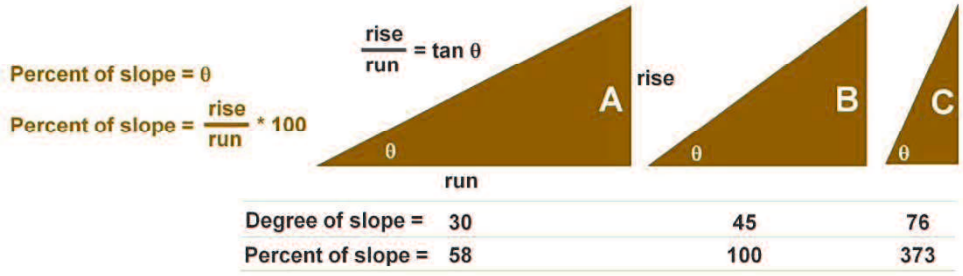

Figure 3.3 Comparing values for slope in degrees versus percent

(3) Hydrology Analysis

Flow direction

In areas where the aspect angle does not follow one of the octagonal directions, upslope area is calculated by apportioning the flow from a cell between the two down-slope cells according to how close the flow angle is to the direct angle to that cells center (see illustration on **Figure 3.4**).

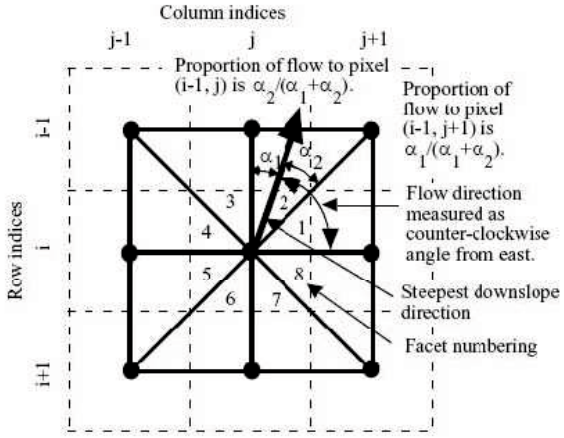

Figure 3.4 The concept of flow direction

This is determined by the direction of steepest descent, or maximum drop, from each cell. This is calculated as follows:

$$maximum\ drop = \frac{change\ in\ z\ value}{distance} \times 100 \qquad \text{(Eq. 3.4)}$$

The distance is calculated between cell centers. Therefore, if the cell size is 1, the distance between two orthogonal cells is 1, and the distance between two

diagonal cells is 1.414 (the square root of 2). If the maximum descent to several cells is the same, the neighborhood is enlarged until the steepest descent is found. When a direction of steepest descent is found, the output cell is coded with the value representing that direction.

Flow Accumulation

The result of flow accumulation is a raster of accumulated flow to each cell, as determined by accumulating the weight for all cells that flow into each down-slope cell. Output cells with a high flow accumulation are areas of concentrated flow and can be used to identify stream channels. Output cells with a flow accumulation of zero are local topographic highs and can be used to identify ridges.

The method used to calculate flow accumulation was to run multiple iterations through the DEM starting at the maximum elevation in the data set and working through elevations one-by-one in a descending order. The final calculation for flow accumulation per cell was determined by :

$$accum1 = accumulation[current\ cell] + [inflow\ accumulation \times inflow\ proportion]$$
$$accum2 = accumulation[current\ cell] + [inflow\ accumulation \times inflow\ proportion]$$
$$total\ accumulation = accum1 + accum2$$

(Eq. 3.5)

(4) Multi Buffering in Proximity Tool

The distance from the coastline (coastal proximity) to the land, calculated using multi-buffering, was used as one of the parameters in vulnerability mapping, which also used an evaluation of historical reports of the maximum run-up in the area concerned. According to Sinaga et al. (2011), the algorithm used for coastal proximity was based on that of Bretschneider and Wybro (1976):

$$\mathrm{Log}X_{max} = \log 1400 + \frac{3}{4}\log\left(\frac{Y_0}{10}\right) \qquad \text{(Eq. 3.6)}$$

in which X_{max} is the maximum reach of the tsunami over land, and Y_0 is the height of the tsunami at the coast.

For evaluation of coastal proximity, five classes of distance are used (in meters). The maximum run-up of the tsunami in the study area from the 2011 Tohoku Earthquake was 11.76 m. Based on the algorithm above: 5 m run-up can reach the distance of 556 m from the coastline; 5–10 m of run-up can reach 556–1400 m; 10–15 m of run-up can reach 1400–2404 m; and 15–20 m of run-up can reach 2404–3528 m. For the vulnerability assessment, the multi buffering distance from the coastline to an area of land was measured in relation to the impact of a tsunami wave. The five classes of distance used (less than 556 m, 556–1400 m, 1400–2404 m, 2404–3528 m, and more than 3528 m) represent: low vulnerability, slightly low vulnerability, medium vulnerability, slightly high vulnerability, and high vulnerability.

3.3 Multi-criteria Analysis

3.3.1 Analytical Hierarchy Process

AHP was developed by Saaty (1980), in which the hierarchy of components of the decisions was used in decision-making process. The AHP is essentially an interactive one where a decision-maker or group of decision-makers relay their preferences to the analyst and can debate or discuss opinions and outcomes (Proctor, 2000). The AHP is based upon the construction of a series of Pair-Wise Comparison Matrices (PCMs), which compare all the criteria to one another. Saaty (1980) suggests a scale of 1 to 9 for PCM elements, wherein the value of 1 suggests that the criteria are equally important and a value of 9 leads one to infer that the criterion under consideration is extremely important in relation to the other criterion with which the comparison is made.

Mathematical expression in AHP, if there are n criteria, then PCM of order $n \times n$ can be written as follows:

$$\begin{bmatrix} w_1/w_1 & w_1/w_2 & \ldots\ldots & w_1/w_n \\ w_2/w_1 & w_2/w_2 & \ldots\ldots & w_2/w_n \\ w_3/w_1 & w_3/w_2 & \ldots\ldots & w_3/w_n \\ \ldots\ldots\ldots & \ldots\ldots\ldots & \ldots\ldots\ldots & \ldots\ldots\ldots \\ w_n/w_1 & w_n/w_2 & \ldots\ldots & w_n/w_n \end{bmatrix} \times \begin{bmatrix} w_1 \\ w_2 \\ w_3 \\ \ldots\ldots \\ w_n \end{bmatrix} = \begin{bmatrix} nw_1 \\ nw_2 \\ nw_3 \\ \ldots\ldots \\ nw_n \end{bmatrix}$$

i.e (Eq. 3.7)

$$\left[A_{(j,j)}\right] \times \left[W_{(1,j)}\right] = \left[nW_{(1,j)}\right]$$

where A is an $n \times n$ PCM in terms of ratio of ratings/weights, W is the ratings or weights (priority rankings/weights) of criteria and n is the order of the PCM matrix. The input matrix is 'A' and the solution for **Equation 3.7** is the common eigen-value problem. The solution to this set of equations is found by solving an nth order equation as follows.

Raise the PCM to powers that are successively squared each time. The rows of the PCM and the squared PCM are normalized (i.e. each row element is divided by the sum of the elements in that row) to give the eigenvectors of the PCM and the raised PCM. The difference between these eigenvectors is checked against a threshold value (i.e. in this study, a value of 0.0001 is used) and if the difference is less than the threshold value, the eigenvector of the raised PCM is the estimated rating/weight vector (Thirumalaivasan et al,. 2003).

In order to calculate the consistency of the result, Saaty and Vargas (1991) suggested using a preference matrix correction if the CR value exceeds 0.1. CR is defined as the ratio between the consistency index (CI) and the random consistency index (RI), and it can be expressed by the following equation:

$$CR = \frac{CI}{RI}, \qquad \text{in which } CI = \frac{(\lambda_{max} - N)}{(N-1)} \qquad \text{(Eq. 3.8)}$$

Where, λ_{max} represents the principal eigen-value, and N is the number of the comparison matrix (number of parameter).

Table 3.7 Assignment of the random consistency index (Saaty, 1982)

Matrix size (N)	*1*	*2*	*3*	*4*	*5*	*6*	*7*	*8*	*9*	*10*
Random consistency index	0	0	0.58	0.90	1.12	1.24	1.32	1.41	1.45	1.49

3.3.2 Weighted Overlay in Spatial Analyst

The Weighted Overlay tool applies one of the most used approaches for overlay analysis to solve multi-criteria problems such as site selection and suitability models. In a weighted overlay analysis, each of the general overlay analysis steps is followed.

The tool combines the following steps:

- Reclassifies values in the input rasters into a common evaluation scale of suitability or preference, risk, or some similarly unifying scale
- Multiplies the cell values of each input raster by the rasters weight of importance
- Adds the resulting cell values together to produce the output raster

In the term of tsunami vulnerability mapping, **Figure 3.5** describes the weighted overlay model to create a final map of tsunami vulnerability based on the criteria that has been set in the input parameter (elevation, slope, coastal proximity, water/river existence, and landuse category).

Each value class in each input raster is assigned a new, reclassified value on an evaluation scale of 1 to 5, where 1 represents the lowest vulnerability and 5 the highest. For instance, in the elevation raster, the lowest elevation is highly vulnerability, while the highland is not. In the coastal proximity, the area that close to the coastal line is more vulnerable to the hinterland area. The weight value is follow a criteria value that have been set in the AHP process.

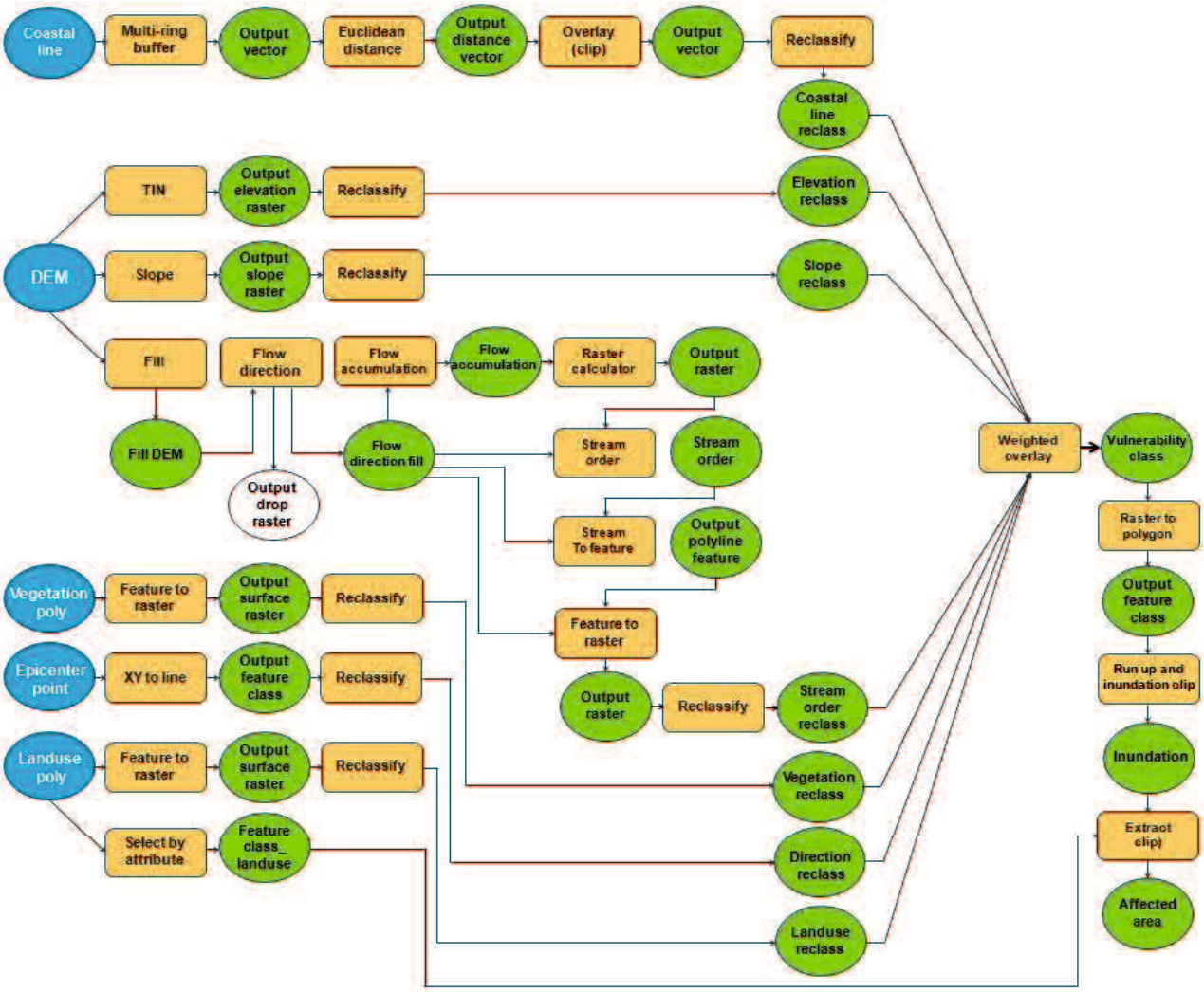

Figure 3.5 Model builder process for weighted overlay

3.4 Satellite Image Processing

3.4.1 DN to Radiance Conversion

Equation 3.9 describes the algorithm for DN to radiance conversion (Bouvet et al., 2007).

$$L_{\lambda} = G_{rescale} \times QCAL + B_{rescale} \quad \text{(Eq. 3.9)}$$

in which L_{λ} is the spectral radiance at the sensor's aperture ($W/m^2/sr/\mu m$), $G_{rescale}$ is the rescaled gain, QCAL is the DN, and $B_{rescale}$ is the rescaled bias. **Table 3.8** describes rescaled gains and biases for ALOS AVNIR-2.

Table 3.8 Rescaling gains and biases used for DN to spectral radiance conversion for ALOS AVNIR 2

Band	$G_{rescale}$	$B_{rescale}$
1	0.5888	0
2	0.5730	0
3	0.5020	0
4	0.8350	0

3.4.2 Radiance to Reflectance Conversion

Equation 3.10 describes the algorithm for radiance to reflectance conversion (Sah et al., 2012).

$$\rho_\lambda = \pi \times L_\lambda \times {d^2}/{ESUN_\lambda} \times \cos\theta_s \quad \text{(Eq. 3.10)}$$

in which ρ_λ is the unitless planetary reflectance, L_λ is the spectral radiance at the sensor's aperture, d^2 is the Earth-sun distance in astronomical units from a nautical handbook, $ESUN_\lambda$ is the mean solar exoatmospheric irradiances, and θ_s is the solar zenith angle in degrees.

3.4.3 NDVI, SAVI, and MSAVI Calculation

NDVI is a measure of the difference in reflectance between these wavelength ranges that takes values between −1 and 1, with values > 0.5 indicating dense vegetation and values < 0 indicating no vegetation including water. **Equation 3.11** was used for NDVI calculation (Hansen et al., 2000).

$$NDVI = \frac{(NIR - VIS)}{(NIR + VIS)} \quad \text{(Eq. 3.11)}$$

in which *NIR* is the reflectance of near infrared band and *VIS* is that of visible band of red band of ALOS AVNIR-2. Band 3 is red, and band 4 is *NIR*. Moreover, SAVI is one of the algorithms developed to generate vegetation index by eliminating soil factor (Gong et al., 2003). Although the SAVI model is not significant in the intra-class analysis, in the similar spectral space, this model presents a reasonable

performance in the characterization of forested and non-forested areas (Araujo et al., 2000). SAVI was developed to minimize soil-brightness, including shadow, influences found in the NDVI by accounting for first-order soil-vegetation spectral interactions as in **Equation 3.12** (Huete, 1988).

$$SAVI = \frac{(NIR - R)}{(NIR + R + L)} \times (1 + L) \qquad \text{(Eq. 3.12)}$$

in which *NIR* is the near infrared band, *R* is the red band, and *L* is the soil calibration factor, $L = 0.5$ (Jensen, 2000). A correction factor (L) was used to minimize the secondary backscattering effect of canopy-transmitted soil background reflected radiation. The *L* value of 1 was optimal in semiarid environments.

MSAVI is a modified version of SAVI, which replaces the constant soil adjustment factor, *L*, with a self-adjusting *L*. SAVI uses a manual adjustment *L*, while MSAVI uses a self-adjusting *L*. The former requires prior knowledge about vegetation densities in order to use an optimal *L* value in the SAVI equation, while the latter automatically adjusts its *L* values to optimal (Qi et al., 1994). **Equation 3.13** describes the algorithm for MSAVI calculation.

$$MSAVI = \frac{1}{2}\left(2NIR + 1 - \sqrt{(2NIR + 1)^2 - 8(NIR - R)}\right) \qquad \text{(Eq. 3.13)}$$

3.4.4 Decision Tree Classification

A decision tree is a classification scheme which generates a tree and a set of rules, representing the model of different classes, from a given dataset. Decision tree is a flow chart like tree structure, where each internal node donates a test on an attribute, each branch represents an outcome of the test and leaf nodes represent the classes or class distribution (Hans and Kamper, 2011). **Figure 3.6** shows the concept of decision tree used in this study, in which NDVI value was used as the basic expression.

Each decision is based on a numerical comparison with a selected threshold index, which makes the whole process easily repeatable. Dall'Osso et al. (2010) have recently used a similar method in creating land use map for assessing tsunami

vulnerability using ASTER imagery. The main advantage of such approach is that data from many different sources and files can be used together to make a single decision tree classifier. Furthermore, the "decision tree" tool is non parametric, therefore it makes no assumptions on the distribution of the input data (Friedl and Brodley, 1997). The NDVI is a simple numerical indicator that can be used to analyze remote sensing measurements, typically but not necessarily from a space platform, and assess whether the target being observed contains live green vegetation.

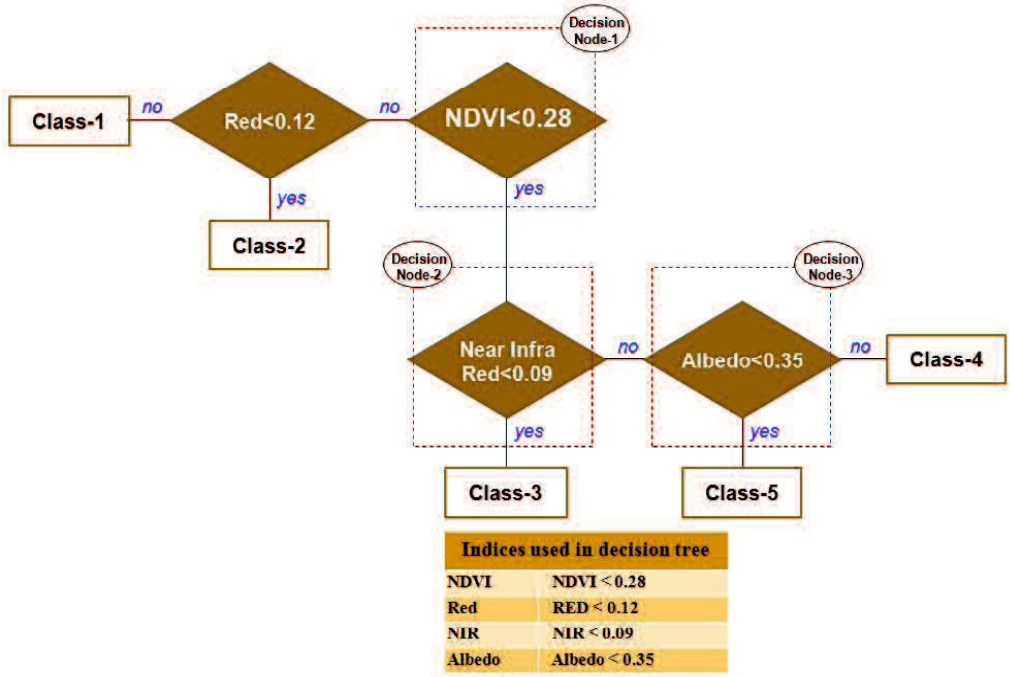

Figure 3.6 Decision tree used in the image classification

1) Entering Decision Tree Rules
   a. The decision tree tool starts with one empty decision node that will divide the pixels in the dataset into two groups, using whatever binary decision expression is entered into that empty node.
   b. The first decision will be based on the medium resolution of satellite image. The decision can be created by adding the decision node labeled.
   c. Expression of the decision can be set in the decision node based on the criteria of analysis (for instance; NDVI < 0.28. This is the text that will appear on the decision node in the graphical view of the decision tree.

d. After adding the expression, the variable/file pairings dialog appears.

2) Pairing the Expression Variable with a File

In this step, an expression that already set will be link to the associate file. This tells the decision tree that when evaluating this decision expression, the expression should be calculated from associate file.

3.4.5 Accuracy Assessment

The accuracy of a classification is usually assessed by comparing the classification with some reference data that is believed to accurately reflect the true land-cover. Sources of reference data include among other things ground truth, higher resolution satellite images, and maps derived from aerial photo interpretation. The result of an accuracy assessment typically provides us with an overall accuracy of the map and the accuracy for each class in the map. For example in a land cover map the water class could be very accurate but some of the vegetation classes might be less accurate. This can have a significant effect on the utility of the map and in some cases may indicate that some classes should be merged.

The results of an accuracy assessment are usually summarized in a confusion matrix. Kappa can be used as a measure of agreement between model predictions and reality (Congalton, 1991) or to determine if the values contained in an error matrix represent a result significantly better than random (Jensen, 1996). Kappa is computed using **Equation 3.14**.

$$k = \frac{N \sum_{i=1}^{r} x_{ii} - \sum_{i=1}^{r} \left(x_{i+} \times x_{+i} \right)}{N^2 - \sum_{i=1}^{r} \left(x_{i+} \times x_{+i} \right)} \qquad \text{(Eq. 3.14)}$$

$$\frac{(total * sum\ of\ correct) - sum\ of\ the\ all\left(row\ total * column\ total\right)}{Total\ squared - sum\ of\ the\ all(row\ total * column\ total)}$$

in which N is the total number of sites in the matrix, r is the number of rows in the matrix, x_{ii} is the number in row i and column i, x_{+i} is the total for row i, and x_{i+} is the total for column i (Jensen,1996).

PART II
RESEARCH APPLICATION (CASE STUDY)

CHAPTER 4

Mapping Tsunami Vulnerability with Spatial Multi-Criteria Analysis Using SRTM DEM V.4, ASTER GDEM V.2, and GSI DEM Japan : a Comparative Study
(Case Study: Miyagi and Iwate Prefectures)

4.1 Introduction

Digital elevation models have become an important input data for the applications of earth observation and environmental sciences. The study of DEM quality is important for many applications, including disaster studies. Errors of DEM can impact on the resulting models of the study. In disaster vulnerability studies, DEM can be used for generating a parameter of elevation, slope, and aspect. Tsunami vulnerability assessment is essential to disaster planning in terms of mitigation, includes pre-planning appropriate response activities in order to minimize the impact of disaster and all possibilities that will happen, and preparing and mitigating for the future events (Papathoma and Dominey-Howes, 2003). The availability of reliable and accurate information concerning the spatial characteristics of elevation data is needed. Thus, a tsunami vulnerability analysis should be developed based on many parameters as possible to get a realistic description of vulnerability area.

Previous studies on DEM comparison have been done and the comparison of different DEM data have been published (Guth, 2010; Hirt et al., 2010; Sertel, 2010; Mangoua, 2008). However, this study used different release of DEM data and different application. The aim of this study is to investigate the elevation data of SRTM (Shuttle Radar Topography Mission) version 4 (published in 2009 by CGIAR-CSI, Italy) and ASTER-GDEM (Advanced Space-borne Thermal Emission and Reflection Radiometer Global Digital Elevation Model) version 2 (made available on October 17, 2011 by NASA, USA and METI, Japan) over the coastal area of Miyagi and Iwate Prefectures in Japan in comparison with GSI-DEM (published by Geospatial Information Authority of Japan) for the application on tsunami vulnerability mapping. In addition, GIS (Geographical Information System) method has been applied in this study to map the vulnerability area due to tsunami disaster. The parameters of tsunami vulnerability was generated using DEM data. Each of tsunami vulnerability parameters weighted based on the impact level of each parameter to the tsunami dis-

aster and calculated in pairwise comparison matrix through AHP (Analytical Hierarchy Process).

In this study SRTM DEM, ASTER GDEM and GSI DEM were compared. The evaluation of each DEM was done before extracting the parameter from each DEM where will be used in the application of raster overlay through spatial multi criteria analysis for assessing tsunami vulnerability.

4.2 DATA AND METHODS

4.2.1 Study Area

The study area is located in the area of Kesennuma city in Miyagi Prefecture, and the area of Rikuzentakata and Ofunato cities in Iwate Prefecture in Japan. Map of study area is shown in **Figure 4.1**. These areas were affected during the 2011 Tohoku earthquake which was reported that triggered huge tsunami waves with maximum run-up heights of greater than 10 m were distributed along 500 km of the coastline (Mori and Takahashi, 2012). The run-up and inundation caused by this tsunami also devastated many cities and villages along the coastline (Mikami et al., 2012).

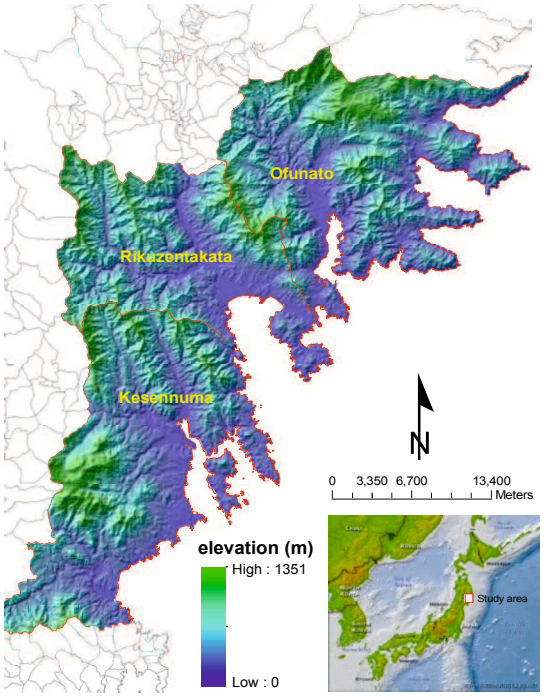

Figure 4.1 Study area

4.2.2 DEM Data

The SRTM data was downloaded from the CGIAR-CSI SRTM 90m database (http://srtm.csi.cgiar.org). The Consortium for Spatial Information (CGIAR-CSI) of the Consultative Group for International Agricultural Research (CGIAR) is offering post-processed 3-arc second DEM data for the globe. This digital elevation data provided has been processed to fill data voids and to facilitate its ease of use by potential users (Jarvis et al. 2008). ASTER-GDEM is a joint product developed and made available to the public by the Ministry of Economy, Trade, and Industry (METI) of Japan and the United States National Aeronautics and Space Administration (NASA). Improvements in the GDEM version 2 result from acquiring 260,000 additional scenes to improve coverage, a smaller correlation kernel to yield higher spatial resolution, and improved water masking (Tachikawa et al., 2011). ASTER-GDEM version 2 was downloaded from http://gdem.ersdac.jspacesystems.or.jp/.

GSI-DEM is the product of Geospatial Information Authority of Japan. GSI is the only national organization that conducts basic survey and mapping and instructs related organizations to clarify the conditions of land in Japan and that provides the results of surveys to help improve this land. GSI-DEM in JPGIS format was used which is later converted into point shapefile and changed into raster format to create elevation data. The original data of GSI-DEM (XML files) was opened and converted to shapefile using FGDV software version 3.10 copyright of GSI Japan. This DEM was 5m grid size (0.2 arc second). The general steps that adopted in this study are shown in **Figure 4.2**.

All studies employing DEMs make use of planar coordinates to have the same measurement units for both (x,y) and elevation. For the analysis, three elevation datasets sampled at different spatial resolution was compared. The pixel size of the ASTER GDEM DEM was 30 m, whereas the SRTM DEM had a pixel dimension of 90 m, as provided by the CGIAR-CSI and GSI DEM was 5 m. In order to compare the two datasets, the ASTER DEM was scaled up to an aggregated pixel size, matching the dimensions of the SRTM grid. This also applied to the GSI DEM.

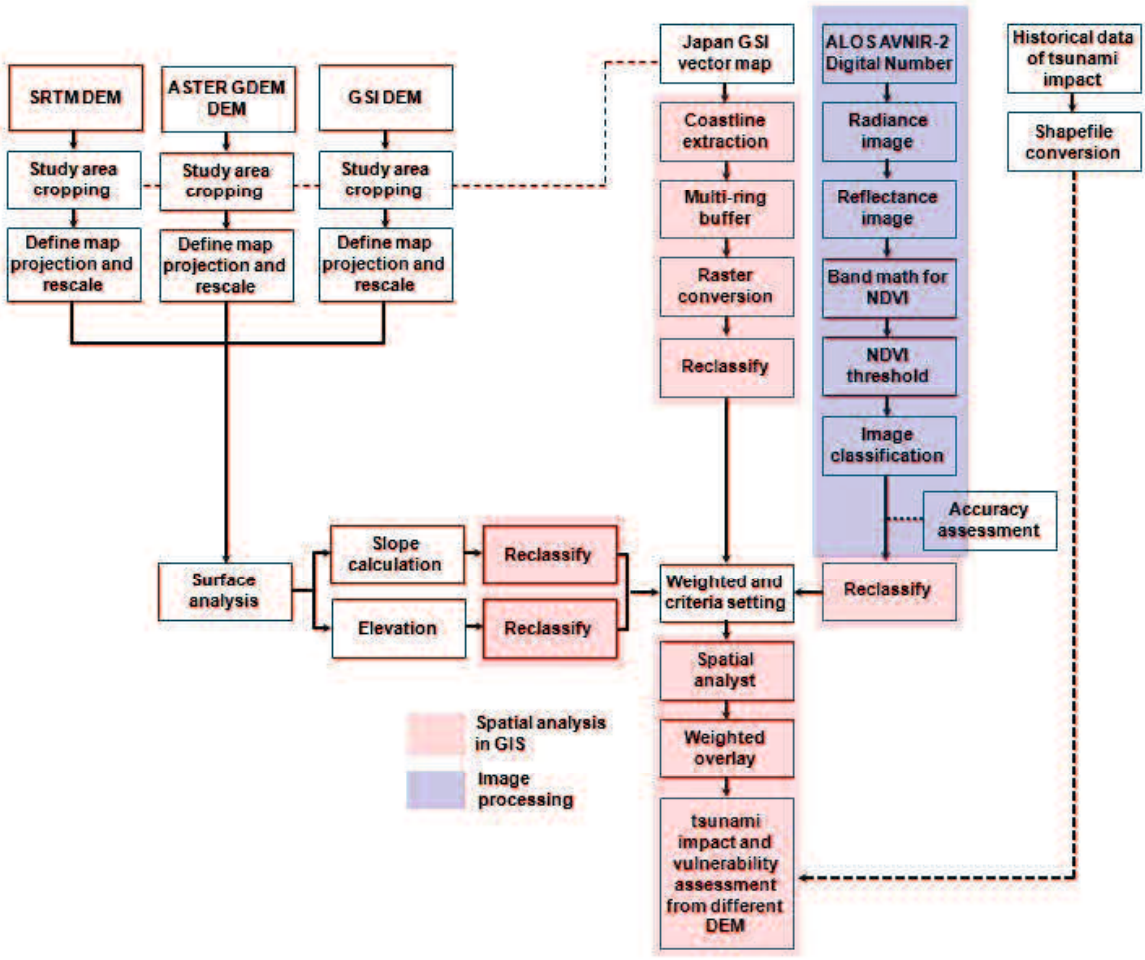

Figure 4.2 The general steps that adopted in this study

4.3 SRTM – ASTER - GSI DEM Comparison

By superimposing the two DEMs for each area, a noteworthy misalignment of the DEM was observed, which had probably been caused by the datum transformation process. In order to evaluate misalignment, several elevation profiles along the North–South and East–West directions for all DEMs were compared. Following the re-registration, the spatial distribution of elevation difference between all DEMs was produced by subtracting the respective images pixel-by pixel. Scatter plots of SRTM–ASTER GDEM–GSI DEM difference versus elevation were used in the comparison procedure.

In order to describe and compare the elevation distributions in each DEM, several descriptive statistic measures were employed, among them skewness and kurtosis (King and Julstrom, 1982). Skewness is a unitless measure of asymmetry in a dis-

tribution (Shaw and Wheeler 1985). Positive skewness indicates a longer tail to the right, while negative skewness indicates a longer tail to the left. A perfectly symmetric distribution, like the normal distribution, has skewness equal to 0. Excess kurtosis is a unitless measure of how sharp the data peak is. Traditionally the value of this coefficient is compared with a value of 0.0, which is the coefficient of kurtosis for a normal distribution. A value larger than 0 indicates a peaked distribution, while a value less than 0 indicates a flat distribution.

The Kolmogorov–Smirnov nonparametric test that does not use any distributional assumptions was used to check the null hypothesis that the distributions are identical for the datasets. Moreover, to obtain the degree of relationship between the SRTM DEM, ASTER GDEM, and GSI DEM, Pearson and Spearman correlation coefficients were calculated for the elevations. Pearson's correlation coefficient represents the association between two variables or the degree of co-variation of the two variables or the tendency of variable to vary together in the sense that one increases as the other increases (positive covariation) or in the sense that one variable increases as the other decreases (negative covariation). The comparisons were made using all elevation data sources.

The analysis indicated that there was a spatial correlation in the original SRTM DEM, ASTER GDEM, and GSI DEM datasets which inflated the corresponding correlation coefficient. For this reason, the correlation analysis was performed again based on spatially uncorrelated points. To do this a sub-sample of all DEMs was used. The sampling was performed at rate that prevented spatial correlations. The sampling rate was defined by analyzing the variograms of all DEMs. Variograms measure spatial variation in regionalized variable. Any random variable whose position in space or time is known is a regionalized variable (Woodcock, et al., 1988).

The variograms for all DEMs are shown in **Figure 4.3**. The range in which the variograms reach their corresponding sills (that is the range where spatial autocorrelation ceases to exist) was too large to allow for a random sample of a satisfactory size. Moreover, **Figure 4.4** shows elevation profile line of North–South and East–West for each pair of DEMs. The East–West elevation profile shows a less noisy pattern while the major terrain variations are similar.

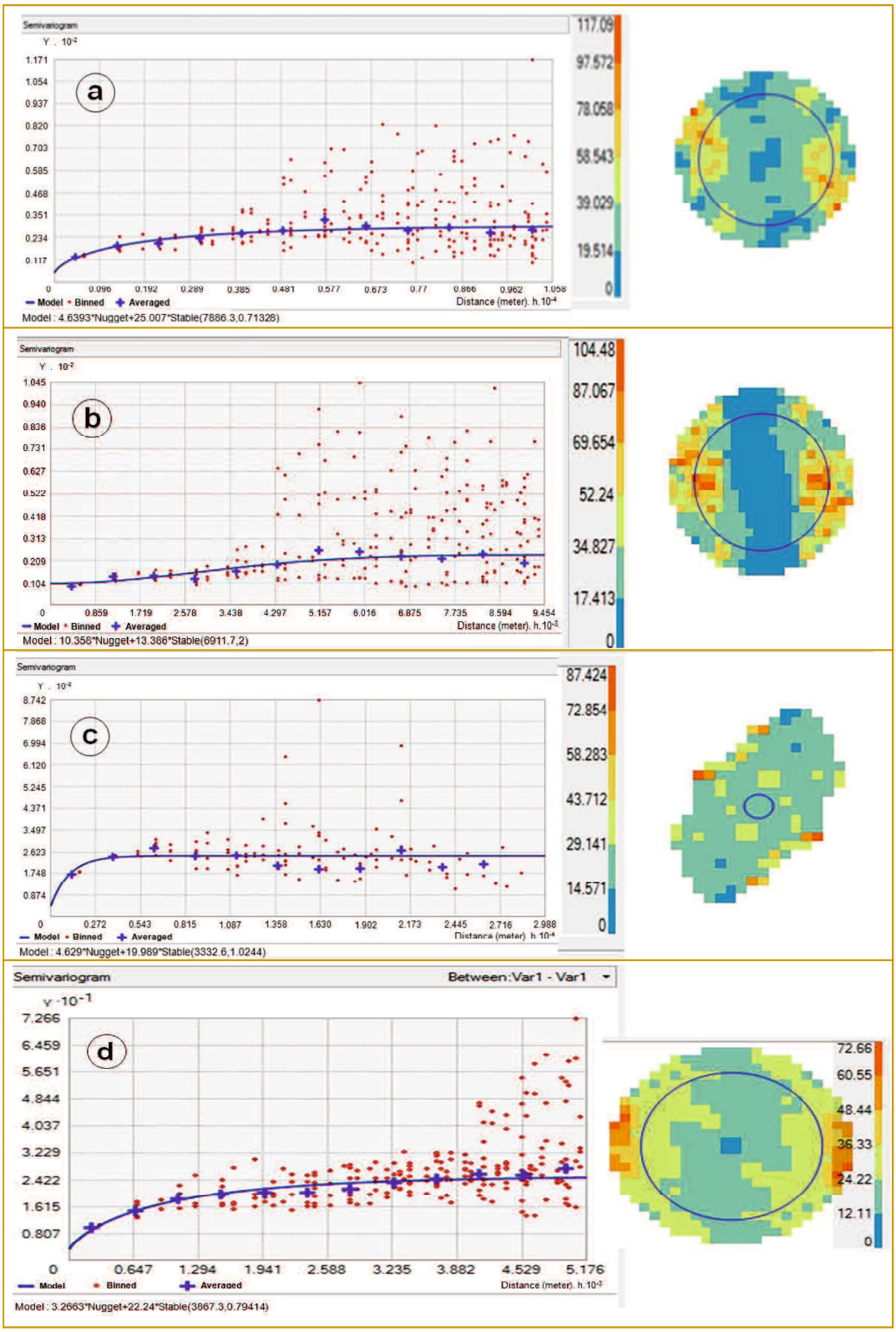

Figure 4.3 The variograms for (a) SRTM DEM; (b) ASTER GDEM; (c) GSI DEM; and (d) SRTM-ASTERGDEM-GSI DEM difference for the area of Kesennuma, Miyagi Prefecture

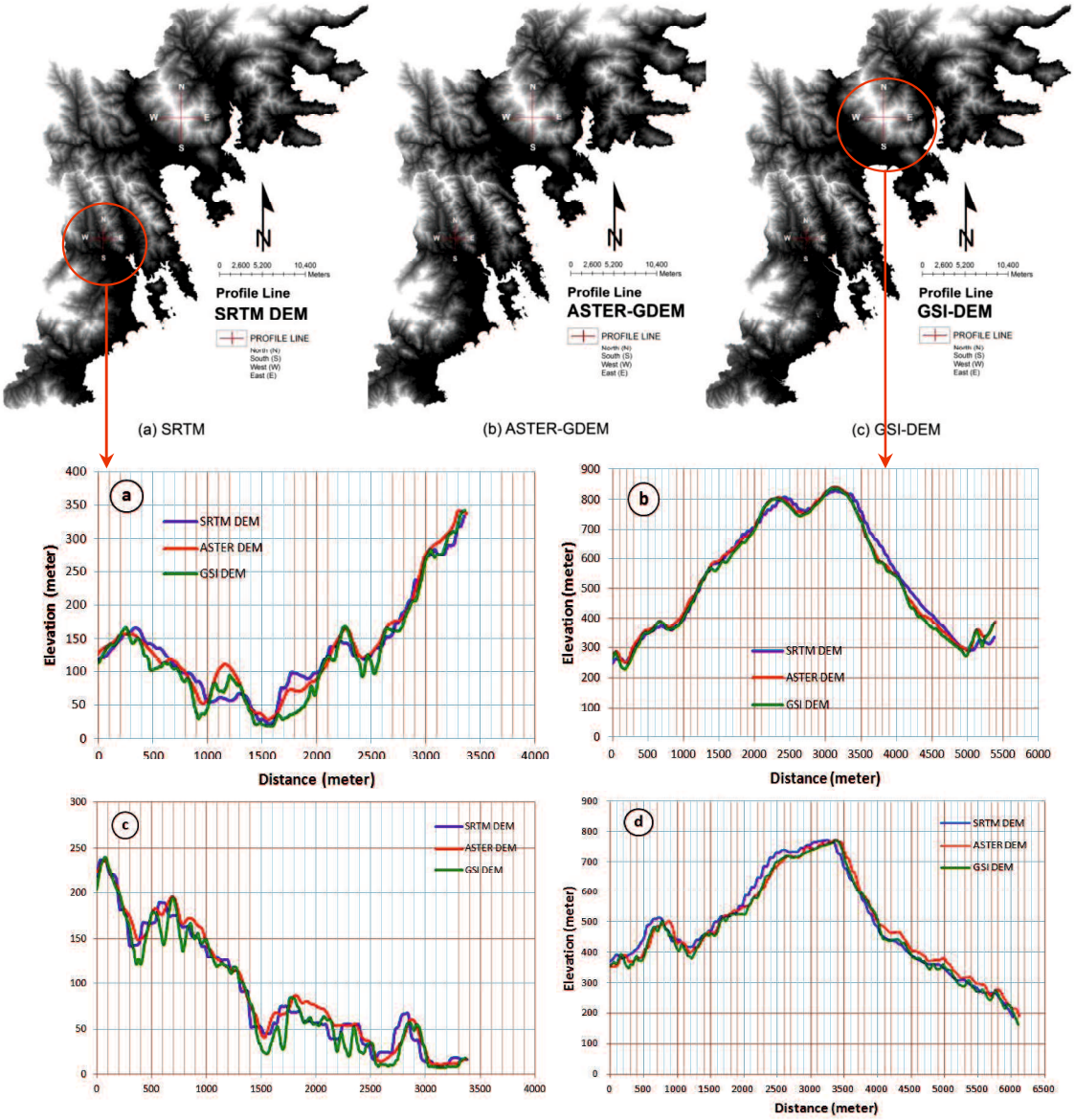

Figure 4.4 Profile elevation of DEM; (a) Kesennuma West-East; (b) Iwate West-East; (c) Kesennuma North-South; and (d) Iwate North-South

The re-register of SRTM DEM, ASTER GDEM, and GSI DEM for the area of Kesennuma, Rikuzentakata, and Ofunato, as well as their histograms, are shown in **Figure 4.5**. The frequency histogram of the values for SRTM DEM and ASTER GDEM seems the same overall pattern of the GSI DEM. The SRTM DEM contains fewer zero values around the coastal area. Several grey values stretches show that the dominant terrain features, large mountains, ridges and troughs are well described in all DEMs. This can also be observed from the similarity of the frequency histograms,

in which several peaks in the histograms co-exist in all datasets. This similarity provides evidence that all DEMs give an analogous representation. The major difference in the two histograms (SRTM DEM and GSI DEM) occurs at the values around zero. These values represent the elevation values around the coastal area where the elevation tend to low. In addition, **Figure 4.6** describes the profile elevation line of all DEMs in diagonal pattern around Rikuzentakata and Ofunato area. This shows a similar pattern of all DEMs.

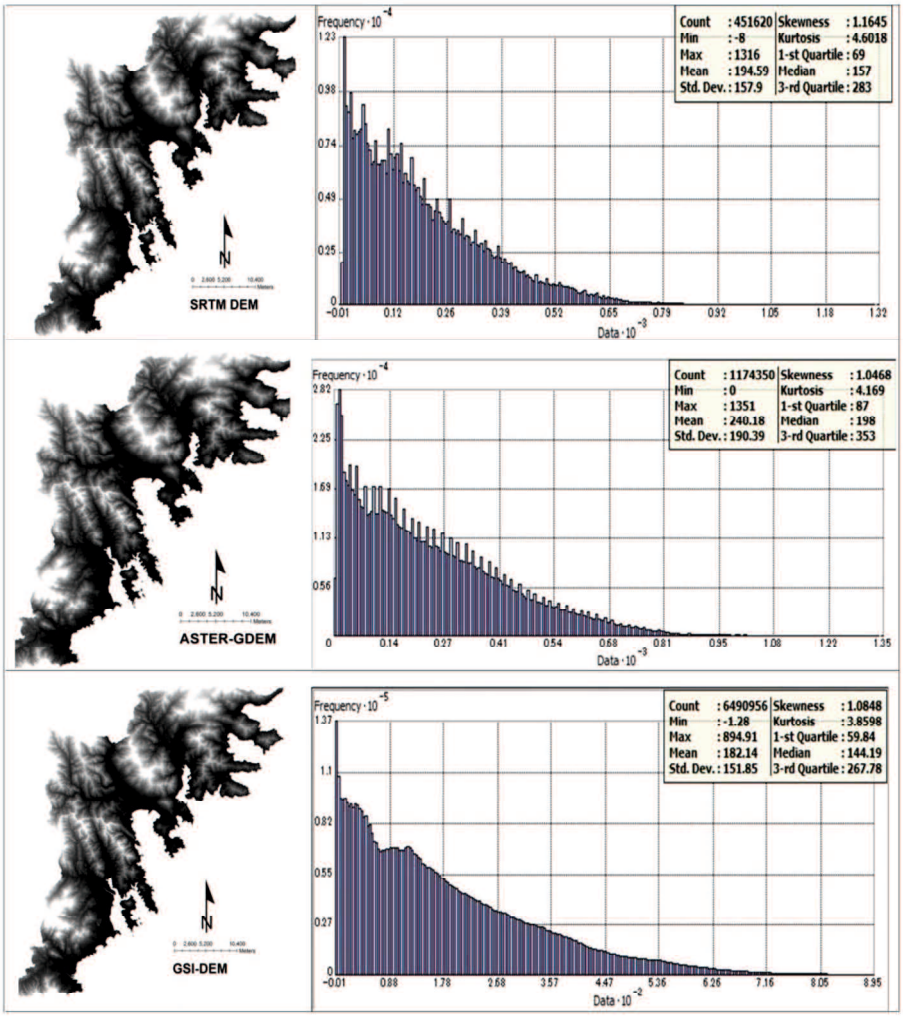

Figure 4.5 SRTM DEM-ASTER GDEM-GSI DEM in the area of Kesennuma, Rikuzentakata and Ofunato related to its frequency histogram

Statistics summary for the elevation profile of GSI DEM, ASTER DEM, and SRTM DEM is described in **Table 4.1**, while Kolmogorov–Smirnov test is shown in **Table 4.2**. Moreover, Pearson and Spearman correlation coefficients is shown in **Table 4.3**. The results were confirmed by a nonparametric test, which does not use

any distributional assumptions. The Kolmogorov–Smirnov shows that the two dataset are not significant different (P<0.05). Pearson and Spearman correlation of The SRTM, ASTER, and GSI show a substantial strong positive correlation.

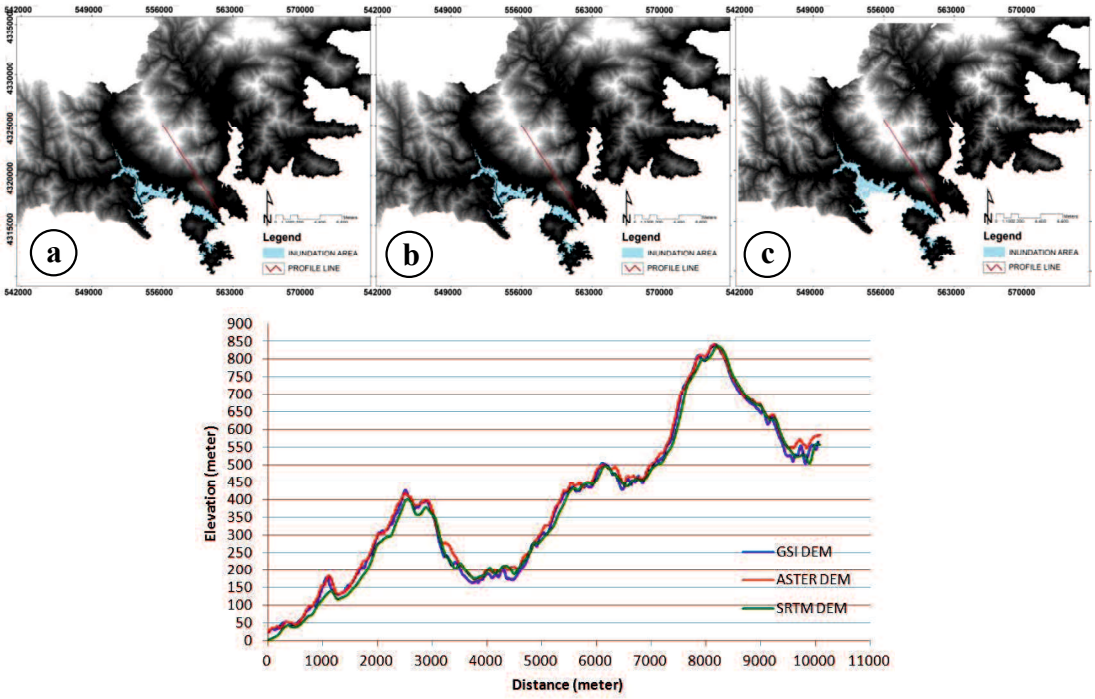

Figure 4.6 Profile elevation line of (a) SRTM DEM ; (b) ASTR GDEM; (c) GSI DEM in the area of Rikuzentakata and Ofunato.
(The high elevation shows similar in the distance of 8000m – 8500m where represented mountain area with the elevation more that 800 m)

Tabel 4.1 Statistics summary for the elevation profile of GSI DEM, ASTER GDEM, and SRTM DEM

	GSI DEM	ASTER GDEM	SRTM DEM
Number of values	100	100	100
Minimum	29.52	29.98	29.97
25% Percentile	166.5	178.6	181.6
Median	304	312.9	300.5
75% Percentile	501.8	498.9	496.5
Maximum	838.9	840.1	836
10% Percentile	84.52	90.55	93.01
90% Percentile	802	805.8	801
Mean	359.9	368.5	364.1
Std. Deviation	247.3	245.7	245.6
Std. Error of Mean	24.73	24.57	24.56
Lower 95% CI of mean	310.8	319.8	315.3
Upper 95% CI of mean	408.9	417.3	412.8

D'Agostino & Pearson omnibus normality test			
K2	12.27	11.95	12.07
P value	0.0022	0.0025	0.0024
Passed normality test (alpha=0.05)?	No	No	No
P value summary	**	**	**
Shapiro-Wilk normality test			
W	0.9012	0.9095	0.903
P value	< 0.0001	< 0.0001	< 0.0001
Passed normality test (alpha=0.05)?	No	No	No
P value summary	****	****	****
Coefficient of variation	68.72%	66.67%	67.47%
Skewness	0.6633	0.6234	0.6583
Kurtosis	-0.7575	-0.774	-0.7529
Sum	35986	36854	36406

Tabel 4.2 Kolmogorov–Smirnov test of GSI DEM, ASTER GDEM, and SRTM DEM

Column A	GSI
vs.	vs.
Column C	SRTM
Kolmogorov-Smirnov test	
P value	0.9938
Exact or approximate P value?	Approximate
P value summary	ns
Significantly different? (P < 0.05)	No
Kolmogorov-Smirnov D	0.06
Mann Whitney test	
P value	0.7945
Exact or approximate P value?	Exact
P value summary	ns
Significantly different? (P < 0.05)	No
One- or two-tailed P value?	Two-tailed
Sum of ranks in column A,C	9943 , 10157
Mann-Whitney U	4893
Difference between medians	
Median of column A	304.0, n=100
Median of column C	300.5, n=100
Difference: Actual	-3.449
Difference: Hodges-Lehmann	4.791

Column B	ASTER
vs.	vs.
Column C	SRTM
Kolmogorov-Smirnov test	
P value	0.9996
Exact or approximate P value?	Approximate
P value summary	ns
Significantly different? (P < 0.05)	No
Kolmogorov-Smirnov D	0.05
Mann Whitney test	
P value	0.8114
Exact or approximate P value?	Exact
P value summary	ns
Significantly different? (P < 0.05)	No
One- or two-tailed P value?	Two-tailed
Sum of ranks in column B,C	10148 , 9952
Mann-Whitney U	4902
Difference between medians	
Median of column B	312.9, n=100
Median of column C	300.5, n=100
Difference: Actual	-12.43
Difference: Hodges-Lehmann	-4.576

Column A	GSI
vs.	vs.
Column B	ASTER
Kolmogorov-Smirnov test	
P value	0.9671
Exact or approximate P value?	Approximate
P value summary	ns
Significantly different? (P < 0.05)	No
Kolmogorov-Smirnov D	0.07
Mann Whitney test	
P value	0.6557
Exact or approximate P value?	Exact
P value summary	ns
Significantly different? (P < 0.05)	No
One- or two-tailed P value?	Two-tailed
Sum of ranks in column A,B	9867 , 10233
Mann-Whitney U	4817
Difference between medians	
Median of column A	304.0, n=100
Median of column B	312.9, n=100
Difference: Actual	8.979
Difference: Hodges-Lehmann	8.376

Tabel 4.3 Pearson and Spearman correlation coefficients

Pearson	*GSI*	*ASTER*	*SRTM*
GSI		0.9051	0.7843
ASTER	0.9051		0.9189
SRTM	0.7843	0.9189	

Spearman	GSI	ASTER	SRTM
GSI		0.9155	0.8271
ASTER	0.9155		0.9145
SRTM	0.8271	0.9145	

P value			
GSI		3.63E-38	4.89E-22
ASTER	3.63E-38		0
SRTM	4.89E-22	0	

P value			
GSI		0	2.89E-26
ASTER	0		0
SRTM	2.89E-26	0	

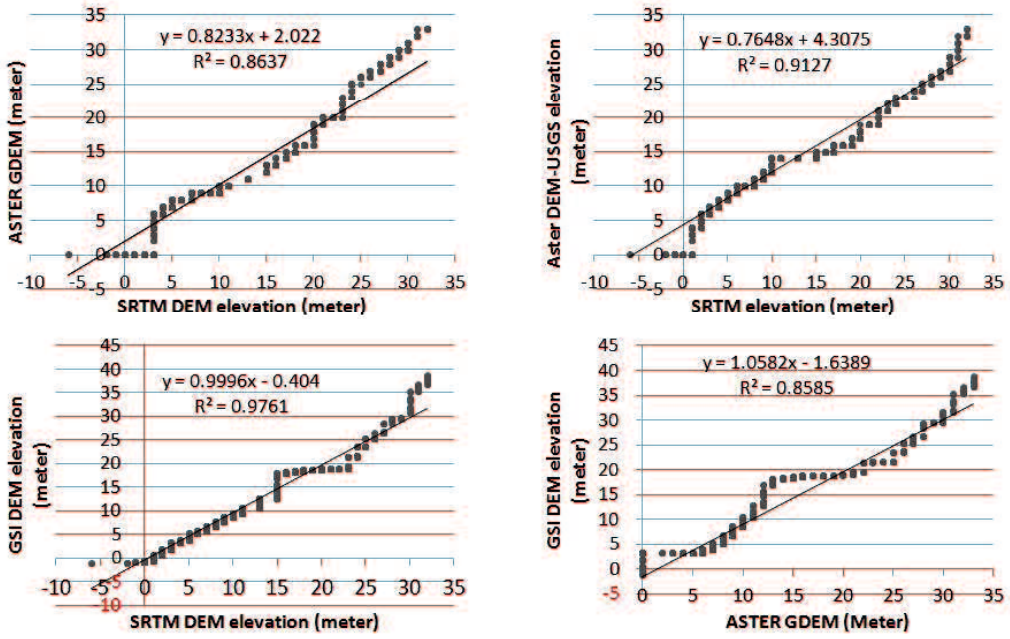

Figure 4.7 Correlation chart of SRTM DEM, ASTER GDEM, and GSI DEM

4.4 Multi-Criteria Analysis for Vulnerability Mapping

4.4.1 Spatial Data Preparation

(1) Surface Analysis

Surface analysis was applied to generate elevation and slope map. Elevation data is one of the principal datasets required for the model to generate vulnerability and inundation area of the tsunami. In addition, slope is the rate of maximum change in z-value from each cell of the image. Slope map was generated using the third-order finite difference method proposed by Horn (1981).

Elevation and slope were classified into five classes of vulnerability based on the criteria as shown in **Table 4.4**. Classified map of elevation and slope is shown in **Figure 4.8** and **Figure 4.9**.

(2) Coastal Proximity

Distance measurement from coastline to the land using multi-ring buffer under the proximity tools of GIS processing was done to divide five classes of vulnerability. The buffering distance was set based on the possibility range of the tsunami to reach the land. The distance is depend on the historical report of the maximum run up in the area of the study, and is expressed by **Equation 4.1** (Bretschneider and Wybro, 1976; Sinaga et al., 2011).

$$\log X_{max} = \log 1400 + \frac{4}{3}\log\left(\frac{Y_o}{10}\right) \qquad \text{(Eq. 4.1)}$$

in which, X_{max} is the maximum reach of the tsunami over land and Y_o is the tsunami height at the coast. The maximum run-up in the study area based on The 2011 Earthquake Tsunami Joint Survey Group was 30.1meter. By using **Equation 4.1**, five range of coastline distance that vulnerable to the tsunami were generated using the criteria as shown in **Table 4.4**. Tsunami vulnerability map based on coastal proximity is shown in **Figure 4.10**.

Table 4.4 Vulnerability class based on elevation (Iida, 1963), slope (Van Zuidam, 1983), coastal proximity, and Landuse

Elevation (meter)	Slope (percentage)	Coastal Proximity (meter)	Land use	Vulnerability class
< 5	0 – 2	0 – 603.50	Urban area	High
5 – 10	2 – 6	603.50 – 1,451.76	Agriculture	Slightly high
10 – 15	6 – 13	2,453.60 – 3,572.06	Bare soil	Medium
15 – 20	13 – 20	3,572.06 – 4,786.75	Lake/fresh water	Slightly low
> 20	> 20	4,786.75 – 6,084.39	Forest	Low

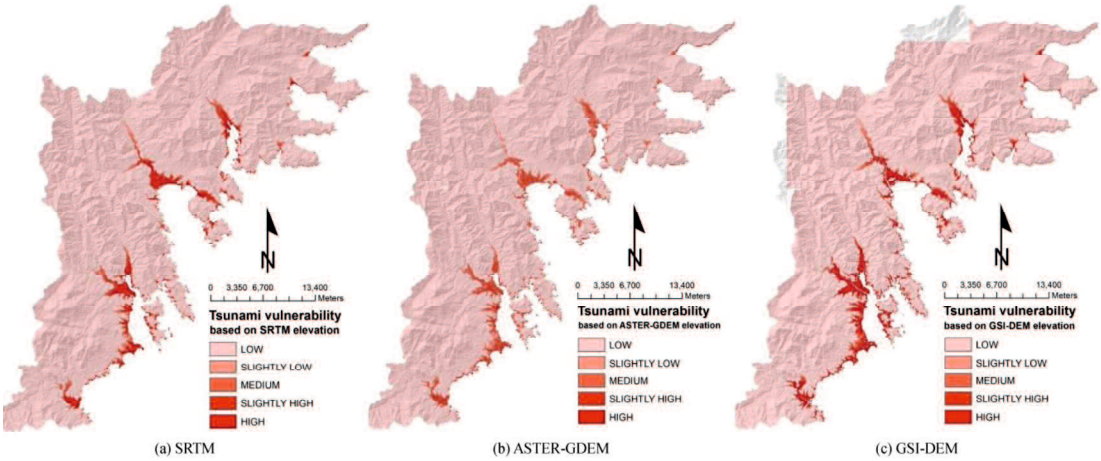

Figure 4.8 Tsunami vulnerability map based on three different elevation data; (a) SRTM DEM; (b) ASTER GDEM; (c) GSI DEM

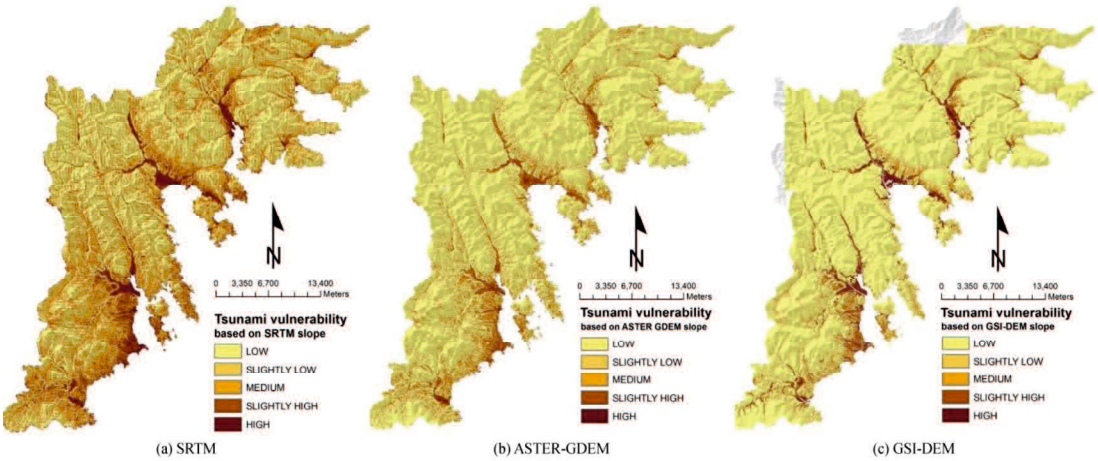

Figure 4.9 Tsunami vulnerability map based on three different slope data; (a) SRTM DEM; (b) ASTER GDEM; (c) GSI DEM

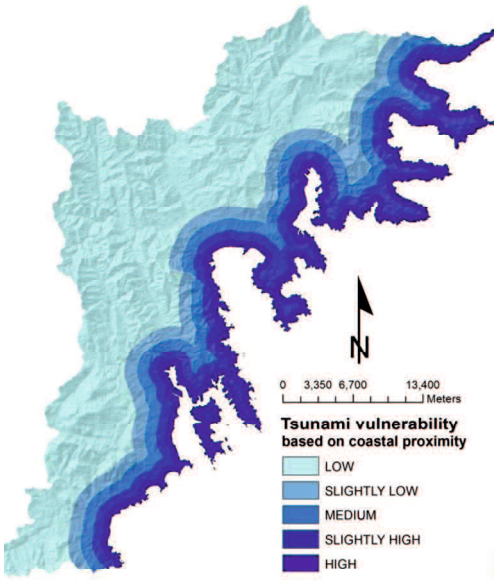

Figure 4.10 Tsunami vulnerability based on coastal proximity

4.4.2 Satellite Image Processing

ALOS AVNIR-2 image acquired on 18 March 2009 was used to map the vegetation coverage. Vegetation density was classified using NDVI (Normalized Difference Vegetation Index) value. NDVI is a measure of the difference in reflectance between red wavelength and near infra-red wavelength ranges. It takes values between −1 and 1, where values less than 0 indicating no vegetation. NDVI was estimated using **Equation 4.2**.

$$NDVI = \frac{(NIR - VIS)}{(NIR + VIS)} \qquad \text{(Eq. 4.2)}$$

in which NIR is Near Infra-Red band and VIS is visible band of red band.

In this study, NDVI shows a minimum value of -0.28 and a maximum value of 1. This map later be classify to create a land use map using a “decision tree” classification methods. A decision tree is a type of multistage classifier that can be applied to a single image or a stack of images. It is made up of a series of binary decisions that are used to determine the correct category for each pixel. The decisions can be based on any available characteristic of the dataset.

After creating a landuse map, and calculating the overall accuracy for the classification map, the raster map will be classified into five classes of vulnerability due to tsunami. This raster re-classification is using the criteria as shown in **Table 4.4**. The result of the classification is shown in **Figure 4.11(a)**, while the map of tsunami vulnerability based on the landuse is shown in **Figure 4.11(b)**. The overall accuracy for the classification map describe that the overall accuracy for the classification is 0.821. **Figure 4.12** describes the reference point map for accuracy assessment.

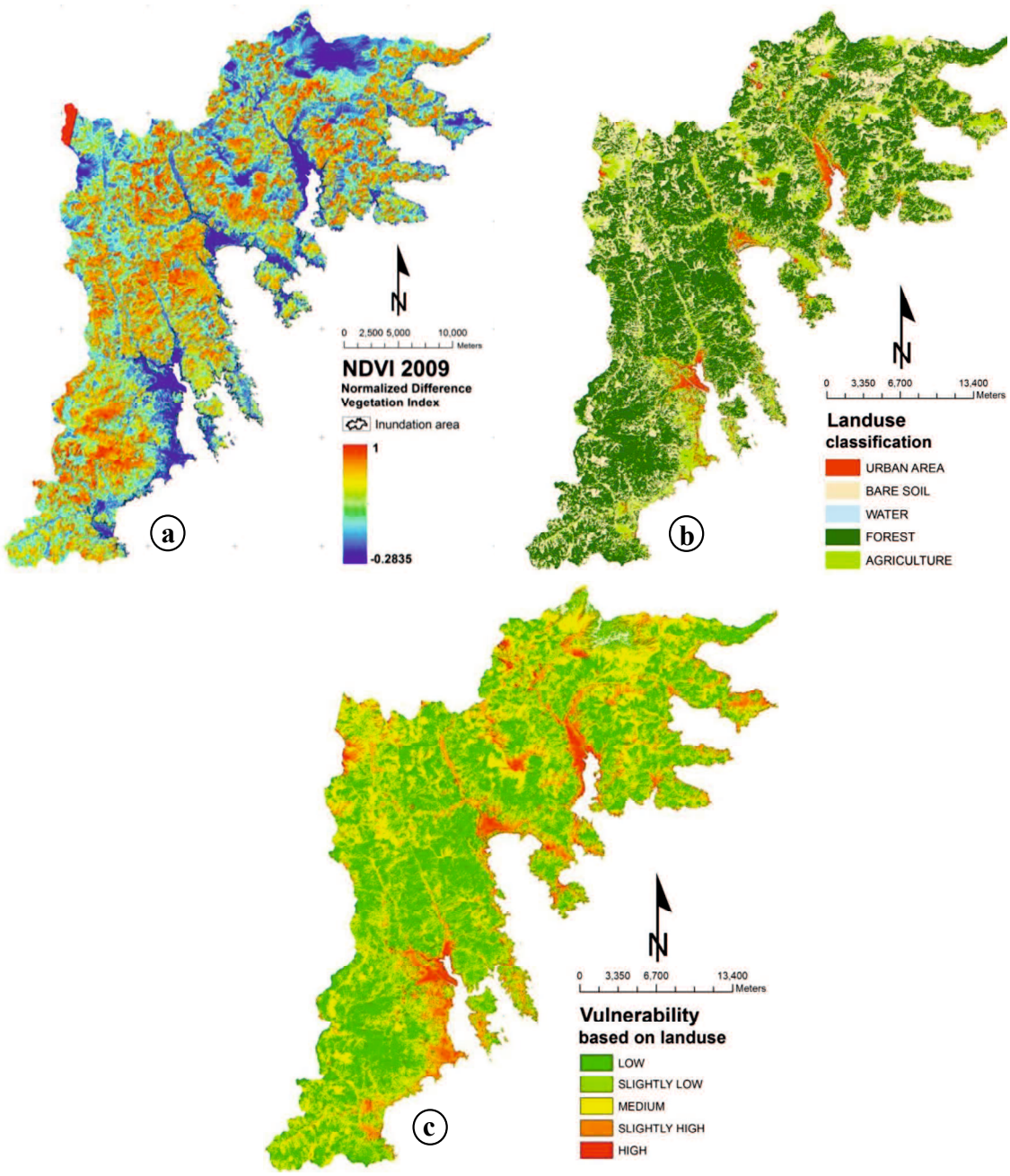

Figure 4.11 (a) NDVI map; (c) landuse map; and (b) tsunami vulnerability based on landuse classification

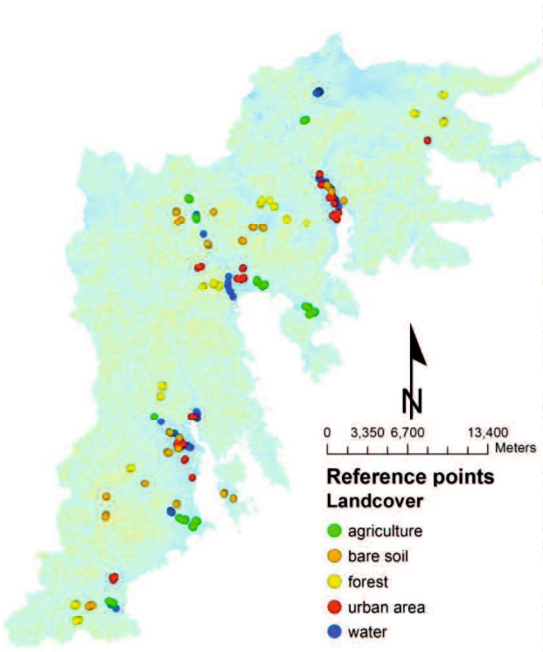

Overall accuracy: 0.821
Kappa : 0.776

Landuse	Class	Ref. 3	Ref. 1	Ref. 4	Ref. 5	Ref. 2	ground truth
water	3	25	0	0	0	0	25
urban	1	18	45	1	0	0	64
forest	4	0	0	49	0	0	49
agriculture	5	8	0	0	45	8	61
baresoil	2	0	5	0	5	42	52
		51	50	50	50	50	251

ground truth	Ref. 3	Ref. 1	Ref. 4	Ref. 5	Ref. 2
water	49.0196	0	0	0	0
urban	35.2941	90	2	0	0
forest	0	0	98	0	0
agriculture	15.6863	0	0	90	16
baresoil	0	10	0	10	84

Comision			
water	0	25	0
urban	1	64	1.5625
forest	0	49	0
agriculture	42	61	68.8525
baresoil	25	52	48.0769

Omision			
water	0.5098	50	1.0196
urban	0.1	50	0.2
forest	0	50	0
agriculture	0.1	50	0.2
baresoil	0.5	50	1

Producers			
water	25	50	50
urban	45	50	90
forest	49	50	98
agriculture	45	50	90
baresoil	42	50	84

Figure 4.12 Reference points map for the accuracy assessment

4.5 Result and Discussion

All parameters in this study were in raster format and classified into five classes of vulnerability. Numbers of 1, 2, 3, 4, and 5 were used to represent low, slightly low, medium, slightly high and high vulnerability. AHP was applied in assigning weights to each of the parameters. AHP helps in creating a scaled set of preferences and describing the importance of each parameter relative to other parameter through pairwise comparisons (Saaty, 1980). The relative weights of each parameter will be produced through pairwise comparison as shown in **Table 4.5**. Hierarchical interactions were calculated based on the respective importance of each parameter by assessing of numerical score. A calculation of the consistency level is necessary due to subjective assessment of the score. Consistency Ratio (CR) is a procedure for determining the index of consistency. It indicates the probability that the matrix judgments were randomly generated (Saaty, 1977). AHP tolerates inconsistency by providing a measure of inconsistency assessment. Acceptable consistency ratio is less than or equal to 10 percent (Forman and Selly, 2001). CR can be expressed using **Equation 4.3**.

$$CR = \frac{CI}{RI}, and\ CI = \frac{(\lambda_{max} - N)}{(N-1)} \quad \text{(Eq. 4.3)}$$

λ_{max} represents the largest eigenvalue and N is the size of comparison matrix. In this study $N = 4$. RI is based on the random consistency, in which $RI = 0.90$ for $N = 4$. To obtain the weight of each parameter, the eigenvector was calculated using five iterations from normalized matrix as shown in **Figure 4.13**. This calculation produces a CI value of 0.057 and a CR value of 6.4%, and shows that elevation is the most important factor followed by slope, coastal proximity, and vegetation density. In order to create the vulnerability map, each raster cell of the parameter was calculated to its weight.

Weighted linear combination is very straightforward in a raster GIS and factors are combined by applying a weight value to each followed by a summation of the results to create a vulnerability map using **Equation 4.4** (Eastman et al., 1995).

$$\sum(W_i \cdot X_i) \quad \text{(Eq. 4.4)}$$

in which, Wi is the weight values of the parameter i, and X_i is the potential rating of the factor. The rating was divided based on vulnerability class and used number of 1 to 5, in which 1 is represented low vulnerability and 5 is for high vulnerability.

The result of tsunami vulnerability in five classes using three different DEM data is shown in **Figure 4.14**, while the comparison of affected area due to tsunami is shown in **Table 4.6** and **Figure 4.15**. It was described that SRTM elevation data was identified the inundation area almost similar to the tsunami event of the 2011 Tohoku earthquake in the area of Kesennuma and Ofunato, while in the area of Rikuzentakata GSI-DEM described better result. Vulnerability is described the potential area to be damaged by natural disasters, and inundation can be defined as the result of a tsunami traveling a long distance inland and is a horizontal measurement of the path of the tsunami. All tsunami vulnerability maps were compared to the historical data of the 2011 Tohoku earthquake and generated the possible inundation area as shown in **Figure 4.16**.

Table 4.5 Pairwise comparison matrix

	Elevation	Slope	Coastal proximity	Landuse
Elevation	1	2	3	3
Slope	1/2	1	2	2 1/2
Coastal proximity	1/3	1/2	1	3
Land use	1/3	0.4	1/3	1

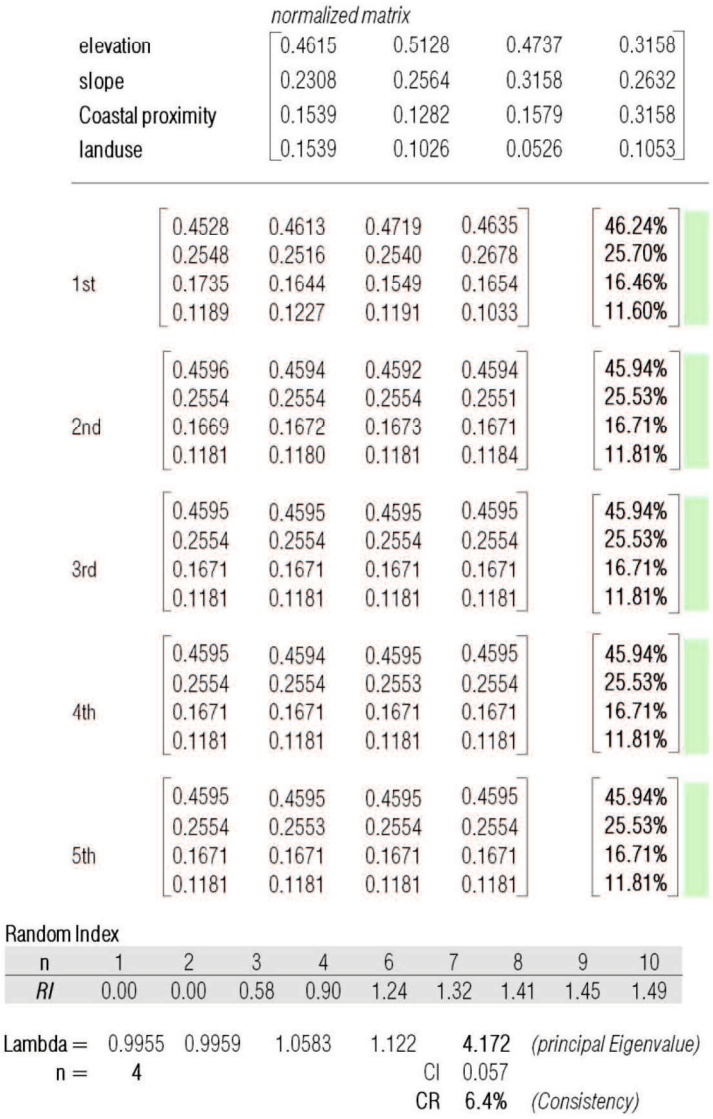

Figure 4.13 Five iterations from normalized matrix of each parameter

This study is a first attempt to assess tsunami vulnerability by comparing the different elevation data using the parameter of vegetation density besides elevation, slope and coastal proximity and apply AHP methods combining with raster overlay

through GIS processing. According to the result of this study, a simple method for inundation prediction can be a valuable step for carrying out a preliminary tsunami vulnerability mapping and impact assessment. Tsunami vulnerability map and inundation map generated in this study can be used for determining a priority for risk prevention, mitigation, and land-use planning to reduce the tsunami risk.

Vulnerability map from SRTM DEM, ASTER-GDEM, and GSI-DEM described that 5.55% of Kesennuma in the slightly high and high class of tsunami vulnerability. This area has possibility as the inundation area due to tsunami. In Rikuzentakata, 4.54% of the area was in slightly high and high class of tsunami vulnerability, and 2.81% of Ofunato area was in slightly high and high class of tsunami vulnerability. The high vulnerability areas were mostly found in the coastal area with the sloping coast type. Inundation areas were predicted in areas that identified as high vulnerability and slightly high vulnerability area. In the scope of tsunami vulnerability mapping using input parameters of elevation, slope, coastal proximity, and vegetation density and compared to the affected area of the 2011 Tohoku earthquake, this study described that SRTM version 4 showed the result that close to the real event in some areas.

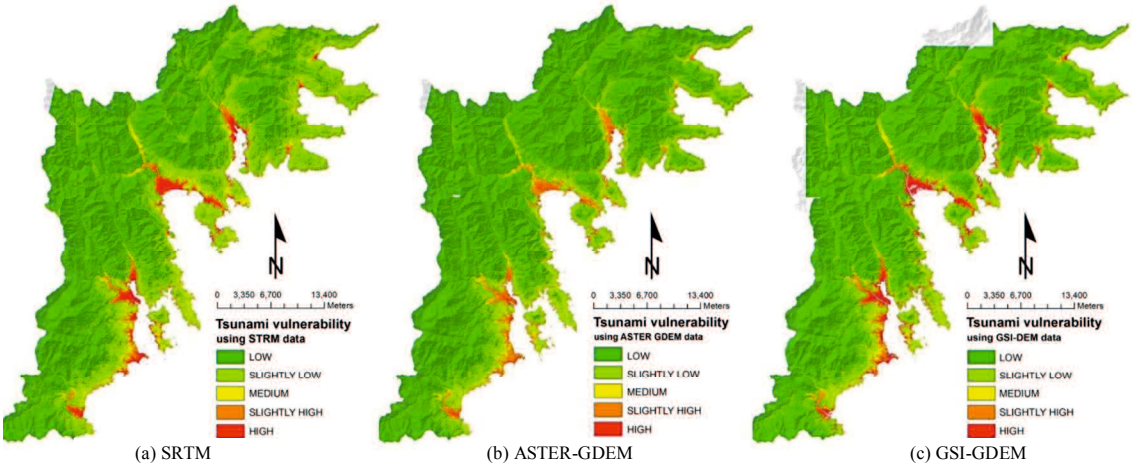

(a) SRTM (b) ASTER-GDEM (c) GSI-GDEM

Figure 4.14 Tsunami vulnerability map; (a) based on SRTM DEM; (b) based on ASTER GDEM; (c) based on GSI DEM in Kesennuma, Rikuzentakata, and Ofunato

Table 4.6 Tsunami vulnerability and inundation in study areas

KESENNUMA	Vulnerability (km²)					Area (km²)	Inundation (km²)	Inundation (km²) (GSI, 2011)
	1	2	3	4	5			
SRTM DEM	224.41	70.78	16.29	9.65	7.93	329.06	17.58	
Aster GDEM	236.61	62.33	15.62	13.49	2.85	330.91	16.34	18
GSI DEM	237.68	55.96	14.36	10.37	10.59	328.97	20.97	

RIKUZENTAKATA	Vulnerability (km²)					Area (km²)	Inundation (km²)	Inundation (km²) (GSI, 2011)
	1	2	3	4	5			
SRTM DEM	167.44	41.06	7.28	4.79	5.92	226.49	10.71	
Aster GDEM	187.77	25.90	5.84	7.14	1.26	227.90	8.40	13
GSI DEM	176.02	21.73	5.28	4.68	6.49	214.20	11.17	

OFUNATO	Vulnerability (km²)					Area (km²)	Inundation (km²)	Inundation (km²) (GSI, 2011)
	1	2	3	4	5			
SRTM DEM	177.87	121.51	8.43	4.73	3.60	316.14	8.33	
Aster GDEM	234.79	71.10	5.59	6.29	1.10	318.87	7.38	8
GSI DEM	217.95	62.59	4.88	5.04	5.21	295.67	10.25	

Vulnerability classes
1 = low, 2 = slightly low, 3 = medium, 4 = slightly high, 5 = high

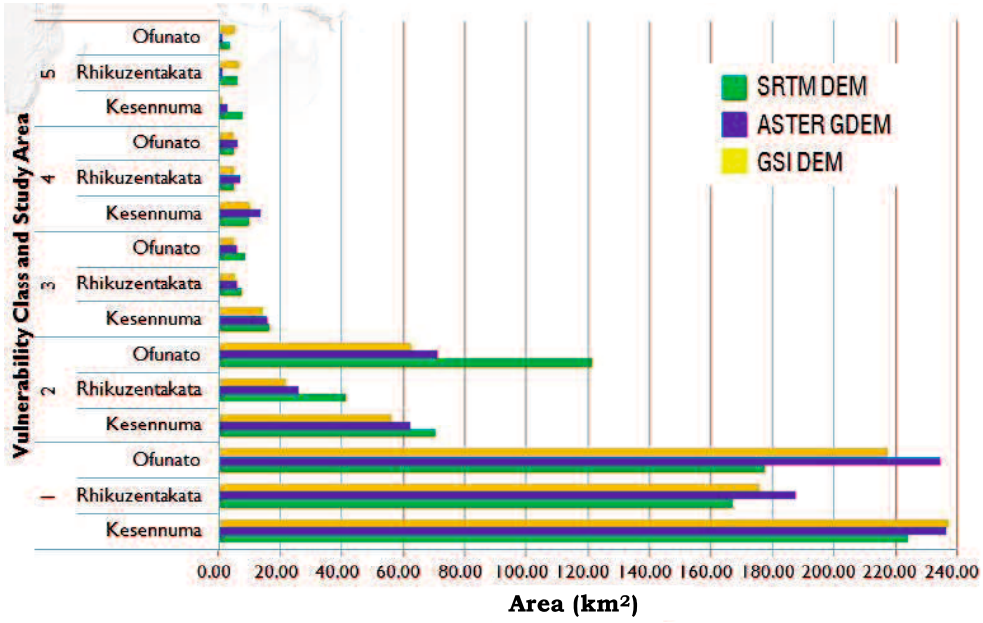

Figure 4.15. Chart of area (in km square) of tsunami vulnerability in Kesennuma, Rikuzentakata, and Ofunato analyzed from SRTM DEM, ASTER GDEM, and GSI DEM

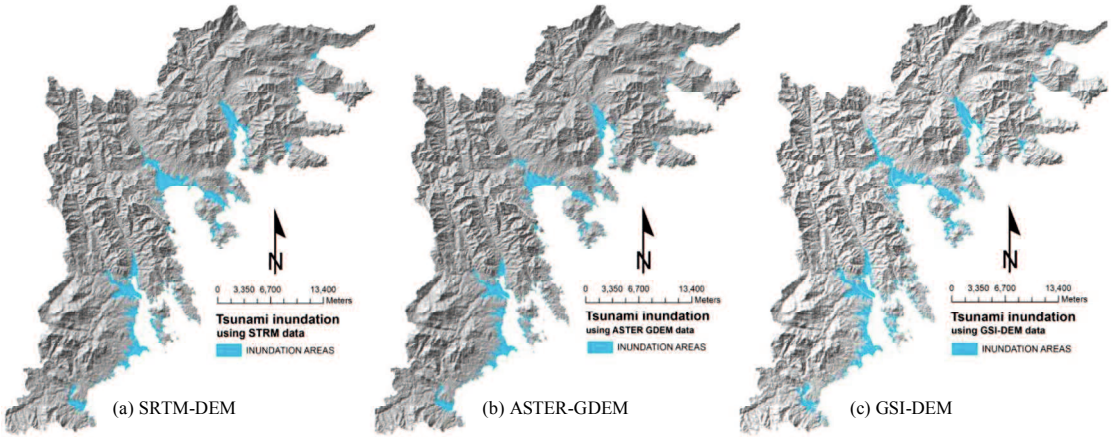

Figure 4.16 Tsunami inundations from three different DEM data

Figure 4.17 describes the validation point in comparison to the vulnerability map along coastal area of Kesennuma city, Rikuzentakata city, and Ofunato city. The point was inundation survey point during the event of the 2011 Japan tsunami. The validation was done by calculating number of pixel in vulnerability class of high and slightly high that classified as the inundation survey points.

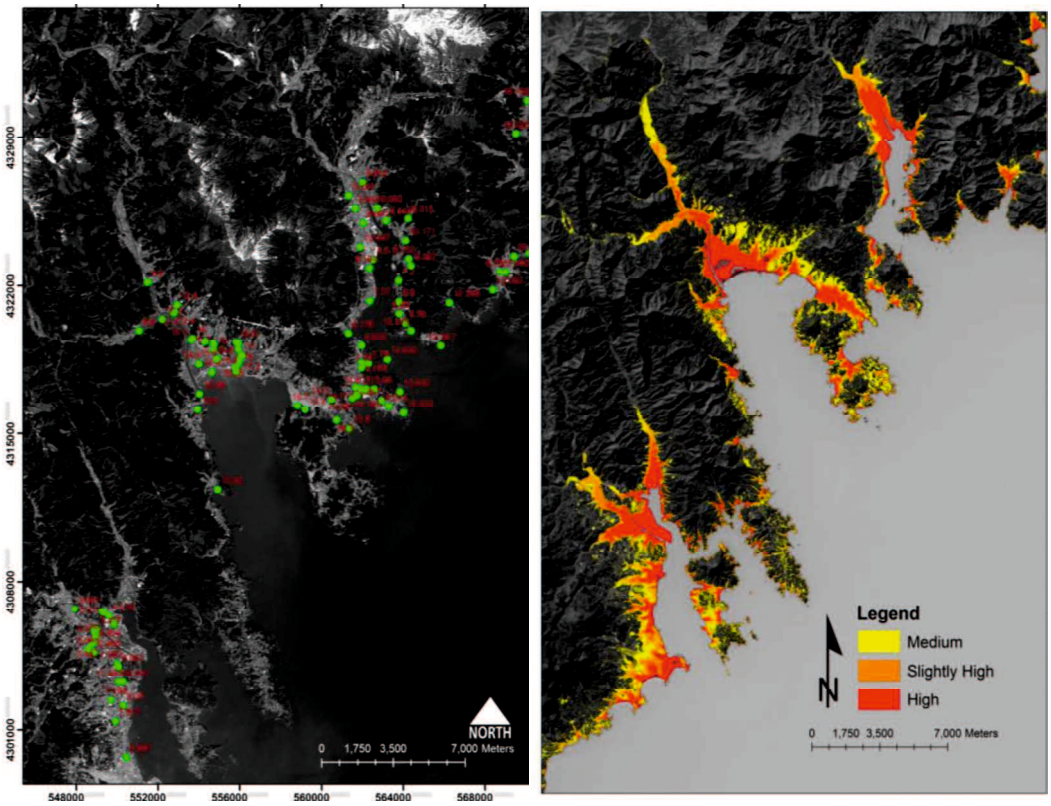

Figure 4.17 Validation points in comparison with vulnerability map

Table 4.7 Multiple comparison of the area calculation in inundation area created from SRTM, ASTER, and GSI DEMs

Number of families	1
Number of comparisons per family	3
Alpha	0.05

Tukey's multiple comparisons test	Mean Diff.	95% CI of diff.	Significant?	Summary
SRTM vs. ASTER	1.533	-0.7817 to 3.848	No	ns
SRTM vs. GSI	-1.9	-6.661 to 2.861	No	ns
ASTER vs. GSI	-3.433	-6.874 to 0.007145	No	ns

Column B vs. Column A	ASTER GDEM vs. SRTM DEM
Unpaired t test	
P value	0.7173
P value summary	ns
Significantly different? (P < 0.05)	No
One- or two-tailed P value?	Two-tailed
t, df	t=0.3887 df=4
How big is the difference?	
Mean ± SEM of column A	12.23 ± 2.764, n=3
Mean ± SEM of column B	10.70 ± 2.815, n=3
Difference between means	1.533 ± 3.945
95% confidence interval	-12.49 to 9.420
R squared	0.03639
F test to compare variances	
F,DFn, Dfd	1.037, 2, 2
P value	0.9819
P value summary	ns
Significantly different? (P < 0.05)	No

Column C vs. Column B	GSI DEM vs. ASTER GDEM
Unpaired t test	
P value	0.4796
P value summary	ns
Significantly different? (P < 0.05)	No
One- or two-tailed P value?	Two-tailed
t, df	t=0.7787 df=4
How big is the difference?	
Mean ± SEM of column B	10.70 ± 2.815, n=3
Mean ± SEM of column C	14.13 ± 3.393, n=3
Difference between means	3.433 ± 4.409
95% confidence interval	-8.808 to 15.67
R squared	0.1316
F test to compare variances	
F,DFn, Dfd	1.453, 2, 2
P value	0.8153
P value summary	ns
Significantly different? (P < 0.05)	No

Column C vs. Column A	GSI DEM vs. SRTM DEM
Unpaired t test	
P value	0.6866
P value summary	ns
Significantly different? (P < 0.05)	No
One- or two-tailed P value?	Two-tailed
t, df	t=0.4341 df=4
How big is the difference?	
Mean ± SEM of column A	12.23 ± 2.764, n=3
Mean ± SEM of column C	14.13 ± 3.393, n=3
Difference between means	1.900 ± 4.377
95% confidence interval	-10.25 to 14.05
R squared	0.04499
F test to compare variances	
F,DFn, Dfd	1.507, 2, 2
P value	0.7978
P value summary	ns
Significantly different? (P < 0.05)	No

4.6 Conclusion

Processing of DEM data through re-scale process, filtering and point interpolation describe a new approach in preparing DEM data for particular application. GIS application followed by AHP method in which DEM data was analyzed is useful for tsunami vulnerability mapping and impact assessment. The result of this study can be used as preliminary study in the scope of tsunami disaster that important for the mitigation, evacuation, and reconstruction plan. It can be concluded that GIS helps in the mapping of the vulnerability area due to tsunami and describe the possibility area that could be affected by tsunami wave. The vulnerability map generated from three different DEM showed that most of the coastal areas with low elevation were vulnerable to tsunami. Most of building area and bare land along coastal area was in the high vulnerability of tsunami. The inundation pattern as the result of this study has shown similar to the tsunami inundation areas due to the 2011 Tohoku earthquake.

By adding other parameters, such as coastal type, relative direction of tsunami, coastal bathymetry, and analysis of building vulnerability, better mapping of tsunami disaster assessment can be done.

CHAPTER 5

Remote Sensing and Spatial Multi-criteria Analysis for Tsunami Vulnerability Assessment
(Case study: Kesennuma, Miyagi Prefecture)

5.1 Introduction

Coastal zones are frequently changing due to the dynamic interactions between land and ocean, human activities, and natural hazards such as tsunamis. Historical data of tsunami events indicates that some of the damage from a tsunami is dependent on the topographic elevation of the coastal area. The 2011 Great East Japan Earthquake (hereafter referred to as the Tohoku earthquake), which had a magnitude of 9.0 (M_W), triggered huge tsunami waves. It was reported that maximum run-up heights of greater than 10 m were distributed along 500 km of the coastline, having a direct impact (Mori and Takahashi, 2012). The run-up and inundation caused by this tsunami devastated many cities and villages, including those in the vicinity of Kesennuma in Miyagi Prefecture (Mikami et al., 2012).

It is impossible to reduce the occurrence of natural phenomena such as tsunamis that cause disasters, but the impact of these events can be minimized by performing an initial assessment by mapping vulnerable areas. Together with hazard probability, exposure, and capacity measures, vulnerability is one of the parameters used to determine disaster risk (Pelling, 2003; Bollin et al., 2003).

The development of remote sensing technology and its applications enable the use of satellite imagery for mapping the distribution of an area damaged by a disaster and to assess vulnerable areas. Satellite images have the advantage of being able to deliver simultaneous images of large areas (Karen et al., 2009; Yamazaki et al., 2006; Yamazaki and Matsuoka, 2007). In addition, with the aid of the Geographical Information System (GIS), spatial multi criteria analysis helps prioritize the decision-making process using geo-reference data. Spatial multi criteria analysis is vastly different from conventional Multi Criteria Decision Making (MCDM) techniques, due to the inclusion of an explicit geographic element. In contrast to conventional MCDM analysis, spatial multi criteria analysis uses information on both the criterion values and the geographical positions of alternatives, in addition to

the decision maker's preferences with respect to a set of evaluation parameters (Carver, 1991; Jankowski, 1995).

Some of the previous studies on tsunami vulnerability have analyzed remote sensing data, primarily to assess the physical vulnerability and risk of coastal areas. In addition to such studies, the application of remote sensing in hazard and vulnerability assessment related to ecological and socio-economic vulnerability has been analyzed. Previous studies have also applied moderate-resolution optical satellite images and integrated analysis using GIS to identify inundation areas due to tsunamis (Eckert et al., 2012; Romer et al., 2012; Mahendra et al., 2011; Strunz et al., 2011). GIS mapping of tsunami vulnerability has also applied using the Shuttle Radar Topography Mission (SRTM) to obtain the topographic data of the study area (Sinaga et al., 2011). Another spatial analysis method has applied soil type, urban form and social type system for the potential natural hazard mapping (Hsien and Sheng, 2011) and has determined the tsunami-vulnerable area by comparing building damage map with the topography data, which is discussed with regard to land elevation, land use, and the distance from the coast (Gokon and Koshimura, 2012). Mapping of the 2011 Tohoku earthquake tsunami inundation and run-up by survey also has been published (Mori et al., 2011).

A novel approach from the Coastal Risk Analysis for Tsunamis and Environmental Remediation (CRATER) project was applied for assessing tsunami vulnerability on a regional scale using ASTER imagery and SRTM-version 3. This work analyzed the vulnerability of coastal zones and inland areas using the parameters of using the parameters of infrastructural, geomorphological and ecological features for coastal zones, and parameters of land use, altimetry and distance from the shoreline for inland areas (Dall'Osso et al., 2010). The Papathoma Tsunami Vulnerability Assessment (PTVA) model is a useful tool for providing initial assessments of the vulnerability of buildings (Papathoma et al., 2003; Papathoma and Dominey-Howes, 2003). In addition, a critique of previous studies was undertaken to revise the original PTVA model by taking account of newly published data related to attributes affecting building vulnerability to tsunamis, and to introduce the use of multi-criteria analysis and Analytic Hierarchy Process (AHP) (Dall'Osso et al., 2009).

In this study, vulnerability mapping was conducted and the inundation was assessed from a tsunami using remote sensing and spatial multi criteria analysis. In choosing multi criteria, the study was applied parameters such as elevation, slope, coastal proximity, and land use maps, as well as results of flow accumulation, in order to map the path of rivers or other water channels, with the assuming that rivers or other water channels in the study area could act as flooding strips to carry the tsunami wave into the hinterland.

Rivers, streams, and flood control channels can cause various effects that alter the level of damage. It has been estimated that a tsunami wave entering a flood control channel could reach up to a kilometer or more inland, particularly if enters at high tide. Water and sewer systems can be affected by flooding associated with tsunami events. Floodwaters can encroach along drainage systems, causing localized flooding (Snohomish County Department of Emergency Management, 2010). It is likely that the effects would also penetrate even further inland, as tsunamis can create standing waves in rivers with the point of maximum amplitude being midway between the river mouth and the most upstream point of tsunami penetration. Tsunamis can penetrate up to 2 to 5 km inland on coastal plains, but up to 10 km along a river (Abe, 1986; Gilles, 2012). Most of the damage caused by tsunamis has been attributed to strong currents created in rivers, bays and channels, and not by the actual tsunami run-up, thereby demonstrating that a tsunami does not need to exceed the high water mark to cause damage and disruption to marine infrastructure. Tsunami penetrates significant distances inland along coastal rivers to areas that people may consider safe (Beccari, 2009).

An entirely new set of attributes that are known to affect the tsunami vulnerability was introduced in this study, those related to hydrology analysis and the use of NDVI value in image classification. We also introduced the use of AHP in spatial multi criteria analysis for the tsunami vulnerability mapping and applied this method in the area of Kesennuma in Miyagi Prefecture, Japan.

We aimed to apply a method that is easy, user-friendly, and flexible enough to be replicable. We believe that a suitable set of parameters can be applied to obtain a result that is close enough to that of a real event. This study used a raster geo-database to solve multi-criteria data, and the AHP approach was applied to

determine the order of importance of the parameters. The flow diagram in **Figure 5.1** shows the general steps adopted in this study.

In the section following the description of spatial data analysis, the analysis of satellite image used to create the land use map was described. Following this, the use of spatial multi-criteria analysis and vulnerability mapping in the results and discussions section was related, which is then followed by the conclusions.

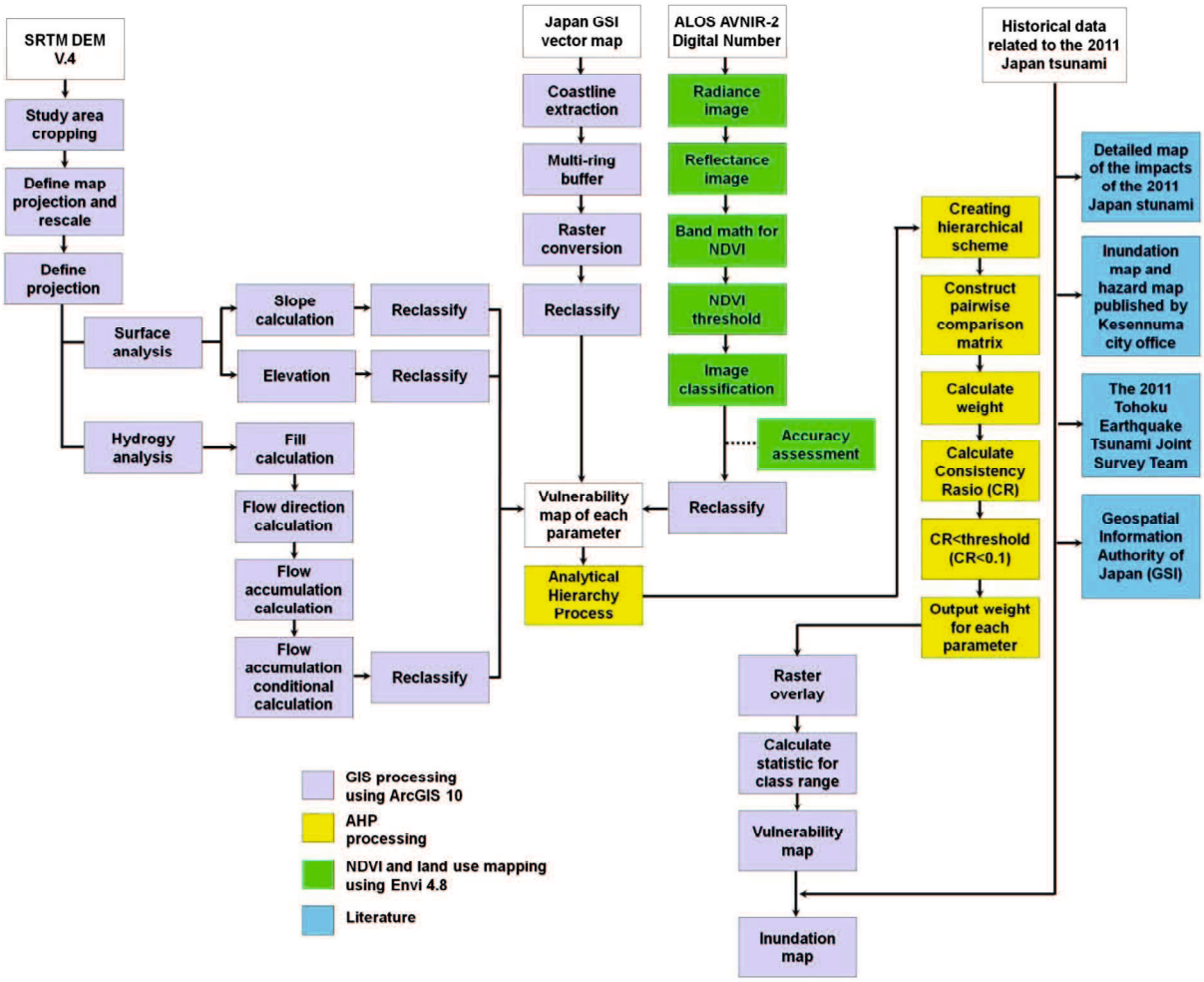

Figure 5.1 The flow diagram describing the methodology of this study

5.2 Spatial Data Analysis

5.2.1 Surface Analysis

(1) Elevation

To create a vulnerability map of the Kesennuma area, the following data were collected: a topographic map, SRTM data, and historical run-up data of the 2011

Tohoku Earthquake. Run-up and inundation information from the 2011 Tohoku Earthquake was recorded in the report entitled "*Detailed Map of the Impacts of the 2011 Japan Tsunami, Vol. 1: Aomori, Iwate, and Miyagi Prefectures"* (Tsuyoshi and Iwamatsu, 2012).

An elevation map was created using SRTM data downloaded from the Global Land Cover Facility (http://glcf.umd.edu/data/srtm/). The analysis began by cropping the area of interest, and continued with the creation of a *Triangulated Irregular Network (*TIN) map. The TIN map represents a surface as a set of contiguous, non-overlapping triangles. It was derived from a DEM based on elevation points on the surface. The TIN model is attractive for use because of its simplicity and economy; it is a significant alternative to the regular raster of the grid model.

(2) Slope

The slope is defined as the rate of maximum change in the *z*-value in each cell of the image. The use of the *z*-value is essential for correct slope calculation when surface *z* units are expressed in units different from those of the ground (*x*, *y* units). The range of values in the output depends on the type of measurement units used. A slope map was created using the third-order finite difference method proposed by Horn (1981). Slope values (*S*) at grid cells, are calculated using:

$$S = \sqrt{\left(\frac{\delta z}{\delta x}\right)^2 + \left(\frac{\delta z}{\delta y}\right)^2} \qquad \text{(Eq. 5.1)}$$

The rate of change (delta) of the surface in horizontal ($\delta z / \delta x$) and vertical ($\delta z / \delta y$) directions away from the center cell determines the slope. At a given point on a surface *z = f(x, y), S* is defined as a function of the gradients at *x* and *y* (i.e., West-East and North-South) directions, where ($\delta z / \delta x$) is the West-East angle and ($\delta z / \delta y$) is the angle for North-South (Smith et al., 2007).

Reclassification of elevation and slope was performed using the criteria as shown in **Table 5.1**. This step was performed in terms of vulnerability to a tsunami. The result of this step is shown in **Figures 5.2(a) and (b)**.

(3) Coastal Proximity

The distance from the coastline (coastal proximity) to the land, calculated using multi-buffering, was used as one of the parameters in vulnerability mapping, which also used an evaluation of historical reports of the maximum run-up in the area concerned. According to Sinaga et al. (2011), the algorithm used for coastal proximity was based on that of Bretschneider and Wybro (1976):

$$\mathrm{Log}X_{\max} = \log 1400 + \tfrac{3}{4}\log\left(\tfrac{Y_0}{10}\right) \qquad \text{(Eq. 5.2)}$$

in which X_{max} is the maximum reach of the tsunami over land, and Y_0 is the height of the tsunami at the coast.

For evaluation of coastal proximity, five classes of distance are used (in meters). The maximum run-up of the tsunami in the study area from the 2011 Tohoku Earthquake was 11.76 m. Based on the algorithm above: a 5 m run-up can reach a distance of 556 m from the coastline; 5–10 m of run-up can reach 556–1400 m; 10–15 m of run-up can reach 1400–2404 m; and 15–20 m of run-up can reach 2404–3528 m. For the vulnerability assessment, the multi buffering distance from the coastline to an area of land was measured in relation to the impact of a tsunami wave. The five classes of distance used (less than 556 m, 556–1400 m, 1400–2404 m, 2404–3528 m, and more than 3528 m) represent: high vulnerability, slightly high vulnerability, medium vulnerability, slightly low vulnerability, and low vulnerability. These classifications are shown in **Figure 5.3**.

Table 5.1 Vulnerability classes based on elevation (Iida, 1963) and Slope (Van Zuidam, 1983)

Criteria		*Vulnerability*
Elevation (meter)	**Slope (percentage)**	
< 5	0–2	High
5–10	2–6	Slightly High
10–15	6–13	Medium
15–20	13–20	Slightly Low
> 20	> 20	Low

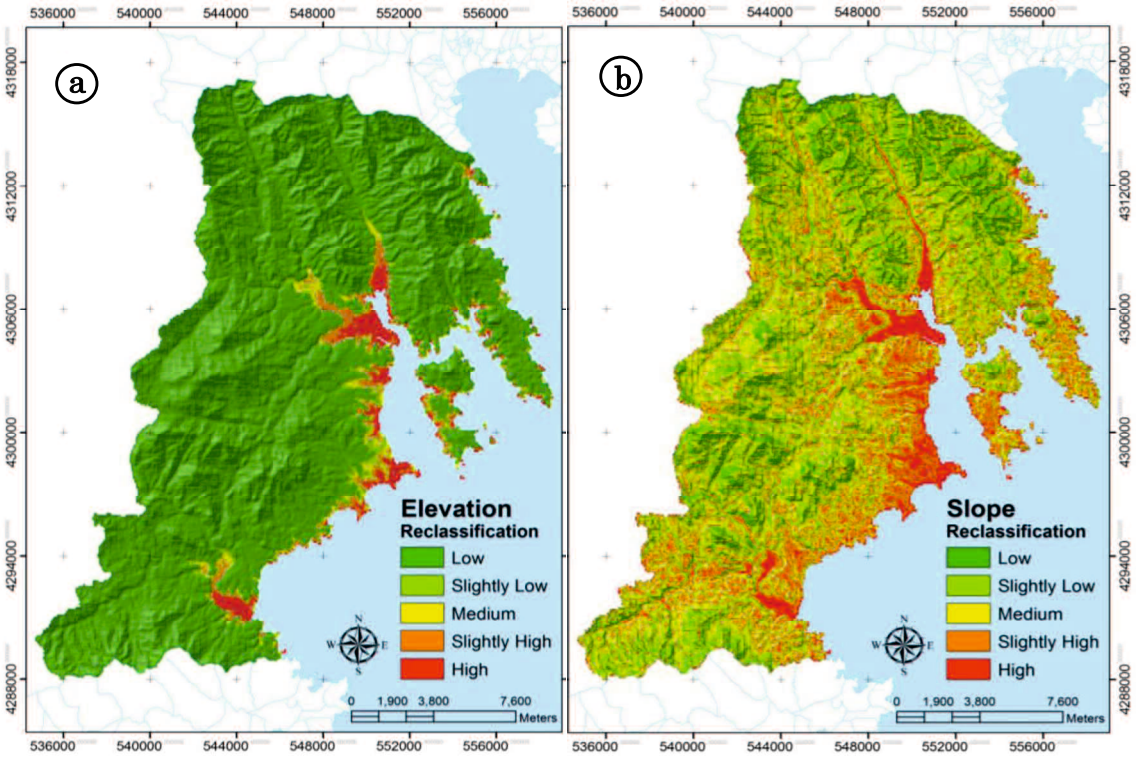

Figure 5.2 Vulnerability map based on (a) elevation and (b) slope.

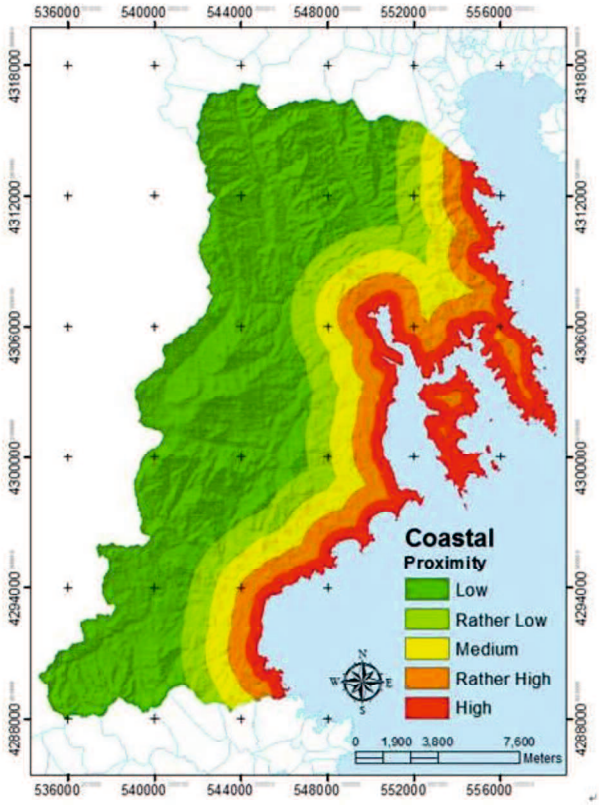

Figure 5.3 Vulnerability map based on coastal proximity

5.2.2 Hydrogy Analysis

The existence of rivers and other water channels is also an important parameter in tsunami risk assessment. To describe the existence of rivers and streams in the study area, river and stream map was generated using the hydrogy analysis tool within GIS based on the SRTM digital elevation model. This is a useful process when a detailed map of waterways is not available.

Hydrogy analysis was applied to the study area to describe the physical surface characteristics, and flow accumulation was calculated to infer areas of drainage. Although we acknowledge that this is commonly used in order to map runoff and watershed, we consider that it has the potential to affect the impact of a tsunami disaster, particularly with regard to the extent of run-up and inundation.

The flow accumulation function calculates the accumulated flow as the accumulated weight of all cells flowing into each down slope cell in the output raster. Cells with a high flow accumulation are considered to be areas of concentrated flow and may be used to identify stream channels. Flow accumulation was calculated using multiple iterations of the DEM, starting at the maximum elevation in the data set and working through elevations one-by-one in a descending order. As shown in **Figure 5.4(a)**, the white line in the study area represents stream channels and indicates the possible accumulation of water. In contrast, cells with a flow accumulation of zero (black-colored area) are areas of high elevation. This map is then reclassified into five classes of vulnerability, as shown in **Figure 5.4(b)**. The five classes of flow accumulation (0–11872.8 cells, 11872–23745.6 cells, 23745.6–35618.4 cells, 35618.4–47491.2 cells, and 47491.2–59364 cells) represent: low vulnerability, slightly low vulnerability, medium vulnerability, slightly high vulnerability, and high vulnerability, respectively. We hypothesized that the main stream channel has a higher vulnerability, and that the vulnerability classes would decrease depending on the class of the stream channel. We then considered the use of this parameter in the spatial multi-criteria analysis described in the next step, even though, to our knowledge, this has not previously been undertaken.

Figure 5.4(b) describes a high vulnerability area, which based on hydrogy analysis is found in an area predicted to be a big river (red line). Water will

accumulate in this area more than in other areas, and we assume that the tsunami wave will flow further inland via this area.

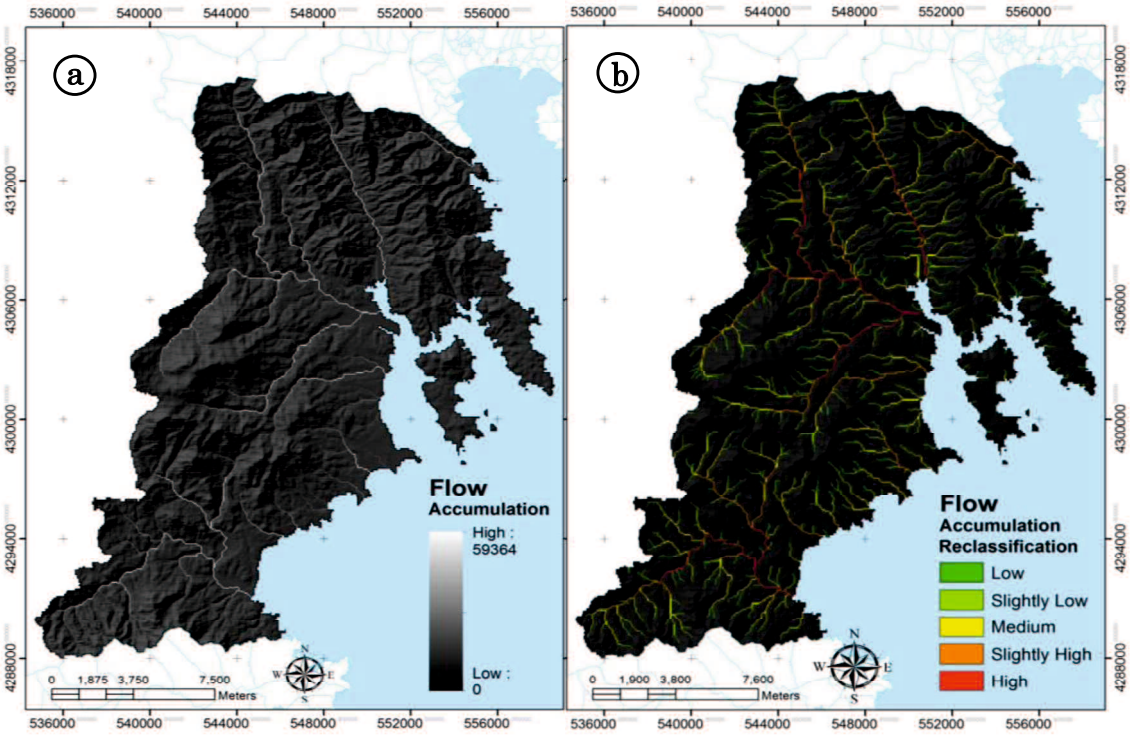

Figure 5.4 (a) Flow accumulation map, and (b) reclassification of flow accumulation.

5.3 Satellite Image Analysis

An ALOS AVNIR-2 satellite image with an acquisition date of March 18, 2009 was used to map the vegetation coverage in the coastal area of Kesennuma. This image was used to classify land use within the study area. The classification process in this study was applied based on a pixel-oriented approach, where each pixel is assigned to a class of land use based on image spectral information. The classification was undertaken using the "decision tree" tool in the ENVI software. This method is used to extract land use classes from MODIS images (Despini et al., 2009). Furthermore, this method is also applied for land use classification in the study of tsunami vulnerability assessment using ASTER imagery (Dall'Osso et al., 2010). The advantage of this method is that data from many different sources and files can be used together to make a single decision tree classifier.

Land use was classified using the Normalized Difference Vegetation Index (NDVI) value. NDVI is a measure of the difference in reflectance between

wavelength ranges. It uses values between -1 and 1, with a value of 0.5 indicating dense vegetation and values less than 0 indicating no vegetation, including water. The principle behind NDVI is that channel 1 is in the red-light region of the electromagnetic spectrum where chlorophyll causes considerable absorption of incoming sunlight, whereas channel 2 is in the near-infrared region of the spectrum where a plant's spongy mesophyll leaf structure creates considerable reflectance (Jackson et al., 1983; Tucker et al., 1991). The NDVI map is described in **Figure 5.5**.

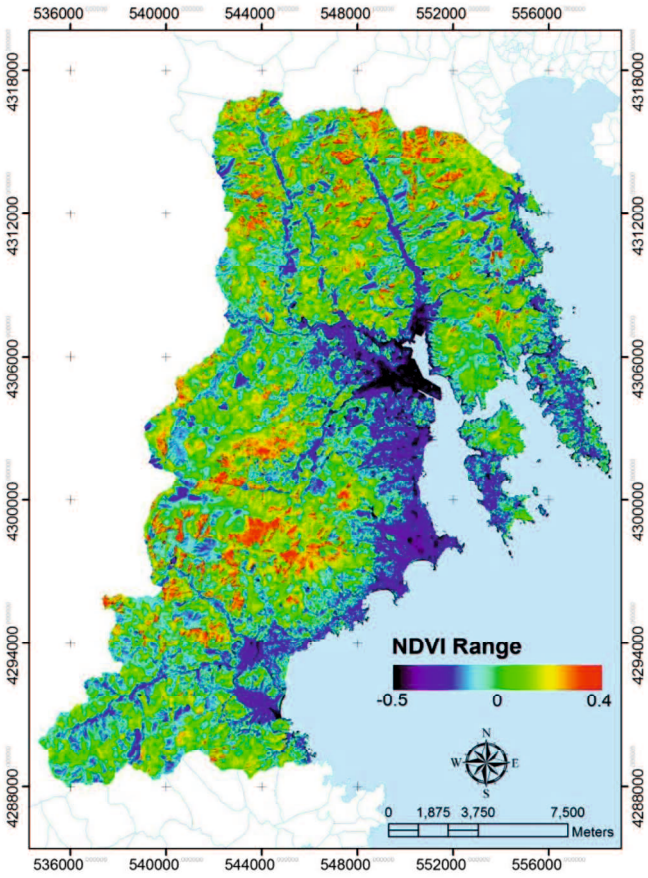

Figure 5.5 NDVI map of the Kesennuma

The “decision tree” procedures was applied for image classification. This tool consists of a number of connected classifiers which jointly perform the pixel classification task through a multistage process made-up of a series of binary decisions (**Figure 5.6**). Each decision is based on a numerical comparison with a selected threshold index, which makes the whole process easily repeatable. The indexes chosen for the classification process are shown in **Table 5.2**. The spectral

bands used in the "decision tree" are band 3 (red; 0.61-0.69μm) and band 4 (NIR; 0.76-0.89μm).

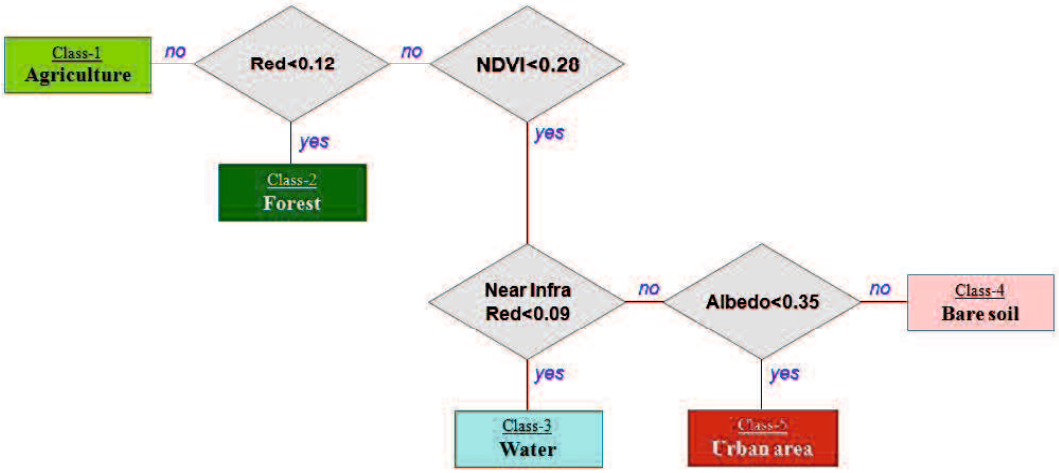

Figure 5.6 Decision tree used in image classification

Table 5.2 Indexes used in the image classification based on NDVI value

Index	Description
NDVI	NDVI < 0.28
RED	RED < 0.12
NIR	NIR < 0.09
Albedo	Albedo < 0.35

Five different land use classes were generated: urban area, agriculture, bare soil, water body (lakes and freshwater), and forest. In this classification, urban area represents a high density urban area. A low density urban area was classified the same as bare soil. The land use map is shown in **Figure 5.7(a)**. After generating the land use map, we reclassified land use based on its vulnerability of tsunami disaster using the criteria shown in **Table 5.3**. We apportioned the five classes of vulnerability to the five classes of land use in the study area ranging from 1 (low vulnerability) to 5 (high vulnerability). The vulnerability map based on land use is shown in **Figure 5.7(b)**.

The vulnerability scores (shown in **Table 5.3**) were assigned based on the actual damage of the object from the tsunami of the 2011 Tohoku Earthquake. The urban area was set as the highest vulnerability score. Based on the damaged area from the tsunami within the study area, most of the area of inundation occurred in the urban area. Water classes in this classification include lakes, pools, and other water bodies with the exception of rivers and streams. Rivers and streams were separated from the class of water body as these were considered to be separate parameters to be analyzed later in spatial multi-criteria, together with land use, elevation, slope and coastal proximity.

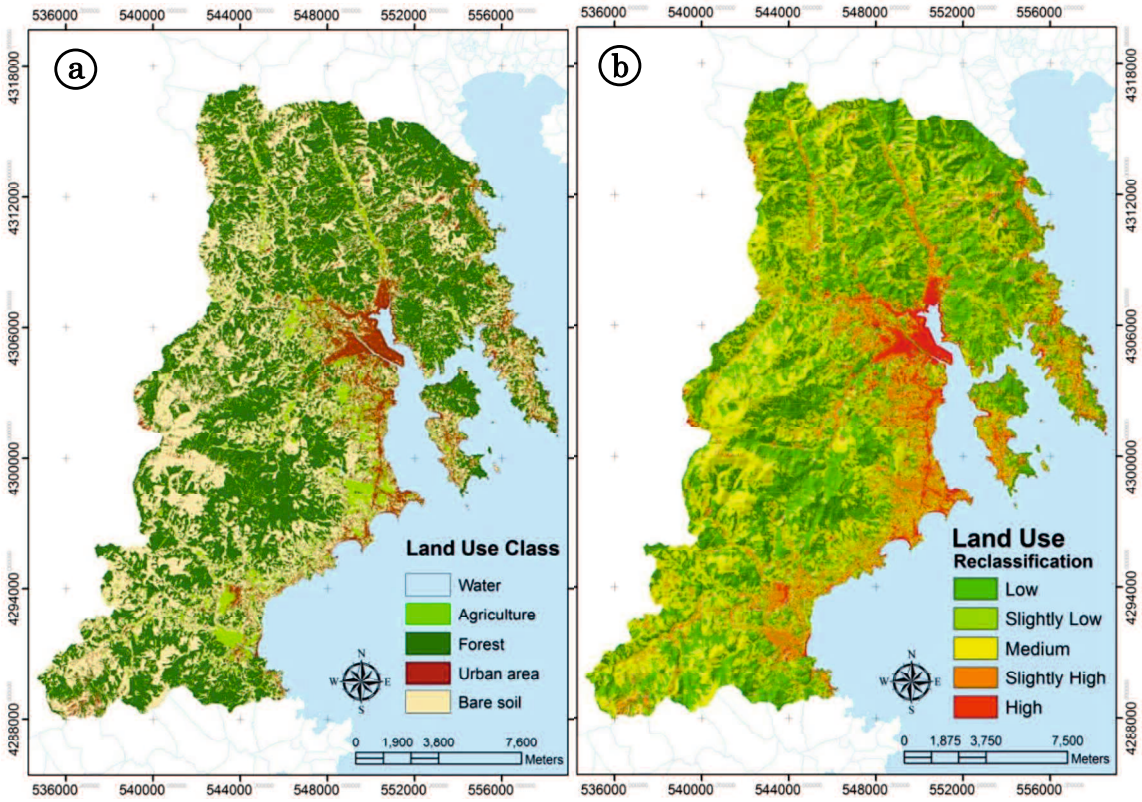

Figure 5.7 (a) Land use map, and (b) vulnerability map based on the land use.

Table 5.3 Vulnerability scores based on the land use class

Land use classes	Vulnerability classes
Urban area	5 (High)
Agriculture	4 (Slightly high)
Bare soil	3 (Medium)
Lakes and freshwater	2 (Slightly low)
Forest	1(Low)

5.4 Results

5.4.1 Spatial Multi Criteria Analysis and Vulnerability Mapping

Cell-based modeling in spatial analysis was used to determine the area of vulnerability. All the parameters used are formatted into a set of grid cells. Each cell has a specific value depending on the value of each parameter. Cells are then classified into five classes of vulnerability, based on their value. All parameters are weighted, and AHP is used to assign a weight to each parameter. AHP is particularly useful for evaluating complex multi-attribute alternatives involving subjective criteria. In multi criteria decision making, AHP helps create a scaled set of preferences and describes the importance of each parameter relative to other parameters through pairwise comparisons (Saaty, 1977, 1980, 1982, 2003).

To determine the comparison scale between each parameter, numbers 1 to 9 are used for the matrix cell values. **Table 5.4** explains the nine-point comparison scale, which depends on the relative importance of each parameter. The relative weights of each parameter are determined through a pairwise comparison as shown in **Table 5.5**. The answers in **Table 5.5** were determined from the results of questionnaires on pairwise comparisons for five parameters completed by experts. We also considered the importance of each parameter using literature reviews and previous studies in the field of tsunami disasters. Hierarchical interactions was calculated based on the respective importance of each parameter by assessing the numerical score. The subjective determination of the investigator in determining the importance of each factor generates these values (Saaty, 2003; Youssef et al., 2010).

Table 5.4 The Saaty nine-point comparison scale (Saaty, 1982).

Intensity of importance	***Definition***	***Explanation***
1	Equal importance	Two parameters contribute equally to the objective
3	Weak importance of one over another	The judgment is to favor one parameter over another, but it is not conclusive
5	Essential or strong importance	The judgment is to strongly favor one parameter over another
7	Demonstrated importance	Conclusive judgment as to the importance of one parameter over another
9	Absolute importance	The judgment in favor of one parameter over another is of the highest possible order of affirmation
2, 4, 6, 8	Intermediate value between	When compromise is needed

	the two adjacent judgments
Reciprocals of above non-zero numbers	If parameter *i* has one of the above non-zero numbers assigned to it when compared with parameter *j,* then *j* has the reciprocal value when compared with *i* (a comparison mandated by choosing the smaller element as the unit to estimate the larger one as a multiple of that unit)

Table 5.5 Pairwise comparison matrix for weight factors.

		Elevation	*Slope*	*Coastal proximity*	*River/water channels*	*Land use*
1	Elevation	1	2	3	5	3
2	Slope	1/2	1	2	3	2 1/2
3	Coastal proximity	1/3	1/3	1	3	3
4	River/water channels	1/5	1/3	1/3	1	1/2
5	Landuse	0.3333	0.4	0.3333	2	1

In the comparison matrix, elevation has the highest score out of the five parameters, and is considered to be more important than slope and even more important than coastal proximity, rivers/streams, and land use. In terms of coastal proximity, we assumed that even if the area is close to coastline, a higher elevation will have low vulnerability. The elevation parameter is considered the only reliable and uniform parameter of the tsunami magnitude to vulnerability functions on buildings that can be observed or measured following all tsunami events (Atillah et al., 2011). The depth of water during a tsunami will differ according to the ground elevation (Papathoma and Dominey-Howes, 2003). In the comparison score we also evaluated that land use had a higher score than river. The land use parameter here consist of five classes, each of which has a different score of vulnerability. As a small number of rivers/streams were identified in the study area compared to the distribution of land use class, we considered the land use score to be more important than the river/stream parameter.

In the original model architecture, the attributes were weighted using expert judgments and developed from a review of the best available published literature dealing with tsunami vulnerability. However, to address concerns of subjective weighting of the attributes, weights have been recalculated through a pair-wise matrix between each of the attributes (Bana e Costa et al., 2004).

To obtain the weight of each parameter, the eigenvector was calculated. The calculation of the eigenvector starts with the multiplication of the pairwise matrix,

and as a result a normalized matrix is created and the sum of each row in the normalized matrix gives the eigenvector. **Table 5.6** explains this normalized matrix and eigenvector calculation. In this process five iterations were performed, which showed that elevation is the most important factor and has the highest weight.

Table 5.6 Normalized matrix and eigenvector calculation

	Normalized matrix					Eigen-vector	Normalized Principal Eigenvector
Elevation	0.4225	0.4724	0.4444	0.3571	0.3000	1.9964	39.76%
Slope	0.2113	0.2362	0.3333	0.2143	0.2500	1.2451	24.80%
Coastal proximity	0.1409	0.1181	0.1429	0.2143	0.3000	0.9162	18.25%
Water channels	0.0845	0.0787	0.0500	0.0714	0.0500	0.3346	6.66%
Landuse	0.1409	0.0945	0.0500	0.1429	0.1000	0.5283	10.52%
	0.4142	0.4208	0.4322	0.4169	0.4277	2.1118	42.23%
	0.2348	0.2315	0.2342	0.2414	0.2482	1.1901	23.80%
1st	0.1660	0.1574	0.1470	0.1659	0.1575	0.7938	15.88%
	0.0725	0.0748	0.0752	0.0700	0.0686	0.3611	7.22%
	0.1128	0.1154	0.1114	0.1058	0.0980	0.5434	10.87%
	0.4204	0.4203	0.4201	0.4204	0.4202	2.1014	42.03%
	0.2359	0.2360	0.2359	0.2358	0.2356	1.1792	23.58%
2nd	0.1598	0.1600	0.1602	0.1599	0.1600	0.7999	16.00%
	0.0729	0.0728	0.0728	0.0729	0.0729	0.3643	7.29%
	0.1110	0.1109	0.1110	0.1111	0.1113	0.5553	11.11%
	0.4203	0.4203	0.4203	0.4203	0.4203	2.1015	42.03%
	0.2359	0.2359	0.2359	0.2359	0.2359	1.1795	23.59%
3rd	0.1600	0.1600	0.1600	0.1600	0.1600	0.8000	16.00%
	0.0728	0.0728	0.0728	0.0728	0.0728	0.3640	7.28%
	0.1110	0.1110	0.1110	0.1110	0.1110	0.5550	11.10%
	0.4203	0.4203	0.4203	0.4203	0.4203	2.1015	42.03%
	0.2359	0.2359	0.2359	0.2359	0.2359	1.1795	23.59%
4th	0.1600	0.1600	0.1600	0.1600	0.1600	0.8000	16.00%
	0.0728	0.0728	0.0728	0.0729	0.0728	0.3641	7.28%
	0.1110	0.1110	0.1110	0.1110	0.1110	0.5550	11.10%
	0.4203	0.4203	0.4203	0.4203	0.4203	2.1015	**42.03%**
	0.2359	0.2359	0.2359	0.2359	0.2359	1.1795	**23.59%**
5th iteration	0.1600	0.1600	0.1600	0.1600	0.1600	0.8000	**16.00%**
	0.0728	0.0728	0.0728	0.0728	0.0728	0.3640	**7.28%**
	0.1110	0.1110	0.1110	0.1110	0.1110	0.5550	**11.10%**
	CI = 0.047						
	CR = 4.22%						

In the normalized matrix and eigenvector calculation, the weight of elevation (42.03%) was higher than any other parameter (slope was 23, 59%, coastal proximity

was 16%, land use was 11.10%, and river/stream was 7.28%). In the study area most of area of damage was in the area of low elevation and the coastal area. This weight is based on the comparison score assigned in the pairwise comparison matrix. For the tsunami vulnerability study, particularly in terms of the physical vulnerability assessment our results showed that the hierarchy of importance of parameters (from high to low) is: elevation, slope, coastal distance, land use, and river/stream.

Because this result was obtained using subjective assessment, a calculation of the consistency level is needed. The consistency ratio (CR) is useful for determining the index of consistency, and it indicates the probability that the matrix judgments were randomly generated (Saaty, 1977). AHP tolerates inconsistency by providing a measure of the inconsistency assessment. This measure is one of the important elements in the hierarchy process based on pairwise comparison. An acceptable consistency ratio is less than or equal to 10%; although in some cases, a consistency ratio greater than 10% can be considered acceptable (Forman and Selly, 2001). In addition, Saaty and Vargas (1991) suggested using a preference matrix correction if the CR value exceeds 0.1. CR is defined as the ratio between the consistency index (CI) and the random consistency index (RI), and it can be expressed by the following equation:

$$\mathrm{CR} = \frac{\mathrm{CI}}{\mathrm{RI}}, \qquad \text{in which } \mathrm{CI} = \frac{(\lambda_{max} - \mathrm{N})}{(\mathrm{N}-1)} \qquad \text{(Eq. 5.3)}$$

Where, λ_{max} represents the principal eigenvalue, and N is the number of the comparison matrix (number of parameter); in this study, N = 5. λ_{max} is calculated from the sum of all parameters and is multiplied by its eigenvector. In this case, λ_{max} is Σ((2.3667*0.4203) + (4.2333*0.2359) + (6.6667*0.16) + (14*0.0728) + (10*0.111)), while the value of RI based on the random consistency index is shown in **Table 5.7**. RI = 1.12 for N = 5.

Table 5.7 Assignment of the random consistency index (Saaty, 1982)

Matrix size (N)	*1*	*2*	*3*	*4*	*5*	*6*	*7*	*8*	*9*	*10*
Random consistency index	0	0	0.58	0.90	1.12	1.24	1.32	1.41	1.45	1.49

As shown in **Table 5.6**, the CR of the matrix is 4.22% for the parameters considered to be influential for tsunami vulnerability mapping in this study. This means that the pairwise matrix is consistent enough to be considered acceptable. In addition, in the GIS application, every raster cell in the image can be located within the decision space according to the level of vulnerability. After the parameter maps have been created, it is fairly simple to multiply each factor map by its weight and then sum the results. Eastman et al. (1995) states that the weighted linear combination is very straightforward in a raster GIS, and factors are combined by applying a weight to each one followed by a summation of the results to create a vulnerability map using the equation of $\Sigma(W_i X_i)$, where W_i is the weight values of the parameter i, and X_i is the potential rating of the factor i.

To create the vulnerability map, the value for every raster cell of the parameter according was calculated to its weight. The rating was divided based on vulnerability class, using numbers 1 to 5; where 1 represents low vulnerability and 5 represents high vulnerability. We then calculated the statistics of the vulnerability map. The statistic calculation of tsunami vulnerability shows that the maximum value of vulnerability is 5 and the minimum value is 1. The vulnerability classes shown in **Table 5.8** were created by subtracting the maximum and minimum values and dividing by the class number. The tsunami vulnerability map is shown in **Figure 5.8**.

Table 5.8 Vulnerability classes.

Vulnerability Class	*from*	*to*	*Area (km²)*	*%*
Low (1)	0.9900	1.7820	193.006	59.02
Slightly low (2)	1.7820	2.5740	87.621	26.80
Medium (3)	2.5740	3.3660	25.386	7.76
Slightly high (4)	3.3660	4.1580	12.811	3.92
High (5)	4.1580	4.9500	8.176	2.50

- Area of inundation (without hydrological analysis) = 17.679 km²
- Area of inundation (including hydrological analysis) = 20.987 km²

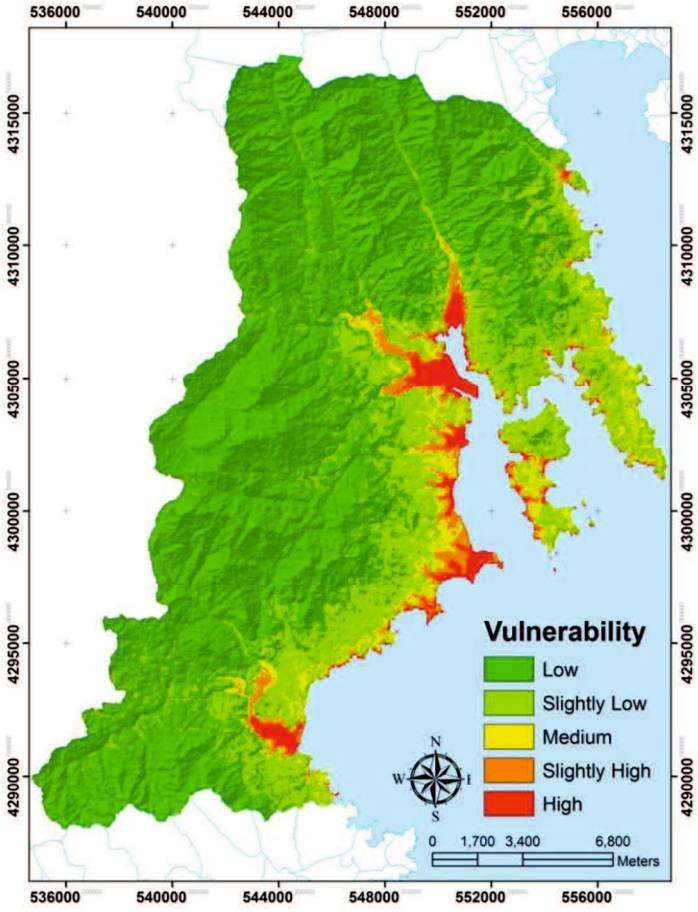

Figure 5.8 Tsunami vulnerability map

5.4.2 Comparison to the 2011 Japan Tsunami

Tsunami vulnerability map here then compared to the existing map of the tsunami inundation area (corresponding to the 2011 Tohoku earthquake), published by the city of Kesennuma. This comparison is described in **Figure 5.9**. As can be seen, most of the inundation occurred in the area of high and slightly high vulnerability, with an area of 8.784 and 8.895 km^2, respectively. Based on these areas, we predict that the total area of possible inundation is 17.679 km^2. This area is based on the analysis of vulnerability mapping without the input parameter of hydrogy analysis. According to the Geospatial Information Authority of Japan (2011), the inundation area in Kesennuma corresponding to the 2011 Tohoku earthquake was 18 km^2. When the result of hydrogy analysis was set as one of the input parameters in muslti-criteria analysis, the predicted inundation area is 20.987 km^2, which described the role of the river in bringing the tsunami water far to the hinterland. The maximum

run-up of the study area reported by Tsuyoshi and Iwamatsu (2012) was 11.79 m, and this was identified as being a high vulnerability area. Moreover, the furthest run-up from the coastline was 2.6 km, and this area was identified as being a location close to the river, an area that identified as having slightly high vulnerability. The survey data from the 2011 Tohoku earthquake is described in **Table 5.9**, and is available from the 2011 Tohoku Earthquake Tsunami Joint Survey Group (taken from 14 – 21 April 2011) (Mori and Takahashi, 2011).

The tsunami vulnerability map was also overlaid with the land use map in order to discover the areas of land use that are vulnerable to tsunami disasters. This result was then compared with the area of inundation from the 2011 Tohoku earthquake (see **Table 5.10** for the comparison). Most of inundation due to the 2011 Tohoku earthquake occurred in urban areas, which was similar to the results of this study, where 7.614 km^2 of urban area was considered to be in the slightly high and high classes of vulnerability, and predicted to be the area of inundation.

In addition, the results of the Joint Survey Group from the area of Kesennuma that was inundated after the 2011 Tohoku earthquake, show that tsunami inundation heights were measured to be more than 10 m at many points outside Kesennuma Bay, and generally less than 10 m inside Kesennuma Bay, (the highest was 11.84 m). Inundation was also observed in a wide low-lying area near the Tsuya River. Sludge, with a thickness of around 10 cm or more in some places, was also carried from the sea and deposited inland, which hindered relief operations. Measured inundation heights around the port were 7.79 m and 11.84 m. At Motoyoshicho-nakajima, which is located about 15 km south of Kesennuma Port, around 300m of coastal erosion was observed. In this area, the low-lying ground extended around the mouth of Tsuya River, and hence a wide area was inundated. Inundation heights near the eroded area were measured to be 9.23 m and 10.88 m (Mikami et al., 2012).

5.5 Discussions

We described a method of generating a vulnerability and inundation map related to a tsunami disaster, using remote sensing data and analyzed via spatial multi-criteria. The vulnerability map shown in **Figure 5.9** (based on multi criteria analysis) shows that 72.06% of the area is considered to have low vulnerability,

18.24% slightly low vulnerability, 4.32% medium, 2.68% slightly high vulnerability, and 2.71% high vulnerability. The high vulnerability areas were mostly found in coastal areas with a sloping coast and a cape area. The low elevation of such areas, the tsunami direction, and the presence of rivers or water channels, are all factors that increase the impact of the tsunami. Inundation areas were predicted to spread in areas identified as having high vulnerability and slightly high vulnerability. A comparison between the inundation map from this study and the existing inundation map from the tsunami that followed the 2011 Tohoku earthquake (published by the Kesennuma city office) shows the similarities between our predicted inundation area and the actual area inundated, confirming that inundation occurred close to rivers (including the Shishiori, Ohkawa and Omose Rivers). The pairwise comparison matrix for weight factors in **Table 5.5** is based on the assumption that the contribution of the input parameter to the overall vulnerability is different. Elevation has the highest weight in the pairwise comparison, and in the study area most of the damage was dependent on the surface elevation. This was confirmed by the fact that some areas that were close to the shoreline but were at a high elevation, suffered less damage. Most of the areas of damage occurred on flat surfaces where the tsunami wave was free to flow without any barrier, as in the area around Kesennuma port.

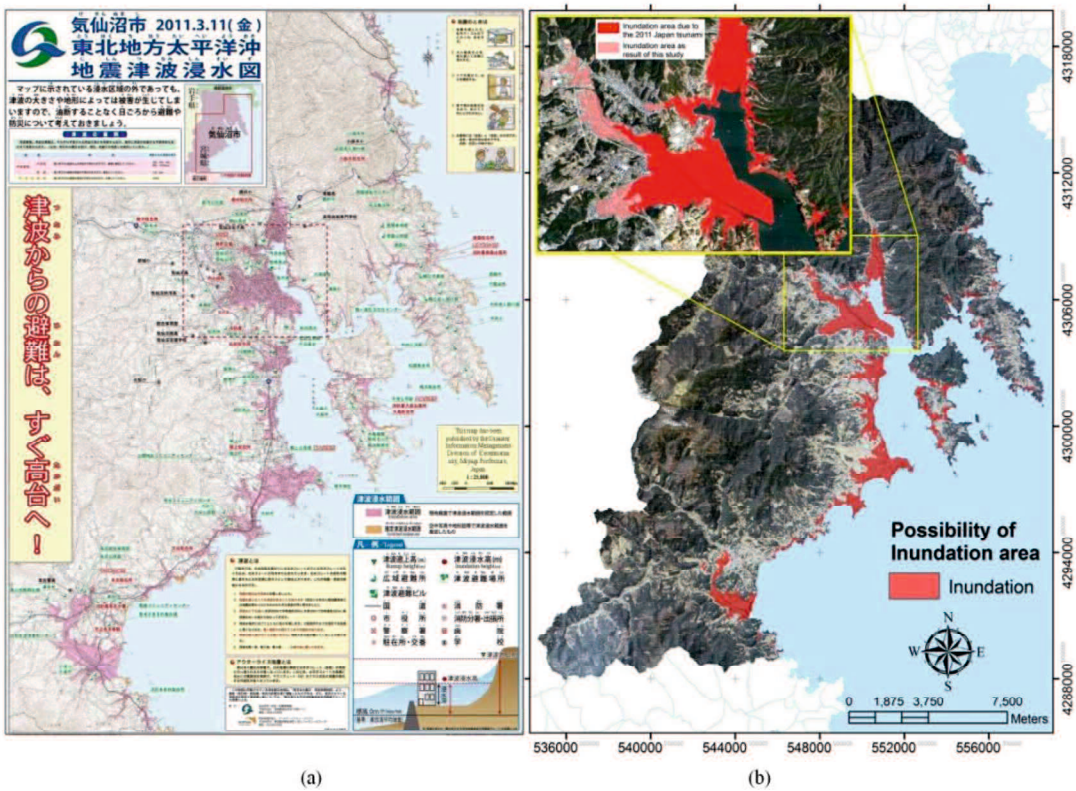

Figure 5.9 Tsunami inundation map. (a) Tsunami inundation area due to the 2011 Tohoku Earthquake adopted from the Disaster Information Management Division of Kesennuma city (2012), and (b) possible inundation area obtained as a result of this study

Table 5.9 Survey point after the 2011 Tohoku earthquake from the 2011 Tohoku Earthquake Tsunami Joint Survey Group (modified)

ID	Coordinate		Run-up Heigh (m)	Distance from coastline (m)	Reflectance of ALOS AVNIR 2	Elevation of SRTM (m)	Vulnerability class
	X	Y					
0	549254	4306573	4.101	667.59	0.015114	10	Slightly high
1	549279	4306617	5.752	606.47	0.013712	10	Medium
2	549359	4306543	5.311	612.75	0.011686	15	Slightly high
3	549612	4306386	4.619	648.75	0.012777	13	Medium
4	549852	4306105	6.528	278.2	0.013868	19	Medium
5	549847	4305966	5.689	325.43	0.016361	17	Medium
6	550016	4304140	7.057	581.04	0.015582	12	Medium
7	550076	4303986	6.001	1541.31	0.016828	15	Medium
8	547920	4306724	3.951	1554.38	0.012621	9	Slightly high
9	548865	4305702	3.314	4091.19	0.014959	8	Slightly high
10	548877	4305631	2.667	2924.76	0.014180	13	Slightly high
11	549002	4305747	3.457	2914.25	0.018387	6	High
12	548941	4305374	3.379	2791.34	0.015738	6	Slightly high
13	548920	4305154	3.354	2678.09	0.015426	8	Slightly high
14	548733	4305020	3.457	2672.02	0.016361	7	Slightly high
15	548555	4304802	3.008	2618.54	0.019010	7	High
16	548916	4304658	2.495	2410.36	0.014180	3	Slightly high
17	550300	4303255	11.363	752.17	0.016205	9	Medium
18	550082	4303245	10.531	946.47	0.016517	32	Slightly high
19	549715	4302407	7.194	1345.11	0.018231	10	Slightly high
20	550301	4302161	8.09	605.63	0.015738	12	Slightly high
21	549915	4301410	7.817	773.31	0.017763	10	Slightly high
22	550453	4299672	5.997	652.198	0.014803	13	Slightly high

Table 5.10 Vulnerability area based on land use class and inundation due to The 2011 Tohoku earthquake

Land use classes	Vulnerability Area (km^2)					Inundation due to The 2011 Tohoku earthquake (km^2)*
	Inundation (km^2)		3	2	1	
	5	4				
Urban area	5.043	2.571	3.419	5.289	3.467	7 (building, arterial traffic)
Agriculture	1.572	2.353	2.946	7.445	3.882	6 (rice field, agriculture land)
Bare soil	1.923	3.404	6.473	30.613	97.722	2 (bare land)
Lakes and freshwater	0.275	0.134	0.123	0.240	0.094	1 (lake, river)
Forest	0.083	0.322	1.198	16.234	131.178	2 (forest)

*GSI (2011b)

5.6 Conclusions

Our approach using remote sensing applications and spatial multi criteria indicates areas that are vulnerable to tsunami and describes areas that could possibly be affected. The vulnerability map shows that most of the coastal areas are vulnerable to tsunamis, and most of the buildings and open land along the coast are also highly vulnerable to a tsunami. The inundation pattern obtained as a result of this study shows similarities in places to the actual inundation area of the 2011 Tohoku earthquake in the area of Kesennuma. The use of hydrogy analysis as one of the parameters in spatial multi criteria analysis helps us to anticipate other areas that could be affected by tsunamis. In short, the use of remote sensing data followed by AHP and spatial multi criteria analysis can be applied, not only for tsunami vulnerability mapping, but also to assess areas that could be affected by inundation due to a tsunami disaster. The result described here can be useful for further analysis in many applications to support regional decision makers in urban planning related to disaster risk management and for disaster mitigation strategies. Furthermore, in the case of no ground truth data, and taking into account the limitations and the availability of the input data required, this method can be applied in other places to obtain an accurate tsunami vulnerability and inundation map. This study only applied the parameters of elevation, slope, coastal proximity, river/stream and land use to map the vulnerability area due to tsunami on a regional scale. By adding other physical parameters, such as coastal type, relative direction of the tsunami, coastal bathymetry, and socio-economic and environmental data, a better mapping of a tsunami disaster assessment can be performed. The use of high spatial resolution satellite images and a high resolution of digital elevation models would also be useful in vulnerability mapping on a more detailed scale.

CHAPTER 6

Integration of Spatial Analysis for Tsunami Inundation and Impact Assessment
(Case Study: Ofunato, Iwate Prefecture)

6.1 Introduction

Natural disaster including tsunami is the natural phenomena which is difficult to prevent. An initial assessment for vulnerability mapping due to disaster is one analysis that can be applied to reduce its impact. Tsunami vulnerability assessment is essential to disaster planning in the term of mitigation. It can provide preliminary information that important for tsunami disaster risk management plans. This includes pre-planning appropriate response activities in order to minimize the impact of disaster and all possibilities that will happen, and preparing and mitigating for the future events (Papathoma and Dominey-Howes, 2003). It can include mapping of evacuation routes and evacuation building, tsunami barriers construction, disaster risk management and regulation and disaster education for public.

In order to prepare those activities for effective implementation, the availability of reliable and accurate information concerning the spatial and temporal characteristics and impact of potentially damaging due to tsunami at different scales of magnitude is needed. Thus, a tsunami vulnerability analysis should be developed based on many parameters as possible to get a realistic description of vulnerability area in both spatial and temporal.

In addition to the hazard probability, exposure, and capacity measures, vulnerability is one of the parameters in determining disaster risk (UNDRO, 1991; Pelling, 2003; Bollin, et al., 2003). It can be defined as the degree to which a person, community or a system is likely to experience harm due to an exposure to an external stress. Vulnerability is described as a set of conditions and processes resulting from physical, social, economic and environmental factors that increase the susceptibility of a community to the impact of hazards (Schmidt-Thome, 2006; Mahendra, 2011).

The application of remote sensing and GIS made the possibilities in order to map the distribution of damage area due to disaster and to assess the vulnerability area. GIS through the spatial multi-criteria analysis helps in making a priority related

to the decision making process using geo-reference data. Spatial multi-criteria analysis need both information on criterion attributes and the geographical references that required by the decision maker's related to the evaluation (Carver, 1991; Jankowski, 1995). Some previous work have applied GIS method for tsunami mapping and overlaid with official land-use map (Sinaga, 2011), and have analyzed tsunami risk using multi-scenario approach (Strunz et al., 2011), and have analyzed the vulnerability using remote sensing data and integrated analysis using GIS to the physical built-up infrastructure, i.e. buildings, and identified the inundation area based on the contour and the highest recorded of tsunami event related to the building vulnerability and human vulnerability (Papathoma and Dominey-Howes, 2003; Papathoma et al., 2003).

The aims of this study are to map the vulnerability area due to tsunami disaster and to assess its impact by mapping the possible inundation area due to tsunami by using GIS. The vulnerability was calculated based on elevation, slope, coastal proximity and vegetation density. In terms of vegetation density, we tried to apply Soil Adjusted Vegetation Index (SAVI) instead of vegetation mapping using Normalized Difference Vegetation Index (NDVI). In addition, the Analytical Hierarchy Process also applied for estimating weights of the parameters.

The study area was Ofunato city in Iwate prefecture, Japan. This area is one of the areas affected by the 2011 Tohoku earthquake tsunami, which is the fourth huge earthquake that caused tsunami since 1900, besides the 1960 Chile Earthquake tsunami, the 1964 Alaska Earthquake tsunami and the 2004 Sumatra Earthquake tsunami (Mori and Takahashi, 2012).

The significant damage to city in previous event was in 1896, 1933 and 1960. The city has an estimated population of 39,136. The total area is 323.28 square kilometers. Population residing in inundated area during the 2011 Tohoku Earthquake tsunami was 19,073. Ofunato faces the Pacific Ocean. Outside its bay, the warm and cold ocean currents meet. In this city, the prefectural government provides hazard mapping to the municipal government who then work with community groups to develop the evacuation maps and identify suitable places for refuge. In other hand there is limited illustration of evacuation routes on the maps (Fraser et al., 2012).

6.2 Materials and Methods

6.2.1 Data

The elevation data used in this study was obtained from the ASTER Global Digital Elevation Model (ASTER GDEM) version 2. The Advanced Space-borne Thermal Emission and Reflection Radiometer (ASTER) GDEM is a joint product developed and made available to the public by the Ministry of Economy, Trade, and Industry (METI) of Japan and the United States National Aeronautics and Space Administration (NASA). It is generated from data collected from a space-borne earth observing optical instrument, namely ASTER.

The ASTER GDEM covers the entire land surface of the Earth at high resolution. Version 2 of the ASTER GDEM is employing an advanced algorithm to improve global digital elevation resolution and elevation accuracy and reprocessing a total of 1.5 million scene data including additional 250,000 scenes acquired after the previous release. The data are posted on a 1 arc-second (approximately 30m at the equator) grid (Tachikawa, 2011).

ALOS AVNIR-2 image was analyzed for vegetation density mapping. Moreover, run up and inundation information of the 2011 Tohoku Earthquake which is recorded in the report book of detailed map of the impacts of the 2011 Japan tsunami in Miyagi Prefecture (Tsuyoshi and Iwamatsu, 2012) was used. The step of analysis starts from data collection, surface analysis of DEM data, vector data processing, vegetation density mapping, AHP process and ends with raster overlay processing through GIS approach (see **Figure 6.1**).

6.2.2 Spatial Analysis

(1) Elevation

Elevation data is one of the principal datasets required for the model to generate vulnerability and inundation of the tsunami. In order to derive a set of parameters that describe the physical vulnerability a digital elevation model was generated by elevation map using ASTER GDEM version 2 data. This data was downloaded from ASTER GDEM website (http://gdem.ersdac.jspacesystems.or.jp/).

Elevation was classified into five classes of vulnerability based on the height of

the surface. It describes that low elevation (in meter) of the surface will have high vulnerability to tsunami wave, as shown in **Table 6.1**. Vulnerability mapping based on elevation data describe that most of coastal area is in the slightly high class of vulnerability (**Figure 6.2(a)**).

(2) Slope

Slope is the rate of maximum change in z-value from each cell of the image. Slope map was created using the third-order finite difference method proposed by Horn (1981). Slope percentages range from 0 to near infinity. A flat surface is 0 percent, and as the surface becomes more vertical, the slope percent becomes increasingly larger. Slope map was created from ASTER GDEM version 2. Slope map was classified into five classes according to the value of tsunami vulnerability as described in **Table 6.1**. Slope classification was applied based on tsunami vulnerability class through reclassify process to generate the vulnerability map (**Figure 6.2(b)**). High vulnerability areas based on slope was identified in the urban area close to the river in the southeast part of Ofunato.

(3) Coastal Proximity

The calculation of the distance from coastline to the land using multi-buffering was done to divide area into five classes of vulnerability. The buffering distance was set based on the possibility range of the tsunami to reach the land. The distance is depend on the historical report of the maximum run up in the area of study, and is expressed by (Sinaga et al., 2011; Bretschneider and Wybro, 1976):

$$\log X_{max} = \log 1400 + \frac{4}{3}\log\left(\frac{Y_o}{10}\right) \qquad \text{(Eq 6.1)}$$

X_{max} is the maximum reach of the tsunami over land, and Y_o is the tsunami height at the coast. Maximum run-up of Ofunato area based on the 2011 Earthquake Tsunami Joint Survey Group was 30.1 m and minimum run up was 5.32 m. By using the algorithm above, five range of coastal proximity that vulnerable to the tsunami were generated as shown in **Table 6.1**. Coastal proximity in vector map of Ofunato was created through GIS processing to generate vulnerability map based on coastal proximity (**Figure 6.2(c)**).

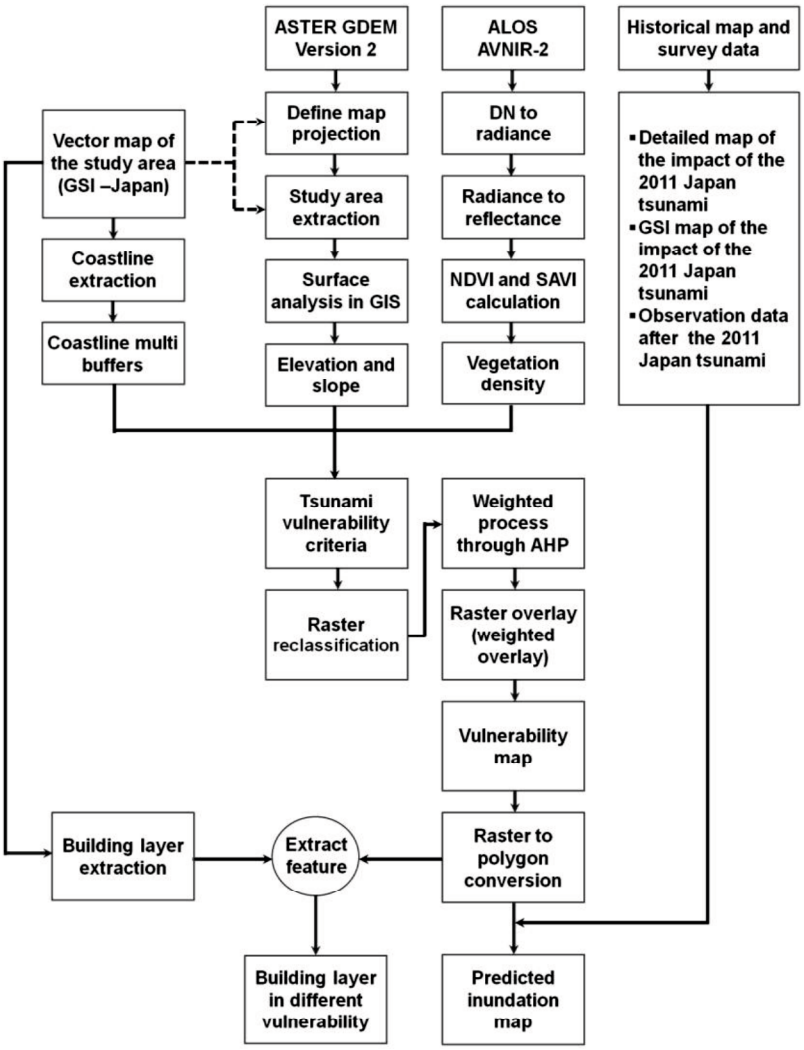

Figure 6.1. General framework of the study

Table 6.1. Vulnerability class based on Elevation (Iida, 1963), slope (Van Zuidam, 1983), and Coastal proximity

Elevation (meter)	Slope (percentage)	Coastal proximity (meter)	Vulnerability class
< 5	0 – 2	0–603.50	High
5 – 10	2 – 6	603.50–1451.76	Slightly high
10 – 15	6 – 13	1451.76–2453.60	Medium
15 – 20	13 – 20	2453.60–3572.06	Slightly low
>20	>20	>3572.06	Low

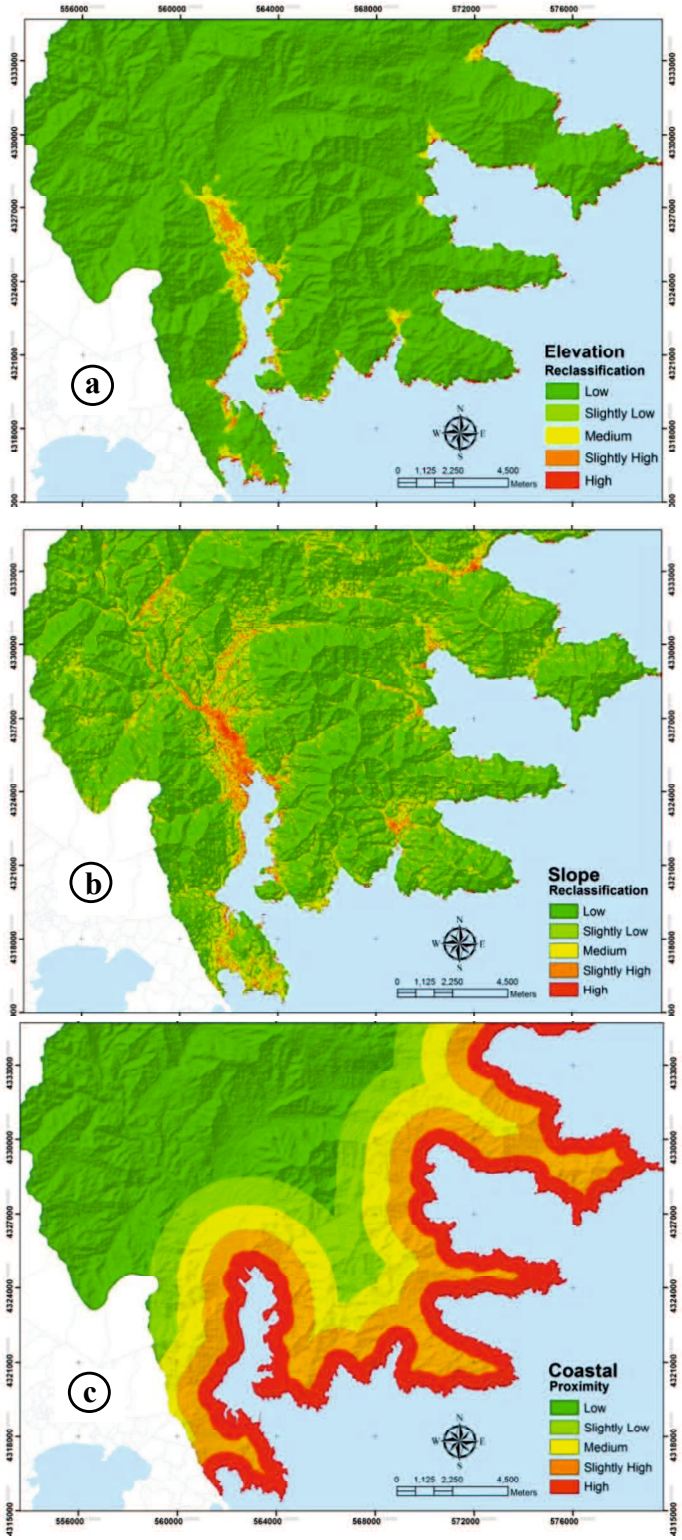

Figure 6.2. Tsunami vulnerability map based on the parameter of (a) Elevation; (b) Slope; and (c) Coastal proximity

6.2.3 ALOS AVNIR-2 Image Processing

In addition to create a vegetation density map, SAVI calculation was applied. The digital numbers of ALOS AVNIR-2 were converted to reflectance values before generating the synthetic NDVI and SAVI images (Huete, 1988; Araujo et al., 2000). The steps to create vegetation density map are as follows.

(1) Reflectance Calculation

Radiance convertion from digital number values is needed before generating reflectance. Calculation of radiance is the fundamental step in relating image data from multiple sensors and platforms into a common radiometric scale (Chander and Markham, 2003). The general equation for DN to radiance conversion as in **Equation 6.2** (Bouvet, 2007).

$$L_\lambda = G_{rescale} \times QCAL + B_{rescale} \quad \text{(Eq. 6.2)}$$

Where, L_λ is spectral radiance at the sensor's aperture (W/m2/sr/μm), $G_{rescale}$ is rescaled gain, QCAL is Digital Number (DN), and $B_{rescale}$ is rescaled bias. Moreover, **Equation 6.3** was used to convert radiance to reflectance (NASA, 2011):

$$\rho_\lambda = \pi \times L_\lambda \times {d^2}/{ESUN_\lambda} \times \cos\theta_s \quad \text{(Eq. 6.3)}$$

Where, ρ_λ is unitless planetary reflectance, L_λ is spectral radiance at the sensor's aperture, d^2 is earth-sun distance in astronomical units from nautical handbook, $ESUN_\lambda$ is the mean solar exoatmospheric irradiances, and θ_s is solar zenith angle in degrees.

(2) NDVI Calculation

NDVI is a measure of the difference in reflectance between these wavelength ranges that takes values between -1 and 1, with values 0.5 indicating dense vegetation and values < 0 indicating no vegetation including water. NDVI was estimated using **Equation 6.4** (Hansen et al., 2000).

$$NDVI = \frac{(NIR - VIS)}{(NIR + VIS)} \quad \text{(Eq. 6.4)}$$

NIR is Near Infra-Red band, and VIS is visible band of red band. ALOS AVNIR-2 band 3 is red and band 4 is NIR.

(3) SAVI Calculation

SAVI is one of the algorithms developed to generate vegetation index by eliminating soil factor (Gong et al., 2003). Although SAVI model is not significant in the intra-class analysis, in the similar spectral space, this model presents a reasonable performance in the characterization of forested and non-forested areas (Araujo et al., 2000). Atmospheric influences lower the NDVI of vegetated areas whereas dark or wet soil backgrounds increase the NDVI for given vegetation canopy (Huete, et al., 1992). SAVI was developed to minimize soil brightness, including shadow, influences found in the NDVI by accounting for first-order soil-vegetation spectral interactions as in **Equation 6.5** (Huete, 1988).

$$SAVI = \frac{(NIR - R)}{(NIR + R + L)} \times (1 + L) \quad \text{(Eq. 6.5)}$$

Where, NIR is Near Infra-Red band, R is red band, and L is soil calibration factor, in which L equal to 0.5 (Jensen, 2000). A correction factor (L) was used to minimize the secondary backscattering effect of canopy transmitted-soil background reflected radiation. L value of 1 was optimal in semiarid environments. SAVI map is shown in **Figure 6.3(a)**.

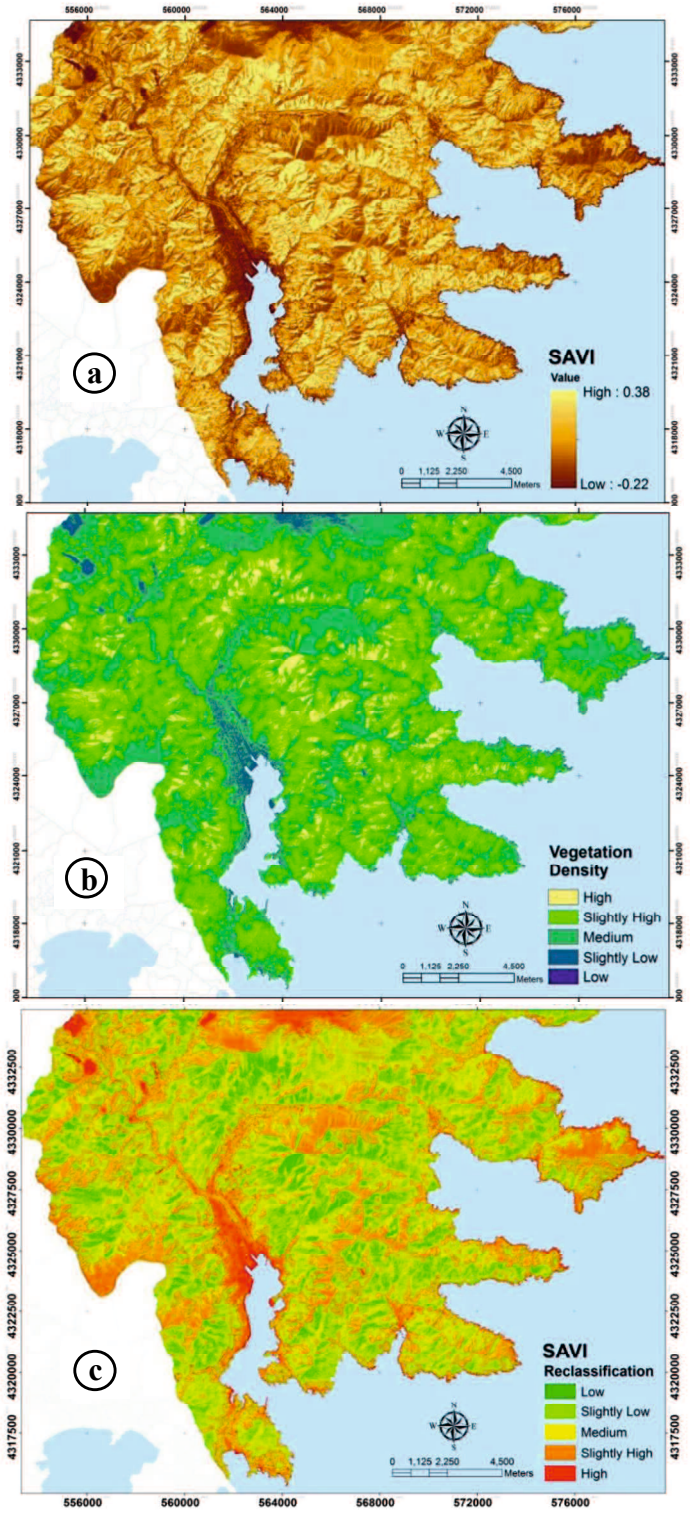

Figure 6.3. (a) SAVI map; (b) Vegetation density map; and (c) SAVI reclassification which is describe the vulnerability map based on vegetation density

SAVI map was used to map the vegetation coverage. The image was used to identify the density of vegetation and to map vulnerability area of tsunami. We assumed that this area is more vulnerable to tsunami attack than another area. Vegetation density of SAVI describes that the minimum value was -0.22, while the maximum was 0.38. SAVI value was reclassified to generate the vegetation density map in five classes (low, slightly low, medium, slightly high and high density) as shown in **Figure 6.3(b)**, which then will be classified based on tsunami vulnerability. We assumed that low density of vegetation has a high vulnerability to tsunami. The result of this classification is shown in **Figure 6.3(c)**. The lowest value of vegetation index found in the coastal area of Ofunato are zones where indicated as building, bare soil, rocky land and water body.

6.3 Results

6.3.1 AHP Processing

All parameters were in grid cells which are then classified into five classes of vulnerability. For the vulnerability classes an integer numbers of 1, 2, 3, 4, and 5 that represent low, slightly low, medium, slightly high and high vulnerability were used. The entire parameter of tsunami vulnerability was then overlaid by using weighting and scoring system. Scoring is intended to assess the limiting factor on each parameter, while weighting is based on the dominant influence of these parameters in determining the class of tsunami vulnerability.

AHP was applied in assigning weights to each of the parameters. By applying pair-wise comparisons, AHP helps in creating a scaled set of preferences and describing the importance of each parameter relative to other parameter (Saaty, 1977; Saaty, 1980; Saaty, 2003). AHP allows the investigators in assessing the vulnerability related to the natural hazard. A number of 1 until 9 as shown in **Table 6.2** is used in comparison scale to create pair-wise comparison matrix. This number is depends on the relative importance of each parameter. The relative weights of each parameter will be produced through pair-wise comparison as shown in **Figure 6.4**.

The calculation of consistency level is needed prior to the spatial analysis. Consistency Ratio (CR) is a procedure for determining the index of consistency. It indicates the probability that the matrix judgments were randomly generated (Saaty,

1977). AHP tolerates inconsistency through the calculation of consistency ratio. Acceptable consistency ratio is less than or equal to 10 percent (Forman and Selly, 2001). CR is the ratio between the consistency index (CI) and random consistency index (RI) and can be expressed using **Equation 6.6**.

$$CR = \frac{CI}{RI}, \quad and\ CI = \frac{(\lambda_{\max} - N)}{(N-1)} \qquad \text{(Eq. 6.6)}$$

Where, λ_{max} represents the largest eigenvalue, and N the size of comparison matrix. In this study N = 4. λ_{max} is calculated from the sum of all parameter and multiply by its eigenvector. RI is based on the random consistency index (RI = 0.09 for four parameters).

Table 6.2. Nine-Point Comparison Scale by Saaty (Saaty, 1996)

Intensity of importance	*Definition*
1	Equal importance
3	Weak importance of one over another
5	Essential or strong importance
7	Demonstrated importance
9	Absolute importance
2,4,6,8	Intermediate value between the two adjacent judgments

Pair - wise comparison matrix

	Elevation	Slope	Coastline distance	Vegetation density
Elevation	1	2	3	3
Slope	1/2	1	2	21/2
Coastal proximity	1/3	1/2	1	3
Vegetation density	1/3	0.4	1/3	1

Normalized matrix

Elevation	0.4615	0.5129	0.4737	0.3158	
Slope	0.2308	0.2564	0.3148	0.2632	
Coastal proximity	0.1539	0.1282	0.1579	0.3158	
Vegetation density	0.1539	0.1026	0.0526	0.1053	
5th iteration	0.4595	0.4595	0.4595	0.4595	45.94%
	0.2554	0.2554	0.2554	0.2554	25.53%
	0.1671	0.1671	0.1671	0.1671	16.71%
	0.1181	0.1181	0.1181	0.1181	11.81%

Figure 6.4. Pair-wise Comparison and Normalized Matrix

Normalized matrix shown in **Figure 6.4** was calculated from the pair-wise

comparison in five iterations, and it shows that CI was 0.057, while CR was 6.4%. The pair-wise comparison describes that elevation is the most important factors followed by slope, coastal proximity, and vegetation density.

6.3.2 Spatial Analysis for Vulnerability Mapping

After creating the parameter maps, weighted overlay was applied through spatial analyst in GIS. The weighted overlay tool was applied to solve multi criteria problems. It is a method for applying a common scale of values to diverse input parameters which have different importance for creating an integrated analysis. The general step of this process is shown in **Figure 6.5(a)**.

A number of 1 (low vulnerability) to 5 (high vulnerability) was used to represent vulnerability classes. Then the statistics of vulnerability map was calculated. The vulnerability classes shown in **Table 6.3** was created using the subtraction of maximum and minimum value and divided by number of class. Subsequently tsunami vulnerability in five classes is mapped in **Figure 6.5(b)**.

Table 6.3. Vulnerability classes

Vulnerability Class	Area (square kilometer)	Percentage (%)
Low (1)	234.79	73.63
Slightly low (2)	71.10	22.30
Medium (3)	5.59	1.75
Slightly high (4)	6.29	1.97
High (5)	1.10	0.34

6.3.3 Tsunami Inundation and Impact Assessment

The result of the study was compared to the survey data from Joint Survey Group of the 2011 Tohoku Earthquake, the existing map of tsunami inundation area due to the 2011 Tohoku Earthquake published by Geographical Survey Institute (GSI) Japan (**Figure 6.6**), and detailed map of the impacts of the 2011 Japan tsunami, vol. 1: Aomori, Iwate and Miyagi Prefecture (Tsuyoshi and Iwamatsu, 2012).

The comparison describes that most of inundation area was occurred in the area of high and slightly high vulnerability with an area of 1.10 km^2 and 6.29 km^2. Based on these areas we estimate that total area of the possibility of inundation is 7.39 km^2

(**Figure 6.7(a)**), while the inundation area due to due to 2011 Tohoku Earthquake based on GSI report is 8 km^2. Maximum run-up of Ofunato area based on The 2011 Earthquake Tsunami Joint Survey Group was 30.1 m and found in the area of Shirahama Sanrikucho Ryori. Minimum run up was 5.32 m at the area of Sakaricho. This area is identified as the high vulnerability area. It was estimated that inundation area will cover 8.13 km^2 of building area along coastal area of Ofunato (**Table 6.4 and Figure 6.7(b)**).

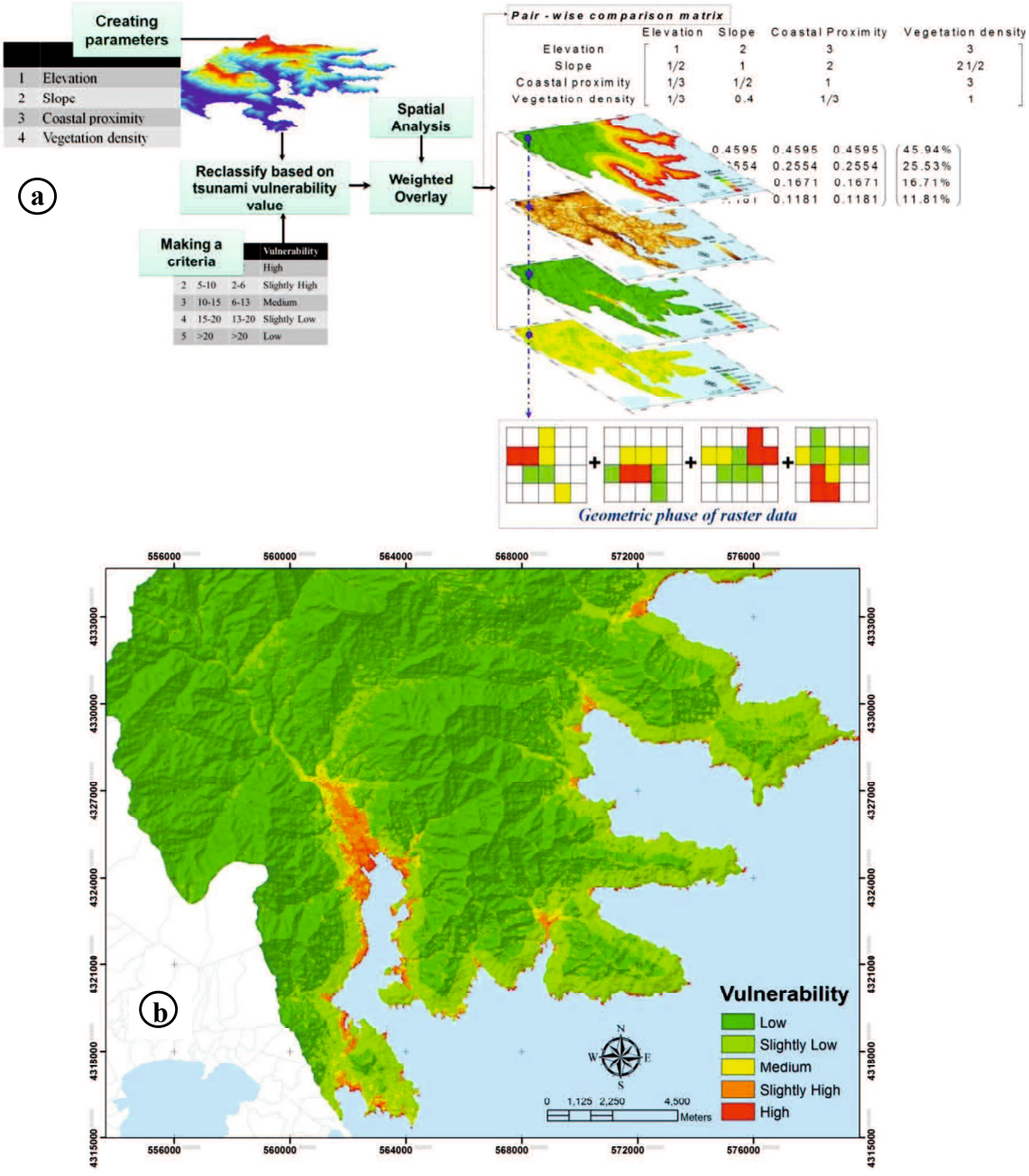

Figure 6.5. (a) Spatial analysis step; (b) Tsunami vulnerability map of Ofunato area

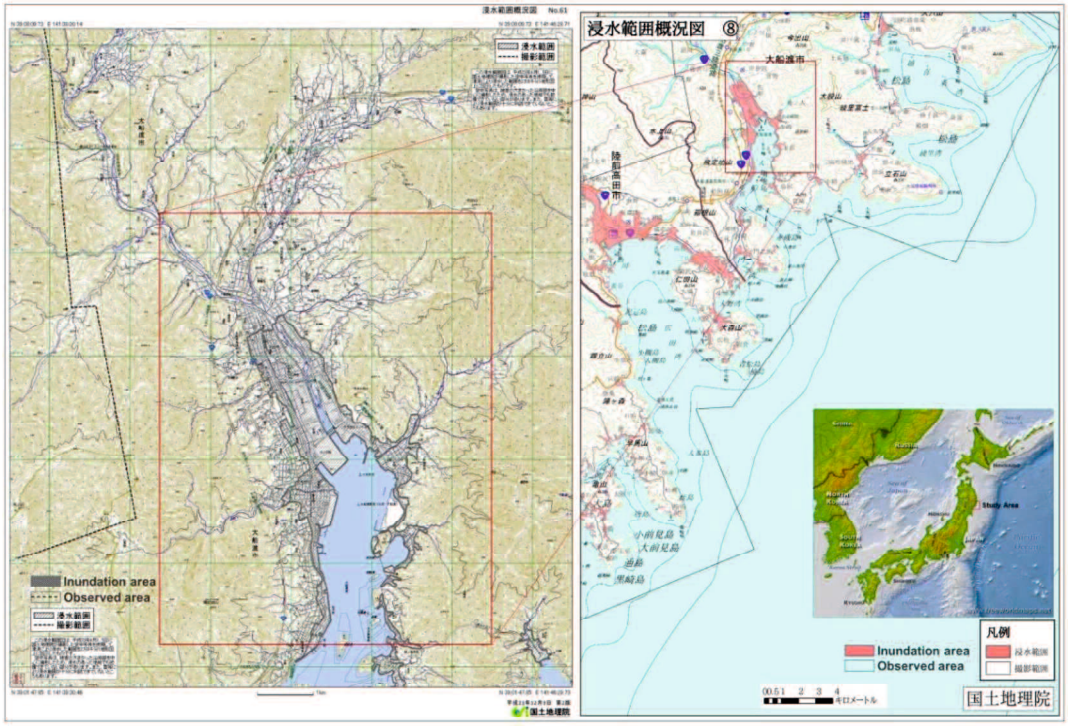

Figure 6.6. Inundation Map of Ofunato during the 2011 Japan Tsunami, Published by GSI, 2011 (modified)

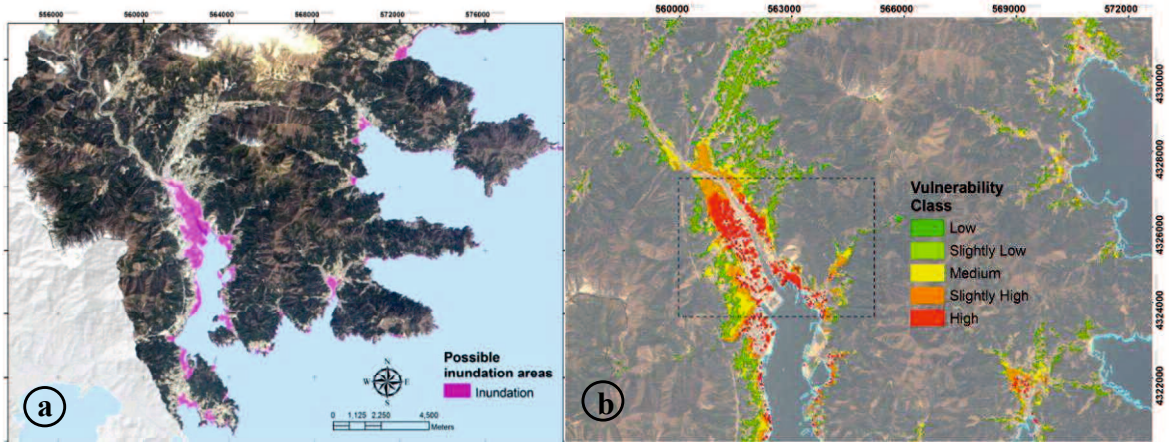

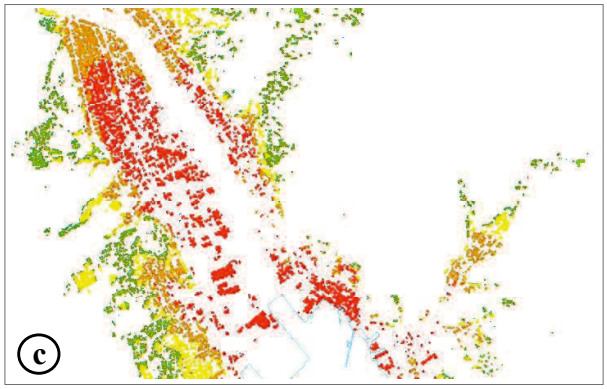

Figure 6.7. (a) Map of possible inundation area in Ofunato; (b)Tsunami vulnerability class of building area in Ofunato; (c) inset map of building area vulnerability

Table 6.4 Vulverability class of building area

Vulnerability Class	5	4	3	2	1
	Inundation Area				
Building area (km^2)	3.35	4.78	6.25	1.71	6.01

Inundation area as shown in **Figure 6.7(a)** describe that the farthest area of inundation could reach until 3.5 km from coastline. In this area, the elevation was 12 m, while reflectance value was 0.13, and SAVI was 0.05. Elevation map created from ASTER GDEM version 2 describes that the highest elevation in the inundation area is 20.5 m.

This method was applied to the larger area that covers Kesennuma, Rikuzentakata, and Ofunato where tsunami vulnerability map is overlaid to the building area. This map is shown in **Figure 6.8 (b)**.

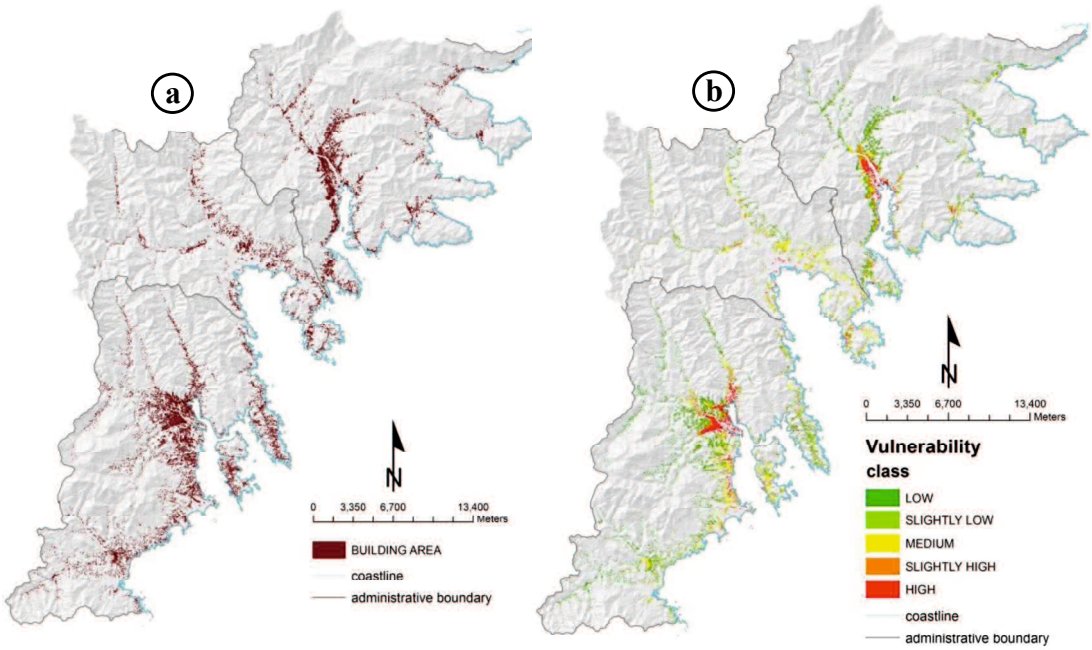

Figure 6.8. (a) Map of building distribution; (b)Tsunami vulnerability building area in the area of Kesennuma, Rikuzentakata, and Ofunato

6.4 Discussion

Vulnerability is related to the capacity to reduce the impact of disaster and mitigation plan. It describes the potential area to be damaged by natural disasters. Class of vulnerability could be based on a physical parameter, such as elevation, slope, coastal proximity, land cover and coastal shape. Moreover, inundation can be

defined as the result of a tsunami traveling a long distance inland and is a horizontal measurement of the path of the tsunami. The analysis of satellite image, elevation data, and survey data followed by multi-criteria analysis through AHP and raster overlay in GIS processing can be used as the basic information for vulnerability mapping, inundation mapping, and impact assessment due to tsunami disaster.

The use of AHP method helps in the analysis of spatial multi-criteria where all of the parameters used in this study were calculated based on its weight factor to create vulnerability map. This study is a first attempt to assess tsunami vulnerability by using the parameter of SAVI besides elevation, slope and coastal proximity, and apply AHP methods combining with raster overlay through GIS processing in Ofunato area. According to the result of this study, a simple method for inundation prediction can be a valuable step for carrying out a preliminary tsunami vulnerability mapping and impact assessment when the high resolution of DEM data and detailed topographic data is not available.

Elevation is the parameter that has the highest weight and 2.31% of the area that identified as slightly high and high class of tsunami vulnerability found in the coastal area which has a lower elevation. Most of the area is highly developed areas with low vegetation density. Tsunami vulnerability map and inundation map generated in this study can be used for determining a priority for risk prevention, mitigation, and land-use planning to reduce the tsunami risk. Particularly, in the slightly high and high vulnerability area that can be identified as possible inundation area describe that 11.85% of building area has potential consequences of a tsunami impact.

In this research, five classes of vulnerability were used. Vulnerability map describes that 73.63% of the area is low vulnerability, 22.30% is slightly low vulnerability, 1.75% is medium, 1.97% is slightly high vulnerability, and 0.34% is high vulnerability. The high vulnerability areas were mostly found in the coastal area with the sloping coast type. Inundation areas were predicted in areas that identified as high vulnerability and slightly high vulnerability area. In addition, we assumed that vegetation may play an important role as tsunami barriers to reduce the impact of the tsunami destruction. Based on the vegetation density that created from SAVI value in the study area, we found that 52.09% of the inundation area was in slightly

low class of vegetation density and 34.05% of the inundation area was in medium class of vegetation density.

6.5 Conclusion

GIS application followed by satellite image processing and AHP approach is useful for tsunami vulnerability mapping and impact assessment. It can be used for the evacuation and reconstruction plan due to tsunami disaster. GIS indicate the vulnerability area due to tsunami and describe the possibility area that could be affected by tsunami wave. In this study four parameters was applied in order to create a tsunami vulnerability map and to predict the possibility of inundation area in the area of Ofunato. The vulnerability map showed that most of the coastal areas are vulnerable to tsunami. Most of buildings area and bare land along coastal area was in the high vulnerability of tsunami. The inundation pattern as the result of this study shown similar compared to inundation area of the 2011 Tohoku Earthquake in the area of Ofunato. ASTER GDEM version 2 is useful for tsunami vulnerability mapping for the area where the high resolution of DEM data is not available. Building and residence area in potentially affected areas should be provided with basic information on tsunami risk because awareness and preparedness are the most important factors to reduce potential losses due to a tsunami impact.

For the application in mitigation plan, we recommend to the user to be aware of the assumptions made, as well as the limitations within this study. Better mapping of tsunami vulnerability can be done by adding other appropriate parameters. The parameters of coastal type, relative direction of tsunami, and coastal bathymetry can be used. Moreover, the use of other DEM data, vulnerability mapping in other location, overlaying the vulnerability map with the current land use map and run up modeling will be future works.

CHAPTER 7

Remote Sensing, GIS, and AHP for Assessing Physical Vulnerability to Tsunami Hazard
(Case Study: Rikuzentakata, Iwate Prefecture)

7.1 Introduction

Natural hazards are natural phenomena whose occurrence is almost impossible to reduce. We only can minimize the impact of these events by performing an initial assessment in order to map the vulnerable areas. Vulnerability is one of the parameters used to determine disaster risk, together with hazard probability, exposure, and capacity measures (Pelling, 2003; Bollin et al., 2003).

The development of remote sensing technology enables the use of satellite imagery for mapping the damage area due to a disaster and for assessing the vulnerable areas. Satellite images have the advantage of observing large areas in both high spatial and high temporal resolution (Joyce et al., 2009; Yamazaki, 2003; Yamazaki and Matsuoka, 2007). Moreover, a Geographical Information System (GIS) is useful for analyzing spatial data due to disaster mitigation planning.

Spatial data analysis via spatial multi-criteria analysis helps prioritize the decision-making process using geo-reference data to manage different spatial information and combine them for better decision making. Spatial multi-criteria analysis uses information on both the criterion values and the geographical positions of alternatives in addition to the decision maker's preferences with respect to a set of evaluation parameters (Carver, 1991; Jankowski, 1995).

Remote sensing data of moderate-resolution optical satellite images has been used to identify the inundation area and to assess the vulnerability and risk in coastal area. GIS is also applied to evaluate the strategy for coastal vegetation belts against tsunami risk and to analyze tsunami risk using a multi-scenario approach (Eckert et al., 2012; Mahendra et al., 2011; Sinaga et al., 2011; Usman and Murakami, 2011).

A previous study analyzed vulnerability using remote sensing data and integrated analysis using the GIS with regard to physical infrastructure (i.e., buildings) and identified the inundation area based on contours and the highest recorded tsunami event related to building vulnerability and human vulnerability

(Yamazaki and Matsuoka, 2007; Strunz et al., 2011; Papathoma and Dominey-Howes, 2003; Yamazaki et al., 2006). Another study developed the Papathoma Tsunami Vulnerability Assessment (PTVA) to provide first-order assessments of building vulnerability to tsunami (Papathoma and Dominey-Howes, 2003; Papathoma et al., 2003). The use of multi-criteria analysis and the analytic hierarchy process (AHP) was introduced in vulnerability mapping and assessing tsunami vulnerability, which have been done at the regional scale using ASTER imagery and digital elevation models of 3 arc-seconds SRTM-version 3 data (Dall'Osso et al., 2009; Dall'Osso et al., 2010).

In this study, we tried to apply input parameters of elevation, slope, coastal proximity, and vegetation density and analyze them via AHP and GIS in terms of spatial multi criteria to map the tsunami vulnerability area. This study was applied in the area of Rikuzentakata in Iwate Prefecture, Japan. The general steps adopted in this study are shown in **Figure 7.1**.

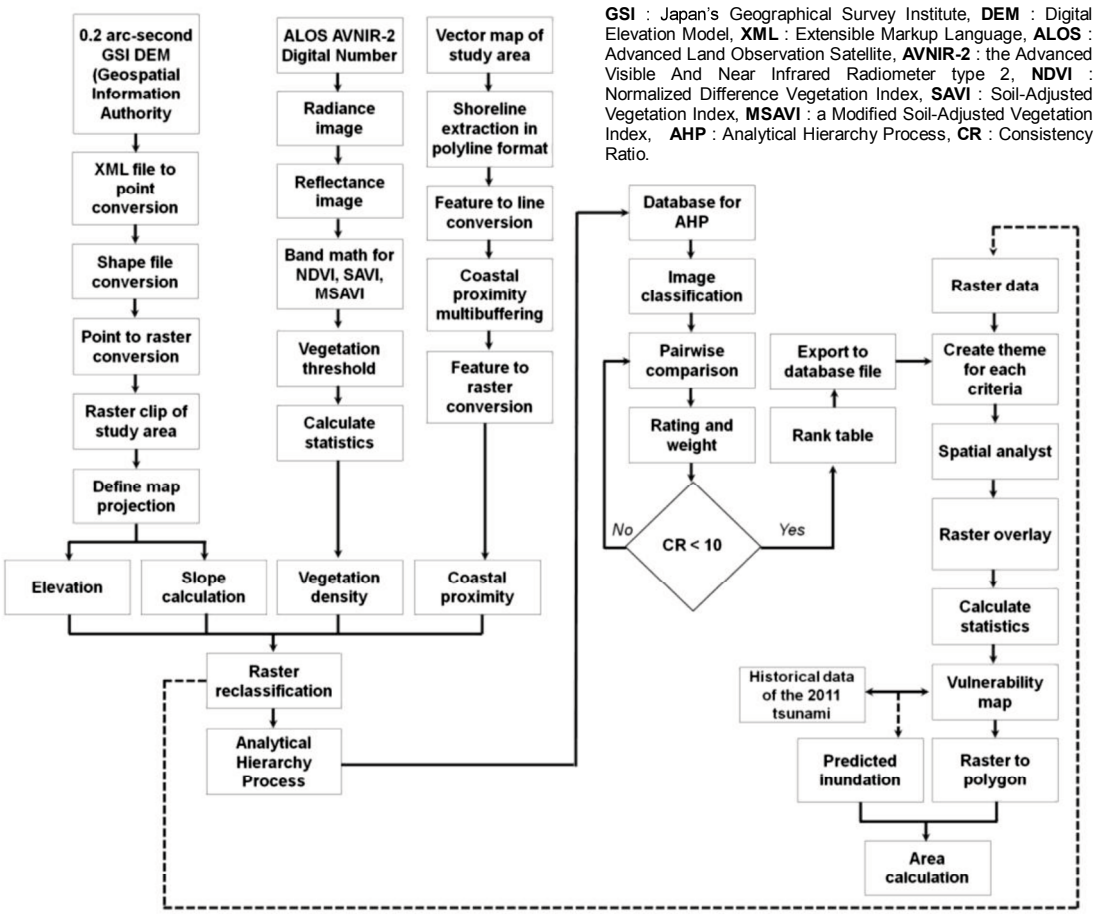

GSI : Japan's Geographical Survey Institute, **DEM** : Digital Elevation Model, **XML** : Extensible Markup Language, **ALOS** : Advanced Land Observation Satellite, **AVNIR-2** : the Advanced Visible And Near Infrared Radiometer type 2, **NDVI** : Normalized Difference Vegetation Index, **SAVI** : Soil-Adjusted Vegetation Index, **MSAVI** : a Modified Soil-Adjusted Vegetation Index, **AHP** : Analytical Hierarchy Process, **CR** : Consistency Ratio.

Figure 7.1 Framework of the study

The parameters of elevation and slope were extracted from a digital elevation model (DEM) obtained from the Geospatial Information Authority of Japan (hereafter referred to as GSI DEM), while the vegetation density is extracted from an ALOS AVNIR-2 image. Coastal proximity was calculated from a vector map of the study area.

7.2 Surface Analysis for Spatial Data

7.2.1 Elevation

Digital elevation model was created from elevation data obtained from GSI. GSI DEM was downloaded from http://fgd.gsi.go.jp/download/GsiDLSelFileServlet for 5 m mesh elevation data (0.2 seconds). The 5 m mesh elevation was created based on the airborne laser survey of the center point grid (mesh) and the data obtained by the photogrammetry with a longitude difference at the surface separated by an interval of 0.2 seconds latitude difference. The height accuracy of the 5m mesh elevation from the airborne laser is 0.3m and the standard deviation of the elevation point from the photogrammetry is 0.7m. The data was in JPGIS format, and it needed several JPGIS data that covered the study area.

Each JPGIS data was converted to shapefile in point format using base map viewer converter software version 3.10 (FGDV) provided by GSI. The shapefile data were then combined using the merge function of ArcGIS 10 based on the area of study, and finally, this point format was converted to raster for creating the digital elevation model. The steps are shown in **Figure 7.2**.

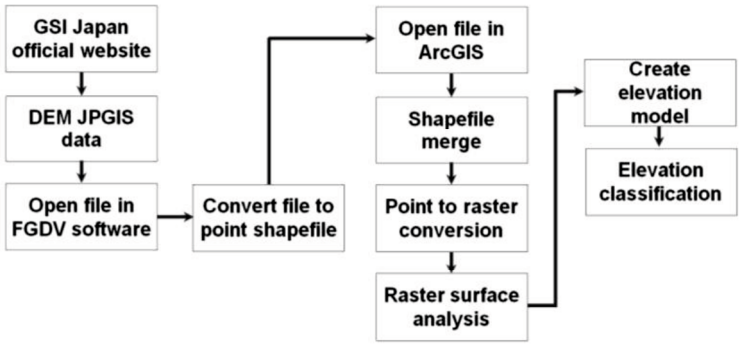

Figure 7.2 Elevation data process

7.2.2 Slope

The slope is the rate of maximum change in *z*-value from each cell of the image. The use of a *z*-value is essential for correct slope calculations when the surface *z* units are expressed in units different from the ground *x*, *y* units. The range of values in the output depends on the type of measurement units. Slope map was created using the surface analyst tools of the ArcGIS 10 software using the third-order finite-difference method (Horn, 1981).

7.2.3 Coastal proximity

Coastal line was created in polyline file for buffering the distance from shoreline to the land. The distance was calculated using a multiring buffer under the proximity tool in the ArcGIS 10 software. The distance is based on the historical report of the maximum run-up in the area of study. **Equation 7.1** is used for coastal proximity buffering (Sinaga et al., 2011).

$$\mathrm{Log}X_{\max} = \log 1400 + \tfrac{3}{4}\log\left(Y_0/10\right) \qquad \text{(Eq. 7.1)}$$

in which X_{max} is the maximum reach of the tsunami over land, and Y_0 is the tsunami height at the coast.

The maximum run-up of the tsunami in the study area due to the 2011 Tohoku earthquake was 18.8m. Based on the algorithm above, five classes of distance buffers were used in order to create a tsunami vulnerability map. It describes that 9.40m to 11.28m of run-up can reach a distance of 1,289.14m from the coastline, 11.28m to 13.16m of run-up can reach 1,643.89m, 13.16m to 15.04m of run-up can reach 2,019m, 15.04m to 16.92m of run-up can reach 2,412.45m, and 16.92m to 18.80m of run-up can reach more than 2,412.45m.

Elevation, slope, and coastal proximity were classified into five classes of vulnerability using the Jenks natural breaks classification. This classification method identifies breaks in the ordered distribution of values that minimizes within class sum of squared. Elevation, slope, and coastal proximity were classified based on the values described in **Table 7.1**. The tsunami vulnerability map based on elevation is shown in **Figure 7.3**, one based on slope is shown in **Figure 7.4**, and one based on coastal proximity is shown in **Figure 7.5**.

Table 7.1 Tsunami vulnerability classess based on elevation, slope, and coastal proximity

Elevation (meter)[a]	Slope (%)[b]	Proximity (meter)	Vulnerability class
< 5	0 – 2	0 – 1,289.14	High
5 –10	2 – 6	1,289.14 – 1,643.89	Slightly high
10 – 15	6 – 13	1,643.89 – 2,019	Medium
15 – 20	13 – 20	2,019 – 2,412.45	Slightly low
> 20	> 20	> 2,412.45	Low

[a]Iida, 1963
[b]Van Zuidam, 1983

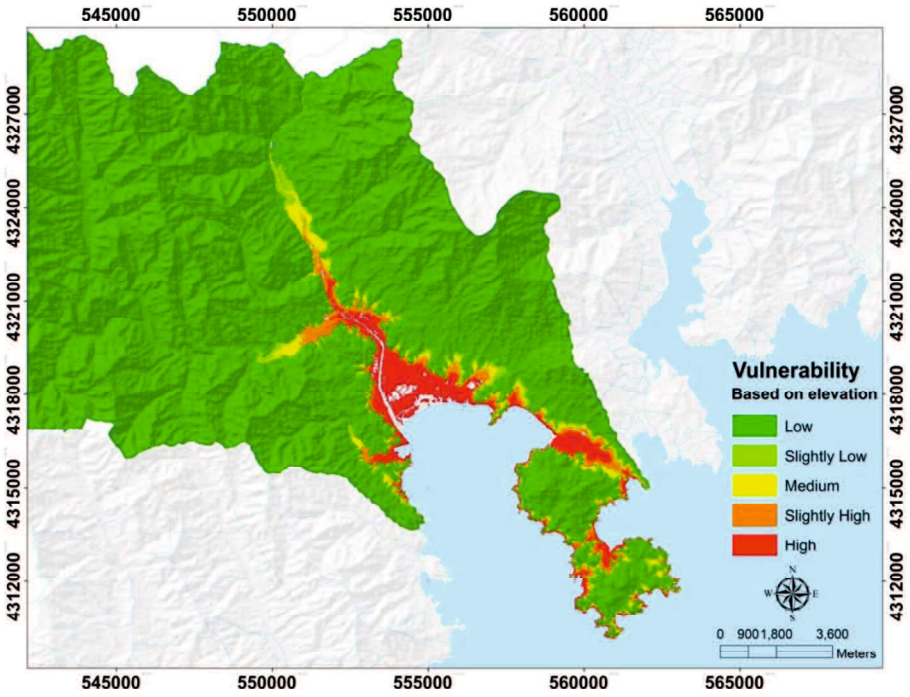

Figure 7.3 Vulnerability map based on elevation

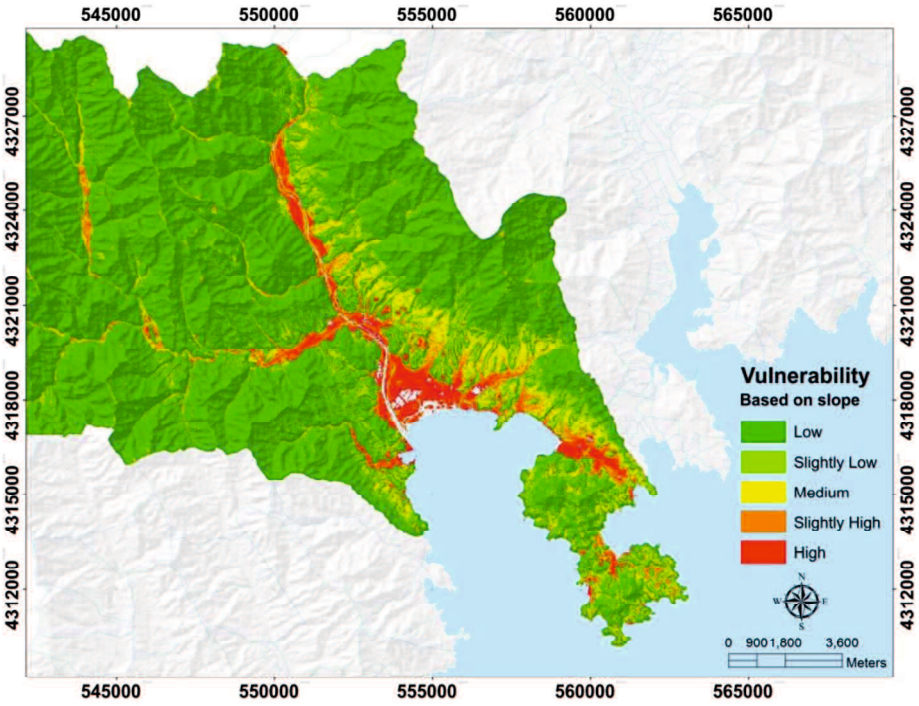

Figure 7.4 Vulnerability map based on slope

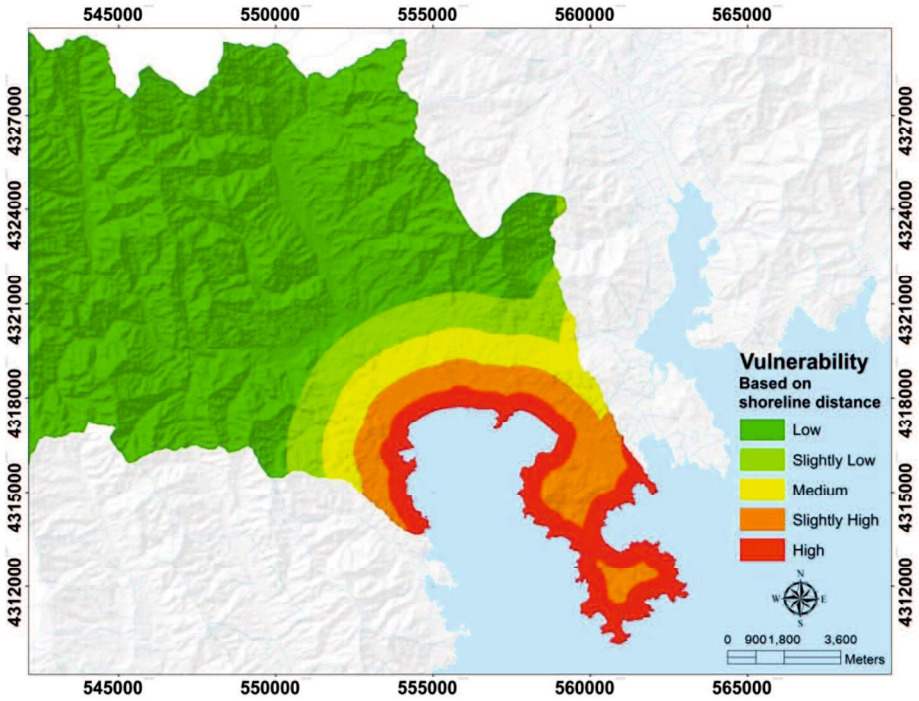

Figure 7.5 Vulnerability map based on coastal proximity

7.3 ALOS AVNIR-2 Processing

ALOS AVNIR-2 was used to generate vegetation density. Normalized difference vegetation index (NDVI), soil-adjusted vegetation index (SAVI), and a modified soil-adjusted vegetation index (MSAVI) were calculated instead of vegetation density. The digital numbers (DN) of ALOS AVNIR-2 were converted to reflectance values before generating the synthetic NDVI and SAVI images (Huete, 1988; Araujo et al., 2000). The steps to create vegetation density map are as follows:

7.3.1 DN to Radiance Conversion

Equation 7.2 describes the algorithm for DN to radiance conversion (Bouvet et al., 2007).

$$L_\lambda = G_{rescale} \times QCAL + B_{rescale} \quad \text{(Eq. 7.2)}$$

in which L_λ is the spectral radiance at the sensor's aperture ($W/m^2/sr/\mu m$), $G_{rescale}$ is the rescaled gain, QCAL is the DN, and $B_{rescale}$ is the rescaled bias. **Table 7.2** describes rescaled gains and biases for ALOS AVNIR-2.

Table 7.2 Rescaling gains and biases used for DN to spectral radiance conversion for ALOS AVNIR 2

Band	$G_{rescale}$	$B_{rescale}$
1	0.5888	0
2	0.5730	0
3	0.5020	0
4	0.8350	0

7.3.2 Radiance to Reflectance Conversion

Equation 7.3 describes the algorithm for radiance to reflectance conversion (Sah et al., 2012).

$$\rho_\lambda = \pi \times L_\lambda \times {d^2}/{ESUN_\lambda} \times \cos\theta_s \quad \text{(Eq. 7.3)}$$

in which ρ_λ is the unitless planetary reflectance, L_λ is the spectral radiance at the sensor's aperture, d^2 is the Earth-sun distance in astronomical units from a nautical handbook, $ESUN_\lambda$ is the mean solar exoatmospheric irradiances, and θ_s is the solar

zenith angle in degrees.

7.3.3 NDVI, SAVI, and MSAVI Calculation

NDVI is a measure of the difference in reflectance between these wavelength ranges that takes values between −1 and 1, with values > 0.5 indicating dense vegetation and values < 0 indicating no vegetation including water. **Equation 7.4** was used for NDVI calculation (Hansen et al., 2000).

$$NDVI = \frac{(NIR - VIS)}{(NIR + VIS)} \quad \text{(Eq. 7.4)}$$

in which *NIR* is near an infrared band and *VIS* is a visible band of red band of ALOS AVNIR-2. Band 3 is red, and band 4 is *NIR*. Moreover, SAVI is one of the algorithms developed to generate vegetation index by eliminating soil factor (Gong et al., 2003). Although the SAVI model is not significant in the intraclass analysis, in the similar spectral space, this model presents a reasonable performance in the characterization of forested and non-forested areas (Araujo et al., 2000). SAVI was developed to minimize soil-brightness, including shadow, influences found in the NDVI by accounting for first-order soil-vegetation spectral interactions as in **Equation 7.5** (Huete, 1988).

$$SAVI = \frac{(NIR - R)}{(NIR + R + L)} \times (1 + L) \quad \text{(Eq. 7.5)}$$

in which *NIR* is the near infrared band, *R* is the red band, and *L* is the soil calibration factor. $L = 0.5$ (Jensen, 2000). A correction factor (L) was used to minimize the secondary backscattering effect of canopy-transmitted soil background reflected radiation. The *L* value of 1 was optimal in semiarid environments.

MSAVI is a modified version of SAVI, which replaces the constant soil adjustment factor, *L*, with a self-adjusting *L*. SAVI uses a manual adjustment *L*, while MSAVI uses a self-adjusting *L*. The former requires prior knowledge about vegetation densities in order to use an optimal *L* value in the SAVI equation, while the latter automatically adjusts its *L* values to optimal (Qi et al., 1994). Equation (7.6) describes the algorithm for MSAVI calculation.

$$MSAVI = \frac{1}{2}\left(2NIR + 1 - \sqrt{(2NIR+1)^2 - 8(NIR - RED)}\right) \quad \text{(Eq. 7.6)}$$

The regression between NDVI and MSAVI values describes that R^2 was 0.9658 (see **Figure 7.6**). MSAVI was used for vegetation density mapping because it provides a vegetation index where soil factors are eliminated. MSAVI values ranged between −0.058 to 0.537 (see **Figure 7.7**). MSAVI was classified into five classes of vulnerability for generating a tsunami vulnerability map based on vegetation density using the Jenks natural breaks classification. The classification was based on the maximum and minimum values of MSAVI as shown in **Table 7.3**.

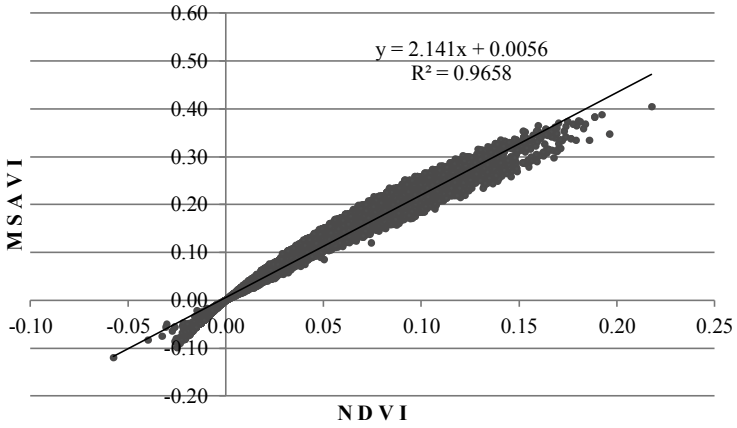

Figure 7.6 Scatter plot of NDVI and MSAVI values

Table 7.3 Tsunami vulnerability classes based on vegetation density

Vegetation density	Vegetation index	Vulnerability class
Rarely	(−)0.05761 – 0.046204	High
Slightly rarely	0.046204 – 0.091981	Slightly high
Medium	0.091981 – 0.133113	Medium
Slightly high	0.133113 – 0.178984	Slightly low
High	0.178984 – 0.537292	Low

A vulnerability map based on vegetation density, as shown in **Figure 7.8**, described that most of high-vulnerability areas were found in the coastal areas of Rikuzentakata and indicated as bare areas.

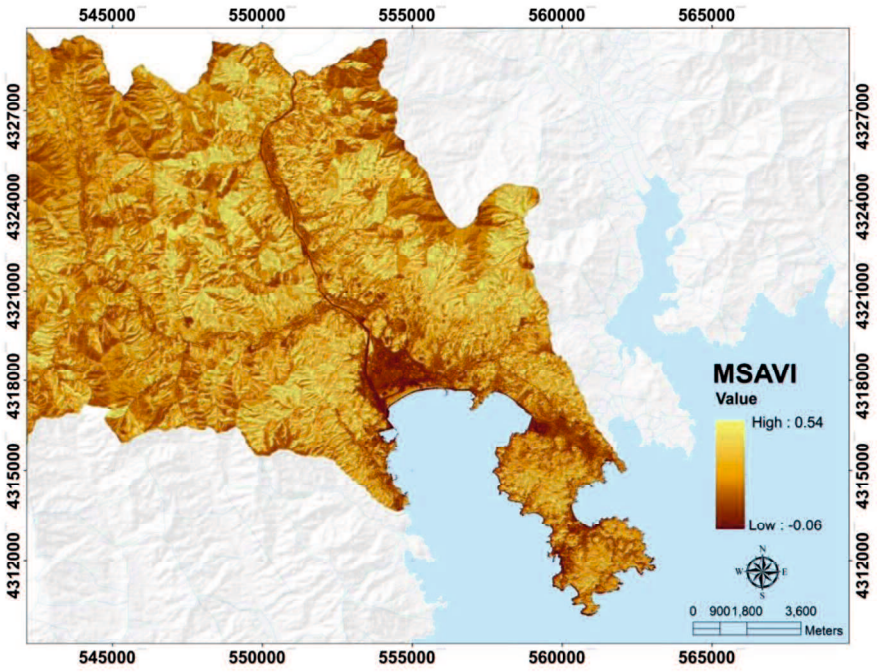

Figure 7.7 Vulnerability map based on vegetation density

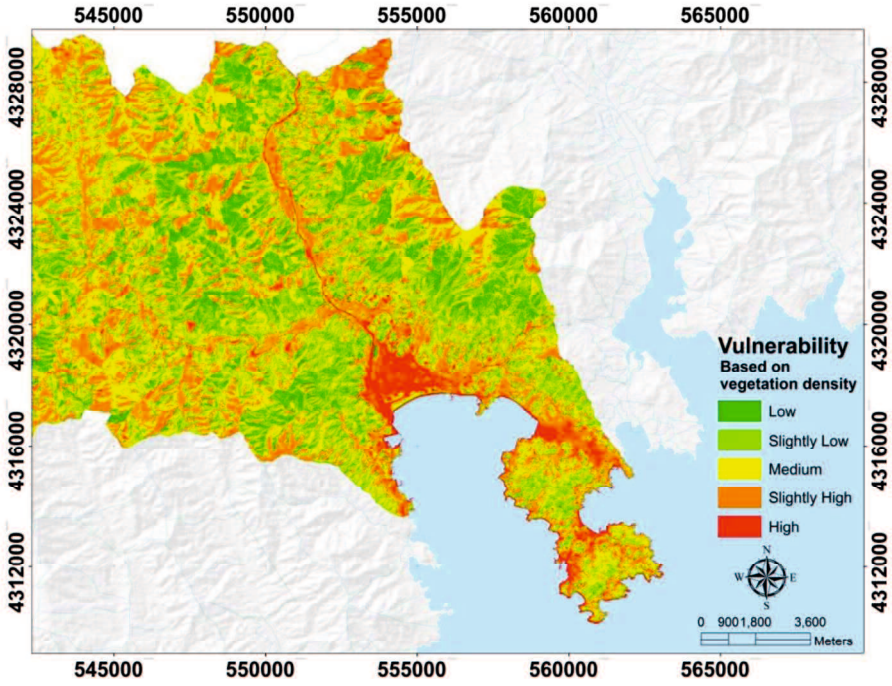

Figure 7.8 Vulnerability map based on vegetation density

7.4 GIS and AHP for Vulnerability Mapping

Cell-based modeling in spatial analysis was applied to determine the

vulnerability area due to tsunami hazard. Cells are classified into five classes of vulnerability in the numbers of 1, 2, 3, 4, and 5, which represent low, slightly low, medium, slightly high, and high vulnerability classes, then overlay the entire parameter of tsunami vulnerability by using a weighting and scoring system. Weighting is based on the dominant influences of these parameters in determining the class of tsunami vulnerability. For this step, AHP was applied.

AHP helps in creating a scaled set of preferences and describing the importance of each parameter relative to other parameters through pairwise comparisons (Saaty, 1977; 1980; 2003). The priorities among the parameters of the hierarchy were established by creating a series of judgments based on pairwise comparisons of the parameters, where a number from 1 to 9 is used in the matrix cell value for scoring the importance of each parameter. **Table 7.4** describes the Saaty nine-point comparison scale. This number depends on the relative importance of each parameter.

Table 7.4 The Saaty nine-point comparison (saaty, 1996)

Score	Definition	Explanation
1	Equal importance	Two parameters contribute equally to the objective.
3	Weak importance of one over another	The judgment is to favor one parameter over another, but it is not conclusive.
5	Essential or strong importance	The judgment is to strongly favor one parameter over another.
7	Demonstrated importance	Conclusive judgment as to the importance of one parameter over another.
9	Absolute importance	The judgment in favor of one parameter over another is of the highest possible order of affirmation.
2, 4, 6, 8	Intermediate values between the two adjacent judgments	Compromise is needed.

The relative weights of each parameter will be produced via pairwise comparison as shown on **Table 7.5**. The hierarchical interactions were calculated based on the respective importance of each parameter by assessing the numerical score. These values are generated by the subjective determination of the investigator in determining the importance of each factor (Saaty, 2003; Youssef et al., 2010).

Table 7.5 Pairwise comparison

	Elevation	Slope	Coastal proximity	Vegetation density
Elevation	1	2	3	3
Slope	1/2	1	2	2 1/2
Coastal proximity	1/3	1/2	1	3
Vegetation density	1/3	2/5	1/3	1

The eigenvector was calculated based on the pairwise comparison matrix in five iterations. The normalized principal eigenvector after five iterations describes that elevation has the highest weight (45.94%), followed by slope (25.53%), coastal proximity (16.71%), and vegetation density (11.81%), as shown in **Figure 7.9**.

$$\begin{array}{c} \\ \text{Elevation} \\ \text{Slope} \\ \text{Coastal proximity} \\ \text{Vegetation density} \end{array} \begin{array}{c} \text{Normalized matrix} \\ \begin{pmatrix} 0.4615 & 0.5129 & 0.4737 & 0.3158 \\ 0.2308 & 0.2564 & 0.3148 & 0.2632 \\ 0.1539 & 0.1282 & 0.1579 & 0.3158 \\ 0.1539 & 0.1026 & 0.0526 & 0.1053 \end{pmatrix} \end{array}$$

$$1^{st}\ \text{iteration} \begin{pmatrix} 0.4528 & 0.4613 & 0.4720 & 0.4635 \\ 0.2548 & 0.2516 & 0.2540 & 0.2678 \\ 0.1735 & 0.1644 & 0.1549 & 0.1654 \\ 0.1190 & 0.1227 & 0.1191 & 0.1033 \end{pmatrix} \begin{pmatrix} 46.24\% \\ 25.70\% \\ 16.46\% \\ 11.60\% \end{pmatrix}$$

$$5^{th}\ \text{iteration} \begin{pmatrix} 0.4595 & 0.4595 & 0.4595 & 0.4595 \\ 0.2554 & 0.2554 & 0.2554 & 0.2554 \\ 0.1671 & 0.1671 & 0.1671 & 0.1671 \\ 0.1181 & 0.1181 & 0.1181 & 0.1181 \end{pmatrix} \begin{pmatrix} 45.94\% \\ 25.53\% \\ 16.71\% \\ 11.81\% \end{pmatrix}$$

Figure 7.9 Normalized eigenvector calculation

AHP tolerates inconsistency by providing a measure of inconsistency assessment, which is shown by consistency ratio (CR). An acceptable CR is less than or equal to 10%, although in some cases a consistency ratio greater than 10% can be considered acceptable (Forman and Selly, 2001). CR is defined as the ratio between the consistency index (CI) and random consistency index (RI). CR indicates the probability that the matrix judgments were randomly generated (Saaty, 1977). **Equation 7.7** describes the algorithm for CR and CI calculation.

$$CR = \frac{CI}{RI}, and\ CI = \frac{(\lambda_{max} - N)}{(N-1)} \qquad \text{(Eq. 7.7)}$$

in which λ_{max} represents the largest eigenvalue and N is the size of the the

comparison matrix. In this study, $N = 4$. λ_{max} is calculated from the sum of all parameters and is multiplied by its eigenvector. The *RI* is based on the random consistency index as shown in **Table 7.6**. *RI* of 0.90 was used for four parameters. Five iterations of normalized matrix in **Figure 7.9** produces the value of *CI* of 0.057 and *CR* of 6.4%.

Table 7.6. Random consistency index

Matrix size	1	2	3	4	5	6	7	8
Random CI	0	0	0.58	0.90	1.12	1.24	1.32	1.41

In order to create the vulnerability map, each raster cell of the parameter was calculated to its weight. A weighted linear combination is very straightforward in a raster GIS, and factors are combined by applying a weight value to each, followed by a summation of the results (Eastman et al., 1995). Raster calculator in map algebra menu using the spatial analyst tools of ArcGIS 10 was used to generate vulnerability mapping by applying **Equation 7.8**. The tsunami vulnerability map in the Rikuzentakata area as result of this calculation is shown in **Figure 7.10**, while the vulnerability class is shown in **Table 7.7**. The statistics of the vulnerability map was calculated, which shows that the vulnerability index of 822,634.39 grid cells ranged between 1 to 5, with a standard deviation of 0.766.

$$\sum (W_i \cdot X_i) \qquad \text{(Eq. 7.8)}$$

in which W_i is the weight values of the parameter i and X_i is the potential rating of the factor.

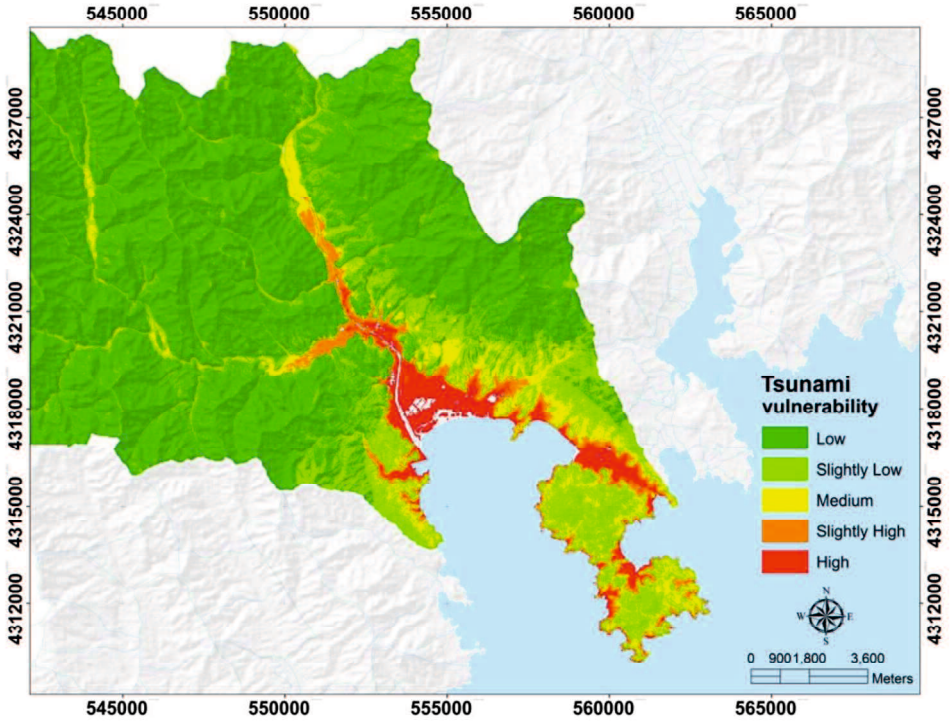

Figure 7.10 Tsunami vulnerability map of Rikuzentakata

Table 7.7 Vulnerability classification

Vulnerability classes	Vulnerability (grid) value	Vulnerability index	Area (km^2)	(%)
Low	1 – 1.8	1	117.88	49.55
Slightly low	1.8 – 2.6	2	67.16	28.23
Medium	2.6 – 3.4	3	38.52	16.19
Slightly high	3.4 – 4.2	4	10.05	4.22
High	4.2 – 5	5	4.30	1.81

This result then compared to the historical data of the impact of the 2011 Tohoku tsunami from GSI (see **Figure 7.11**) and the 2011 Earthquake Tsunami Joint Survey Group. The comparison describes that most of inundation areas are areas of high and slightly high vulnerability.

The inundation area, as result of this study, was 14.35km^2 as shown in **Figure 7.12**, while GSI reported that the inundation area in Rikuzentakata was 13 km^2. The maximum run-up in Rikuzentakata based on the 2011 Earthquake Tsunami Joint Survey Group was 18.81m and found in the area of Yamanawashiro (in the latitude of 39.021 and longitude of 141.647). This area was identified as a bare area and in the class of slightly high vulnerability. The farthest area reached by the tsunami

during the 2011 Tohoku tsunami was about 7.50 km from the coastal line, with an inundation height of 11.08 m (in the latitude of 39.063 and longitude of 141.589). This area was close to the river and identified in the class of slightly high vulnerability.

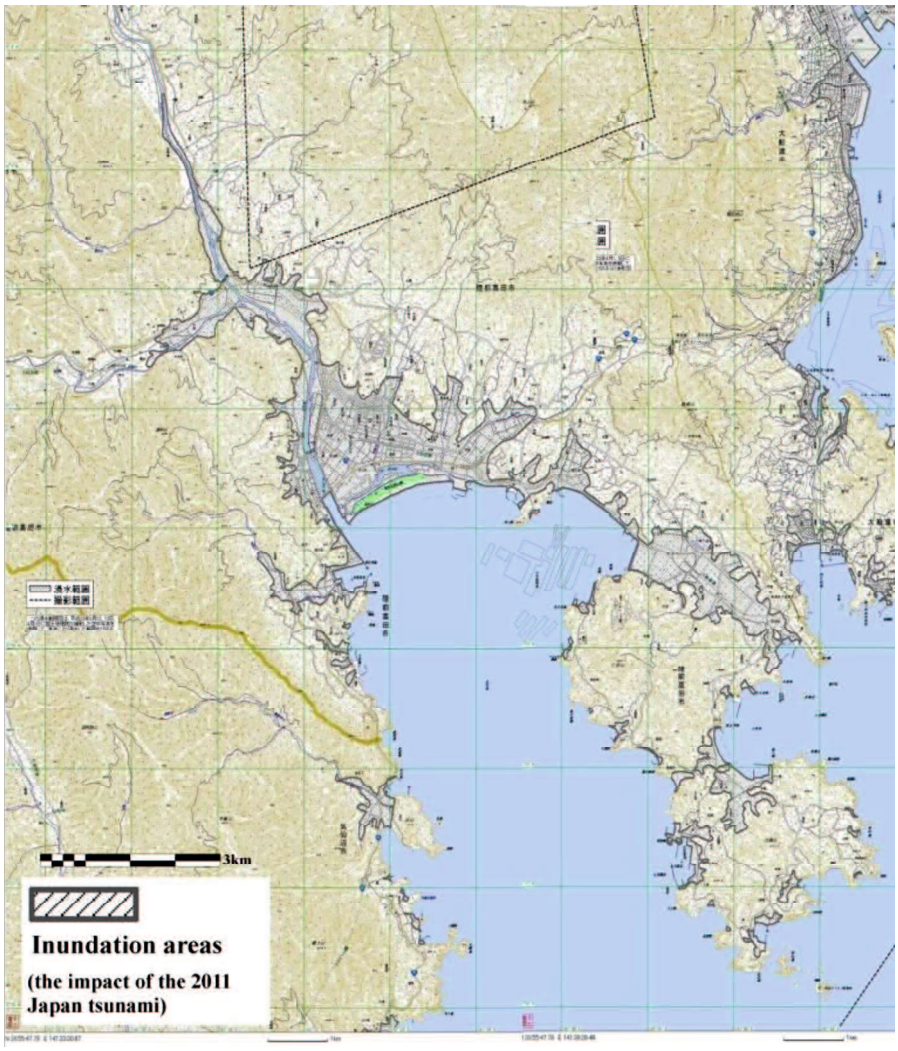

Figure 7.11 Map of the impact of the 2011 Japan tsunami in Rikuzentakata, published by GSI, 2013

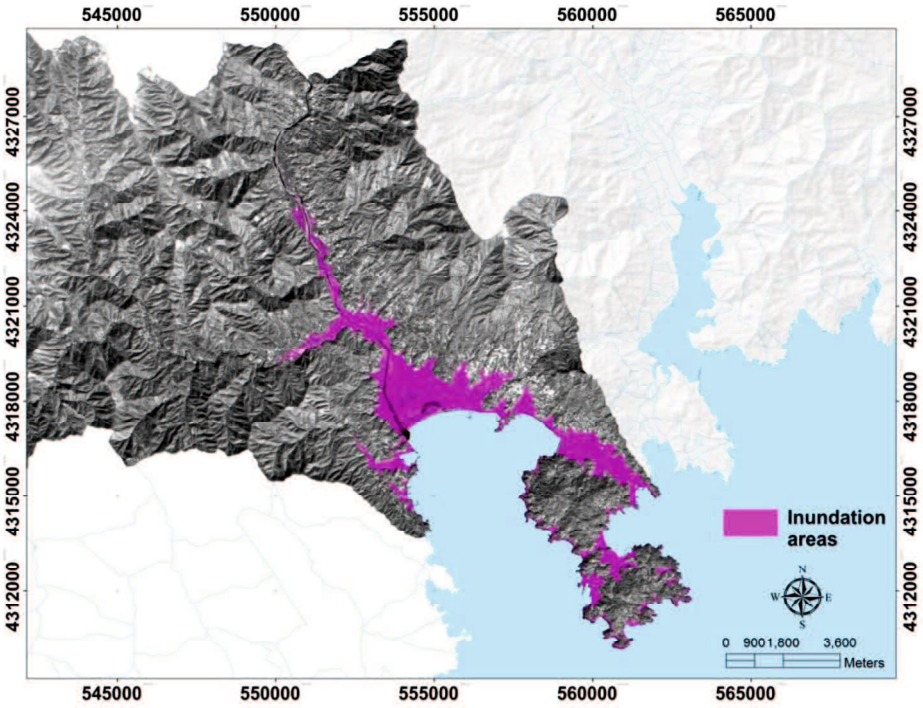

Figure 7.12 Map of possible inundation areas in Rikuzentakata

In addition, **Table 7.8** describes the value of some data that were used as the parameters in this study. Based on the vulnerability class that is described in the previous section (see **Table 7.1** and **Table 7.3**), in general, these values are included in the class of high vulnerability.

Table 7.8 Parameters value in the area of inundation

Parameters	Average value
Elevation (meter)	4.425
Slope (%)	8.052
NDVI	0.089
SAVI	0.048
MSAVI	0.040
ALOS AVNIR-2 reflectance (18 March 2009)	0.244
ALOS AVNIR-2 reflectance (14 March 2011)	0.137

7.5 Discussion

Vulnerability describes the potential area that can be damaged by natural hazards. Vulnerability class could be based on a physical parameter, such as elevation, slope, coastal proximity, and vegetation density. Moreover, inundation can be defined as the result of a tsunami traveling a long distance inland and is a

horizontal measurement of the path of the tsunami. The analysis of satellite remote sensing data, elevation data, and survey data followed by multi-criteria analysis through AHP and raster overlay in GIS processing can be used as the basic information for vulnerability mapping and inundation assessment due to tsunami hazard. The use of AHP method helps in the analysis of spatial multi-criteria where all the parameters used in this study were calculated based on their weight factors to create a vulnerability map.

This study is a first attempt to assess tsunami vulnerability by using the parameter of MSAVI instead of vegetation index mapping besides elevation, slope, and coastal proximity and applying AHP method combined with raster overlay through GIS processing in the Rikuzentakata area. A simple method for inundation prediction that was performed in this study can be a valuable step for carrying out a preliminary tsunami vulnerability mapping and impact assessment when the high resolution of digital elevation model data and detailed topographic data are not available.

Remote sensing can be effective for deriving information about the input parameters for tsunami vulnerability mapping and impact assessment. For the large area of study, several indicators of vulnerability can be obtained using a middle-resolution satellite. ALOS AVNIR-2 is useful for preparing the input parameters of vegetation density. Although obtaining the digital elevation model from GSI DEM needs some processing, it was very useful to derive information about the digital elevation model in high spatial resolution, especially for areas of study around Japan. GIS is a powerful tool for processing and combining spatial data of each parameter and analyzing the result of AHP in order to generate a vulnerability map.

In this research, five classes of vulnerability were used. The tsunami vulnerability map describes that 117.88 km^2 of the area was in low vulnerability, 67.16 km^2 was in slightly low vulnerability, 38.52 km^2 was in medium vulnerability, 10.05 km^2 was in slightly high vulnerability, and 4.30 km^2 was in high vulnerability. The high-vulnerability areas were mostly found in the coastal areas of the sloping coast type. Inundation areas were predicted in areas identified as high-vulnerability and rather-high-vulnerability areas. In addition, we assumed that vegetation may play

an important role as tsunami barriers to reduce the impact of tsunami destruction, and a river or another water channel can act as a flooding strip that transports inundation into the hinterland. The run-up of the tsunami comes up to the hinterland not only through the flat surface of the area but also because of the river. This is shown in the inundation map, which described that the farthest area reached by tsunami was about 7.50km from the shoreline, and this area was close to the river. The tsunami vulnerability map and inundation map generated in this study can be used for determining the priority for land-use planning related to tsunami hazard risk management.

In this study, the combination analysis of digital elevation data, middle-resolution of satellite images, tsunami historical data, AHP, and spatial multi-criteria processing via GIS was introduced to provide a tsunami vulnerability map and inundation map. As a preliminary study, the reflectance value of ALOS AVNIR-2 images before and after the 2011 Tohoku tsunami was calculated. In the next study, the analysis of satellite images to assess the characteristics of the inundation area by comparing before and after images of the disaster event will be focused.

7.6 Conclusion

GIS application followed by satellite image processing and AHP method in multi-criteria analysis is useful for tsunami vulnerability mapping and impact assessment. GIS indicate the vulnerability area due to tsunami and describe the possibility areas that could be affected by tsunami waves. In the scope of disaster mitigation planning, this study can be used for the evacuation and reconstruction plan due to tsunami hazards. In this study, four parameters were applied in order to create a tsunami vulnerability map and to map the inundation areas in the area of Rikuzentakata, Iwate Prefecture, Japan. The vulnerability map showed that most of the coastal areas are vulnerable to tsunami hazard. The inundation pattern, as the result of this study, showed similarities to the inundation areas of the 2011 Tohoku earthquake in the area of Rikuzentakata. This study used high resolution of DEM for the input parameters of elevation and slope. MSAVI was calculated also for the parameter of vegetation index.

In the case of data limitation, the use of other DEM is needed. By adding other parameters, such as coastal type, relative direction of tsunami, and coastal bathymetry, better tsunami vulnerability mapping can be done. We recommend to the user to be aware of the assumptions made as well as the limitations within this study. Environmental vulnerability assessment as well as social and economic data can be applied for further works.

In conclusion, the use of remote sensing data followed by AHP processing and spatial multi-criteria analysis via the GIS approach can be applied not only for tsunami vulnerability mapping but also for the assessment of the areas that could be affected by tsunami hazard.

CHAPTER 8

Remote Sensing Approach for Observing Tsunami-Affected Area

8.1 Introduction

The use of remote sensing products and geo-information systems has become an integrated, well developed and successful tool in disaster risk management. Hazard and risk assessments are carried out at different scales of analysis, ranging from a global scale to a community level. Each of these levels has its own objectives and spatial data requirements for hazard inventories, environmental data, triggering factors, and elements-at-risk. An overview is given of the use of spatial data with emphasis on remote sensing data, and of the approaches used for hazard assessment. This is illustrated with examples from different types of hazards, such as earthquakes, windstorms, drought, floods, volcanic eruptions, landslides and forest fires.

From a temporal perspective, remote sensing contributions to assess earthquake risk have a long research tradition. Remote sensing imagery is already used for hazard-related applications since the advent of research oriented satellite systems and sensors four decades ago. However, especially for vulnerability-related analysis, remote sensing is a less-established methodological element and is perceived increasingly only in recent years as a valuable source of information (Tronin, 2010; Nassel and Voigt, 2006; Deichmann et al., 2011; Geiß and Taubenbo¨ck, 2012).

Several aspects of pre-event earthquake hazard analysis are tackled by means of remotely sensed data. Especially in pre-event geological observations, remote sensing addresses the need for quantitative observational parameters on landforms, land cover and tectonic features (Philip, 2010; Deichmann et al.,2011) note that remote sensing can contribute valuable information for microscale zonation by deriving information for producing geological, seismic or soil maps. Post-event hazard-related applications deal mainly with the quantification and measurement of earthquake-induced changes of the land surface.

This study tried to develop a method to assess the affected area due to tsunami disaster by using middle-resolution of satellite images. The area of Kesennuma in Miyagi Prefecture, Rikuzentakata, and Ofunato in Iwate Prefecture were selected as

case studies which are the areas affected by the 2011 Tohoku earthquake. **Figure 8.1** shows the flow diagram of the study.

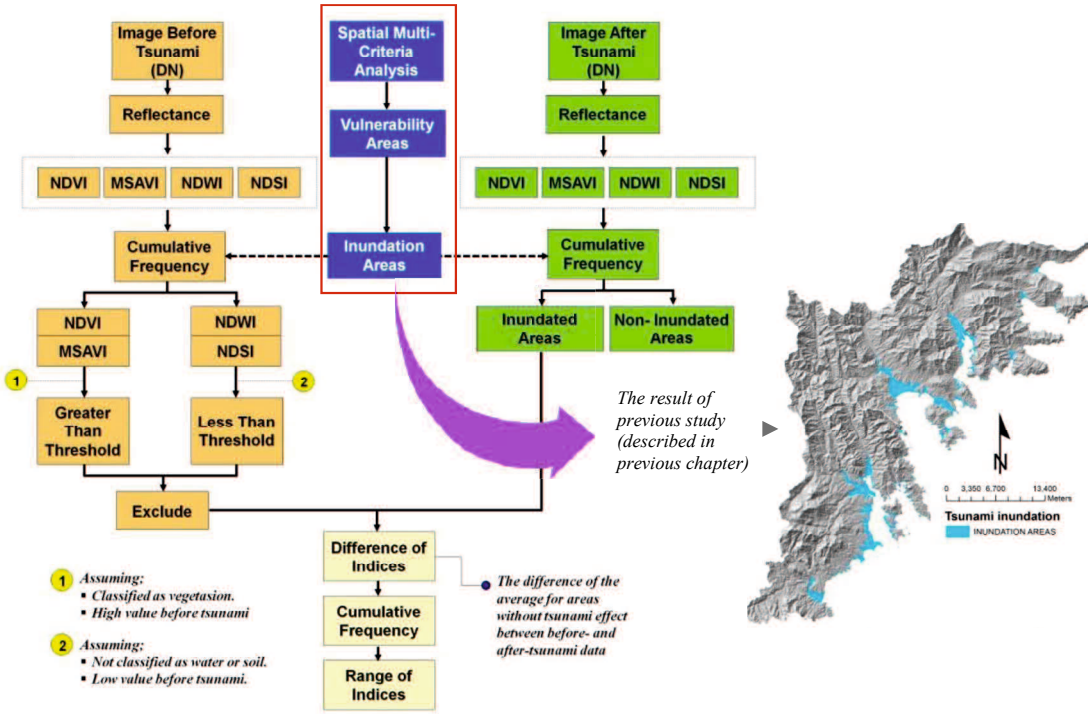

Figure 8.1 Flow diagram of the study

8.2 Image Analysis for Tsunami Affected Area Observation

ALOS AVNIR-2 images in two different time acquisition were used to analysis the surface change in the study area due to tsunami attack. The images include surface coverage on March 18, 2009 (before-event image) and March 14, 2011 (after-event image). **Figure 8.2** shows satellite observed coastal area of Tohoku three days after the tsunami attack published by The Japan Aerospace Exploration Agency (JAXA). Moreover, the visual sighting of the study area which is observed by ALOS AVNIR-2 images for before and after-event is shown in **Figure 8.3**.

Equipped with the Advanced Visible and Near Infrared Radiometer type 2 (AVNIR-2) sensors with 10m of spatial resolution (at Nadir) and 70km of swath, make ALOS became one of the powerful satellites for observing land and coastal zones. ALOS collects the data of Blue (band-1), Green (Band-2), Red (Band-3), and Near Infra Red/NIR (Band-4). Reflectance of the NIR is assigned to red component, red band to the green component, and green to the blue component. Comparing these

images, it could be observed that the reflectance of the near-infrared band in the affected areas became weak after the tsunami, which roughly means that, due to the tsunami, vegetation there might be removed and that the land cover class might be changed to soil (Yamazaki et al., 2006).

ALOS AVNIR-2 data with middle-resolution is useful for detecting tsunami affected areas quickly due to the red and near-infrared bands are considered to give the good indicators of land cover characteristics, including the change of the land cover and can be used to calculate the vegetation index, soil, and water index. Using the combination of NIR band, red band, and blue band in ALOS ANVIR-2, the normalized difference vegetation (NDVI), soil (NDSI) and water (NDWI) indices, also modified soil-adjusted vegetation (MSAVI) can be calculated.

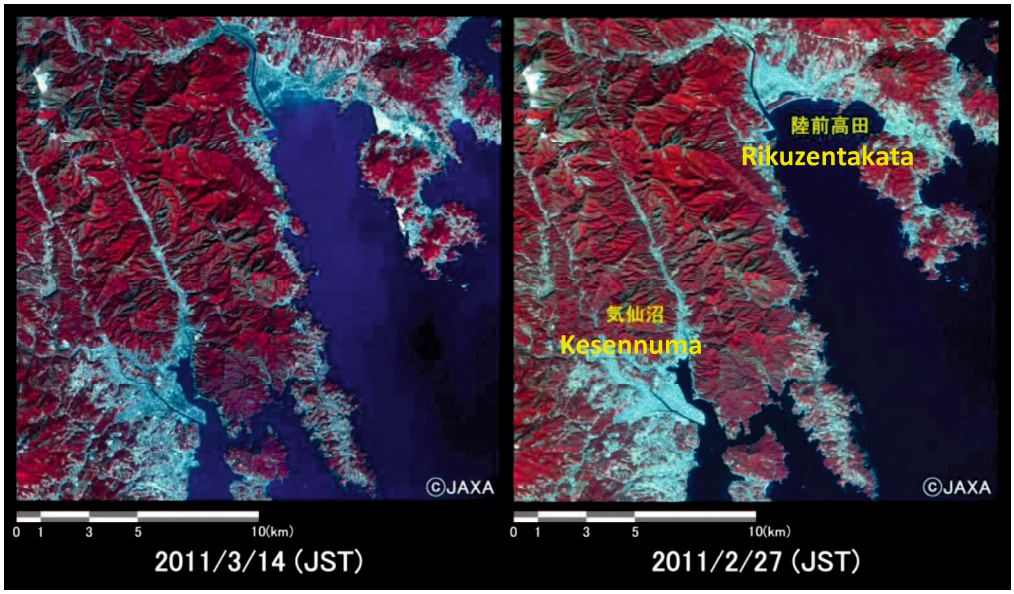

Figure 8.2 ALOS satellite image of flooded areas in Kesennuma city and Rikuzentakata (2011/3/18: ALOS/PALSAR Observation Results of the Magnitude-9.0 Earthquake off the Pacific coast of Tohoku-Kanto District in Japan in 2011, Product of JAXA)

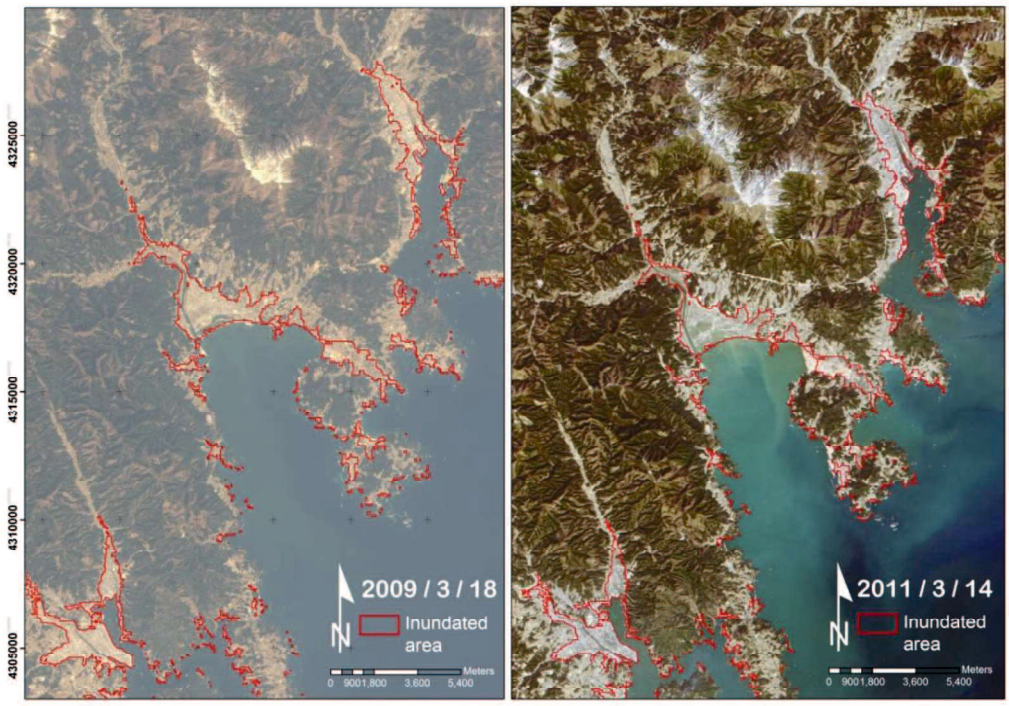

Figure 8.3 ALOS AVNIR-2 satellite images used in this study
(Describes before and after-event of tsunami and inundated areas)

8.2.1 Data Processing

The parameters used require physical units, such as at-sensor radiance or top-of-atmosphere (TOA) reflectance, rather than the raw quantized calibrated pixel value (DN). There are three advantages to using TOA reflectance instead of at-sensor spectral radiance when comparing images from different sensors (Karsli et al., 2011; Chander et al., 2009). First, TOA reflectance removes the cosine effect at different solar zenith angles due to the time difference between data acquisitions.

Second, TOA reflectance compensates for different values of the exo-atmospheric solar irradiance arising from spectral band differences. Third, TOA reflectance corrects for the variation in the earth-sun distance between different data acquisition dates. TOA reflectance can be obtained from the quantized calibrated pixel value, as given by **Equation 8.1**.

$$\rho_\lambda = \pi \times L_\lambda \times {d^2}/{ESUN_\lambda} \times \cos\theta_s \qquad \text{(Eq. 8.1)}$$

where ρ_λ is the TOA reflectance of wavelength λ [unitless], d is the earth-sun distance [astronomical units], $ESUN_\lambda$ is mean exo-atmospheric solar irradiance

[W/(m^2·μm)], θ_s is the solar zenith angle [degrees], and L_λ is the spectral radiance at wavelength λ at the sensor's aperture [W/(m^2·sr·μm)]. L_λ can be obtained from the quantized calibrated pixel value also as given by **Equation 8.2**.

$$L_\lambda = \left(\frac{LMAX_\lambda - LMIN_\lambda}{Q_{cal\max} - Q_{cal\min}} \right)(Q_{cal} - Q_{cal\min}) + LMIN_\lambda \qquad \text{(Eq. 8.2)}$$

where $LMAX_\lambda$ is the spectral at-sensor radiance that is scaled to Q_{calmax} [W/(m^2 sr μm)], $LMIN_\lambda$ is spectral at-sensor radiance that is scaled to Q_{calmin} [W/(m^2·sr·μm)], Q_{calmax} is the maximum quantized calibrated pixel value corresponding to $LMAX_\lambda$ [DN], Q_{calmin} is the minimum quantized calibrated pixel value corresponding to $LMIN_\lambda$ [DN], and Q_{cal} is the quantized calibrated pixel value [DN].

The Normalised Difference Water Index (NDWI) is derived using similar principles to the Normalized Difference Vegetation Index (NDVI). In an NDVI (the comparison of differences of two bands, red and near-infra-red (NIR), the presence of terrestrial vegetation and soil features is enhanced while the presence of open water features is suppressed because of the different ways in which these features reflect these wavelengths (McFeeters 1996). The NDVI index is calculated as follows:

$$NDVI = \frac{(NIR - VISred)}{(NIR + VISred)} \qquad \text{(Eq. 8.3)}$$

If the equation is reversed and the green band used instead of the red, then the outcome would also be reversed, the vegetation suppressed and the open water features enhanced (McFeeters 1996). The equation for an NDWI is:

$$NDWI = \frac{(VISgreen - NIR)}{(VISgreen + NIR)} \qquad \text{(Eq. 8.4)}$$

Where *VISgreen* is visible green band of ALOS satellite and *NIR* is Near Infra Red.

The selection of these wavelengths maximizes the reflectance properties of water. That is: maximize the typical reflectance of water features by using green wavelengths, minimize the low reflectance of NIR by water features; and maximize the high reflectance of NIR by terrestrial vegetation and soil features. The outcomes from this equation are water features that have positive values whilst soil and

terrestrial vegetation have zero or negative values (McFeeters 1996). The equation of NDSI that used to apply from the ALOS AVNIR-2 is follow:

$$NDSI = \frac{(VISred - VISblue)}{(VISred + VISblue)} \quad \text{(Eq. 8.5)}$$

Where *VISred* is visible red band of ALOS satellite and *VISblue* is visible blue band.

In addition, modified soil-adjusted vegetation index replaces the constant soil adjustment factor (*L*), with a self-adjusting *L* in the equation of soil-adjusted vegetation index (SAVI). SAVI uses a manual adjustment *L*, while MSAVI uses a self-adjusting *L*. The former requires prior knowledge about vegetation densities in order to use an optimal *L* value in the SAVI equation, while the latter automatically adjusts its *L* values to optimal. Equation 8.6 is used for MSAVI calculation.

$$MSAVI = \tfrac{1}{2}\left(2NIR + 1 - \sqrt{(2NIR+1)^2 - 8(NIR - VISred)}\right) \quad \text{(Eq. 8.6)}$$

In terms of remote-sensing, all radiation incident on soil is either absorbed or reflected. Although the absolute reflectance may be variable between soils, they all tend to show a rather smooth increase in reflectance from the visible to the near infrared, as shown in **Figure 8.4**, in which in Figure (a) shows the reflectance spectrum for a rye-grass sward, with the sharp increase at 700 nm, and a black-loam soil, together with the reflectance spectrum for a desiccated grass sward illustrating the loss of the sharp transition at 700 nm.

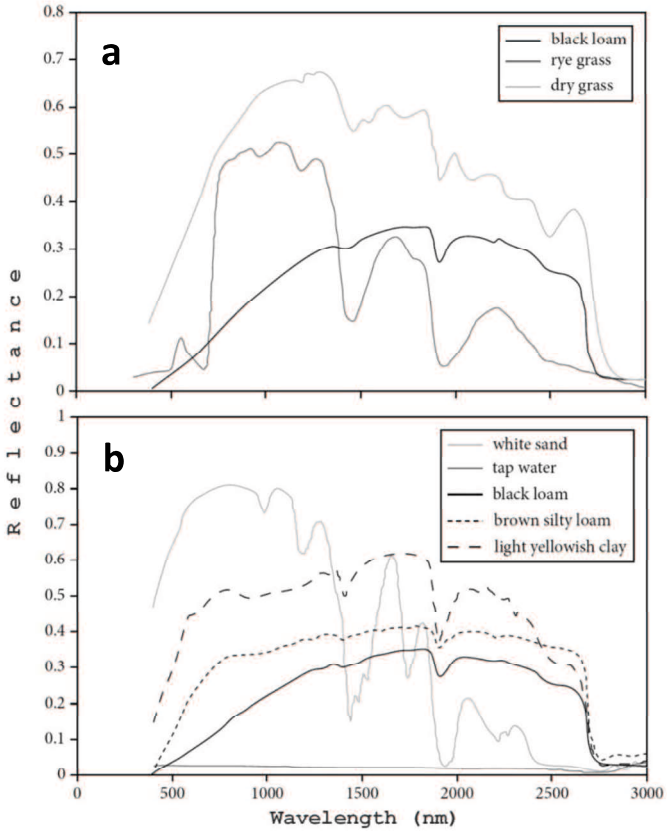

Figure 8.4 Spectral reflectance; (a) typical spectral reflectance characteristics of soil as compared with vegetation, (b) spectral reflectances of a range of different soils and water over the 400–3000 nm wavelength (datafrom ASTER spectral library; Baldridge *et al*., 2009)

8.2.2 NDVI-NDWI-NDSI-MSAVI Mapping

The thematic maps of NDVI, NDSI, NDWI, and MSAVI are shown in **Figures 8.5, 8.6, 8.7,** and **8.8**. The higher value of NDVI indicates the more probable the area is covered by dense vegetation. It is also for the case of NDSI for soil and NDWI for water. The analysis starts with the comparison of the four indices in the inundated areas and non-inundated areas using before-after images, and then determines the thresholds for detecting tsunami-inundated areas. One of the assumings is the vegetation density in the study area will decrease due to tsunami wave, in which described by the decreasing of NDVI value, on the other hand soil and water value assumed to be rise.

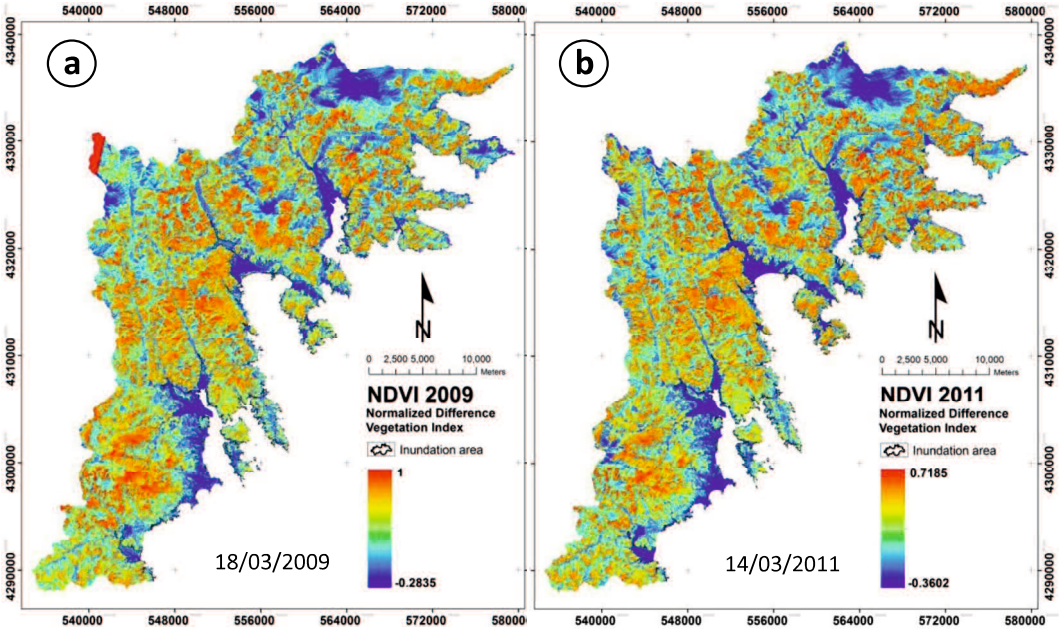

Figure 8.5 Computed NDVI for; (a) before-tsunami event; and (b) after-tsunami event using ALOS AVNIR-2

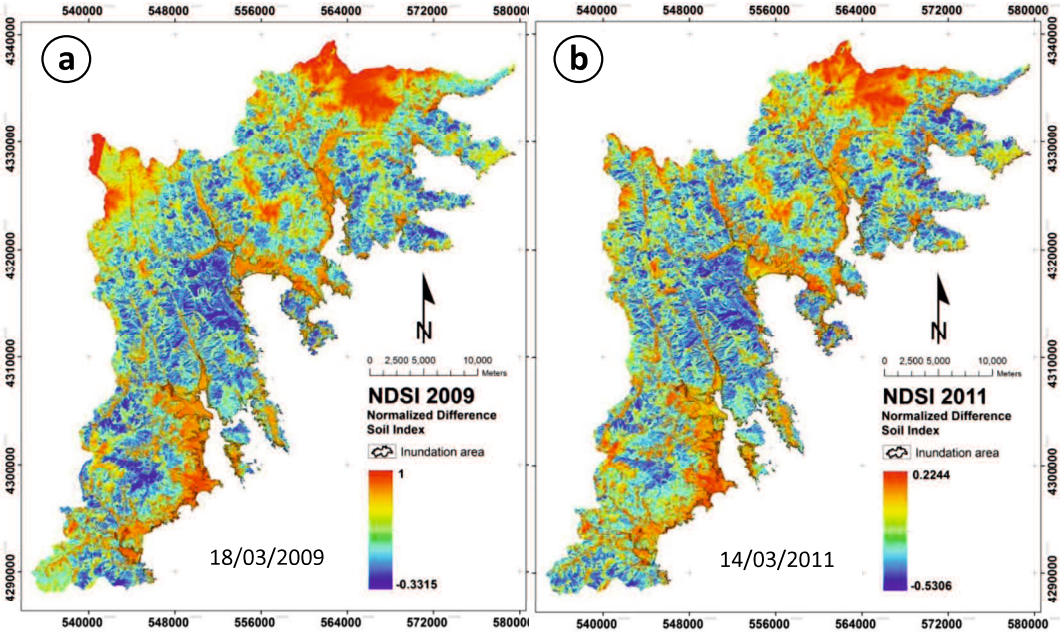

Figure 8.6 Computed NDSI; (a) before-tsunami event; and (b) after-tsunami event using ALOS AVNIR-2

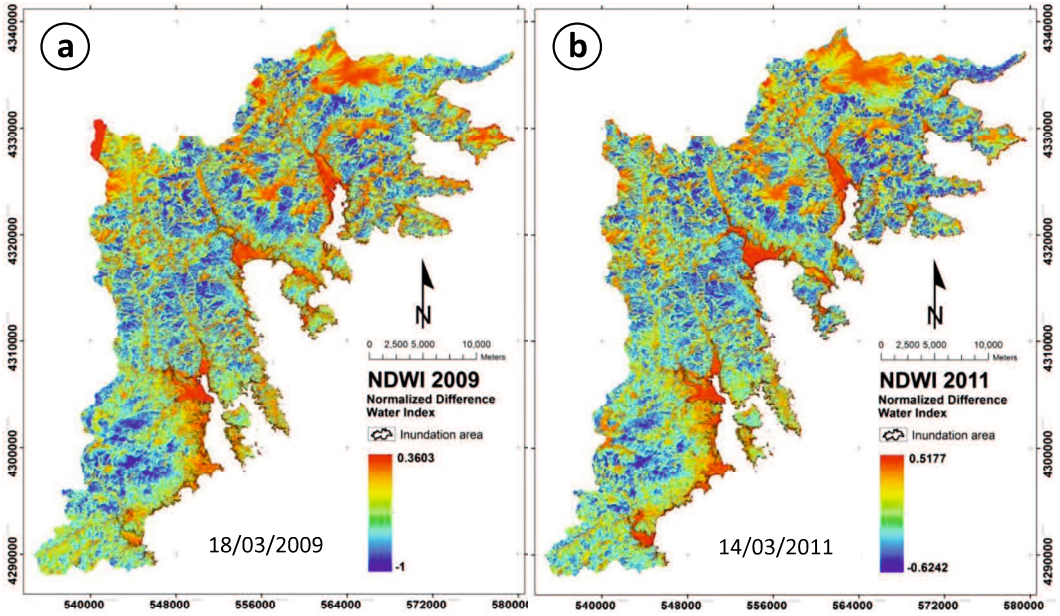

Figure 8.7 Computed NDWI; (a) before-tsunami event; and (b) after-tsunami event using ALOS AVNIR-2

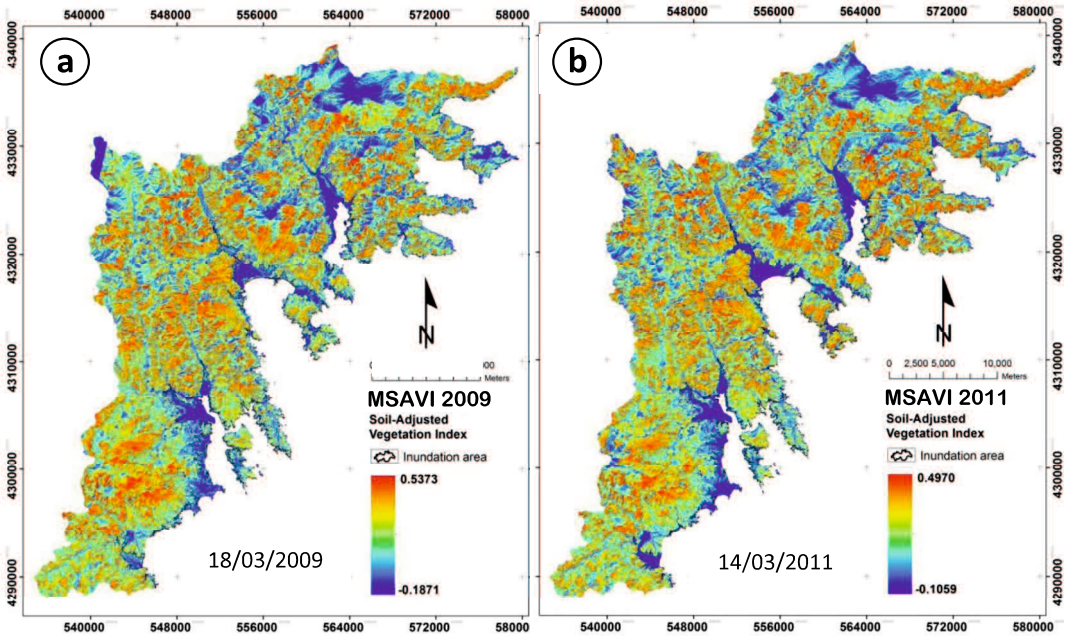

Figure 8.8 Computed MSAVI; (a) before-tsunami event; and (b) after-tsunami event using ALOS AVNIR-2

The cumulative frequency distributions of NDVI, NDSI, NDWI, and MSAVI in the inundated areas and non inundated areas are shown in **Figure 8.9**. Each graph shows clear differences of index distributions between two plots that indicate

inundated and non-inundated areas. The values between 20 and 80 percent in cumulative frequency distributions are connected by a straight line, in which the intersection between its extensions from the 0 percent line to the 100 percent line is assumed as range value of inundated areas. These ranges are listed in **Table 8.1**. By using before-after images, the pixels which have all of the indices in these ranges are identified as inundated areas in tsunami damage detection.

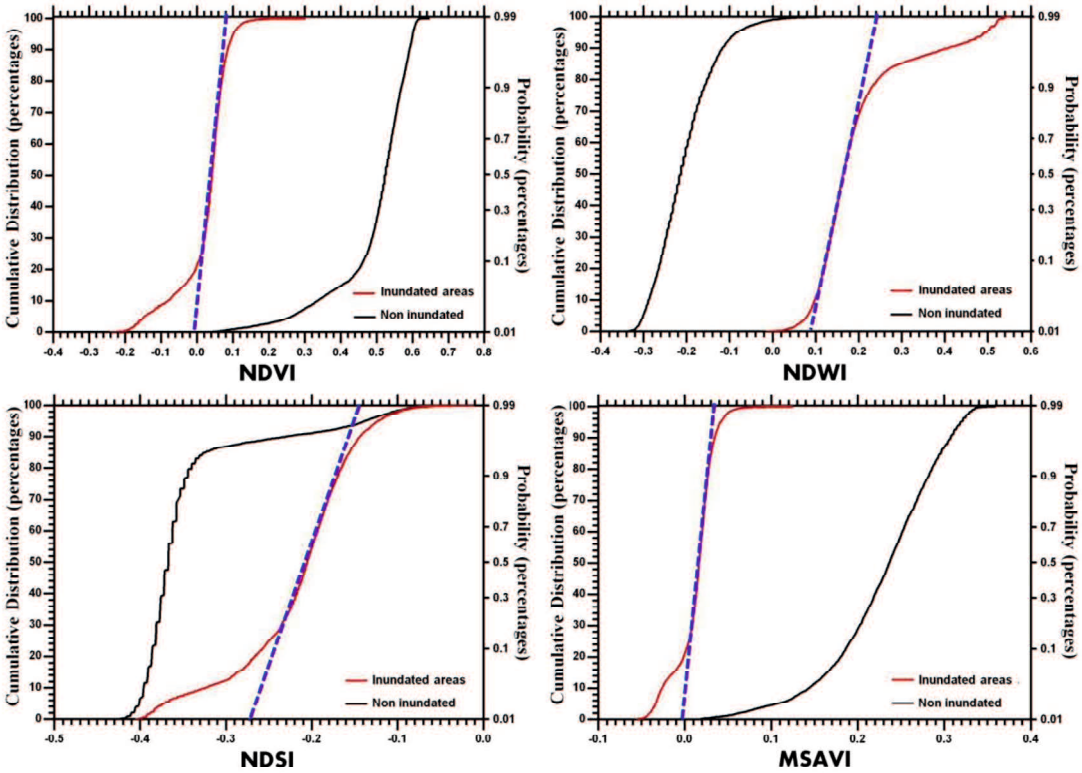

Figure 8.9 Cumulative frequency distribution of NDVI, NDWI, NDSI, and MSAVI (analysis from before-after images)

Table 8.1 Range value that the indices have in the inundated areas and non inundated areas

	Inundated area		*Non-inundated (others)*	
	Min	***Max***	***Min***	***Max***
NDVI	0.12	-0.08	0.45	0.5
NDWI	0.24	0.08	-0.3	-0.1
NDSI	-0.16	-0.125	-0.4	-0.35
MSAVI	0.0	0.03	0.312	0.225

Moreover, to know the average concentration value of NDVI, NDWI, and NDSI for before and after-tsunami event, a difference vs average; Bland-Altman graph was created. The average value of NDVI is 0.05 − 0.08 with the different tend

to the negative value, while NDWI is 0.09 – 0.1, and NDSI is (-)0,15 – (-)0.18. This graphic is shown in **Figure 8.10(b)**, while the survey inundation point is mapped in **Figure 8.10(a)**.

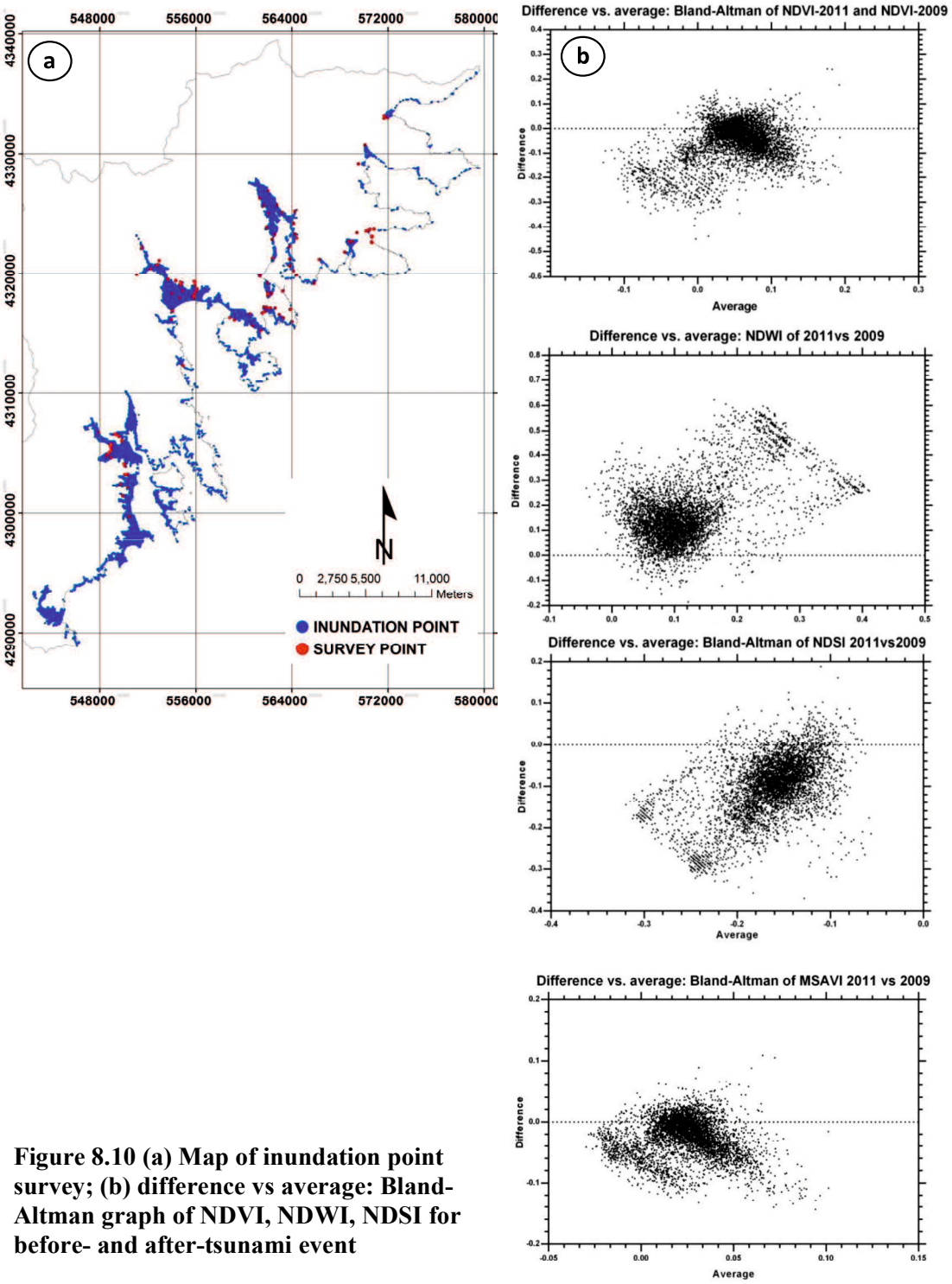

Figure 8.10 (a) Map of inundation point survey; (b) difference vs average: Bland-Altman graph of NDVI, NDWI, NDSI for before- and after-tsunami event

Yamazaki et al. (2006), states that the variation of the indices depending on the season, and the initial vegetation distribution should be considered and corrected. Moreover, water index and soil index might be influenced by the weather condition and the time passage after the tsunami. Because it has to be ensured that indices give clear difference between inundated areas and non-inundated areas, then the analysis of indices difference between before and after-event images as the indicators of tsunami damage could be given a better result. Tsunami caused vegetation to be removed, soil to be exposed, and water to exist in the soil. These are corresponding to the decreasing of NDVI, and increasing of NDSI and NDWI after the tsunami. Therefore, it might be possible to identify the pixels where all the indices have changed significantly in the inundated areas due to tsunami.

Pixels in the before image where indicate NDVI and MSAVI are high enough to specify the existence of vegetation were extracted and used for the subsequent operations. For this case, pixels with NDVI and MSAVI value less than 20 percentile of its cumulative frequency distribution in the inundated areas based on the before-event data were excluded. The pixels more than 0.125 wer used in the calculation to compare the different between before and after-event data. Moreover, for the value of NDSI and NDWI, only the pixels where the indices are less than 80 percentile of their cumulative frequency distributions from the before-event data were extracted. In this case, the thresholds for analyzing the difference indices of two event, before and after-tsunami, were more than 0.125 for vegetation index, more than 0.06 for soil-adjusted vegetation index, less than 0.12 for water index, and less than -0.075 for soil index (see **Figure 8.11**). These indices need to be corrected by the time factors, in which derived from the average differences of the indices from before and after-event in the non-inundated area as shown in **Table 8.2**.

Table 8.2 Average of each index for the non-inundated areas and its differences between before and after data

	Non-inundated area		
	Before	***After***	***Difference***
NDVI	0.3289	0.4785	-0.1496
NDWI	-0.0617	-0.1744	0.1127
NDSI	-0.2338	-0.3436	0.1098
MSAVI	0.1465	0.2140	-0.0675

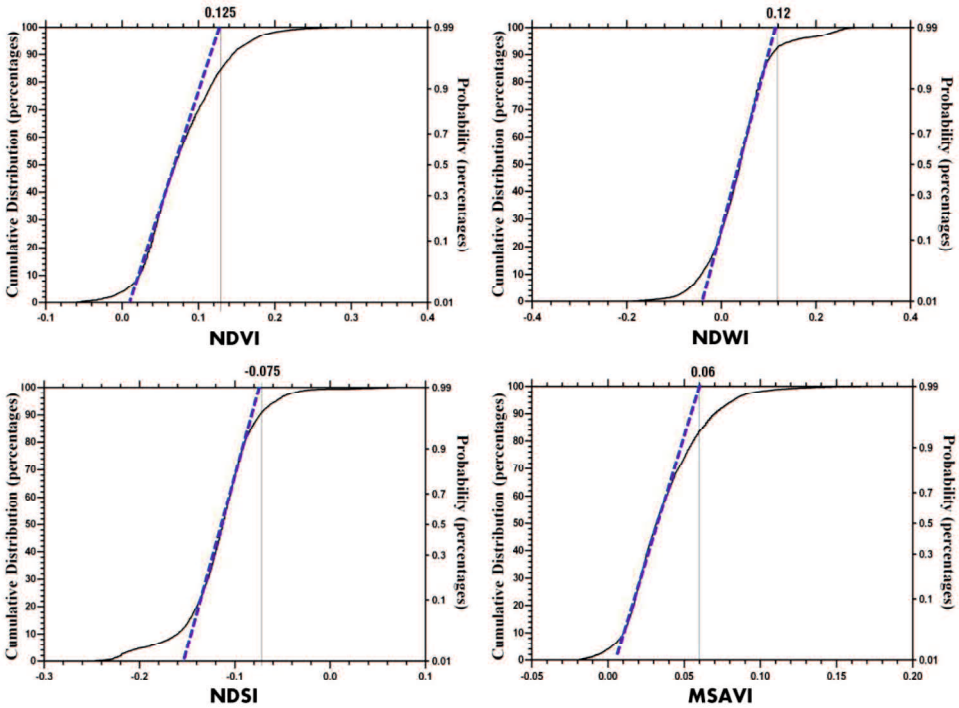

Figure 8.11 Thresholds of the indices to determine the target pixels for differences computation between before and after-event data

The distribution of difference for vegetation, water, soil indices in the inundated and non-inundated areas was determined by using the difference data of before and after-images. These ranges are plotted in **Figure 8.12** and **Table 8.3**.

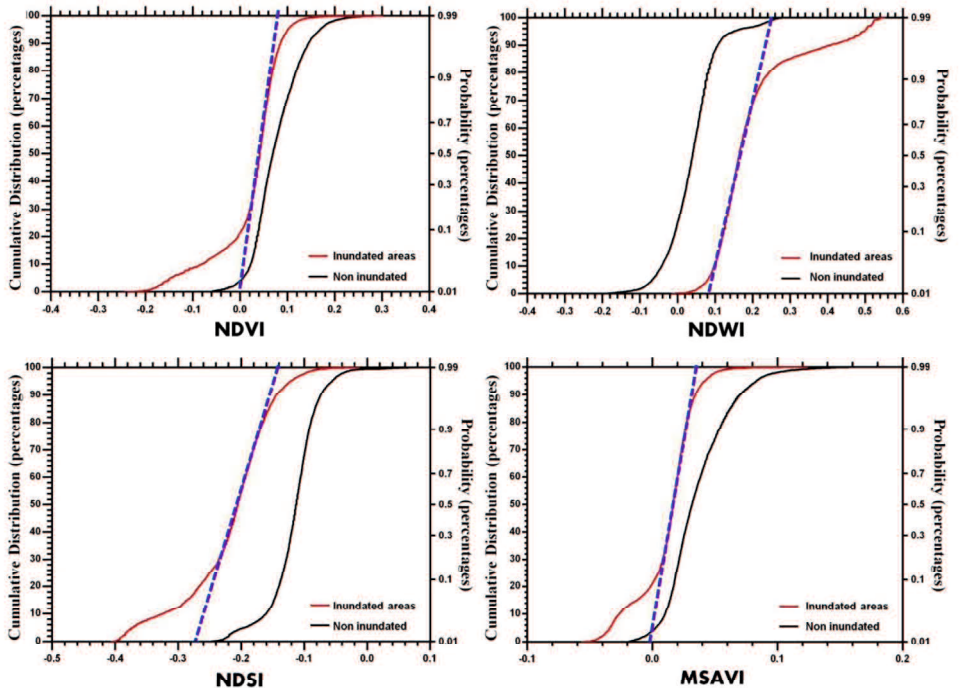

Figure 8.12 Cumulative frequency distributions of the differences of the indices

Table 8.3 Range value that the indices have in the inundated and non inundated areas

	Inundated area		*Non-inundated*	
	Min	***Max***	***Min***	***Max***
NDVI	0.00	0.075	0.0	0.15
NDWI	0.075	0.25	-0.025	0.1
NDSI	-0.237	-0.137	-0.15	-0.075
MSAVI	0.012	0.037	0.012	0.062

Visually extracted tsunami run-up boundary was used as the truth data. But for the case with no truth data, digital elevation models, topographic condition, and the distance from the coast line should be employed to obtain an accurate tsunami inundation map (Yamazaki and Matsuoka, 2007).

8.3 Comparison of Calculated Parameter

Figure 8.13 and **Figure 8.14** describe the map of each calculated parameter in the inundated area and followed by its histogram distribution. The number of pixels in the inundated area was 476,745, in which describe that the NDVI range of in the inundated areas was -0.351 – 0.640, with the mean of 0.113. The mean of NDWI, NDSI, and MSAVI in inundated areas were 0.103, -0.214, and 0.052. The pattern of both NDVI and MSAVI in the inundated area showed similar, where the values were low. In contrast, NDWI and NDSI values in the inundated area mostly spread from medium to high.

Skewness quantifies how symmetrical the distribution is. A symmetrical distribution has a skewness of zero. An asymmetrical distribution with a long tail to the right (higher values) has a positive skew. An asymmetrical distribution with a long tail to the left (lower values) has a negative skew. If the skewness is greater than 1.0 (or less than -1.0), the skewness is substantial and the distribution is far from symmetrical. If skewness is between -1 and -0.5 or between 0.5 and 1, the distribution is moderately skewed. If skewness is between -0.5 and 0.5, the distribution is approximately symmetric. Moreover, kurtosis quantifies whether the shape of the data distribution matches the Gaussian distribution.

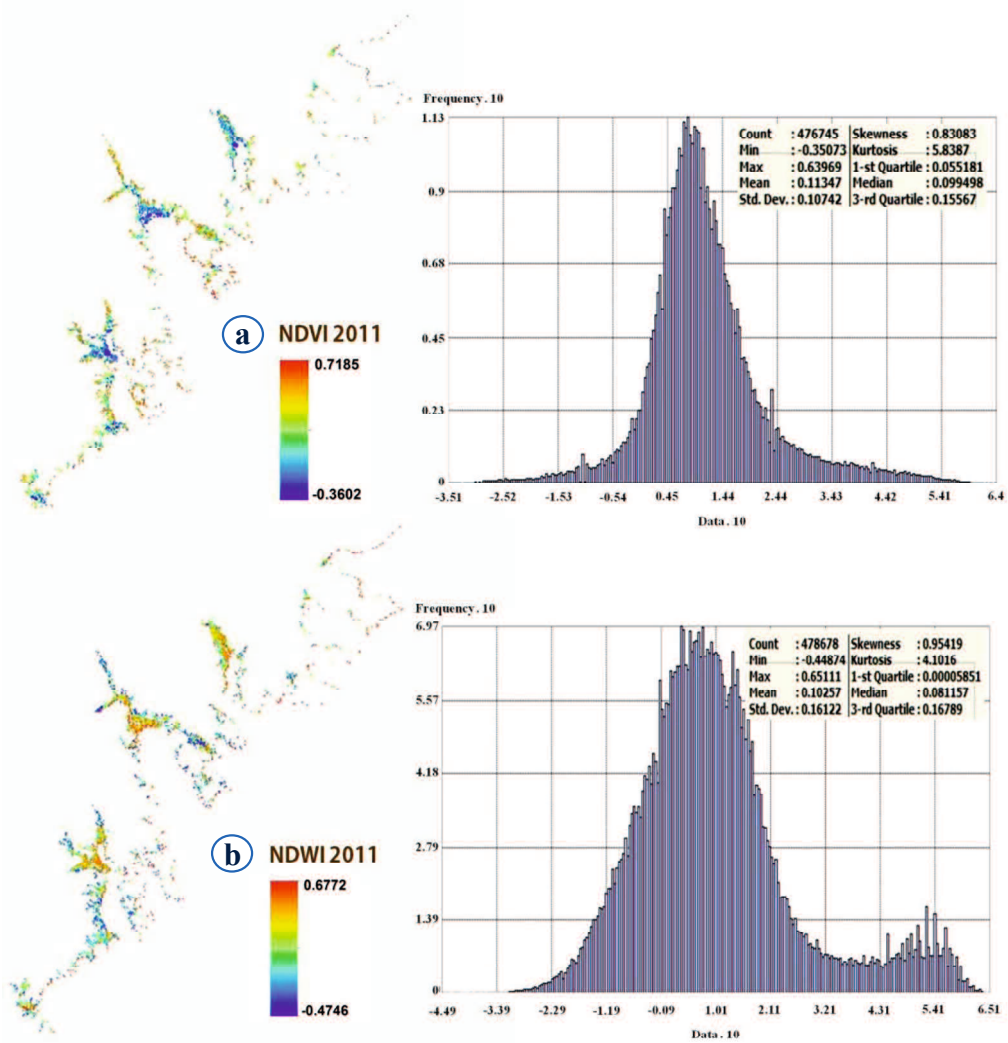

Figure 8.13 (a) NDVI and (b) NDWI value in inundation areas

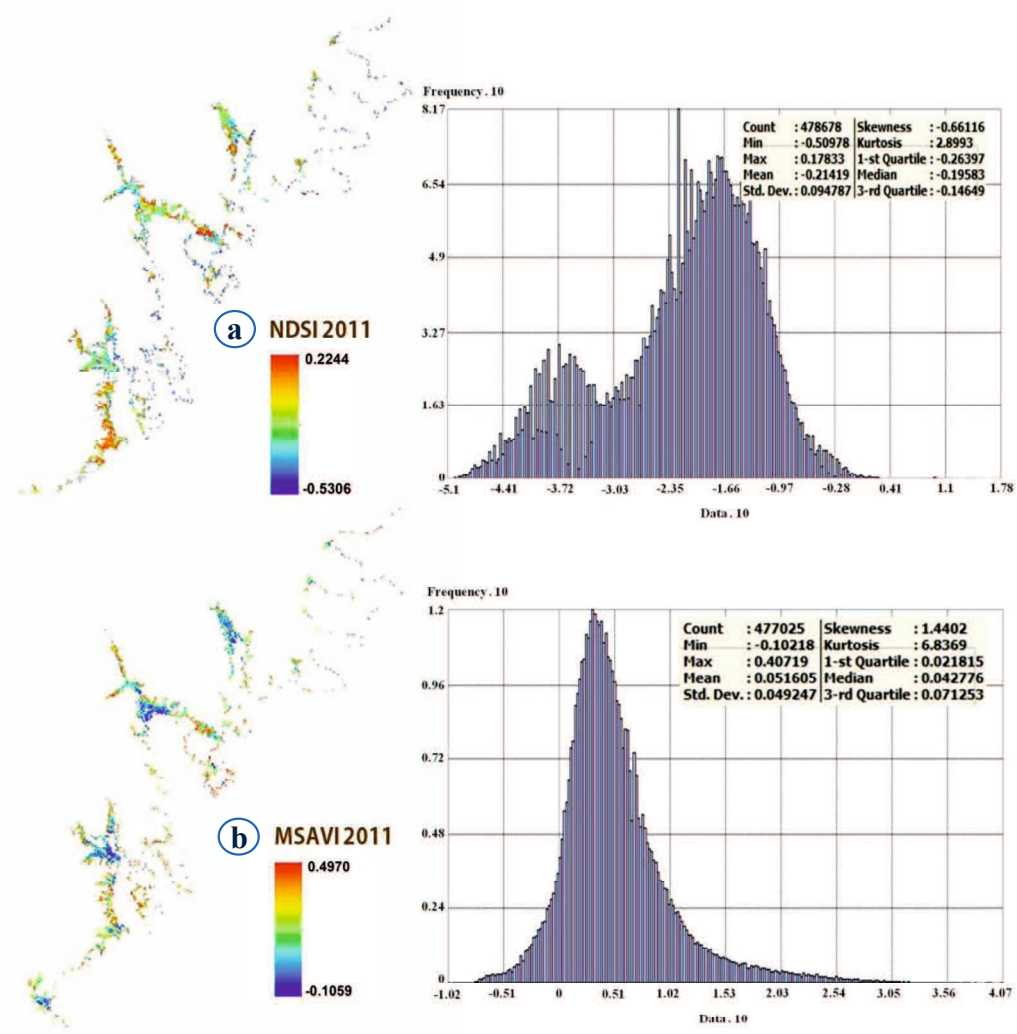

Figure 8.14 (a) NDSI and (b) MSAVI value in inundation areas

In terms of statistical approach, a multiple comparison of each parameter was calculated. The analysis shows that there was a significant different between each calculated parameter in inundated and non-inundated areas. **Table 8.4** describes statistics summary for all indices in inundated and non-inundated areas using after-tsunami data, and **Tabel 8.5** describes multiple comparison of vegetation index, water index, and soil index in inundated and non-inundated areas, while **Table 8.6** describes kolmogorov-Smirnov test of vegetation index, water index, and soil index in inundated and non-inundated areas. It shows that based on the after-event data there is a significant different between NDVI value in inundated and non-inundated areas. This also similar to the NDWI, NDSI, and MSAVI.

Table 8.4 Statistics summary for all indices using after-tsunami data in inundated and non-inundated areas

	NDVI-after Inundated area	NDVI-after Non-inundated area	NDWI-after Inundated area	NDWI-after Non-inundated area	NDSI-after Inundated area	NDSI-after Non-inundated area	MSAVI-after Inundated area	MSAVI-after Non-inundated area
Minimum	-0.3224	0.1072	0.0549	-0.3085	-0.3618	-0.4102	-0.0757	0.0403
25% Percentile	-0.1313	0.4316	0.1283	-0.2363	-0.2678	-0.3825	-0.031	0.185
Median	0.02695	0.487	0.1668	-0.194	-0.2063	-0.369	0.01085	0.2147
75% Percentile	0.0568	0.5465	0.3049	-0.1412	-0.1691	-0.3261	0.02145	0.2651
Maximum	0.1329	0.602	0.5595	0.0413	-0.1005	-0.1184	0.0368	0.3497
20% Percentile	-0.194	0.407	0.119	-0.2468	-0.2876	-0.3861	-0.05094	0.1639
80% Percentile	0.0579	0.5571	0.4117	-0.1211	-0.162	-0.3036	0.0231	0.2754
Mean	-0.04324	0.4696	0.2365	-0.1814	-0.2226	-0.3368	-0.00577	0.215
Std. Deviation	0.1321	0.1111	0.15	0.07867	0.06336	0.07752	0.03518	0.06108
Std. Error of Mean	0.01868	0.01571	0.02121	0.01113	0.008961	0.01096	0.004975	0.008638
Lower 95% CI of mean	-0.08078	0.4383	0.1938	-0.2038	-0.2406	-0.3588	-0.01576	0.1976
Upper 95% CI of mean	-0.00569	0.5014	0.2791	-0.1591	-0.2046	-0.3148	0.004231	0.2323
D'Agostino & Pearson omnibus normality test								
K2	8.18	22.7	8.254	5.115	3.762	21.3	8.086	3.502
P value	0.0167	< 0.0001	0.0161	0.0775	0.1524	< 0.0001	0.0175	0.1736
Passed normality test (alpha=0.05)?	No	No	No	Yes	Yes	No	No	Yes
P value summary	*	****	*	ns	ns	****	*	ns
Shapiro-Wilk normality test								
W	0.8298	0.8551	0.8323	0.9565	0.9545	0.7537	0.8459	0.9748
P value	< 0.0001	< 0.0001	< 0.0001	0.0637	0.0524	< 0.0001	< 0.0001	0.3576
Passed normality test (alpha=0.05)?	No	No	No	Yes	Yes	No	No	Yes
P value summary	****	****	****	ns	ns	****	****	ns
Coefficient of variation	305.54%	23.64%	63.44%	43.36%	28.46%	23.02%	610.06%	28.41%
Skewness	-0.8531	-1.599	1.041	0.7445	-0.4163	1.693	-0.8427	-0.4953
Kurtosis	-0.7646	2.916	-0.2666	0.3133	-0.7499	1.919	-0.7674	0.6912
Sum	-2.162	23.49	11.82	-9.071	-11.13	-16.84	-0.2883	10.75

Table 8.5 Multiple comparison of vegetation index, water index, and soil index in inundated and non-inundated areas

Dunn's Multiple Comparisons Test			Rank Sum Diff.	Significant	Summary
NDVI-afected	vs.	NDVI-non afected	-185	Yes	****
NDVI-afected	vs.	NDWI-afected	-120	Yes	****
NDVI-afected	vs.	NDWI-nonafected	66	No	ns
NDVI-afected	vs.	NDSI-afected	87	Yes	*
NDVI-afected	vs.	NDSI-nonafected	141	Yes	****
NDVI-afected	vs.	MSAVI-afected	-9	No	ns
NDVI-afected	vs.	MSAVI-nonafected	-124	Yes	****
NDVI-non afected	vs.	NDWI-afected	65	No	ns
NDVI-non afected	vs.	NDWI-nonafected	251	Yes	****
NDVI-non afected	vs.	NDSI-afected	272	Yes	****
NDVI-non afected	vs.	NDSI-nonafected	326	Yes	****
NDVI-non afected	vs.	MSAVI-afected	176	Yes	****
NDVI-non afected	vs.	MSAVI-nonafected	61	No	ns
NDWI-afected	vs.	NDWI-nonafected	186	Yes	****
NDWI-afected	vs.	NDSI-afected	207	Yes	****
NDWI-afected	vs.	NDSI-nonafected	261	Yes	****
NDWI-afected	vs.	MSAVI-afected	111	Yes	***
NDWI-afected	vs.	MSAVI-nonafected	-4	No	ns
NDWI-nonafected	vs.	NDSI-afected	21	No	ns
NDWI-nonafected	vs.	NDSI-nonafected	75	No	ns
NDWI-nonafected	vs.	MSAVI-afected	-75	No	ns
NDWI-nonafected	vs.	MSAVI-nonafected	-190	Yes	****
NDSI-afected	vs.	NDSI-nonafected	54	No	ns
NDSI-afected	vs.	MSAVI-afected	-96	Yes	**
NDSI-afected	vs.	MSAVI-nonafected	-211	Yes	****
NDSI-nonafected	vs.	MSAVI-afected	-150	Yes	****
NDSI-nonafected	vs.	MSAVI-nonafected	-265	Yes	****
MSAVI-afected	vs.	MSAVI-nonafected	-115	Yes	****

Table 8.6 Kolmogorov-Smirnov test of vegetation index, water index, and soil index from after-tsunami data in inundated and non-inundated areas

t-test NDVI	
NDVI-after Inundated area	
vs.	
NDVI-after Non-inundated area	
Kolmogorov-Smirnov test	
P value	< 0.0001
Exact or approximate P value?	Approximate
P value summary	****
Significantly different? (P < 0.05)	Yes
Kolmogorov-Smirnov D	0.98
Mann Whitney test	
P value	< 0.0001
Exact or approximate P value?	Exact
P value summary	****
Significantly different? (P < 0.05)	Yes
One- or two-tailed P value?	Two-tailed
Sum of ranks in column A,B	1277 , 3773
Mann-Whitney U	2
Difference between medians	
Median of column A	0.02695, n=50
Median of column B	0.4870, n=50
Difference: Actual	0.46
Difference: Hodges-Lehmann	0.4939

t-test NDSI	
NDSI-after Inundated area	
vs.	
NDSI-after Non-inundated area	
Kolmogorov-Smirnov test	
P value	< 0.0001
Exact or approximate P value?	Approximate
P value summary	****
Significantly different? (P < 0.05)	Yes
Kolmogorov-Smirnov D	0.72
Mann Whitney test	
P value	< 0.0001
Exact or approximate P value?	Exact
P value summary	****
Significantly different? (P < 0.05)	Yes
One- or two-tailed P value?	Two-tailed
Sum of ranks in column E,F	3446 , 1604
Mann-Whitney U	329
Difference between medians	
Median of column E	-0.2063, n=50
Median of column F	-0.3690, n=50
Difference: Actual	-0.1628
Difference: Hodges-Lehmann	-0.1328

t-test NDWI	
NDWI-after Inundated area	
vs.	
NDWI-after Non-inundated area	
Kolmogorov-Smirnov test	
P value	< 0.0001
Exact or approximate P value?	Approximate
P value summary	****
Significantly different? (P < 0.05)	Yes
Kolmogorov-Smirnov D	1
Mann Whitney test	
P value	< 0.0001
Exact or approximate P value?	Exact
P value summary	****
Significantly different? (P < 0.05)	Yes
One- or two-tailed P value?	Two-tailed
Sum of ranks in column C,D	3775 , 1275
Mann-Whitney U	0
Difference between medians	
Median of column C	0.1668, n=50
Median of column D	-0.1940, n=50
Difference: Actual	-0.3608
Difference: Hodges-Lehmann	-0.3825

t-test MSAVI	
MSAVI-after Inundated area	
vs.	
MSAVI-after Non-inundated area	
Kolmogorov-Smirnov test	
P value	< 0.0001
Exact or approximate P value?	Approximate
P value summary	****
Significantly different? (P < 0.05)	Yes
Kolmogorov-Smirnov D	1
Mann Whitney test	
P value	< 0.0001
Exact or approximate P value?	Exact
P value summary	****
Significantly different? (P < 0.05)	Yes
One- or two-tailed P value?	Two-tailed
Sum of ranks in column G,H	1275 , 3775
Mann-Whitney U	0
Difference between medians	
Median of column G	0.01085, n=50
Median of column H	0.2147, n=50
Difference: Actual	0.2038
Difference: Hodges-Lehmann	0.2191

8.4 Conclusions

The analysis is focus in on the land change due to tsunami event. The change was observed using the indicator of vegetation value, water value, and soil value where calculated using the algorithm of NDVI, NDWI, NDSI, and MSAVI for the before and after-tsunami event. The analysis shows that the tsunami caused the decrease of NDVI and the increase of NDSI and NDWI. The ranges which the

indices in the tsunami-inundated areas would have were calculated using only the after-event image. It is considered that the pixels which have all of the indices in these ranges could be identified as tsunami inundation areas (in tsunami damage detection using only the after-event image). The study showed the possibility use of the vegetation index, water index, soil index and soil-adjusted vegetation index for observing the area that could be affected by tsunami disaster. This could be the fundamental analysis towards tsunami damage detection techniques using moderate-resolution satellite imagery.

CHAPTER 9

Conclusions

Natural hazards are natural phenomena whose occurrence is almost impossible to reduce. We only can minimize the impact of these events by performing counter measures such as an initial assessment in order to map the vulnerable areas, and so forth. The development of remote sensing technology and its applications including Geographical Information System (GIS) application enable the use of satellite imagery for mapping the distribution of an area damaged by a disaster and to assess vulnerable areas. Satellite images have the advantage of being able to deliver simultaneous images of large areas. Disaster mitigation and reconstruction plan due to tsunami can be implemented with various actions. An integration of spatial analysis through GIS application and multi-criteria analysis through Analytical Hierarchy Process (AHP) is one of the methods for tsunami inundation and impact assessment. Moreover, Spatial data analysis via spatial multi-criteria analysis helps prioritize the decision-making process using geo-reference data to manage different spatial information and combine them for better decision making.

This research is dealing with vulnerability mapping due to tsunami hazards in which remote sensing approach was applied in order to prepare the entire data. The analysis was carried out using spatial multi-criteria analysis through AHP and GIS work. The main target of this study is vulnerability mapping, and analysis of satellite images to assess the impact of tsunami hazards. The research aimed to apply a method that is easy, user-friendly, and flexible enough to be replicable. A suitable set of parameters can be applied to obtain a result that is close enough to that of a real event. This study used raster geo-database to solve multi-criteria data, and AHP approach was applied to determine the order of importance of the parameters.

The research try to develop an integrative remote sensing and GIS approach in vulnerability assessment to tsunami hazard, to develop a methods for vulnerability assessment using integration of spatial data and AHP in a concept of spatial data modeling, to recognize potentially affected area by tsunami hazard, and to develop a new concept and method for extracting the required information from satellite

images for the purpose of vulnerability analysis to tsunami hazard. All study cases are in Japan, both Miyagi and Iwate Prefecture.

It can be concluded that the research questions in Chapter 1, Sub 1.4 have been answered and the research objectives were achieved. Further details of these achievements are concluded below;

9.1 Data Collection

Appropriate input parameters were derived from Digital Elevation Model (DEM) data, satellite remote sensing and field data, and were analyzed through GIS to create tsunami vulnerability map. DEMs data were collected from SRTM V.3 and V.4 from CGIAR-CSI, ASER GDEM V.2 from both The United States Geological Survey (USGS) and Japan Space System (J-spacesystems), and GSI DEM from Geospatial Information Authority of Japan. Moreover ALOS AVNIR-2 in two different time acquisitions were used, images before and after tsunami event in Japan provided by JAXA Japan. These parameters include elevation, slope, coastal proximity, water accumulation, vegetation density, and land use. The research introduced an entirely new set of attributes that are known to affect the tsunami vulnerability, those related to hydrogy analysis and the use of NDVI value in image classification.

9.2 DEM Comparison for Tsunami Vulnerability Mapping

In the analysis of DEM data comparison, some DEM data from different product have been analyzed. This work showed that the difference was not significant although SRTM V.4 predicted tsunami inundation area was most close to the real event. An interpolation of elevation points derived from Geospatial Information Authority of Japan (GSI) made the availability of the high spatial resolution of elevation data compared with DEM data which has low spatial resolution.

9.3 Vulnerability Mapping

In this stage, this study answered to the objectives of the research; to develop an integrative remote sensing and GIS approach in vulnerability assessment to

tsunami hazard, to develop a method for vulnerability assessment using integration of spatial data and AHP in a concept of spatial data modeling, and to recognize potentially affected area by tsunami hazard.

In the work of tsunami vulnerability, the AHP shows that a parameter of elevation is more important than other input parameters. Moreover, beside the use of NDVI in determining vegetation density map, SAVI and MSAVI calculation also gave an important result to provide a vegetation observation. A weighted raster overlay that applied in the spatial multi-criteria analysis helped in determining the vulnerability area. A combination of AHP result and weighed raster overlay give another chance in data mining related to the spatial multi-criteria analysis. By analyzing the vulnerability map and the historical data of tsunami event, including observation data, the prediction of inundated areas could be generated. This predicted inundation map showed the area similar to the real event of tsunami. In the Kesennuma area, the result showed close to the actual tsunami inundation event. The difference resulted in some areas because of the application of hydrological analysis as one of the input parameters in spatial multi-criteria analysis and weighed raster overlay in which the object of river or water canal was used as one of the input parameters and showed that the effect of the tsunami wave could reach more to the hinterland via this canal. It means that the affected areas that were produce from this work would be a little larger than actual event.

9.4 Satellite Image Analysis

In this stage, this study answered to the objective of the research; to recognize potentially affected area by tsunami hazard from satellite images. In the analysis of ALOS AVNIR-2 data, an index of vegetation, soil, and water were calculated to predict the impact of the tsunami disaster. Satellite images before- and after-tsunami event were applied. The study showed that there was a significant difference of vegetation index, water index and soil index in before- and after-tsunami event in the inundated area. The analysis showed that the index of vegetation (NDVI) decrease in the after-tsunami satellite image, while soil and water index increase in the area that affected by tsunami. This area is predicted as inundated area due to tsunami.

Acknowledgements

I would like to express my sincere gratitude to my supervisor Prof. Fusanori Miura for the continuous support of my doctoral study, for his patience, motivation, and immense knowledge.

I would like to thank the rest of my dissertation committee: Prof. Norikazu Shimizu, Prof. Toshihiko Aso, Prof. Hideaki Nakamura, and Assoc. Prof. Koji Asai, for their encouragement and insightful comments.

My sincere thanks also goes to Dr. Maria Papathoma, Nathan J. Wood, Ph.D. Dr. Dall'Osso, and Dr. JC Gaillard, for their expertise, comments, and great publications.

I recognize that this research would not have been possible without the financial assistance of Indonesia Directorate General of Higher Education, support of Brawijaya University Indonesia, Disaster Prevention System Laboratory of Yamaguchi University Japan, the 2011 Tohoku earthquake tsunami joint survey team, city office of Kesennuma, Rikuzentakata, and Ofunato, Geospatial Information Authority of Japan (GSI), the Japan Aerospace Exploration Agency (JAXA), and I express my gratitude to those agencies.

I thank my fellow laboratory mates in Disaster Prevention System Laboratory of Yamaguchi University Japan and I offer my regards to all of those who supported me in any respect.

I heartily dedicate to my parent, my wife, my lovely son, and all my family.

REFERENCES

Abe, K., 1986. Tsunami propagation in rivers of the Japanese Islands, *Continental Shelf Research,* Vol. 5 No. 6, 665-677.

Abella, E., A., C., 2008. Multi-scale Landslide Risk Assessment in Cuba. ITC The Netherlands.

Alexander, D, 2000. Confronting Catastrophe, Terra Publishing, 282 pp.

Araujo L. S., Joao Roberto dos Santos and Yosio Edemir Shimabukuro, 2000. Relationship Between SAVI and Biomass Data of Forest and Savanna Contact Zone and the Brazilian Amazonia, *International Archives of Photogrammetry and Remote Sensing, XXXIII, Part B7*, Amsterdam, 2000, pp 77-81.

Atillah, A., El Hadani, D., Moudni, H., Lesne, O., Renou, C., Mangin, A. and Rouffi, F., 2011. Tsunami vulnerability and damage assessment in the coastal area of Rabat and Sal´e, Morocco, *Nat. Hazards Earth Syst. Sci*., Vol. 11, 3397–3414.

Bana e Costa, C. A., Da Silva, P. A. and Correia, F. N., 2011. Multicriteria Evaluation of Flood Control Measures: The case of Ribeira do Livramento, *Water Resour. Manag.*, Vol. 18, 263–283.

Beccari, B., 2009. NSW State Emergency Service Measurements and Impacts of the Chilean Tsunami of May 1960 in New South Wales, Australia, Report by NSW SES, State Headquarters.

Belward, A.S., Stibig, H.J., Eva, H., Rembold, F., Bucha, T., Hartley, A., Beuchle, R., Khudhairy, D., Michielon, M., and Mollicone, D., 2007. Mapping Severe Damage to Land Cover Following the 2004 Indian Ocean Tsunami using Moderate Spatial Resolution Satellite Imagery, International Journal of Remote Sensing, 28 (13), 2977 - 2994.

Birkmann, J., 2005. Danger need not spell disaster – But how vulnerable are we? Research Brief of the United Nations University, United Nations University. No. 1/2005,.

Bogardi, J., and Birkmann, J., 2004. Vulnerability Assessment: the first step towards sustainable risk reduction. Disasters and Society - From hazard assessment to risk reduction. D. Malzahn and T. Plapp. Berlin, Logos Verlag: 75-82.

Blaikie, P., 1994. At risk : natural hazards, people's vulnerability and disasters. London etc., Routledge.

Bollin, C., Cardenas, C., Hahn, H., and Vasta, K., S., 2003. Disaster Risk Management by Communities and Local Governments, Inter-American Development

Bank, Washinton, DC.. http://www.iadb.org/sds/doc/GTZ%2DStudyFinal.pdf.

Bouvet M., Chander, G., Goryl, P., Santer R., and Saunier, 2007. Preliminary Radiometric Calibration Assessment of ALOS AVNIR-2, *Geoscience and Remote Sensing Symposium, IGARSS,* Barcelona, 2007, pp. 2673-2676.

Bretschneider C., L., and Wybro P.G., 1976, Tsunami inundation prediction. *Proceedings of the 15th ASCE Conference on Coastal Engineering*, Honolulu, Hawaii, 11-17 July 1976, pp. 1006-1024.

Cardona, O., D., 1999. Environmental Management and Disaster Prevention: Two Related topics: A Holistic Risk Assessment and management Approach, in: J.Ingleton, ed., Natural Disaster Management, London: Tudor Rose.

Carver, S., J., 1991. "Integrating multi-criteria evaluation with geographical information systems", *International Journal of Geographical Information Systems,* Vol. 5 No. 3, pp. 321-339. http://dx.doi.org/10.1080/02693799108927858.

Cees van Westen and Kingma, N., 2009. Guide book Session 5: Vulnerability assessment. ITC The Netherlands.

Chander G., and Markham, B., 2003. Revised Landsat-5 TM Radiometric Calibration Procedures and Post Calibration Dynamic Ranges, *IEEE Transactions on Geoscience and Remote Sensing*, Vol. 41, No. 11, 2003, pp. 2674-2677. http://dx.doi.org/10.1109/TGRS.2003.818464.

Chatenoux B., and Peduzzi P., 2007. Impacts from the 2004 Indian Ocean Tsunami: Analysing the Potential Protecting Role of Environmental Features. Natural Hazards, 40, 289–304.

Dall'Osso, F., Gonella, M., Gabbianelli, G., Withycombe, G., and Dominey-Howes, D., 2009. A revised (PTVA) model for assessing the vulnerability of buildings to tsunami damage, *Nat. Hazards Earth Syst. Sci.*, vol. 9, pp. 1557−1565, doi:10.5194/nhess-9-1557-2009.

Dall'Osso, F., Bovio, L., Cavalletti, A., Immordino, F., Gonella, M., and Gabbianelli, G., 2010. A novel approach (the CRATER method) for assessing tsunamivulnerability at the regional scale using ASTER imagery, *Italian Journal of Remote Sensing*, vol. 42, no. 2, pp. 55−74.

Deichmann U., Ehrlich D., Small C., and Zeug G., 2011. Using high resolution satellite data for the identification of urban natural disaster risk. Global Facility for Disaster Reduction and Recovery, Washington, DC.

Despini F., Teggi S., Bovio L., and Immordino F., 2009. Applications of Terra MODIS data for Iraq marshland monitoring, *Proceedings of the SPIE Europe's International Symposium on Remote Sensing (ERS09)*, 31 August-3 September Berlin.

Disaster Information Management Division, 2012. The 2011 Tohoku Earthquake and Tsunami Map of Kesennuma, Disaster Information Management Division, Kesennuma, Japan.

Eastman, J. R., Jin, W., Kyem, P. A. K. and Toledano, J., 1995. Raster procedures for multi-criteria/multi-objective decisions, *Photogrammetric Engineering & Remote Sensing, American Society for Photorammetry and Remote Sensing,* Vol. 61 No. 5, pp. 539-547.

Eckert, S., Jelinek, R., Zeug, G. and Krausmann, E., 2012. Remote sensing-based assessment of tsunami vulnerability and risk in Alexandria, Egypt, *Applied Geography,* Vol. 32 No. 2, pp. 714-723.

EERI Special Earthquake Report, 2011. Learning from Earthquakes. The March 11, 2011, Great East Japan (Tohoku) Earthquake and Tsunami: Societal Dimensions.

Forman, E. H. and Selly, M. A., 2001. *Decision by Objectives: How to Convince Others That You Are Right,* World Scientific Publishing Company, Singapore.

Fraser S., I. Matsuo, G. S. Leonard and Murakami, H., 2011. Tsunami Evacuation: Lessons from the Great East Japan Earthquake and Tsunami of March 11th 2011, GNS Science Report 2012/17. Institute of Geological and Nuclear Sciences Limited, 2012.

Friedl M.A., and Brodley, C.E., 1997. Decision Tree Classification of Land Cover from Remotely Sensed Data. Remote Sensing of Environmental. 61: 399-409.

Geiß C., and Taubenbo¨ck, H., 2012. Remote sensing contributing to assess earthquake risk: from a literature review towards a roadmap. Nat Hazards (2013) 68:7–48. doi 10.1007/s11069-012-0322-2

Geospatial Information Authority of Japan (GSI), 2011a. Tsunami inundation area of the 2011 Japan Earthquake (Part 5), Geospatial Information Authority of Japan, available at: http://web.archive.org/web/20110623011856/http://www.gsi.go.jp/common/000059939.pdf (accessed 18 April 2011).

Geospatial Information Authority of Japan (GSI), 2011b. Tsunami inundation and land use area of the 2011 Japan Earthquake, Geospatial Information Authority of Japan, available at: http://www.gsi.go.jp/BOUSAI/h23_tohoku.html (accessed 12 March 2013).

Geospatial Authority of Japan (GSI), 2013. *Map of inundation area due to the 2011 Great East Japan Earthquake*, Map number 61, 62, 65, 66, 68, 69, 70, 71, available at www.gsi.go.jp/kikaku/kikaku40016.html., Accessed on 25 June 2013.

Gilles, N., 2012. How Far Could a Tsunami Penetrate Upriver?, Confluence, Winter, Vol. 1, Issue 1, Accessed 18 July 2013.

Gong, P., Pu, R., Biging, G., S., and Larrieu, M., R., 2003. Estimation of Forest Leaf Area Index Using Vegetation Indices Derived from Hyperion Hyperspectral Data, *IEEE Transactions on Geoscience and Remote Sensing*, Vol. 41, No. 6, 2003, pp. 1355-1362. http://dx.doi.org/10.1109/TGRS.2003.812910.

Gokon, H., and Koshimura, S., 2012. Mapping of building damage of the 2011 Tohoku earthquake tsunami in Miyagi Prefecture, *Coastal Engineering Journal, World Scientific Publishing Company and Japan Society of Civil Engineers,* Vol. 54 No. 1, pp. 12.

Guth P. L., 2010, Geomorphometric comparison of aster GDEM and SRTM, *A special joint symposium of ISPRS Technical Commission IV & AutoCarto in conjunction with ASPRS/CaGIS*, Fall Specialty Conference, November 15-19, 2010 Orlando, Florida.

Han, J., Kamper, 2011. Data Mining Concept and Techniques,, Morgan Kaufmann Publisher.

Jensen, J. R., 1996. *Introductory Digital Image Processing: A Remote Sensing Perspective* (Second edition). Prentice Hall, Inc., Upper Saddle River, New Jersey, USA.

Congalton, R. G., 1991. A review of assessing the accuracy of classifications of remotely sensed data. *Remote Sensing of Environment* 37:35-46.

Hansen, M., C., Defries, R., S., Townshend, J., R., G., and Sohlberg, R., 2000. Global land cover classification at 1km spatial resolution using a classification tree approach, *International Journal of Remote Sensing,* Vol. 21, 1331-1364. http://dx.doi.org/10.1080/014311600210209.

Henderson, F., M., and Lewis, A., J., 1998. Principles and applications of imaging radar, Manual of Remote Sensing, 2, John Wiley & Sons, Inc., New York.

Hirt C., Filmer, M., S., and Featherstone, W., E., 2010, Comparison and validation of the recent freely available ASTER-GDEM ver1, SRTM ver4.1 and GEODATA DEM-9S ver3 digital elevation models over Australia, *Australian Journal of Earth Sciences*, (57: 3) 337-347.

Horn, B., 1981. Hill shading and the reflectance map, *Proceedings of IEEE*, Vol. 69 No. 1, pp. 14-47. http://dx.doi.org/10.1109/PROC.1981.11918

Hsien, L., C., and Sheng, C., H., 2011. The use of spatial analysis techniques in mapping potential natural hazard areas: a case study of Taiwan, *Procedia*

Environmental Sciences, Vo. 10, Part B, pp. 1092-1097.

Https://earth.esa.int/c/document_library/get_file?folderId=19584&name=DLFE-262.pdf.

Http://earthquake.usgs.gov/earthquakes/shakemap.

Http://extremeplanet.me/2014/02/04/detailed-imagery-of-the-2011-japan-tsunami/comment-page-1.

Http://www.jaxa.jp/projects/sat/alos/index_e.html.

Http://www.jma.go.jp/jma/en/Activities/earthquake.html.

Http://www.jma.go.jp/jma/en/2011_Earthquake/Information_on_2011_Earthquake.html.

Http://www.satimagingcorp.com/satellite-sensors/alos.html.

Http://pubs.usgs.gov/circ/c1187/ (Tsunami generation).

Http://quake.abag.ca.gov/shaking/mmi/

Huete A., R., 1988. A Soil-Adjusted Vegetation Index (SAVI), *Remote Sensing of Environment*, Vol. 25, No. 3, 1988, pp. 295-309. http://dx.doi.org/10.1016/0034-4257(88)90106-X.

Huete, A., R., Hua, G., Qi, J., Chehbouni A., and Van Leeuwen, W., J., D., 1992. Normalization of Multidirectional Red and NIR Reflectances with the SAVI, *Remote Sensing of Environment*, Vol. 41, No. 2-3, 1992, pp. 143-154. http://dx.doi.org/10.1016/0034-4257(92)90074-T.

Iida, K., 1963. Magnitude, energy and generation mechanisms of tsunamis and a catalogue of earthquakes associated with tsunamis, *Proceeding of Tsunami Meeting at the 10th Pacific Science Congress*, pp. 7-18.

Iverson, L., R., and Prasad, A., M., 2007. Using Landscape Analysis to Assess and Model Tsunami Damage in Aceh Province, Sumatra. Landsc. Ecol., 22, 323–331.

Jarvis A., Reuter H., I., Nelson A., and Guevara E., 2008, Hole-filled seamless SRTM data V4, International Centre for Tropical Agriculture (CIAT), available from http://srtm.csi.cgiar.org.

Jackson, R., D., Slater, P., N., and Pinter, P., J., 1983. Discrimination of growth and water stress in wheat by various vegetation indices through clear and turbid atmospheres, *Remote Sensing of the Environment* 1983, Vol. 15,187-208. http://dx.doi.org/10.1016/0034-4257(83)90039-1.

Jensen J. R., 2000. Remote Sensing of the Environmental: An Earth Resources Perspective, Prentice Hall. New Jersey-USA.

Jankowski, P., 1995. Integrating geographic information systems and multiple criteria decision making methods, *International Journal of Geographic Information System,* Vol. 9 No. 3, pp. 251-273. http://dx.doi.org/10.1080/02693799508902036.

Karen E., Joyce, Kim C., Wright, Sergey V., Samsonov and Vincent G., Ambrosia, 2009. Remote Sensing and The Disaster Management Cycle, Advances in Geoscience and Remote Sensing, Gary Jedlovec (Ed.), ISBN:978-953-307-005-6, InTech Published.

Kawasaki, Koji, et al., 2011. Survey report on 2011 Tohoku, Japan, tsunami disaster, # I: Tsunami Damage.

King, R., S., and Julstrom, B., 1982, Applied Statistics Using the Computer, Sherman Oaks,CA: Alfred Pub. Co.

Koshimura, S., and Matsuoka, M., 2010. Detecting tsunami affected area using satellite SAR imagery, *Journal of Japan Society of Civil Engineers*, Ser. B2 (Coastal Engineering), 66(1), 1426–1430 (in Japanese with English abstract).

Liu, H., Shimozono, T., and Takagawa, T., 2013. The 11 March 2011 Tohoku Tsunami Survey in Rikuzentakata and Comparison with Historical event. *Pure and Applied Geophysics*, Vol. 170, pp. 1033-1046.

Mahendra, R. S., Mohanty, P. C., Bisoyi, H., Kumar, T. S. and Nayak, S., 2011. Assessment and management of coastal multi-hazard vulnerability along the Cuddalore Villupuram, east coast of India using geospatial techniques, *Ocean & Coastal Management,* Vol. 54 No. 4, pp. 302-311. http://dx.doi.org/10.1016/j.ocecoaman.2010.12.008.

Mangoua F. H., and Goïta K., 2008, A comparison between Canadian Digital Elevation data (CDED) and SRTM data of Mount Carleton in New Brunswick (Canada). *The International Archives of the Photogrammetry, Remote Sensing and Spatial Information Sciences. Vol. XXXVII. Part B4,* Beijing.

Massonnet, D., Rossi, M., Carmona, C., Adragna, F., Peltzer, G., Fiegl, K., and Rabaute, T., 1993. The displacement field of the Landars earthquake mapped by radar interferometry, *Nature*, 364, pp.138-142.

Matsuoka, M., and Nojima, N., 2009. Estimation of building damage ratio due to earthquakes using satellite L-band SAR imagery, *Proceedings of the 7th International Workshop on Remote Sensing and Disaster Response*, University of Texas, Texas, United States, 22−23 October 2009.

McAdoo, B., G., Richardson, N., and Borrero, J., 2007. Inundation Distances and Run-up Measurements from ASTER, QuickBird and SRTM Data, Aceh Coast, Indonesia. International Journal of Remote Sensing, 28 (13-14), 2961 – 2975.

Menard, S., 1995. Applied logistic regression analysis. Sage University Paper Series on Quantitative Applications in Social Sciences, vol. 106. Thousand Oaks, California. 98 pp.

Michael de Smith and Paul Longley, and Mike Goodchild, 2006. Geospatial Analysis - A comprehensive guide to principles, technique and software tools, A free web-based GIS resource -. University College London, UC Santa Barbara, Tehe Winchelsea Press 2006-2013.

Mikami, T., Shibayama, T. and Esteban, M., 2012. Field survey of the 2011 Tohoku earthquake and tsunami in Miyagi and Fukushima Prefecture, *Coastal Engineering Journal, World Scientific Publishing Company and Japan Society of Civil Engineers,* Vol. 54 No. 1, pp. 26.

Mori, N., and Takahashi, T., 2012. Nationwide post event survey and analysis of the 2011 Tohoku earthquake and tsunami, *Coastal Engineering Journal, World Scientific Publishing Company and Japan Society of Civil Engineers,* Vol. 54 No. 4, pp. 27. http://dx.doi.org/10.1142/S0578563412500015.

Mori, N., Takahashi, T., Yasuda, T. and Yanagisawa, H., 2011. Survey of 2011 Tohoku earthquake tsunami inundation and run-up, *Geophys. Res. Lett,* Vol. 38, L00G14, doi: 10.1029/2011GL049210.

Mori, N. and Takahashi, T., 2011. Nationwide Field Survey of the 2011 Off the Pacific Coast of Tohoku Earthquake Tsunami, The 2011 Tohoku Earthquake Tsunami Joint Survey Group, *Journal of Japan Society of Civil Engineers*, Series B, Vol. 67, No.1 pp.63-66.

Nassel M., and Voigt S., 2006. Vulnerability assessment of the built environment. In: Birkmann J, Fernando N,Hettige S, Amarasinghe S, Jayasingham T, Paranagama D, Nandana MDA, Nassel M, Voigt S, Grote U, Engel S, Schraven B, Wolferts J (eds) Rapid and multidimensional vulnerability assessment in Sri Lanka at the local level. UNU-EHS, Colombo, pp 10–22.

National Aeronautics and Space Administration (NASA), 2011. Data Users Handbook-Data Products, Chapter11, 2011. http://landsathandbook.gsfc.nasa.gov/pdfs/Landsat7_Handbook.pdf]. Accessed 14 October 2011.

National Geophysical Data Center / World Data Service (NGDC/WDS), 2014. Global Historical Tsunami Database. National Geophysical Data Center, NOAA. doi:10.7289/V5PN93H7 [accessed 4 March 2014].

National Police Agency of Japan, 2011. Damage situation and police countermeasures associated with 2011 Tohoku district - off the Pacific Ocean earthquake, July 5. Accessed July 5, 2011 from http://www.npa.go.jp/archive/keibi/biki/index_e.htm

News & information from the Oregon Department of Geology and Mineral Industries WINTER 2012 Cascadia is published by the Oregon Department of Geology and Mineral Industries. 800 NE Oregon Street, #28, Suite 965, Portland, OR 97232.

P. Schmidt-Thome (editor), 2006. Natural and Technological Hazards and Risks Affecting the Spatial Development of European Regions, Geological Survey of Finland. Special Paper 42.

Papathoma, M., Dominey-Howes, D., Zong, Y. and Smith, D., 2003. Assessing tsunami vulnerability, an example from Herakleio, Crete, *Nat. Hazards Earth Syst. Sci*., Vol. 3, pp. 377–389. http://dx.doi.org/10.5194/nhess-3-377-2003.

Papathoma, M., and Dominey-Howes, D., 2003. Tsunami vulnerability assessment and its implications for coastal hazard analysis and disaster management planning, Gulf of Corinth, Greece, *Natural Hazards and Earth System Sciences,* Vol. 3 No. 6, pp. 733-747.. http://dx.doi.org/10.5194/nhess-3-733-2003.

Pelling, M., 2003. The vulnerability of Cities: Natural Disasters and Social Resilience, Earthscan Publication, London.

Proctor, W., 2000. Towards sustainable forest management—an application of multi-criteria analysis to Australian forest policy. In: Third International Conference of the European Society for Ecological Economics, May 3--6, Vienna, Austria.

Qi, J., Chehbouni, A., Huete, A., R., Kerr, Y., H., and Sorooshian, S., 1994. A Modified Soil Adjusted Vegetation Index, *Remote Sens. Environ.*, vol. 48, pp. 119−126.

Rao, M., Sastry, S., V., C., Yadar, P., D., Kharod, K., Pathan, S., K., Dhinwa, P.,S., Majumdar, K.,L., Sampat Kumar, D., Patkar, V., N., and Phatak, V., K., 1991. A Weight Index Model for Urban Suitability Assessment – a GSI Approach, Bombay Metropolitan Regional Developtment Authority, Bombai, India.

Reuter, H., I., Nelson, A., and Jarvis, A., 2007. An evaluation of void filling interpolation methods for SRTM data. International Journal of Geographical Information Science Volume 21 Issue 9, January 2007 Pages 983-1008.

Romer, H., Willroth, P., Kaiser, G., Vafeidis, A.T., Ludwig, R., Sterr, H. and Diez, J.R, 2012. Potential of remote sensing techniques for tsunami hazard and vulnerability analysis - a case study from Phan-Nga province, Thailand, *Natural Hazards and Earth System Sciences,* Vol. 12 No. 6, pp. 2103-2126.

Saaty, T., L., 1980. The Analytic Hieharchy Process, Planning, Priority Setting, Resource Allocatio,. McGraw-Hill, New York.

Saaty, T., L., 1982. Decision Making for Leaders; The Analytical Hierarchy Process for Decisions in a Complex World, RWS Publication, Pittsburgh.

Saaty, T., L., and Vargas, L. G., 1991. Prediction, Projection, and Forecasting: Application of The Analytic Hierarchy Process in Economics, Finance, Politics, Games, and Sports, Kluwer Academic Publishers, Boston.

Saaty T., L., 1996. Decision Making for Leaders: The Analytical Hierarchy Process for Decisions in a Complex World, The Analytical Hierarchy Process Series, RWS Publication, 1996.

Saaty T., L., 1997. A Scaling Method for Priorities in Hierarchical Structures, *Journal of Mathematical Psychology*, Vol. 15, No. 3, 1977, pp. 234-281. http://dx.doi.org/10.1016/0022-2496(77)90033-5.

Saaty, T., L., 2003. Decision-making with the AHP: why is the princippal eigenvector necessary, *European Journal of Operational Research,* Vol. 145, pp. 85-91. http://dx.doi.org/10.1016/S0377-2217(02)00227-8.

Sah, A., K., Sah, B., P., Honji, K., Kubo, N., and Senthil, S., 2012. Semi-automated cloud/shadow removal and land cover change detection using satellite imagery, *International Archives of the Photogrammetry, Remote Sensing and Spatial Information Sciences*, vol. XXXIX-B7, XXII ISPRS Congress, Melbourne, Australia, 25 August–01 September 2012, pp. 335−340.

Sertel E., 2010. Accuracy assessment of ASTER GLOBAL DEM over Turkey, *A special joint symposium of ISPRS Technical Commission IV & AutoCarto in conjunction with ASPRS/CaGIS,* Fall Specialty Conference November 15-19, 2010 Orlando, Florida.

Shaw, G., and Wheeler, D., 1985, Statistical Techniques in Geographical Analysis, Chichester: Wiley.

Sinaga, T. P., Adhi, N., Yang-Won Lee, and Yongcheol, S., 2011. GIS mapping of tsunami vulnerability: case study of the Jembrana Regency in Bali, Indonesia, *KSCE Journal of Civil Engineering,* Vol. 15 No. 3, pp. 537-543.http://dx.doi.org/10.1007/s12205-011-0741-8.

Smith, M., Goodchild, M. F. and Longley, P. A., 2007. Geospatial Analysis; a Comprehensive Guide to Principle, Techniques and Software Tools, Matador, Leicester, UK.

Snohomish County Natural Hazard Mitigation Plan Update, 2010. “Planning-Area-Wide Elements”, Volume 1:Part 2 - Risk Assessment. Chapter 16 - Tsunami/Seiche. Snohomish County Department of Emergency Management. Online

government infrmation and service. http://www1.co.snohomish.wa.us/Departments/Emergency_Management/Information/Plans_Reports/. Accessed 18 July 2013.

Strunz, G., Post, J., Zosseder, K., Wegscheider, S., Muck, M., Riedlinger, T., Mehl, H., Dech, S., Birkmann, J., Gebert, N., Harjono, H., Anwar, H. Z., Sumaryono, Khomarudin, R. M. and Muhari, A., 2011. Tsunami risk assessment in Indonesia, *Natural Hazards and Earth System Science,* Vol. 11, pp. 67-82. http://dx.doi.org/10.5194/nhess-11-67-2011.

Suppasri, A., Koshimura, S., Matsuoka, M., Gokon, H., and Kamthonkiat, D., 2012. Application of Remote Sensing for Tsunami Disaster, Remote Sensing of Planet Earth, Dr Yann Chemin (Ed.), ISBN: 978-953-307-919-6, InTech, Available from: http://www.intechopen.com/books/remotesensing-of-planet-earth/application-of-remote-sensing-for-tsunami-disaster.

Tachikawa T., Kaku, M., Iwasaki, A., Gesch, D., Oimoen, M., Zhang, Z., Danielson, J., Krieger, T., Curtis, B., Haase, J., Abrams, M., Crippen R., and Carabajal, C., 2011. ASTER Global Digital Elevation Model Version 2 - Summary of Validation Results, August 31, 2011, the NASA Land Processes Distributed Active Archive Center and the Joint Japan-US ASTER Science Team. https://lpdaacaster.cr.usgs.gov/GDEM/Summary_GDEM2_validation_report_final.pdf.

Thirumalaivasan D., Karmegam, M., and Venugopal, K., 2003. AHP-DRASTIC: software for specific aquifer vulnerability assessment using DRASTIC model and GIS. Environmental Modelling & Software 18 (2003) 645–656.

Tronin A., 2010. Satellite remote sensing in seismology. A review. Remote Sensing 2:124–150.

Tsuyoshi H. and A. Iwamatsu, 2012. Detailed Map of the Impacts of the 2011 Japan Tsunami. Vol. 1: Aomori, Iwate and Miyagi Prefecture, Kokon-shoin Publishers Ltd., Tokyo.

Tucker C. J., 1979. Red and Photographic Infrared Linear Combinations for Monitoring Vegetation, *Remote Sensing of Environment*, Vol. 8, No. 2, 1979, pp. 127-150. http://dx.doi.org/10.1016/0034-4257(79)90013-0.

Tucker, C.J, Newcomb, W.W, Los, S.O., and Prince, S.D., 1991. Mean and inter-year variation of growing-season normalized difference vegetation index for the Sahel 1981-1989, *International Journal of Remote Sensing* 1991, Vol. 12, 1113-1115. http://dx.doi.org/10.1080/01431169108929717.

Turner, B. L., and Kasperson, R. E., 2003. A framework for vulnerability analysis in sustainability science. Proceedings Of The National Academy Of Sciences Of The United States Of America 100(14): 8074-8079.

UN - ISDR (2004). Living with Risk, UN.
http://www.unisdr.org/eng/about_isdr/bd-lwr-2004-eng.htm.

UNDP, 2004. Reducing Disaster Risk a challenge for development. A Global Report. United Nations Development Programme Bureau for Crisis Prevention and Recovery.

UNU-EHS. UNU. No 4/2006.

United Nations-International Strategy for Disaster Reduction (UN-ISDR), 2005. United Nations. Bureau for Crisis Prevention and Recovery. Reducing Disaster Risk: A Challenge for Development.

United Nations Disaster Relief Coordinator (UNDRO), 1991. Mitigation Natural Disasters: Phenomena, Effects and Options, A Manual for Policy Makers and Planners, United Nations Publication, NewYork.

Usman, F., and Murakami, K., 2011. Preliminary evaluation for strategy on coastal vegetation belt againt tsunami hazard in Pacitan, Indonesia, *European Journal of Scientific Research*, vol. 63, no. 4, pp. 530−542.

Van Zuidam, R. A., 1983. *Guide to Geomorphologic - Aerial Photographic Interpretation and Mapping,* International Institute for Geo-Information Science and Earth Observation, Enschede, The Netherlands.

Vicki S. McConnell, 2012. Notes from your State Geologist — Building a Culture of Preparedness. Published by the Oregon Department of Geology and Mineral Industries. Oregon.

Villagrán de Leon, J. C., 2006. Vulnerability A Conceptual and Methodological Review.

Wood, N. and Stein, D., 2001. A GIS-based vulnerability assessment of Pacific Northwest ports and harbours to tsunami hazards, in: ITS 2001 Proceedings, Session 1, 1–13, 367–374.

Woodcock, C. E., Strahler, A. H., and Jup, D.L., 1988. The use of Variograms in Remote Sensing: I. Scene Models and Simulted Images. Remote Sensing of Environment 25:323-348.

Yamazaki, F., Yano, Y., and Matsuoka, M., 2005. “Visual damage interpretation of buildings in Bam city using Quickbird images following the 2003 Bam, Iran earthquake,” *Earthquake Spectra*, vol. 21, no. S1, pp. S329−S336.

Yamazaki, F., Kouchi, K. and Matsuoka, M., 2006. Tsunami damage detection using moderate-resolutuion satellite imagery, *Proceeding of the 8th U.S. National Conference on Earthquake Engineering*, California, US.

Yamazaki, F., and Matsuoka, M., 2007. Remote sensing technology in post-disaster damage assessment, *Journal of Earthquakes and Tsunamis*, *World Scientific Publishing Company*, vol. 1, no. 3, pp. 193−210.

Yeh, H., Sato, S., and Tajima, Y., 2013. The 11 March 2011 East Japan Earthquake and Tsunami: Tsunami Effect on Coastal Infrastructure and Buildings. *Pure and Applied Geophysics*, Vol. 170, pp. 1019-1031.

Yeh, H., and Stein, R., 2011. Presentations, Seismic Risk Mitigation Leadership Forum, San Francisco, 5/2-3. Oregon State University and USGS.

Youssef, A. M., Pradhan, B. and Tarabees, E., 2010. Integrated eveluation of urban development suitability based on remote sensing and GIS techniques: constribution from the analytic hierarchy process, *Arab J Geosci,* Vol. 4, pp. 463-473.